

PhD Thesis

# Falling Weight Deflectometer tests on multi-layered pavement structures: Innovative experiments and multi-method structural simulations

submitted in satisfaction of the requirements for the degree  
Doctor of Science in Civil Engineering  
of the TU Wien, Faculty of Civil and Environmental Engineering

---

Dissertation

## Fallgewichtsdeflektometerversuche auf mehrschichtigen Fahrbahnkonstruktionen: Innovative Experimente und multi-methodische Struktursimulationen

ausgeführt zum Zwecke der Erlangung des akademischen Grads  
Doktor der technischen Wissenschaften  
eingereicht an der TU Wien, Fakultät für Bau- und Umweltingenieurwesen

Dipl.-Ing. **Rodrigo Díaz Flores**

Matr.Nr.: 01529689

- Betreuung: Univ. Prof. Dipl.-Ing. Dr. techn. **Bernhard L.A. Pichler**  
Ao. Univ. Prof. Dipl.-Ing. Dr. techn. **Mehdi Aminbaghai**  
Institut für Mechanik der Werkstoffe und Strukturen  
Technische Universität Wien  
Karlsplatz 13/202, 1040 Wien, Österreich
- Begutachtung: Univ. Prof. Dipl.-Ing. Dr. techn. **Benjamin Kromoser**, B.Sc.  
Institut für Hochbau, Holzbau und kreislaufgerechtes Bauen  
Universität für Bodenkultur Wien  
Peter-Jordan-Straße 82, 1190 Wien, Österreich
- Begutachtung: Univ. Prof. Dipl.-Ing. Dr. techn. **Bernhard Hofko**  
Institut für Verkehrswissenschaften  
Technische Universität Wien  
Lilienthalgasse 14, OC, E230-3, 1030 Wien, Österreich

Wien, im Februar 2023

---



# Acknowledgements

At the end of this incredible and exciting journey, I look back with the utmost gratitude to all those persons and moments that have accompanied me through the years. It was them who walked with me and guided me along the way. I hereby name only a few, without whom it would not have been possible to endeavor this challenge.

To my supervisors, Bernhard Pichler and Mehdi Aminbaghai, I express my deepest gratitude. Your advice, mentoring, dedication, and passion for science has given me the inspiration to become better every day. I specially thank you for teaching me the craft of writing scientific papers, and am very grateful for the countless hours of discussion, your prompt advices, your patience, your amazing ideas, and your permanent readiness to help me, whatever the circumstance. I will always cherish these moments.

To the co-authors of the papers that comprise this thesis: Valentin Donev, Lukas Eberhardsteiner, Luis Zelaya-Lainez, Christian Hellmich, Ronald Blab, Martin Buchta, and Raphael Höller, I thank you. Your input was pivotal for the success of this work. I look forward to future collaborations strengthened by our shared experiences. A special thanks is dedicated to Franz-Josef Ulm for various fruitful discussions, leading to a deeper understanding of the physical problem that we have attempted to solve. My gratitude is also expressed to the reviewers of this thesis, Bernhard Hofko and Benjamin Kromoser.

To the colleagues located in the Science Center from the IMWS and from the IVWS, as well as the colleagues from Nievelt GmbH, who have performed many of the laboratory tests presented, and who accompanied me to install sensors at whatever time and place that meant, I am sincerely grateful: Olaf Lahayne, Wolfgang Dörner, Dominic Hassan, Michael Haminger, Constantin Kreil, as well as Stefan Hofbauer, Bernhard Hadler, and David Valentin.

To my colleagues from the Baustatik-Team: Sophie Schmid and Maximilian Sorgner. Thank you for making me learn to enjoy even correcting exams. Your support has gone much beyond our work together. May our future collaborations, conversations, and scientific discussions be as exciting and fruitful as the ones we have had during these years. To Nabor, Petr, and all the other fellow colleagues at the IMWS: Thank you for making my days at the institute more enjoyable, as well your support whenever I needed it. To Martina Pöll, Gabriele Ostrowoski, and Astrid Schuh, for the help regarding administrative issues related to project and academic affairs, as well as conference planning. To David Kaufmann and Jan Vales, for the technical support, especially needed during the last few years.

Finally, my warmest gratitude goes to my friends, for their kindness; to my girlfriend, Anna, for motivating me, staying by my side, and keeping me sane; and to my family, for their everlasting support and their unconditional tender affection, which I treasure wherever we may be. All that I am, I owe to you. I dedicate and celebrate this success with all of you.



# Abstract

Falling Weight Deflectometer (FWD) tests are non-destructive in situ experiments performed to gain insight into the structural health of rigid and flexible pavement structures. The impact of the falling weight induces a damped vibration of the hit pavement structure. Displacement sensors called geophones measure the maximum deflections at specific distances from the axis of the falling weight along the driving direction. Two associated challenges provide the motivation for the present thesis: (i) As regards concrete slabs of rigid pavements, the described standard FWD test cannot detect potential asymmetries of the structural behavior. (ii) Performing *nominally identical* FWD tests on *the same* multi-layered pavement structure, but at different dates, usually yields *different* surface deflections. The present thesis tackles these two challenges in the context of engineering mechanics approaches which combine innovative experimental techniques and efficient structural simulations performed with multiple methods.

Chapter 2 deals with quantification of asymmetries of the structural behavior of rigid pavement structures where the topmost layer consists of rectangular concrete slabs. The main contribution is an experimental innovation: During central FWD tests, the deflections are measured along *eight different radial directions*, and at nine different distances from the center of the falling weight. This results in a dense grid of points at which deflections are measured. The collected experimental data enable the unprecedented assessment of asymmetries of the behavior of the tested pavement structures, based on a new deflection basin parameter called asymmetry indicator. An old concrete slab, which had been in service for 22 years, shows significant asymmetries. A newly built slab, in turn, is found to behave in a virtually double symmetric fashion, albeit not in a radial-symmetric fashion. This provides the motivation to use a finite-slab-size model for the elastostatic re-analysis of the FWD test of the new slab. The model consists of a Kirchhoff-Love plate with free edges, supported by a Winkler foundation. The stiffness of the plate is set equal to that of the concrete slab. The model reproduces the measured deflections accurately, after optimization of two variables: the modulus of subgrade reaction and a newly introduced auxiliary surface load. Thus, the proposed model provides an interesting alternative to the standard radial-symmetric “dense-liquid” modeling approach, referring to an *infinite* plate on a Winkler foundation, where the stiffness of the plate and the modulus of subgrade reaction are optimized in order to best reproduce measured deflections.

In Chapter 3, FWD tests with a T-shaped arrangement of geophones are proposed with the aim to combine the advantages of (i) the standard FWD testing approach, namely: rapid in situ characterization, and (ii) the innovative FWD test protocol of Chapter 2, namely: expressiveness regarding the assessment of asymmetric structural behavior. The main innovation refers to a new arrangement of the geophones: seven are placed along the driving direction, and another two along an axis orthogonal to the driving direction, one left and one right of the falling weight. In order to optimize the distance of the lateral geophones from the center of the falling weight, FWD tests with multi-directional measurements of deflections are performed on ten slabs: four newly-installed slabs, and six decades-old slabs. Two additional deflection basin parameters are introduced: (i) the effective asymmetry index,  $\mathcal{A}_{28}^*$ , which summarizes all asymmetries detected by means of FWD tests with multi-directional measurement of deflections into just one expressive number, and (ii) the lateral asymmetry index, LASIX, which is customized for the evaluation of FWD tests with a T-shaped arrangement of geophones. The distance of the two lateral geophones from the center of the falling weight is optimized such that corresponding values of LASIX correlate best with values of the effective asymmetry index. The optimal distance is found to amount to 1.20 m. The origin of the asymmetric behavior of the slabs is explored. Small values of LASIX, representative for mild asymmetries, emerge mostly due to the finite size of the slabs

and/or slab-to-slab interaction. Large values of LASIX, representative for strong asymmetries, emerge due to the additional long-term exposure of the pavement structure to service loads that cause a non-uniform degradation of the subgrade. Values of LASIX are shown to correlate well with the coefficients of directional variation the AREA7 parameter which is used in the standard dense-liquid model as the basis for quantification of the modulus of subgrade reaction. Thus, LASIX allows for clarifying whether the assumption of a uniform modulus of subgrade reaction is reasonable or questionable. The recommended T-shaped arrangement of geophones is also appealing from the viewpoint of practical applicability, because it renders highly automated and, therefore, rapid FWD testing feasible, with on-site efforts equal to those known from standard FWD testing, while allowing for the unprecedented quantification of asymmetric slab behavior.

Chapter 4 is devoted to the innovative instrumentation of three FWD field-testing sites. One rigid and two flexible pavement structures were equipped with temperature sensors, asphalt strain gauges, and accelerometers. This allows for capturing the temperature distribution inside the pavement structure, the deformation of asphalt at selected points during FWD testing, and the propagation of fronts of elastic waves travelling through individual layers of the pavement structure. The experience with the design, the instrumentation, and the operation of the field-testing sites is shared. As regards the installation of asphalt strain gauges, it is recommended to install steel dummies as place-holders into the surface of hot asphalt layers, immediately after their construction and right before their compaction, and to replace the dummies by the actual sensors right before the installation of the next layer. First data from dynamic testing at the field-testing sites are presented. FWD tests performed at different temperatures deliver, as expected, different surface deflections. Sledgehammer strokes onto a metal plate, transmitted to the pavement via a rubber pad, are introduced as a cheap, simple-to-perform, and quickly repeatable dynamic test method for measuring the speed of longitudinal elastic waves propagating from one accelerometer to another. This allows for quantifying the stiffness of individual layers of pavement structures, based on the theory of propagation of elastic waves through isotropic media. As regards flexible pavements, it is found that the seasonal variation of FWD results can be primarily traced back to the temperature-dependent stiffness variation of asphalt layers, as other layers present significantly milder stiffness variations. As regards rigid pavements, the sledgehammer tests are shown to allow for situations with full-face contact along all interfaces from situations suffering from temperature-gradient-induced curling of concrete slabs, leading to partial loss of contact along an interface between two neighboring layers.

Chapter 5 refers to the asphalt-related temperature correction of deflections measured during FWD testing of a concrete-over-asphalt composite pavement structure. Five FWD tests were performed at one of the field-testing sites described in Chapter 4 (rigid pavement structure). These tests were carried out in summer, winter, and transitional periods. The measured deflections are influenced by temperature-dependent stiffness changes of the asphalt layer and by seasonal stiffness changes of the subgrade. The main innovation refers to correcting the measured deflections such that they contain information on the seasonal stiffness changes of the subgrade only. To this end, several steps are necessary. At first, the stiffnesses of the materials of the four topmost layers of the pavement structure are determined as follows. Two types of concrete and asphalt are characterized in the laboratory by means of non-destructive uniaxial compression tests and cyclic tension-compression tests (Dynamic Mechanical Analysis), respectively. The stiffness of the cement-stabilized layer is quantified in situ using the sledgehammer tests described in Chapter 4. The seasonally variable elastic modulus of the subgrade, together with its constant thickness, are back-calculated using multi-layered elastostatic simulations, such that simulated deflections agree almost perfectly with measured deflections. The fitted model is corroborated, because predicted strains of asphalt agree sufficiently well with in situ measurements. The multi-layered model is used to compute deflections for asphalt temperatures between  $-5^{\circ}\text{C}$  and  $+30^{\circ}\text{C}$ , while the

thicknesses and the stiffnesses of all other layers are set equal to seasonal averages. The numerical results allow for developing a Westergaard-inspired formula that translates measured deflections into corrected deflections which refer to an asphalt temperature of 20°C. Thus, the remaining seasonal variation of the corrected deflections refers to the seasonal variation of the stiffness of the subgrade. The AREA4 method of the dense-liquid model is used to quantify, from the corrected deflections, values of a uniform spring stiffnesses per unit area. These  $k$ -values correlate well with the seasonally varying stiffness of the subgrade. The elaborated knowledge regarding the influence of the stiffness of asphalt and of the subgrade, respectively, on surface deflections, allows for the development of another correction approach. It is particularly well suited for application in the engineering practice, because it is very simple and requires only measured deflections as required input. This approach consists of uniformly increasing or decreasing the deflections measured during FWD testing on a reference date, such that the shifted deflection at a distance of 1500 mm from the center of the falling weight, is equal to the deflection measured at that distance during FWD testing performed on any other date. Again,  $k$ -values are quantified from corrected deflections, and they are shown to correlate reasonably well with seasonal stiffness changes of the subgrade. The developed method is also appealing because it provides corrected deflections (rather than corrected values of quantities derived from deflections), and this allows for applying all methods typically used for the interpretation and/or evaluation of FWD test results, including deflection basin parameters and structural models.





# Kurzfassung

Fallgewichtsdeflektometer (FWD)-Versuche sind zerstörungsfreie in-situ-Experimente, die durchgeführt werden, um Einblick in den strukturellen Zustand starrer und flexibler Fahrbahnkonstruktionen zu erhalten. Der Aufprall des Fallgewichts erzeugt eine gedämpfte Schwingung der getroffenen Fahrbahnkonstruktion. Verschiebungsmessensoren, sogenannte Geophone, messen die maximalen Auslenkungen in bestimmten Abständen von der Fallgewichtsachse entlang der Fahrtrichtung. Zwei damit verbundene Herausforderungen bilden die Motivation für die vorliegende Arbeit: (i) Bei Betonplatten starrer Fahrbahnkonstruktionen kann der beschriebene Standard-FWD-Versuch mögliche Asymmetrien des Tragverhaltens nicht erkennen. (ii) Die Durchführung von *nominell identischen* FWD-Versuchen auf *derselben* mehrschichtigen Fahrbahnkonstruktion, aber zu unterschiedlichen Zeitpunkten, ergibt normalerweise *unterschiedliche* Oberflächendurchbiegungen. Die vorliegende Dissertation befasst sich mit diesen beiden Herausforderungen im Kontext ingenieurmechanischer Ansätze, die innovative experimentelle Versuchsprotokolle und effiziente Struktursimulationen kombinieren, die mit mehreren Methoden durchgeführt werden.

Kapitel 2 befasst sich mit der Quantifizierung von Asymmetrien des Tragverhaltens starrer Fahrbahnkonstruktionen, wobei die oberste Schicht aus rechteckigen Betonplatten besteht. Der Hauptbeitrag ist eine experimentelle Innovation: Bei in Betonplattenmitte durchgeführten FWD-Versuchen werden die Durchbiegungen in *acht verschiedenen radialen Richtungen* und in neun verschiedenen Abständen vom Zentrum des Fallgewichts gemessen. Daraus ergibt sich ein dichtes Gitter von Punkten, an denen Durchbiegungen gemessen werden. Die dort gewonnenen experimentellen Daten erlauben die bisher unmögliche Bewertung von Asymmetrien des Verhaltens der getesteten Fahrbahnkonstruktionen, basierend auf einem neuen Deflektionsmuldenparameter, der als Asymmetrie-Indikator bezeichnet wird. Eine alte Betonplatte, die 22 Jahre in Betrieb war, weist erhebliche Asymmetrien auf. Eine neu gebaute Platte verhält sich wiederum praktisch doppelsymmetrisch, wenn auch nicht radialsymmetrisch. Das liefert die Motivation, ein Modell mit endlicher Plattengröße für die elastostatische Nachrechnung des FWD-Versuchs auf der neuen Platte zu verwenden. Das Modell besteht aus einer Kirchhoff-Platte mit freien Rändern, die auf einer Winkler-Bettung gelagert ist. Die Steifigkeit der simulierten Platte wird gleich jener der realen Betonplatte gesetzt. Nach Optimierung von zwei Variablen: dem Bettungsmodul und einer neu eingeführten Oberflächenhilfslast, reproduziert das Modell die gemessenen Durchbiegungen sehr zufriedenstellend. Somit bietet das vorgeschlagene Modell eine interessante Alternative zum üblicherweise verwendeten, radialsymmetrischen *dense-liquid*-Modell (*unendliche* Platte auf Winkler-Bettung), bei dem die Steifigkeit der Platte und der Bettungsmodul optimiert werden, um gemessene Durchbiegungen bestmöglich zu reproduzieren.

In Kapitel 3 werden FWD-Versuche mit einer T-förmigen Anordnung von Geophonen vorgeschlagen, gleichsam als Kombination der Vorteile (1) des Standard-FWD-Versuchs, nämlich: schnelle in-situ Charakterisierung und (2) des innovativen FWD-Testprotokolls von Kapitel 2, nämlich: Aussagekraft bezüglich der Bewertung von asymmetrischem Strukturverhalten. Die Hauptinnovation bezieht sich auf eine neue Anordnung der Geophone: Sieben sind entlang der Fahrtrichtung platziert, und zwei weitere entlang einer Achse orthogonal zur Fahrtrichtung, eines links und eines rechts des Fallgewichts. Um den Abstand der seitlichen Geophone vom Zentrum des Fallgewichts zu optimieren, werden FWD-Versuche mit multidirektionalen Durchbiegungsmessungen an zehn Platten durchgeführt: vier neu gebaute Platten und sechs alte Platten, die jahrzehntelang in Betrieb waren. Zwei zusätzliche Deflektionsmuldenparameter werden eingeführt: (i) der effektive Asymmetrieindex,  $\mathcal{A}_{28}^*$ , der alle Asymmetrien, die mittels FWD-Versuchen mit multidirektionaler Messung von Durchbiegungen festgestellt werden können, in nur eine aussagekräftige Zahl zusammenfasst und (ii) der laterale Asymmetrieindex,

LASIX, der für die Auswertung von FWD-Versuchen mit einer T-förmigen Anordnung von Geophonen maßgeschneidert ist. Der Abstand der beiden seitlichen Geophone vom Zentrum des Fallgewichts wird so optimiert, dass entsprechende Werte von LASIX bestmöglich mit Werten des effektiven Asymmetrieindex korrelieren. Als optimal erweist sich ein Abstand von 1,20 m. Weiters wird der Ursprung des asymmetrischen Verhaltens der Platten untersucht. Kleine LASIX-Werte, die für leichte Asymmetrien stehen, treten hauptsächlich aufgrund der endlichen Größe der Platten und/oder der Interaktion zwischen benachbarten Platten auf. Große LASIX-Werte, die für starke Asymmetrien stehen, entstehen durch die zusätzliche Langzeitbeanspruchung der Fahrbahnkonstruktion durch Gebrauchslasten, die zu einer ungleichmäßigen Schädigung des Untergrunds führen. Die LASIX-Werte korrelieren nachweislich gut mit den Richtungsvariationskoeffizienten des Parameters AREA7, der im *dense-liquid*-Standardmodell als Grundlage für die Quantifizierung des Bettungsmoduls verwendet wird. Damit ermöglicht LASIX die Klärung, ob die Annahme eines einheitlichen Bettungsmoduls sinnvoll oder fraglich ist. Die empfohlene T-förmige Anordnung von Geophonen ist vom Blickwinkel der praktischen Anwendbarkeit attraktiv, da sie hochautomatisierte und daher schnelle FWD-Versuche durchführbar macht, wobei der Vor-Ort-Aufwand jenem von Standard-FWD-Versuchen entspricht und gleichzeitig ein noch nie dagewesenes Quantifizieren des asymmetrischen Plattenverhaltens ermöglicht.

Kapitel 4 ist der innovativen Instrumentierung von drei FWD-Feldmessstellen gewidmet. Ein starrer und zwei flexible Fahrbahnkonstruktionen wurden mit Temperatursensoren, Asphalt-Dehnungsmesssensoren und Beschleunigungsaufnehmern ausgestattet. Dies ermöglicht die Erfassung der Temperaturverteilung in der Fahrbahnkonstruktion, der Verformung des Asphalts an ausgewählten Punkten während der FWD-Versuche und der Ausbreitung von Fronten elastischer Wellen, die durch die Schichten der Fahrbahnkonstruktionen laufen. Die mit dem Entwurf, der Herstellung und dem Betrieb der Feldmessstellen gesammelten Erfahrungen werden geteilt. Hinsichtlich des Einbaus von Asphalt-Dehnungsmesssensoren wird empfohlen, in heiße Asphalt-schichten unmittelbar nach deren Einbau und unmittelbar vor deren Verdichtung Stahlattrappen als Platzhalter für die Asphalt-Dehnungsmesssensoren in die Oberfläche einzubauen und kurz vor Installation der nächsten Schicht durch den eigentlichen Sensor zu ersetzen. Erste Daten aus dynamischen Tests an den Feldmessstellen werden präsentiert. Bei unterschiedlichen Temperaturen durchgeführte FWD-Versuche liefern erwartungsgemäß unterschiedliche Oberflächendurchbiegungen. Schläge mit einem Vorschlaghammer auf eine Metallplatte, die über eine Hartgummiplatte auf die Fahrbahn übertragen werden, werden als kostengünstiges, einfach durchzuführendes und schnell wiederholbares dynamisches Testverfahren eingeführt. Die Versuche erlauben die Messung der Geschwindigkeit von elastischen Longitudinalwellen, die sich von einem Beschleunigungsaufnehmer zum anderen ausbreiten. Das ermöglicht die Quantifizierung der Steifigkeit einzelner Schichten von Fahrbahnkonstruktionen, basierend auf der Theorie zur Ausbreitung elastischer Wellen durch isotrope Materialien. Bei flexiblen Fahrbahnkonstruktionen wird gezeigt, dass saisonale Schwankungen der FWD-Ergebnisse hauptsächlich auf temperaturabhängige Steifigkeitsänderungen von Asphalt-schichten zurückzuführen sind, da andere Schichten deutlich geringere Steifigkeitsschwankungen aufweisen. Bei der starren Fahrbahnkonstruktion wird gezeigt, dass Vorschlaghammertests es ermöglichen, Situationen mit Vollflächenkontakt entlang aller Schichttrennflächen von Situation zu unterscheiden, bei denen es zu Temperaturgradienten-induziertem Aufwölben der Betonplatte kommt, was zu einem teilweisen Kontaktverlust entlang einer Schichttrennfläche führt.

Kapitel 5 bezieht sich auf die asphaltbezogene Temperaturkorrektur von Durchbiegungen, die während FWD-Versuchen auf einer Fahrbahnverbundkonstruktion gemessen wurden. An einer der im Kapitel 4 beschriebenen Feldmessstellen (starre Fahrbahnkonstruktion) wurden fünf FWD-Versuche im Sommer, im Winter bzw. in der Übergangszeit durchgeführt. Die gemessenen Durchbiegungen ergeben sich durch temperaturabhängige Steifigkeitsänderungen der

Asphaltschicht und durch jahreszeitliche Steifigkeitsänderungen des Untergrunds. Die wesentliche Neuerung besteht darin, die gemessenen Durchbiegungen so zu korrigieren, dass sie nur noch Informationen über die saisonalen Steifigkeitsänderungen des Untergrunds enthalten. Dazu sind einige Schritte erforderlich. Zuerst werden die Steifigkeiten der Materialien der vier obersten Schichten des Fahrbahnaufbaus wie folgt ermittelt. Zwei Betonarten und Asphalt werden im Labor durch zerstörungsfreie einachsige Druckversuche bzw. zyklische Zug-Druck-Versuche (Dynamisch-Mechanische Analyse) charakterisiert. Die Steifigkeit der zementstabilisierten Schicht wird in-situ mit den in Kapitel 4 beschriebenen Vorschlaghammerversuchen quantifiziert. Der jahreszeitlich veränderliche Elastizitätsmodul des Untergrunds wird zusammen mit seiner konstanten Dicke durch mehrschichtige elastostatische Simulationen zurückgerechnet, sodass die simulierten Verformungen nahezu perfekt mit den gemessenen Verformungen übereinstimmen. Die Aussagekraft des angepassten Modells wird dadurch bestätigt, dass vorhergesagte Asphaltdehnungen hinreichend gut mit in-situ-Messungen übereinstimmen. Das mehrschichtige Modell wird verwendet, um Durchbiegungen für Asphalttemperaturen zwischen  $-5^{\circ}\text{C}$  und  $+30^{\circ}\text{C}$  zu berechnen, während die Dicken und Steifigkeiten aller anderen Schichten mit konstanten saisonale Durchschnittswerten in Rechnung gestellt werden. Die numerischen Ergebnisse ermöglichen die Entwicklung einer von Westergaard inspirierten Formel zur Umwandlung von gemessenen Durchbiegungen in korrigierte Durchbiegungen, die sich auf eine Asphalttemperatur von  $20^{\circ}\text{C}$  beziehen. Somit resultieren die verbleibenden jahreszeitliche Schwankungen der korrigierten Durchbiegungen auf jahreszeitlichen Schwankungen der Steifigkeit des Untergrunds. Mit der AREA4-Methode des *dense-liquid*-Modells werden Bettungsmoduln aus den korrigierten Durchbiegungen quantifiziert. Diese Bettungsmoduln korrelieren gut mit saisonalen Schwankungen des Elastizitätsmoduls des Untergrunds. Die gewonnenen Erkenntnisse betreffend den Einfluss der Steifigkeit des Asphalts bzw. des Untergrunds auf die Oberflächendurchbiegungen ermöglichen die Entwicklung eines weiteren Korrekturansatzes. Er ist besonders gut für die Anwendung in der Ingenieurpraxis geeignet, da er sehr einfach ist und ausschließlich gemessene Durchbiegungen als Eingabewerte erfordert. Dieser Ansatz besteht darin, die bei einem FWD-Versuch an einem Referenzdatum gemessenen Durchbiegungen gleichmäßig zu erhöhen oder zu verringern, sodass die verschobene Durchbiegung, die sich auf einen Abstand von 1500 mm vom Zentrum des Fallgewichts bezieht, gleich jener Durchbiegung ist, die in dieser Distanz während eines FWD-Versuchs an einem anderen Datum gemessen wurde. Abermals werden Bettungsmoduln aus korrigierten Durchbiegungen quantifiziert, und es wird gezeigt, dass sie gut mit saisonalen Steifigkeitsänderungen des Untergrunds korrelieren. Das entwickelte Verfahren ist auch deshalb attraktiv, weil es korrigierte Durchbiegungen (anstelle von korrigierten Werten von aus Durchbiegungen abgeleiteten Größen) liefert, und somit die Anwendung aller Methoden ermöglicht, die üblicherweise für die Interpretation und/oder Auswertung von FWD-Versuchsergebnissen verwendet werden. Das schließt sowohl verschiedene Deflektionsmuldenparameter als auch diverse Strukturmodelle ein.



# Contents

<b>1</b>	<b>Introduction</b>	<b>1</b>
1.1	Motivation . . . . .	1
1.2	Back-calculation of subgrade properties . . . . .	1
1.3	Multi-directional and T-shaped arrangement of geophones during FWD tests . . . . .	4
1.4	Seasonal variations of FWD results - innovative instrumentation of FWD field-testing sites . . . . .	4
1.5	Outline . . . . .	6
1.5.1	Multi-directional Falling Weight Deflectometer (FWD) testing and quantification of the effective modulus of subgrade reaction for concrete roads . . . . .	7
1.5.2	T-shaped arrangement of geophones for rapid quantification of asymmetric behavior of concrete slabs in central FWD tests . . . . .	8
1.5.3	Instrumentation of field-testing sites for dynamic characterization of the temperature-dependent stiffness of pavements and their layers . . . . .	9
1.5.4	Asphalt-related temperature correction of deflections measured in central FWD tests on concrete-over-asphalt composite pavements . . . . .	10
<b>2</b>	<b>Multi-directional Falling Weight Deflectometer (FWD) testing and quantification of the effective modulus of subgrade reaction for concrete roads</b>	<b>11</b>
2.1	Introduction . . . . .	11
2.2	Multi-directional FWD Testing . . . . .	13
2.2.1	Test protocol . . . . .	13
2.2.2	Experimental Data from the New Plate . . . . .	15
2.2.3	Experimental Data from the Old Plate . . . . .	17
2.2.4	Asymmetries of the structural behavior of the tested plates . . . . .	18
2.2.5	Revisiting symmetry of the plate behavior based on hypothesis testing . . . . .	20
2.3	Structural analysis of the new plate . . . . .	22
2.3.1	Static structural analysis: identification of the modulus of subgrade reaction . . . . .	24
2.3.2	Static structural analysis: extension towards consideration of an auxiliary surface load . . . . .	24
2.3.3	Static structural analysis: effective modulus of subgrade reaction . . . . .	26
2.3.4	Dynamic structural analysis: effective modulus of subgrade reaction . . . . .	28
2.4	Conclusions . . . . .	30
Appendix 2.A	Results of multi-directional FWD testing on the new plate . . . . .	33
Appendix 2.B	Results of multi-directional FWD testing on the old plate . . . . .	36
Appendix 2.C	Convergence analysis . . . . .	38
Appendix 2.D	Fourier coefficients of the deflection ansatz of Eq. (2.15), $N = 33$ . . . . .	39

<b>3</b>	<b>T-shaped arrangement of geophones for rapid quantification of asymmetric behaviour of concrete slabs in central FWD tests</b>	<b>41</b>
3.1	Introduction . . . . .	41
3.2	Optimisation of a T-shaped arrangement of geophones for rapid quantification of the asymmetric behavior of concrete slabs in central FWD tests . . . . .	43
3.2.1	Detailed asymmetry characterisation of ten concrete slabs subjected to central FWD testing . . . . .	43
3.2.2	Quantification of the asymmetry of the structural behavior by means of the new deflection basin parameter $\mathcal{A}_{28}^*$ . . . . .	47
3.2.3	Quantification of asymmetric structural behavior based on T-shaped testing and the deflection basin parameter LASIX . . . . .	47
3.2.4	Optimal distance $c$ of the lateral geophones from the center of the slab . . . . .	49
3.2.5	Arrangement of the geophones remaining aligned with the driving direction . . . . .	50
3.3	Discussion . . . . .	54
3.3.1	Reasons for asymmetric slab behavior . . . . .	54
3.3.2	Back-calculation of subgrade properties based on deflections known from FWD testing . . . . .	55
3.3.3	Relation between LASIX and the coefficient of directional variation of AREA7 (“COVAREA7”) . . . . .	57
3.3.4	Variation of the modulus of subgrade reaction back-calculated from eight direction-specific values of AREA7 per slab . . . . .	59
3.3.5	Limitations and future outlook . . . . .	61
3.4	Conclusions . . . . .	61
	Appendix 3.A Results of multi-directional FWD testing of all slabs . . . . .	65
<b>4</b>	<b>Instrumentation of field-testing sites for dynamic characterization of the temperature-dependent stiffness of pavements and their layers</b>	<b>75</b>
4.1	Introduction . . . . .	75
4.2	Overview of the three field-testing sites . . . . .	77
4.2.1	Field-testing site #1 on motorway A10 . . . . .	78
4.2.2	Field-testing site #2 on motorway A3 . . . . .	79
4.2.3	Field-testing site #3 on expressway S31 . . . . .	81
4.3	Installation of the accelerometers . . . . .	83
4.3.1	State-of-the-art applications . . . . .	83
4.3.2	Theoretical fundamentals . . . . .	84
4.3.3	Sensor selection . . . . .	84
4.3.4	Data acquisition rate and system . . . . .	85
4.3.5	Sensor installation . . . . .	86
4.4	Installation of the asphalt strain gauges . . . . .	88
4.4.1	State of the art applications . . . . .	88
4.4.2	Sensor selection . . . . .	88
4.4.3	Design of the installation position of the strain gauges . . . . .	88
4.4.4	Installation method A: Cut, install, and cover after asphalt placement . . . . .	89
4.4.5	Installation method B: Installation in a fixation tool, before asphalt placement . . . . .	91
4.4.6	Installation method C: Use of steel dummy place-holders for the real sensors . . . . .	92
4.5	First data from dynamic testing at the field-testing sites . . . . .	93
4.5.1	Results from dynamic field testing on the rigid pavement . . . . .	93
4.5.2	Results from dynamic field testing on a flexible pavement . . . . .	96
4.6	Conclusions and future outlook . . . . .	100

<b>5 Asphalt-related temperature correction of deflections measured in central FWD tests on a concrete-over-asphalt composite pavement</b>	<b>103</b>
5.1 Introduction . . . . .	103
5.2 In situ and laboratory characterisation of the temperature-dependent stiffness of a composite pavement and its layers . . . . .	105
5.2.1 Field-testing site equipped with temperature sensors, strain gauges, and accelerometers (Donev et al., 2023) . . . . .	105
5.2.2 In situ stiffness characterisation of the composite pavement structure by means of FWD testing . . . . .	107
5.2.3 Laboratory stiffness characterisation of concrete by means of uniaxial compression tests . . . . .	108
5.2.4 Laboratory stiffness characterisation of asphalt by means of cyclic uniaxial tension-compression tests . . . . .	108
5.2.5 In situ stiffness characterisation of the cement-stabilized layer by means of accelerometer measurements recorded during sledgehammer tests . . . . .	111
5.3 Elastostatic simulations of the multi-layered pavement structure allowing for the derivation of an asphalt-related temperature correction of deflections measured during FWD testing . . . . .	112
5.3.1 Multi-layered simulations: a boundary value problem . . . . .	112
5.3.2 Back-calculation of subgrade properties from measured deflections and validation based on measured strains . . . . .	115
5.3.3 Development of an asphalt-related temperature correction for measured surface deflections . . . . .	118
5.3.4 Application of the asphalt-related temperature correction to deflections measured during FWD testing . . . . .	119
5.3.5 Quantification of the $k$ -value by means of the dense-liquid model and the AREA-method . . . . .	120
5.3.6 Correlation of stiffness properties quantified by means of multi-layered and dense-liquid models . . . . .	122
5.3.7 Robustness of results with respect to the uncertainty regarding $D$ . . . . .	123
5.4 Alternative correction approach requiring measured deflections only . . . . .	124
5.4.1 Influence of asphalt and subgrade stiffness on surface deflections . . . . .	124
5.4.2 Engineering correction, based on measured deflections only . . . . .	124
5.4.3 Application of the AREA4-approach for quantification of $k$ -values from corrected deflections . . . . .	125
5.5 Conclusions . . . . .	126
Appendix 5.A Solution of a multi-layered pavement structure subjected to a vertical surface load and rearrangement as transfer relations . . . . .	129
Appendix 5.B Effective bending stiffness of the sandwich plate consisting of the two topmost layers of concrete . . . . .	131
<b>6 Summary, conclusions, and outlook</b>	<b>133</b>
6.1 Experimental mechanics contributions . . . . .	133
6.2 Structural analysis of FWD tests . . . . .	136
6.3 Future outlook . . . . .	139
<b>Bibliography</b>	<b>141</b>

---

<b>Personal information</b>	<b>155</b>
Curriculum Vitae . . . . .	155
Scientific Dissemination . . . . .	156



# Chapter 1

## Introduction

### 1.1 Motivation

The attempt to mechanically characterize pavement structures has a near-century-old tradition. Ever since the first pioneering developments of Westergaard (1926, 1948), until the advent of modern soft-computing methods and artificial-intelligence-enhanced techniques, pavement engineers have developed increasingly more complex models that evaluate the current state of pavement structures and predict their long term performance with high accuracy. Such techniques require knowledge of the properties of the materials that constitute the structure. However, these properties are often difficult to obtain, given that the site-dependent level of compaction, humidity, temperature, and others typically affect a pavement's structural behavior. This context has given rise to the development of non-destructive tests performed in situ. Deflection-based tests are the common alternative of choice of such non-destructive tests, ever since a correlation was found between the deflections experienced by a pavement structure and its fatigue response (Hveem, 1955). Perhaps the most common deflection-based test is the Falling Weight Deflectometer (FWD). FWD tests are performed by letting a standardized weight impact a pavement (in the case of concrete slabs, this is generally the center of the slab) as it freely falls upon it from a defined height. The deflection histories at different distances from the location of impact of the falling weight are measured by geophones. The measured deflections may be used as indicators of the state of the pavement and its subgrade through the use of deflection-basin parameters or, alternatively, they conform the input for evaluation methods supported by complex back-calculation procedures.

### 1.2 Back-calculation of subgrade properties

Back-calculation methods attempt to approximate the deflections measured as accurately as possible by optimizing the stiffness and/or the the thickness of the subgrade and the layers within the pavement structure. The most popular mechanical models used for the back-calculation can be divided into two groups: (i) "Dense-liquid" models, which idealize the concrete pavement slabs as a plate on top of a bed of springs (Winkler foundation), see (Winkler, 1867; Biot, 1937; Vesić, 1961) for its theoretical basis and (Westergaard, 1926, 1948) for their first applications to pavement structures; and (ii) multi-layered models, resolving the actual nature of pavement structures in significantly greater detail. The latter were based on Boussinesq's theory (Boussinesq, 1885), first applied to pavement structures by Burmister (1945b,a), and further extended through the use of efficient layer stiffness matrices (Thomson, 1950; Haskell, 1953; Kausel and Roësset, 1981), arriving at explicit solutions for general surface and dislocation loads acting on a transversely

isotropic half-space (Pan, 1989a,b). “Dense-liquid” models usually optimize one or two variables, while multi-layered models include the optimization of the stiffness and/or the thickness of each of the many layers of a pavement structure. Both types of models may be seen as constituting two extremes in terms of pavement behavior (Ioannides, 2006). In sight of this, many researchers have attempted to develop models that were more complex than the models based on a Winkler foundation, but more practical than the multi-layered approach, while ensuring an accurate reproduction of the behavior of the pavement. The most prominent of these attempts include (i) the addition of a shear layer to reproduce the shear interactions in the support of the plate given by continuous layers, and which cannot be given by the separate springs of the Winkler model (Pasternak, 1954); and (ii) the addition of an extra bed of springs on top of the Pasternak foundation (Kerr, 1964, 1965), providing an even more realistic distribution of soil pressures, but with the disadvantage of using three optimization variables. However, the simplicity of the Winkler foundation and the derived “dense-liquid” models, coupled with its accuracy in reproducing the deflections of concrete pavement structures has rendered it the most popular model for rigid pavement structures.

“Dense-liquid” models are used almost exclusively on rigid pavements, where the concrete slab on the top may be realistically regarded as a plate. Below this plate, the whole pavement structure and the subgrade are idealized as a bed of separate springs with one *uniform* spring constant per unit area: the modulus of subgrade reaction. The back-calculation usually refers to the estimation of the stiffness of the plate (in many cases, *a priori* unknown) and of the modulus of subgrade reaction. The methods to obtain these properties rely on Westergaard’s solutions (Westergaard, 1926, 1948) for the deflections due to a circular uniform load applied in the center of the plate, either for the case of interior loading (Losberg, 1960) or of edge and corner loading (Ioannides, 1990). Typically, a value of the modulus of subgrade reaction is found either by fitting the measured deflections or by means of the AREA method. The latter is a closed-form method that uses a deflection-basin parameter called AREA (Hoffman and Thompson, 1980), and its unique relationship with the radius of relative stiffness  $l_k$  of the slab (Ioannides, 1990; Ioannides et al., 1989) to optimize the modulus of subgrade reaction and the stiffness of the plate (Hall, 1991; Darter et al., 1995; Hall et al., 1997). Both the AREA method and the best-fit method have been compared for different types of sensor configurations, slab sizes, and temperature profiles (Khazanovich et al., 2001), and constitute the current state-of-the-art in the context of the mechanistic-empirical design and evaluation of rigid pavements (Ioannides, 2006; Smith et al., 2017a). As for the application of the method, it is noteworthy that heat-conduction-induced curling of slabs and the load transfer via dowels and tie bars may considerably affect FWD measurements (Ioannides and Khazanovich, 1998; Khazanovich et al., 2001, 2003). Much of the recent work has therefore been devoted to the characterization of the influence of slab curling (Vandenbossche, 2007; Schmid et al., 2022), dynamic effects (Khazanovich, 2000a), and the load transfer efficiency of the slabs (Khazanovich et al., 2001; Setiawan, 2020; Muslim et al., 2021), as well as providing best-practice guidances to maximize the accuracy in the back-calculation (Pierce et al., 2017; Alland et al., 2018). Nonetheless, general guidelines for tackling slab-curling in rigid pavements are still an open topic of research.

Multi-layered models idealize the pavement structure as an axisymmetric multi-layered arrangement in which specific stiffness and/or thickness values are assigned to each individual layer. They may be used on both rigid and flexible pavements, and are generally regarded as being more accurate than the “dense-liquid” models (Ioannides et al., 1984), albeit at the expense of optimizing many more material parameters. The back-calculation usually refers to the estimation of the elastic properties and the thickness of each individual layer. Given that a typical pavement structure consists of many layers, the optimization of the properties of all layers is rather complex. The advent of modern soft-computing techniques has allowed researchers to provide increasingly

more accurate back-calculations by making use of artificial neural networks (Sharma and Das, 2008; Ghanizadeh et al., 2020; Wang et al., 2021), genetic algorithms (Rakesh et al., 2006; Li and Wang, 2019), data mining (Gopalakrishnan et al., 2013), and many others, while using either experimental measurements or Finite Element (FE) simulations to train the networks (Zaghloul, 1993; Li, 2017; Assogba et al., 2020, 2021). Nonetheless, the ill-posed nature of the mathematical problems may lead to different results even if using the same input data (Romeo et al., 2023). Further difficulties in the interpretation arise due to the seasonal variations of FWD results, as layers within the pavement structure are affected by temperature and moisture changes. The correct interpretation of seasonally variable flexible pavement structures is still an open topic of research.

Both types of models assume semi-infinite pavement dimensions and point symmetry in the behavior of the structure with respect to a vertical axis passing through the point of loading. This carries about the consequence of undervaluing the influence of the finite size of the slab and of potential asymmetries in the layer properties. Such asymmetries have been experimentally observed in (Díaz Flores et al., 2021, 2022, 2023), see Chapters 2 and 3. Attempts have been made to account for the influence of the finite slab size through correction factors, see e.g. (Korenev, 1954; Crovetto and Crovetto, 1994). Their models have been observed, however, to deliver inaccurate results for some cases (Setiadji and Fwa, 2007). Further solutions that account for the finite slab size have been performed based on one-slab models (Shi et al., 1994), leading up to a nine-slab model in a  $3 \times 3$  grid accounting for load transfer between slabs (Liu and Fwa, 2007). A study comparing all the different models (Setiadji and Fwa, 2007) concluded that the nine-slab model provided the most accurate results. However, it required assumptions regarding the load transfer efficiency between slabs, and was only marginally better than semi-infinite plate models like the dense-liquid model. This context provided the motivation to develop a finite-slab-size model that accounts for the real slab dimensions.

A novel finite-slab-size model was developed in Chapter 2. It is an extension of the Principle of Virtual Power (Germain, 1972)-based amendment to the solution of the Winkler problem provided by Vlasov (1966), as presented in (Höller et al., 2019). The inspiration for this method was drawn from calculations performed in the context of a hybrid analysis within the New Austrian Tunneling Method (NATM) (Rabcewicz, 1965). There, displacement sensors are placed at the shotcrete shell along a given measurement cross-section (Schubert and Lauffer, 2012). By monitoring the position of the sensors at different times, pointwisely-determined displacements are obtained. The displacements are then interpolated to obtain a continuous function. This function depicts a three-dimensional representation of how the pressure around the tunnel increasingly compresses the cross-section of the tunnel with time. Based on the measured deflections, the deformation field of the shell cross-section could be determined. By using an appropriate material law, the stress field inside the shell is obtained. These stresses are then compared with the current strength of the material (Hellmich et al., 2001), and can also be used to obtain the pressure exerted in the inaccessible outer surface of the shell (Ullah et al., 2013). In the method designed for pavement engineering, ansatz functions are used to reproduce the measured deflections while fulfilling Kirchhoff's plate equation and free-edge boundary conditions, see Chapter 2. In order to fee the method with sufficiently many measured deflections, capture such asymmetries, FWD tests with multi-directional measurement of deflections are performed, and a T-shaped arrangement of geophones is developed.

### 1.3 Multi-directional and T-shaped arrangement of geophones during FWD tests

The measurement and interpolation of a very accurate surface deflection field is a prerequisite for the elaboration of hybrid analyses. In this context, standard FWD tests are expanded to “multi-directional FWD tests”, see Chapter 2. Deflections are measured not only radially along the driving direction, but also along seven other directions. This way, a set of deflections measured along eight directions provides an accurate depiction of the two-dimensional deflection field of the pavement structure. New deflection basin parameters were introduced so that asymmetries in the deflection field can be rapidly recognized directly from the measurements. The asymmetry indicator,  $A_{d,\delta}$ , which compares deflections along two different directions ( $d$  and  $\delta$ ), is developed in Chapter 2. It quantifies the level of asymmetry present in the slabs, and is used to assess the asymmetries of ten slabs. An effective asymmetry index,  $\mathcal{A}_{28}^*$ , further summarizes the information from all 28 possible values of  $A_{d,\delta}$  that are found for one slab, see Chapter 3. Despite the clear advantages of multi-directional FWD testing in terms of the detailed quantification of asymmetric behavior, multi-directional FWD testing requires significantly more in situ efforts compared to standard FWD testing. This provided the motivation to develop a practice-oriented extension of multi-directional FWD tests.

An innovative T-shaped arrangement of geophones is developed, see Chapter 3, with the aim of reducing the related in situ efforts to those known from standard FWD testing, while retaining the expressiveness of multi-directional FWD testing as far as the assessment of asymmetric structural behavior is concerned. In the proposed arrangements, seven geophones are placed along the driving direction, while two other geophones are placed along an axis orthogonal to the driving direction, one left and one right of the center of the slab. Both geophones on these lateral directions are placed at the same radial distance from the center of the slab. The main task is then to optimize the radial distance of the geophones at the lateral directions such that their measurements deliver the most amount of information (i.e., to maximize their expressiveness) regarding the asymmetric behavior of the slab. In order to assess their expressiveness, the FWD results of ten multi-directional FWD tests are evaluated. T-shaped FWD tests are simulated by evaluating subsets of each of the multi-directional FWD tests. A deflection basin parameter called LASIX was developed specifically for T-shaped tests. It compares the deflections along the three radial distances measured during T-shaped FWD tests: the driving direction and the two lateral directions. With the help of the proposed deflection basin parameters, an optimal radial distance from the center of the slab for the geophones located along the lateral directions is found. A connection to the AREA method, commonly used for the back-calculation of subgrade properties, is established, and first conclusions regarding the implications of asymmetric slab behavior on the back-calculation of subgrade properties while using standard methods are given.

### 1.4 Seasonal variations of FWD results - innovative instrumentation of FWD field-testing sites

The dependence of the pavement structure on changing hygrothermal conditions is a key challenge in the context of interpreting FWD results and back-calculating layer properties. In the case of rigid pavements, slab-curling occurs due to large temperature gradients within the rigid slab, which have been observed to significantly affect FWD results (Khazanovich et al., 2001; Vandenbossche, 2003). In the case of flexible pavements, the viscoelastic properties of asphalt may change significantly when conditioned to different temperatures. Unbound layers and the subgrade are also critically affected by moisture changes (Salour and Erlingsson, 2013; Bayat,

2009). Thus, the same pavement structure may deliver different results when subjected to identical FWD tests performed at different seasons. The interpretation of FWD results in monitored pavements is further hindered, as variations in measured deflections may be wrongly assigned to either a degradation of the structure or to seasonal variations of one or more of its layers. This provided the motivation to instrument and monitor FWD field-testing sites in rigid and flexible pavements in a way that a complete and detailed evaluation of FWD tests is possible during different seasons. The results of this evaluation is then used to develop a method to correct deflections obtained during FWD tests due to changing temperatures.

Three field-testing sites have been instrumented with a combination of temperature sensors, asphalt strain gauges, and accelerometers placed at the interfaces between layers within the pavement structure, see Chapter 4. The field-testing sites refer to one rigid pavement and two flexible pavements located on the main highways in Austria. As regards the rigid pavement, the sensors are used to detect the occurrence of slab curling, and to characterize the stiffness of a cement-stabilized granular layer in situ. As regards flexible pavements, the sensors are used to characterize the stiffness properties of asphalt, lean concrete, and unbound layers in situ. This in situ characterization of layers is carried out with the help of an innovative test, named “sledgehammer test”, inspired by similar experiments performed by (Pichler et al., 2003) to identify gravel elasticity. The idea behind “sledgehammer tests” is to use the theory of elastic wave propagation through isotropic solids to determine the stiffness properties of individual layers. During these tests, a rubber pad is placed on the top surface of a pavement structure, vertically above the place where the sensors have been located. A metal plate is placed on top of the rubber pad, and this sandwich structure is then hit with a hammer, generating an elastic wave. The acceleration sensors are then used to determine the arrival time of the elastic wave at each interface. Based on the difference of these arrival times, the time of flight, and hence the velocity of the elastic wave across the investigated layer can be obtained. This velocity is related to the stiffness properties of the layer. A salient feature of such tests is that they take only a few seconds to be performed. This allows for a reliable statistical evaluation of a large amount of tests to be carried out, further increasing the accuracy of in situ characterization.

The results of FWD tests and of “sledgehammer tests” on the rigid pavement are used in multi-layered structural simulations with the purpose of developing an asphalt-related temperature correction for FWD test results, see Chapter 5. In these simulations, the properties of most individual layers are determined before-hand, as a result of laboratory tests or in situ “sledgehammer tests”. In particular, uniaxial compression tests are used to obtain the stiffness of concrete layers, cyclic direct tension-compression tests are used to obtain the temperature and frequency-dependent viscoelastic properties of asphalt layers, and “sledgehammer tests” are used to obtain the in situ stiffness properties of bound and unbound layers. Two optimization variables are used to fit the measured deflections: the stiffness and the thickness of the subgrade. Furthermore, the deformations measured by the asphalt strain gauges are used to independently corroborate the results. An additive correction of deflections is then developed and proposed such that deflections measured at any testing temperature can be translated into corrected deflections that would be obtained if the same test was performed at a reference asphalt temperature  $T_a = 20^\circ\text{C}$ . At this temperature, deflections can be directly compared with each other, thus facilitating the interpretation of FWD results and the observation of deterioration of subgrade properties. Notably, by correcting the deflections and not only the back-calculated moduli, other indexes and deflection basin parameters, such as the ones proposed to quantify asymmetry, can be calculated and compared with each other, thus projecting a more comprehensive and in-depth characterization of the pavement structure.

## 1.5 Outline

This work is divided as follows. Chapter 2 refers to the experimental development of multi-directional FWD tests, the quantification of its asymmetric behavior, and the finite-slab-size method to back-calculate double-symmetric effective moduli of subgrade reaction. Chapter 3 refers to the development of a T-shaped arrangement of geophones and the associated quantification of its asymmetric behavior with the help of newly-introduced deflection basin parameters. In Chapter 4, the experience gathered during the instrumentation of the three field-testing sites is presented, along with the obtained experimental data. Chapter 5 is devoted to the multi-layered simulation based on the results of the instrumented field-testing sites and to the development of a temperature correction of deflections for FWD tests. Finally, Chapter 6 contains a brief summary and general conclusions of this work. Each chapter is related to a different scientific publication that is either already published, under review, or soon to be submitted for publication. The corresponding abstracts are presented below.

### 1.5.1 Multi-directional Falling Weight Deflectometer (FWD) testing and quantification of the effective modulus of subgrade reaction for concrete roads

**Authored by:** Rodrigo Díaz Flores, Mehdi Aminbaghai, Lukas Eberhardsteiner, Ronald Blab, Martin Buchta, Bernhard L.A. Pichler

**Published in:** *International Journal of Pavement Engineering (2021): 1-19.*

The final publication is available at: <https://doi.org/hcnx>.

**Abstract:** Falling Weight Deflectometry (FWD) tests are performed around the centers of two rectangular concrete plates, with geophones measuring vertical deflections in eight directions. Experimental results allow for quantifying asymmetries regarding the structural behavior. Significant asymmetries are found for a 22-year-old plate scheduled for replacement. A new plate, tested a few weeks after production, is found to behave in a virtually double-symmetric fashion. Structural analysis of the new plate is based on Kirchhoff-Love plate theory, using free-edge boundary conditions. Support of the plate is provided by a Winkler foundation. Performing a static analysis, the uniform modulus of subgrade reaction is optimized to reproduce the measured deflections. The result is not convincing. The model is extended towards consideration of a second optimization variable: a uniform auxiliary surface load. This allows for reproducing the measured deflections. The auxiliary load is superimposed with the pressure resulting from the Winkler foundation. This yields a realistic distribution of subgrade pressure. Dividing it by the deflections results in the distribution of the effective modulus of subgrade reaction. Finally, the analysis is extended towards consideration of inertia forces. They increase the effective moduli of subgrade reaction determined by means of static analysis by less than 3.5%.

**Contributions by the author:** The first author acted as the team member at the front, played a central role in the discussion of the research questions, with a particular focus on the newly proposed deflection basin parameters, evaluated the asymmetries of the tested slabs, elaborated the part on hypothesis testing, performed all calculations, drew all figures, and prepared the first draft of the paper.

**Keywords:** field testing; concrete; modulus of subgrade reaction; static analysis; dynamic analysis; FWD

### 1.5.2 T-shaped arrangement of geophones for rapid quantification of asymmetric behavior of concrete slabs in central FWD tests

**Authored by:** Rodrigo Díaz Flores, Mehdi Aminbaghai, Lukas Eberhardsteiner, Ronald Blab, Martin Buchta, Bernhard L.A. Pichler

**Publication outlook:** At the time of finalizing the thesis, this paper was accepted for publication in *International Journal of Pavement Engineering*.

**Abstract:** The assessment of asymmetric slab behavior is out of reach in *standard* Falling Weight Deflectometer (FWD) tests, because deflections are measured along the driving direction only. Herein, a new T-shaped arrangement of the geophones is proposed. It allows for rapid quantification of asymmetric slab behavior in central FWD testing of concrete slabs. One geophone is positioned at the center of impact (= center of the slab), six along the driving direction, one right and one left of the center. The “Lateral Asymmetry Index (LASIX)” is introduced as a corresponding dimensionless deflection basin parameter. Its value increases with increasing asymmetric behavior of the slab. The main research challenge tackled herein is to optimize the radial distance of the lateral geophones from the center of the slab, such as to maximize the expressiveness of LASIX for the quantification of asymmetric slab behavior. In this context, the “effective asymmetry index ( $\mathcal{A}_{28}^*$ )” is introduced as another new dimensionless deflection basin parameter. It summarizes the asymmetric behavior based on deflection differences quantified for all 28 pairs of directions which can be combined out of the eight available measurement directions. The optimal radial distance of the lateral geophones from the center of the slab is found as 1.20 m. Corresponding values of LASIX larger than 8% refer to coefficients of directional variation of the AREA7 parameter larger than 5%. This indicates directional degradation of the pavement structure resulting from eccentric traffic loads. T-shaped FWD testing requires in situ efforts equivalent to those of standard testing, while allowing for a rapid and reliable quantification of asymmetric behavior. It allows for the assessment of whether the standard evaluation of *uniform* moduli of subgrade reaction is realistic or questionable.

**Contributions by the author:** The first author acted as the team member at the front, played a central role in the definition and the discussion of the research questions, with a particular focus on the arrangement of the geophones and the newly proposed deflection basin parameters, evaluated the asymmetries of the tested slabs, performed all calculations, drew all figures, and prepared the first draft of the paper.

**Keywords:** concrete slabs; falling weight deflectometer; FWD; multi-directional testing; T-shaped testing; deflection basin parameters; asymmetric slab behaviour



### 1.5.3 Instrumentation of field-testing sites for dynamic characterization of the temperature-dependent stiffness of pavements and their layers

**Authored by:** Valentin Donev, Rodrigo Díaz Flores, Lukas Eberhardsteiner, Luis Zelaya-Lainez, Christian Hellmich, Martin Buchta, Bernhard L.A. Pichler

**Publication outlook:** At the time of finalizing the thesis, it is planned to submit this paper to *Structural Control and Health Monitoring*.

**Abstract:** Falling Weight Deflectometer (FWD) tests are performed worldwide to assess the health of pavement structures. It is challenging to interpret surface deflections measured during FWD tests, because the stiffness of pavement structures is temperature-dependent. This provides the motivation to instrument one rigid and two flexible pavement structures with temperature sensors, asphalt strain gauges, and accelerometers. Most of these sensors are installed at layer interfaces. The study delivers two main results. (i) Experience with instrumentation of pavements during new construction is shared. This includes the comparison of three different methods for installation of the strain gauges. Eventually, it is recommended to install a steel dummy as a place-holder into the surface of hot asphalt layers, immediately *after* their construction and right *before* their compaction, and to replace the dummy by the actual sensor right before the installation of the next layer. (ii) First data from dynamic testing at the field-testing sites are presented. FWD tests performed at different temperatures deliver, as expected, different surface deflections. As for the rigid pavement, sledgehammer strokes onto a metal plate, transmitted to the pavement via a rubber pad, yield accelerometer readings that allow for detection of curling (= temperature-gradient-induced partial loss of contact of the concrete slab from lower layers). In the absence of curling, the sledgehammer tests yield accelerometer readings that allow for quantification of the runtime of longitudinal waves through asphalt, cement-stabilized, and unbound layers, such that their stiffness can be quantified using the theory of elastic wave propagation through isotropic media.

**Contributions by the author:** The second author played an essential role in the design and the installation of the field testing sites as well as in the discussion of the research questions, performed the simulations used for deciding on the location of the sensors, was hands-on involved in the installation of the sensors on all field-testing sites, evaluated the testing results of the A10, performed the first complete round of improvements of the first draft of the paper, put it in L<sup>A</sup>T<sub>E</sub>X, and aided in further editing of it.

**Keywords:** dynamic stiffness characterization; temperature-dependent stiffness; field testing; Pt100 sensors; accelerometers; strain gauges; wave propagation; rigid pavements; flexible pavements; concrete; asphalt

### 1.5.4 Asphalt-related temperature correction of deflections measured in central FWD tests on concrete-over-asphalt composite pavements

**Authored by:** Rodrigo Díaz Flores, Valentin Donev, Mehdi Aminbaghai, Raphael Höller, Lukas Eberhardsteiner, Martin Buchta, Bernhard L.A. Pichler

**Publication outlook:** At the time of finalizing the thesis, it is planned to submit this paper to *Road Materials and Pavement Design*.

**Abstract:** An asphalt-related temperature correction of deflections measured during FWD tests on a concrete-over-asphalt composite pavement is developed. Five FWD tests were performed at a well-instrumented field-testing site; in summer, winter, and transitional periods. The stiffnesses of concrete, asphalt, and the cement-stabilised layer are characterized using suitable laboratory and field testing methods. The elastic modulus of the subgrade is back-calculated using multi-layered elastostatic simulations, such that simulated deflections agree optimally with measured deflections. The multi-layered model is used to compute deflections for different asphalt temperatures. Results allow for translating measured deflections into corrected deflections referring to an asphalt temperature of 20°C. Corresponding  $k$ -values are quantified using the AREA4 method. They correlate well with seasonal variations of the stiffness of the subgrade. Finally, an engineering correction approach is developed which requires not more information than just measured deflections. Also this approach delivers reliable estimates of relative seasonal stiffness changes of the subgrade.

**Contributions by the author:** The first author acted as the team member at the front, played a central role in the definition and the discussion of the research questions, evaluated the material tests on asphalt and the cement-stabilized granular layer, performed all the structural analyses, contributed to the conception of both methods for the asphalt-related temperature correction of measured deflections, was responsible for their implementation, drew all figures, and prepared the first draft of the paper.

**Keywords:** field testing; multi-layered; non-destructive testing; seasonal variation; composite slabs; FWD

## Multi-directional Falling Weight Deflectometer (FWD) testing and quantification of the effective modulus of subgrade reaction for concrete roads

### 2.1 Introduction

Falling Weight Deflectometry (FWD) allows for quantifying and evaluating the state of concrete roads and of the subgrade beneath them. A FWD test consists of dropping a standardized mass (= “falling weight”) from a defined height onto a load plate placed on top of the pavement’s surface. During the impact, displacement sensors (= “geophones”) capture the deflection history of several points at the surface of the pavement, along one specific radial direction, typically the driving direction. The measured deflections are the basis for back-calculating stiffness properties of the pavement plate and of the layers of the subgrade underneath. The present paper is focused on *centric* FWD tests on pavement plates made of *concrete*.

The evaluation of a FWD test is an inverse problem. Properties of the subgrade are back-calculated such as to obtain deflections agreeing with the ones by the displacement sensors. Back-calculation may be performed in a dynamic (Khazanovich, 2000b; Sawant, 2009) or quasi-static context. Evaluation of centric FWD tests is typically performed under the assumption that the deflection of the pavement is radially symmetric with respect to the center of the impact. Several types of structural models are used, including plates resting on elastic foundations (Winkler, 1867; Biot, 1937; Vesić, 1961), multi-layered plates on top of a Winkler foundation (Girija Vallabhan et al., 1991), and continuum mechanics of multi-layered solids (Pan, 1989a,b; Kausel and Roësset, 1981; Rahim and George, 2003; Abd El-Raof et al., 2018). In the latter context, the modulus of elasticity and/or the thickness of each individual layer of the subgrade is back-calculated. A variety of methods are used for the simulation of the structural problem, including axisymmetric Finite Element models accounting for either elastic (Loizos and Scarpas, 2005; Wang and Li, 2016) or viscoelastic (Li et al., 2017) material behavior, artificial neural networks and genetic algorithms, again accounting either for elastic (Sharma and Das, 2008; Li and Wang, 2019) or viscoelastic (Varma et al., 2013) material behavior, hybrid neural network structures (Han et al., 2021), and other methods (Levenberg, 2013; Goktepe et al., 2006). Despite their wide use, it has

been noted (Mehta and Roque, 2003) that the inverse problem is mathematically “ill-posed”, because different structures consisting of layers with different combinations of modulus of elasticity and thickness result under the same loading in the same deflection field. This underlines that the inverse problem has multiple solutions rather than a unique one. Thus, expert knowledge, experience and care are needed when using back-calculation procedures.

The present study is inspired by inverse calculations performed in the New Austrian Tunnelling method (Rabcewicz, 1965), where cylindrical shotcrete tunnel shells are monitored by means of measuring three-dimensional displacement vectors of “measurement points” in “measurement cross-sections” (Schubert and Lauffer, 2012). Back-calculations are aimed at computing the stresses in the lining and comparing them with the current strength of the material (Hellmich et al., 2001) as well as computing the spatial distributions of ground pressure and shear exerted from the ground mass onto the inaccessible outer surface of the shotcrete shell (Ullah et al., 2013). Following these lines, a multi-directional mode of centric FWD tests is proposed in the present paper. The deflections captured by the displacement sensors are used to compute the distribution of (i) the pressure exerted from the subgrade onto the inaccessible bottom surface of the pavement plate, and (ii) the effective modulus of subgrade reaction. The tool for structural analysis is a Kirchhoff-Love plate resting on a Winkler foundation. Herein, a series solution derived in the framework of the Principle of Virtual Power (Germain, 1972) is used, see Höller et al.’s amendment of Vlasov’s approach (Vlasov, 1966; Höller et al., 2019).

A Winkler foundation summarizes the properties of the whole subgrade by one value: the modulus of subgrade reaction (Winkler, 1867). The influence of different absolute values of the modulus of subgrade reaction on the stresses and deflections of short-panelled concrete plates subjected to traffic loads was studied by means of the Finite Element method by Gupta (2021). The modulus of subgrade reaction, however, is a structural rather than a material property (Aristorenas and Gómez, 2014), and the assumption of a spatially uniform modulus of subgrade reaction may lead to unrealistic results (Smith, 1970; Eisenberger, 1990; Daloglu and Vallabhan, 2000; Larkela et al., 2013). As a remedy, non-uniform distributions of the modulus of subgrade reaction were introduced, e.g. in the context of the analysis of concrete slabs (Roesler et al., 2016), and of vibrations of thin circular plates (Foyouzat et al., 2016). In the present paper, a method is developed which allows for determination of a realistic distribution of the modulus of subgrade reaction for centric FWD tests on concrete pavements. The method is essentially based on the quantification of a realistic distribution of the pressure exerted from the subgrade onto the inaccessible bottom surface of the pavement plate. Such a pressure distribution is realistic, provided that (i) it is in equilibrium with the dead load of the plate and the falling weight, (ii) the deflections of the plate agree well with the measurements from multi-directional FWD testing and (iii) the field equation of Kirchhoff-Love theory as well as the boundary conditions of the plate are satisfied.

In this study, centric FWD tests are performed along eight different radial directions (Section 2.2). Such a novel multi-directional testing scheme provides insight into possible asymmetries of the structural behavior of the characterized plate and its subgrade. The proposed test protocol is applied to two plates: a new one that had never been exposed to regular traffic loads, and an old plate already scheduled for replacement. The new plate had been installed only a few weeks before testing. Merely site traffic had potentially passed over it. The old plate had been in service for 22 years. The leftmost 1.05 metres were part of the first lane; the rest was part of the emergency lane. Thus, service loads were running mainly along the left edge of the plate, resulting in localized degradation of the subgrade. Based on the results of multi-directional FWD testing, an index value is proposed, which quantifies the level of asymmetry of the structural behavior. As for the virtually double-symmetric behavior of the new plate, structural analysis is performed with the aim to quantify a realistic distribution of the pressure exerted by the subgrade onto the

plate (Section 2.3). At first, it is confirmed that a spatially uniform modulus of subgrade reaction is unsuitable to explain the multi-directional deflection measurements. Therefore, the structural model is extended towards consideration of an auxiliary surface load. The extended model is capable of reproducing the multi-directional deflection measurements. It allows for computing a realistic distribution of the subgrade pressure and of the modulus of subgrade reaction, with and without accounting for inertia forces resulting from the dynamic nature of FWD testing. The present paper ends with conclusions drawn from the results of the presented study (Section 2.4).

## 2.2 Multi-directional FWD Testing

FWD tests were performed on two concrete plates of the Austrian highway “A1”, near the junction “Steinhäusl”, in Lower Austria. The geometric dimensions of the tested plates amounted to  $5.5\text{ m} \times 4.2\text{ m} \times 0.22\text{ m}$ , the maximum force produced by the falling weight to 199 kN, and the measurement frequency of the geophones to 10 kHz, see Table 2.1.

**Table 2.1**

Properties of the plates and of the equipment used.

Property	Value
Length of Plate, $a$	5.50 m
Width of Plate, $b$	4.20 m
Thickness of Plate, $h$	0.22 m
Flexural Stiffness of Plate, $K$	49.5 MNm
Maximum Impact Force	199 kN
Measurement Frequency of Geophones	10 kHz
Modulus of Elasticity of Concrete, $E$	36.5 GPa
Poisson’s Ratio of Concrete, $\nu$	0.2
Mass Density of Concrete, $\rho$	2,452 kg/m <sup>3</sup>

Both tested plates were located at the right side of the highway. The rightmost 2.90 m were part of the emergency lane, the leftmost 1.05 m were part of the first lane, with the traffic line of 0.25 m in between. Along three edges, the tested plates were connected by means of steel bars to their neighbors: the left edge (tie bars) and the two edges orthogonal to the driving direction (dowels). The right lateral surfaces of the plates were free edges.

### 2.2.1 Test protocol

Multi-directional FWD testing was carried out in eight directions described by a local cardinal directional system, with N referring to the driving direction (Fig. 2.1). Because of structural constraints of the FWD machine, the angles between neighboring directions amounted to either  $38^\circ$  or  $52^\circ$  (Fig. 2.1), rather than to  $45^\circ$ , see also Table 2.2. FWD testing started in the N direction and continued clockwise: NE, E, SE, S, SW, W and NW. As for every specific direction, three tests were carried out, one right after the other, in order to capture data that allows for assessing the quality of test repeatability. After three tests in each of the eight directions, another set of three tests was carried out in the N direction. In other words, the first three tests and the last three tests referred to the driving direction. These in total six tests allow for checking whether or not the same results are obtained at the start and at the end of multi-directional FWD testing.

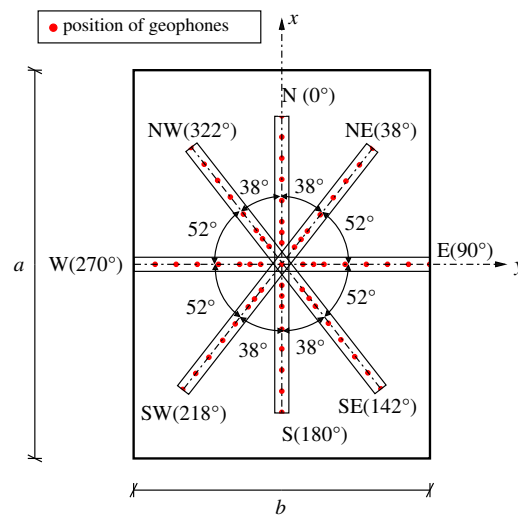


**Fig. 2.1.** Novel multi-directional arrangement of the FWD measurements described by a local cardinal directional system, with N referring to the driving direction.

**Table 2.2**

Polar angle  $\varphi_d$  as a function of the measurement direction

	Test Direction							
	N $d = 1$	NE $d = 2$	E $d = 3$	SE $d = 4$	S $d = 5$	SW $d = 6$	W $d = 7$	NW $d = 8$
polar angle	0°	38°	90°	142°	180°	218°	270°	322°

Nine geophones recorded the deflection histories during every single FWD test (Fig. 2.2). Geophone 1 was always located at the center of the falling weight experiments. The other eight



(a)



(b)

**Fig. 2.2.** Multi-directional FWD testing: (a) experiment with geophones positioned in the SE direction, and (b) load plate through which the falling weight was transferred to the pavement.

geophones were fixed to a bar, ensuring that the radial distances between them were always the same. As for the tests in the N, NE, E, S, W and NW directions, the distance of the geophone-bar to the center of the falling weight was equal to the default value of the used machine (Table 2.3). As for the tests in the SE and SW directions, the geophone-bar had to be positioned 15 cm further away from the center (Table 2.3), again because of structural constraints of the FWD machine. When testing in the W direction, the outermost geophone was located at the neighboring plate. The respective data are excluded from the present analysis, because explicit consideration of the

interaction of neighboring plates is beyond the scope of this work.

### 2.2.2 Experimental Data from the New Plate

The first test location referred to a concrete pavement plate at the kilometre 33.360 of the highway “A1”. The tested plate was only a few weeks old at the time of testing. Before that, only site traffic had potentially passed over the plate.

The deflections recorded by the geophones are bell-shaped functions of time, see Fig. 2.3. The duration of the dynamic behavior of the plate amounted to some 30 ms. This period of

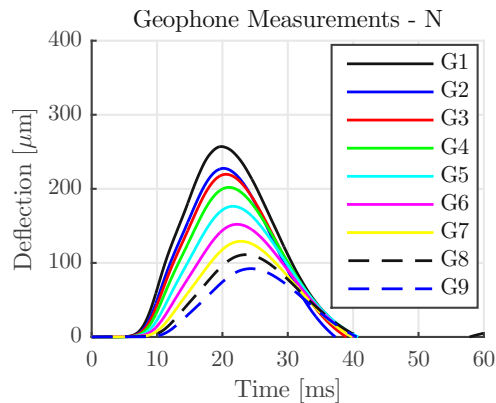


**Fig. 2.3.** Results from the first out of 27 FWD tests of the new plate: deflections measured as a function of time by the nine geophones along the N direction.

time is resolved by some 300 readings of the geophones, noting the measurement frequency of 10 kHz. A total of 27 individual FWD tests were carried out within 45 minutes, given that three tests were performed in every direction and that the N direction was measured twice. A total of 240 individual displacement histories were recorded, since nine geophones documented every single test, except for the W direction where only eight geophones were positioned on the plate of interest, see above. The corresponding 240 displacement maxima (Table 2.A.1 in Appendix 2.A) are illustrated in Fig. 2.4.

The circle and star symbols in Fig. 2.4 refer to the described 240 displacement maxima. Because the three to six measurements at every location resulted in virtually the same results, the corresponding three to six symbols are hardly distinguishable. The solid lines in Fig. 2.4 are splines interpolating between the average deflection maxima measured at each location. Using index  $d$  for measurement directions, with  $d = 1 \Leftrightarrow N$ ,  $d = 2 \Leftrightarrow NE$ ,  $\dots$ ,  $d = 8 \Leftrightarrow NW$ , index  $g$  for

**Table 2.3**

Radial distances  $r_{d,g}$  [m] of nine geophones from the axis of impact, as a function of the measurement direction:  $d = 1$  (N),  $d = 2$  (NE),  $d = 3$  (E),  $d = 4$  (SE),  $d = 5$  (S),  $d = 6$  (SW),  $d = 7$  (W),  $d = 8$  (NW).

Test Directions	Geophone								
	$g = 1$	$g = 2$	$g = 3$	$g = 4$	$g = 5$	$g = 6$	$g = 7$	$g = 8$	$g = 9$
$d \in [1, 2, 3, 5, 7, 8]$	0.00	0.30	0.45	0.60	0.90	1.20	1.50	1.80	2.10
$d \in [4, 6]$	0.00	0.45	0.60	0.75	1.05	1.35	1.65	1.95	2.25

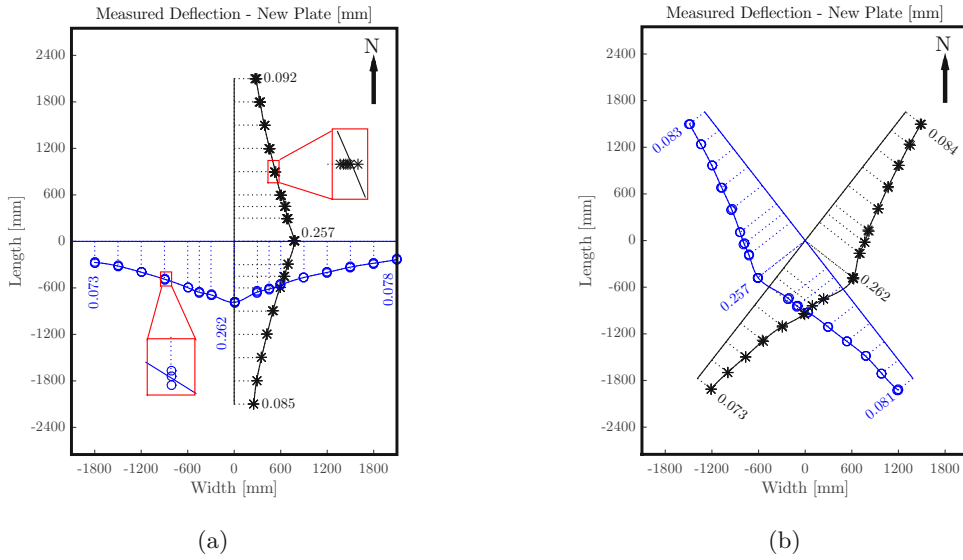


**Fig. 2.4.** Results from multi-directional FWD testing on the new plate: 240 deflection maxima measured by the geophones along the (a) N, S, E and W directions, as well as (b) the diagonal directions; the lines refer to splines interpolating between the average deflections measured at each location, see Eq. (2.1).

the geophones and index  $i$  for the  $i^{\text{th}}$  test in direction  $d$ , the average values are computed as

$$\bar{w}_{d,g} = \frac{1}{n_d} \sum_{i=1}^{n_d} \max_t w_{d,g,i}(t), \quad (2.1)$$

where  $n_d$  stands for the number of tests performed in direction  $d$ . As for Fig. 2.4, results from all six tests in the N direction are included, resulting in  $n_1 = 6$ . For the other seven measurement directions,  $n_d = 3$ .

Test repeatability is studied statistically based on coefficients of variation (= mean values divided by standard deviations):

$$CV_{d,g} = \frac{\sigma_{d,g}}{\bar{w}_{d,g}}. \quad (2.2)$$

The standard deviations read as

$$\sigma_{d,g} = \sqrt{\frac{1}{n_d - 1} \sum_{i=1}^{n_d} \left[ \max_t w_{d,g,i}(t) - \bar{w}_{d,g} \right]^2}. \quad (2.3)$$

In order to quantify the quality of repeatability regarding all sets of three nominally identical tests, carried out immediately one after the other in the same direction, Eqs. (2.1)–(2.3) are evaluated for all of the nine sets of three tests, and for each one of the nine geophones (except for the W direction, where only eight geophones were positioned at the plate of interest), see Table 2.A.2. The obtained 80 coefficients of variation are smaller than 5%. This indicates a satisfactory level of test repeatability.

In order to quantify the quality of repeatability regarding the the first set of three tests in the N direction, performed at the start of multi-directional testing, and the second set of three tests in the same direction, performed at the end of multi-directional testing, these six tests are evaluated as one statistical sample ( $n_d = 6$ ). The obtained coefficients of variation are smaller than 2%, see Table 2.4. This indicates a very satisfactory level of test repeatability.



**Table 2.4**

Coefficients of variation,  $CV_{N,g}$ , of the maximum deflections measured by each geophone in the  $N$ -direction of the new plate, calculated according to Eqs. (2.1)–(2.3), based on the results of the first and the last three tests ( $n_d = 6$ ), see also Table 2.A.1.

Geophone								
$g = 1$	$g = 2$	$g = 3$	$g = 4$	$g = 5$	$g = 6$	$g = 7$	$g = 8$	$g = 9$
0.58%	0.59%	0.89%	1.25%	0.89%	0.47%	0.38%	1.42%	1.91%

### 2.2.3 Experimental Data from the Old Plate

The second test location referred to a concrete pavement plate at the kilometre 33.354 of the highway “A1”. The tested plate was 22 years old at the time of testing. It was scheduled to be replaced shortly after the multi-directional FWD testing. The traffic had mainly passed along the Eastern edge of the plate, because the leftmost 1.05 m of the width of the plate were part of the first lane.

The deflections recorded by the geophones are bell-shaped functions of time, see Fig. 2.5. The dynamic behavior of the plate lasted for some 30 ms, resolved by some 300 readings of the

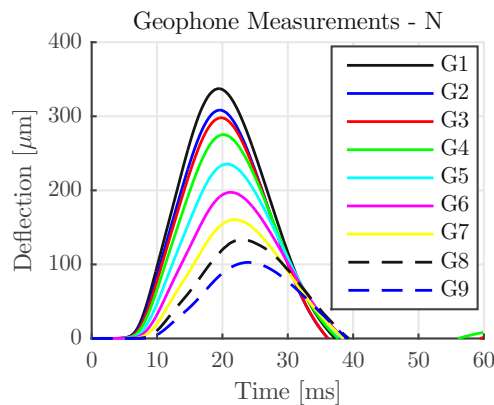


**Fig. 2.5.** Results from the first out of 27 FWD tests of the old plate: deflections measured as a function of time by the nine geophones along the  $N$  direction.

geophones. 27 individual FWD tests were carried out within 45 minutes, leading to a total of 240 individual displacement histories. The corresponding 240 displacement maxima (Table 2.B.1 in Appendix 2.B) are illustrated in Fig. 2.6.

The circle and star symbols in Fig. 2.6 refer to the described 240 displacement maxima. Because the three to six measurements at every location resulted in virtually the same results, the corresponding three to six symbols are hardly distinguishable. The solid lines in Fig. 2.4 are splines interpolating between the average deflection maxima measured at each location, computed based on Eq. (2.1) with  $n_1 = 6$  and  $n_d = 3$  otherwise.

In order to quantify the quality of repeatability regarding all sets of three nominally identical tests, carried out immediately one after the other in the same direction, Eqs. (2.1)–(2.3) are evaluated for all of the nine sets of three tests, and for each one of the nine geophones (except for the  $W$  direction, where only eight geophones were positioned at the plate of interest), see Table 2.B.2. The obtained 80 coefficients of variation are smaller than 3%. This indicates a satisfactory level of test repeatability.

In order to quantify the quality of repeatability regarding the initial set of three tests and the final set of three tests in the  $N$  direction, these six tests are evaluated as one statistical sample

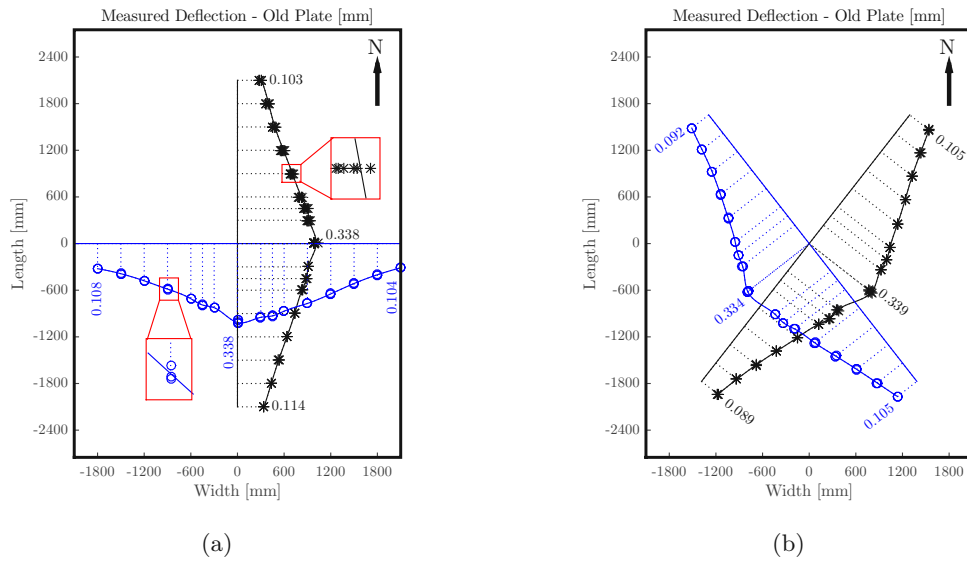


**Fig. 2.6.** Results from multi-directional FWD testing on the old plate: 240 deflection maxima measured by the geophones along the (a) N, S, E and W directions, as well as (b) the diagonal directions; the lines refer to splines interpolating between the average deflections measured at each location, see Eq. (2.1).

( $n_d = 6$ ). The obtained coefficients of variation are smaller than 6%, see Table 2.5. This indicates an acceptable level of test repeatability.

**Table 2.5**

Coefficients of variation,  $CV_{N,g}$ , of the maximum deflections measured by each geophone in the N-direction of the old plate, calculated according to Eqs. (2.1)–(2.3), based on the results of the first and the last three tests ( $n_d = 6$ ), see also Table 2.B.1.

Geophone								
$g = 1$	$g = 2$	$g = 3$	$g = 4$	$g = 5$	$g = 6$	$g = 7$	$g = 8$	$g = 9$
2.18%	2.01%	2.50%	2.62%	2.51%	3.24%	3.55%	5.60%	4.90%

## 2.2.4 Asymmetries of the structural behavior of the tested plates

Results from multi-directional FWD experiments (Figs. 2.4 and 2.6) are used to assess asymmetries of the structural behavior of the tested plates. As regards the new plate, asymmetries may result from the dowels and tie bars connecting it to its neighbors in the N, S and W directions. As for the old plate, asymmetries may also result from long-term service loads from traffic running mainly along the Eastern edge.

The development of a suitable index for the quantification of the asymmetry of the structural behavior is based on the discussion of possible symmetries of the new plate.

- If the dowels and tie bars influenced the structural behavior of the new plate, its deflections could be expected to be virtually symmetric with respect to the E-W axis running through the center of the plate. The deflections would be virtually symmetric in the N and S, the NE and SE as well as the SW and NW directions.

- If the dowels and tie bars had no significant influence on the structural behavior of the new plate, its deflections could be expected to be virtually double-symmetric with respect to the E-W and N-S axes running through the center of the plate. Not only the deflections discussed after the first bullet point would be virtually the same, but also those in the E and W, the NE and NW, the SW and SE, the NE and SW as well as the NW and SE directions.

The described symmetries are checked based on the deflections illustrated in Figs. 2.4 and 2.6. The spline in  $d$  direction is referred to as  $w_d(r)$ , where  $r \geq 0$  denotes the radial coordinate. The level of asymmetry of the deflections in the  $d$  and  $\delta$  directions is quantified based on the squared differences of the related splines, normalized with respect to their maximum values at the center of the impact ( $r = 0$ ):

$$A_{d,\delta} = \sqrt{\frac{1}{2.1 \text{ m}} \int_{r=0}^{2.1 \text{ m}} \left[ \frac{w_d(r)}{w_d(0)} - \frac{w_\delta(r)}{w_\delta(0)} \right]^2 dr}. \quad (2.4)$$

If the deflections in the  $d$  and  $\delta$  directions are identical,  $A_{d,\delta}$  is equal to zero. Thus, the larger  $A_{d,\delta}$ , the larger is the asymmetry of the deflections in the  $d$  and  $\delta$  directions. The asymmetry indicators  $A_{N,S}$ ,  $A_{NE,SE}$ ,  $A_{SW,NW}$ ,  $A_{E,W}$ ,  $A_{NE,NW}$  and  $A_{SW,SE}$ , evaluated both for the new and the old plate, are listed in Table 2.6.

**Table 2.6**

Asymmetry indicators for both plates, computed according to Eq. (2.4)

New Plate	Old Plate
$A_{N,S} = 3.98\%$	$A_{N,S} = 4.94\%$
$A_{NE,SE} = 3.09\%$	$A_{NE,SE} = 4.98\%$
$A_{SW,NW} = 2.79\%$	$A_{SW,NW} = 5.05\%$
.....	.....
mean value = 3.29%	mean value = 4.99%
$A_{E,W} = 3.49\%$	$A_{E,W} = 12.00\%$
$A_{NE,NW} = 2.55\%$	$A_{NE,NW} = 7.47\%$
$A_{SW,SE} = 2.43\%$	$A_{SW,SE} = 7.34\%$
$A_{NE,SW} = 4.44\%$	$A_{NE,SW} = 3.01\%$
$A_{NW,SE} = 1.24\%$	$A_{NW,SE} = 12.19\%$
.....	.....
mean value = 2.83%	mean value = 8.40%

As for the new plate, the eight asymmetry indicators are on average equal to 3.00%. The mean value of the first three asymmetry indicators is slightly smaller than that of the last five indicators, see Table 2.6. This underlines that the plate behaved virtually in a double symmetric fashion and that the dowels and tie bars connecting the new plate to its neighbors in the N, S and W directions had no significant influence on the structural behavior during FWD testing at the center of the plate. Consequently, a structural analysis of the FWD tests on the new plate can be based on free-edge boundary conditions, see Section 2.3.

As for the old plate, the eight asymmetry indicators are on average equal to 7.12%. Thus, the asymmetry of the old plate is by a factor of 2.37 larger than that of the new plate. The largest values of the asymmetry indicators of the old plate are  $\geq 12\%$  and refer to the E-W and the NE-SE axes. From these results it is concluded that the old plate behaved in a significantly

asymmetric fashion, because of its long-term service with traffic running mainly along its Eastern edge. If the plate had not already been scheduled for replacement, the asymmetry indicators evaluated herein would suggest such a necessity for repair.

The index defined in Eq. (2.4) is appealing, because it allows for direct comparison of FWD tests in which deflections were measured at *different* distances from the center of the falling weight. In order to corroborate the expressiveness of the index, hypothesis testing is used.

## 2.2.5 Revisiting symmetry of the plate behavior based on hypothesis testing

Statistical hypothesis testing (Lehmann and Romano, 2006) is based on the comparison of deflection maxima measured at the *same* distances to the center of the falling weight, but in *different* directions, see Table 2.3. As regards the symmetry with respect to the E-W axis, the comparison regards deflections measured along the N and the S direction. As regards the symmetry with respect to the N-S axis, the comparison regards deflections measured along the E and the W direction, the NE and the NW direction as well as the SE and the SW direction.

Inspired by the approach of Abd El-Raof et al. (2018), mean values of deflection maxima measured in one direction are plotted over corresponding mean values referring to the other direction, see e.g. Fig. 2.7. If the structure behaved in an asymmetric fashion, see Fig. 2.7(b),

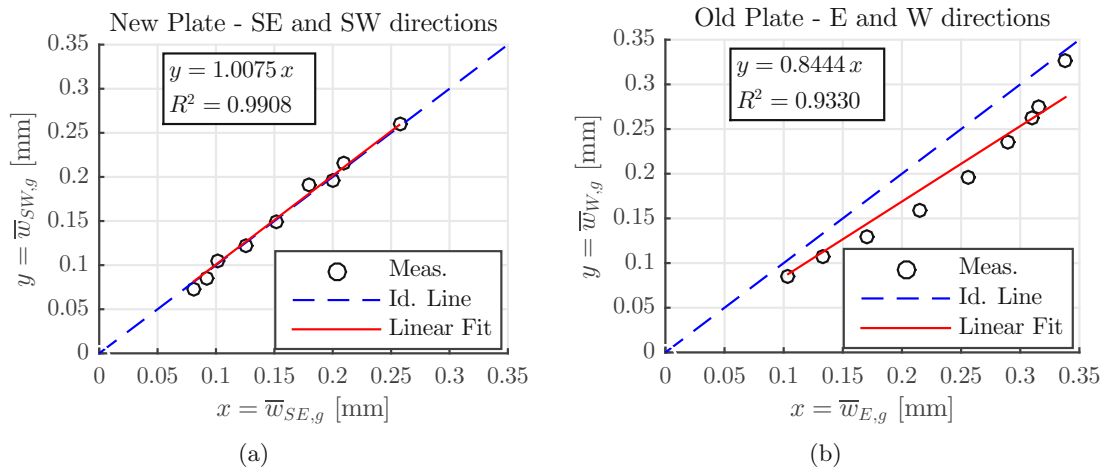


**Fig. 2.7.** Comparison between the mean of the deflection maxima measured at each geophone (a) on the new plate along the SE direction ( $\bar{w}_{SE,g}$ ) and the SW direction ( $\bar{w}_{SW,g}$ ), see also Table 2.7, and (b) on the old plate along the E direction ( $\bar{w}_{E,g}$ ) and the W direction ( $\bar{w}_{W,g}$ ), see also Table 2.8.

then the individual points lie in a considerable distance to the identity line. However, if the structure behaved in a virtually symmetric fashion, see Fig. 2.7(a), then the individual points fall very close to the identity line. The latter passes through the origin of the graph and has a slope which is equal to one. This is the motivation to fit the data points by the best linear regression function which passes through the origin. Accordingly, the following null hypotheses are written:

- The slope of the linear regression function is one:

$$H_{0,1}^{d,\delta} : \frac{dy}{dx} = 1, \quad (2.5)$$

where  $d$  and  $\delta$  refer to the two compared directions.

- The mean difference between the measurements in both directions is equal to zero (paired difference test following a Student's  $t$ -distribution):

$$H_{0,2}^{d,\delta} : \quad \bar{D} = \frac{1}{n_g} \sum_{g=1}^{n_g} (\bar{w}_{d,g} - \bar{w}_{\delta,g}) = 0, \quad (2.6)$$

where  $n_g$  is the number of geophones.

Statistical significance is assumed if the observed measurements lie outside of a 99% confidence interval, i.e. the hypotheses are rejected if  $p < 0.01$ . This value ensures a small probability of so-called Type I errors referred to as “false positives” (Lehmann and Romano, 2006). The rejection of any one of the two hypotheses suggests that the structure behaved asymmetrically with respect to the investigated axis.

As for the new plate, the hypotheses of symmetric structural behavior cannot be rejected, as indicated by values of  $p$  which are larger than 0.01 in all cases, see Table 2.7. The assumption of symmetric behavior has survived eight serious attempts of falsification. According to Popper (1962), this corroborates that the new plate indeed behaved in a *virtually* double-symmetric fashion.

**Table 2.7**

Results obtained from testing whether or not the new plate behaved in a symmetric fashion, based on the hypotheses (2.5) and (2.6); the  $p$ -values indicate virtually symmetric behavior in all investigated directions.

Test	$R^2$	Hypothesis	Coefficient	Standard error	$t$ -stat	$p$
$\bar{w}_{N,g} \Leftrightarrow \bar{w}_{S,g}$	0.9808	$H_{0,1}^{N,S}$	0.9739	0.0142	-1.8406	0.1029
		$H_{0,2}^{N,S}$	–	–	–	0.0142
$\bar{w}_{E,g} \Leftrightarrow \bar{w}_{W,g}$	0.9872	$H_{0,1}^{E,W}$	1.0261	0.0141	+1.8469	0.1021
		$H_{0,2}^{E,W}$	–	–	–	0.2658
$\bar{w}_{NE,g} \Leftrightarrow \bar{w}_{NW,g}$	0.9939	$H_{0,1}^{NE,NW}$	1.0253	0.0091	+2.7701	0.2420
		$H_{0,2}^{NE,NW}$	–	–	–	0.0549
$\bar{w}_{SE,g} \Leftrightarrow \bar{w}_{SW,g}$	0.9908	$H_{0,1}^{SE,SW}$	1.0075	0.0118	+0.6351	0.5411
		$H_{0,2}^{SE,SW}$	–	–	–	0.9686

As for the old plate, the hypotheses of symmetric structural behavior with respect to the E-W axis cannot be rejected, see the values of  $p$  for  $H_{0,1}^{N,S}$  and  $H_{0,2}^{N,S}$  in Table 2.8. The hypotheses of symmetric structural behavior with respect to the the N-S axis, however, are rejected, see the values of  $p$  for  $H_{0,1}^{E,W}$ ,  $H_{0,2}^{E,W}$ ,  $H_{0,1}^{NE,NW}$ ,  $H_{0,2}^{NE,NW}$ ,  $H_{0,1}^{SE,SW}$  and  $H_{0,2}^{SE,SW}$  in Table 2.8. These results emphasize that the old plate behaved in an asymmetric fashion with respect to the N-S axis.

In order to assess the expressiveness of the proposed symmetry index, see Eq. (2.4), values of the index listed in Table 2.6 are compared with results from statistical hypothesis testing, see Tables 2.7 and 2.8. All pairs of measurement directions, which were qualified by statistical hypothesis testing as to refer to symmetric structural behavior, have values of the index smaller 5%. Vice versa, all pairs of measurement directions, which were qualified by statistical hypothesis testing as to refer to asymmetric structural behavior, have values of the index larger than 7%. It is concluded that statistical hypothesis testing has corroborated the expressiveness of the symmetry index of Eq. (2.4).

**Table 2.8**

Results obtained from testing whether or not the old plate behaved in a symmetric fashion, based on the hypotheses (2.5) and (2.6); the  $p$ -values indicate virtually symmetric behavior in the  $N$ - $S$  direction, and asymmetric behavior in the  $E$ - $W$ ,  $NE$ - $NW$ , and  $SE$ - $SW$  directions.

Test	$R^2$	Hypothesis	Coefficient	Standard error	$t$ -stat	$p$
$\bar{w}_{N,g} \Leftrightarrow \bar{w}_{S,g}$	0.9851	$H_{0,1}^{N,S}$	1.0109	0.0144	+0.7584	0.4687
		$H_{0,2}^{N,S}$	–	–	–	0.1135
$\bar{w}_{E,g} \Leftrightarrow \bar{w}_{W,g}$	0.9330	$H_{0,1}^{E,W}$	0.8444	0.0257	-6.0494	< 0.0001
		$H_{0,2}^{E,W}$	–	–	–	0.0001
$\bar{w}_{NE,g} \Leftrightarrow \bar{w}_{NW,g}$	0.9680	$H_{0,1}^{NE,NW}$	0.8895	0.0182	-6.0766	< 0.0001
		$H_{0,2}^{NE,NW}$	–	–	–	< 0.0001
$\bar{w}_{SE,g} \Leftrightarrow \bar{w}_{SW,g}$	0.9693	$H_{0,1}^{SE,SW}$	0.8957	0.0174	-5.9851	0.0003
		$H_{0,2}^{SE,SW}$	–	–	–	< 0.0001

## 2.3 Structural analysis of the new plate

The virtually double-symmetric behavior of the new plate is studied based on Kirchhoff-Love linear theory of thin plates. A Cartesian coordinate system is used, with the  $x$ -axis oriented in the driving direction, see Fig. 2.1.

The boundary value problem consists of one field equation and boundary conditions. The field equation reads as (Vlasov, 1966)

$$K \left( \frac{\partial^4 w(x, y)}{\partial x^4} + 2 \frac{\partial^4 w(x, y)}{\partial x^2 \partial y^2} + \frac{\partial^4 w(x, y)}{\partial y^4} \right) + \rho h \frac{\partial^2 w(x, y)}{\partial t^2} + k w(x, y) = p(x, y), \quad (2.7)$$

where  $K = E h^3 / [12(1 - \nu^2)]$  denotes the flexural stiffness of the plate,  $E$  the modulus of elasticity of concrete,  $\nu$  its Poisson's ratio and  $\rho$  its mass density, see Table 2.1. Furthermore,  $w(x, y)$  denotes the deflection of the plate,  $p(x, y)$  its external vertical load per area and  $k$  the modulus of subgrade reaction. As for the boundary conditions, all four lateral edges of the rectangular plate are stress-free boundaries (= "free edges"). Denoting components of Cauchy's stress tensor as  $\sigma_{ij}$  with  $\{i, j\} = \{x, y, z\}$ , the boundary conditions at  $x = \pm a/2$  read as (Vlasov, 1966; Höller et al., 2019)

$$\sigma_{xx} = 0 \Rightarrow m_{xx} = \int_{-h/2}^{+h/2} \sigma_{xx} z \, dz = -K \left[ \frac{\partial^2 w}{\partial x^2} + \nu \frac{\partial^2 w}{\partial y^2} \right] = 0, \quad (2.8)$$

$$\sigma_{xy} = 0 \Rightarrow m_{xy} = \int_{-h/2}^{+h/2} \sigma_{xy} z \, dz = -K(1 - \nu) \frac{\partial^2 w(x, y)}{\partial x \partial y} = 0, \quad (2.9)$$

$$\sigma_{xz} = 0 \Rightarrow q_x = \int_{-h/2}^{+h/2} \sigma_{xz} \, dz = -K \left[ \frac{\partial^3 w(x, y)}{\partial x^3} + \frac{\partial^3 w(x, y)}{\partial y^2 \partial x} \right] = 0, \quad (2.10)$$

and at  $y = \pm b/2$  as (Vlasov, 1966; Höller et al., 2019)

$$\sigma_{yx} = 0 \Rightarrow m_{yx} = \int_{-h/2}^{+h/2} \sigma_{yx} z \, dz = -K(1-\nu) \frac{\partial^2 w(x, y)}{\partial x \partial y} = 0, \quad (2.11)$$

$$\sigma_{yy} = 0 \Rightarrow m_{yy} = \int_{-h/2}^{+h/2} \sigma_{yy} z \, dz = -K \left[ \frac{\partial^2 w}{\partial y^2} + \nu \frac{\partial^2 w}{\partial x^2} \right] = 0, \quad (2.12)$$

$$\sigma_{yz} = 0 \Rightarrow q_y = \int_{-h/2}^{+h/2} \sigma_{yz} \, dz = -K \left[ \frac{\partial^3 w(x, y)}{\partial x^2 \partial y} + \frac{\partial^3 w(x, y)}{\partial y^3} \right] = 0, \quad (2.13)$$

where  $m_{xx}$  and  $m_{yy}$  stand for bending moments per length,  $m_{xy} = m_{yx}$  for twisting moments per length and  $q_x$  and  $q_y$  for shear forces per length.

The deflection field  $w(x, y)$  is computed based on Höller et al.'s (Höller et al., 2019) amendment of Vlasov's approach (Vlasov, 1966). In more detail: based on the Principle of Virtual Power (Germain, 1972), a series solution is obtained from the following weak formulation of the field equation (2.7) and the boundary conditions (2.8)–(2.13):

$$\begin{aligned} & \int_{-a/2}^{+a/2} \int_{-b/2}^{+b/2} \left[ K \left( \frac{\partial^4 w}{\partial x^4} + 2 \frac{\partial^4 w}{\partial x^2 \partial y^2} + \frac{\partial^4 w}{\partial y^4} \right) + \rho h \frac{\partial^2 w}{\partial t^2} + k w - p \right] \dot{w} \, dy \, dx \\ & - \int_{-b/2}^{+b/2} \left[ m_{xx} \frac{\partial \dot{w}}{\partial x} + m_{xy} \frac{\partial \dot{w}}{\partial y} - q_x \dot{w} \right] \Big|_{x=-a/2}^{x=+a/2} \, dy \\ & - \int_{-a/2}^{+a/2} \left[ m_{yx} \frac{\partial \dot{w}}{\partial x} + m_{yy} \frac{\partial \dot{w}}{\partial y} - q_y \dot{w} \right] \Big|_{y=-b/2}^{y=+b/2} \, dx = 0. \end{aligned} \quad (2.14)$$

where  $\dot{w}$  stands for the virtual velocities. As for the deflections  $w(x, y)$ , an ansatz is made. It consists of a Fourier series of double-symmetric deflection modes:

$$w(x, y) = \sum_{m=0}^N \sum_{n=0}^N C_{m,n} \cos \frac{m\pi x}{a} \cos \frac{n\pi y}{b}, \quad \begin{cases} m = 0, 1, 3, 5, \dots, N, \\ n = 0, 1, 3, 5, \dots, N. \end{cases} \quad (2.15)$$

The number of unknown Fourier coefficients  $C_{m,n}$  is equal to the number of deflection modes and amounts to  $[(N+3)/2]^2$  for  $N \geq 1$ . A system of algebraic equations for these coefficients is obtained by choosing an approach similar to Eq. (2.15) also for the virtual velocities, see (Höller et al., 2019) for details. In the sequel,  $N$  in Eq. (2.15) is set equal to 33, resulting in 324 Fourier coefficients. This yields a well-converged solution in terms of displacements, see the related convergence analysis in Appendix 2.C.

The structural analysis is focused on the time instant at which the falling weight produces the maximum force. The corresponding external loading of the plate reads as

$$p(x, y) = \begin{cases} \frac{199 \text{ kN}}{R^2 \pi} \dots \sqrt{x^2 + y^2} \leq R, \\ 0 \dots \dots \dots \sqrt{x^2 + y^2} > R, \end{cases} \quad (2.16)$$

with  $R = 0.15 \text{ m}$  denoting the radius of the load plate through which the dynamic force was introduced into the pavement, see Fig. 2.2(b).

The term  $\rho h \partial^2 w / \partial t^2$  in Eqs. (2.7) and (2.14) denotes inertia forces per area. Their importance will be quantified in Subsection 2.3.4. Before that, *static* structural analyses are performed, i.e. the inertia forces are set equal to zero.

### 2.3.1 Static structural analysis: identification of the modulus of subgrade reaction

The modulus of subgrade reaction  $k$  is optimized in the interval  $[0.05; 0.60]$  MPa/mm, in order to reproduce the measured deflections in the best possible fashion. The residual differences between measured deflections and corresponding simulation results are quantified based on the following square-root of sum of squared errors:

$$SRSSSE = \sqrt{\frac{1}{71} \sum_{d=1}^8 \sum_{g=1}^{m_d} [\bar{w}_{d,g} - w(x_{d,g}, y_{d,g})]^2}, \quad (2.17)$$

with  $m_7 = 8$  and  $m_d = 9$  otherwise. The Cartesian coordinates of the positions of the geophones follow from their radial distances  $r_{d,g}$  and polar angles  $\varphi_d$  as  $x_{d,g} = r_{d,g} \cos \varphi_d$  and  $y_{d,g} = r_{d,g} \sin \varphi_d$ , see Tables 2.2 and 2.3.

$k = 0.20$  MPa/mm yields the best reproduction of the measured deflections, see Fig. 2.8. The residual error according to Eq. (2.17) amounts to  $52 \mu\text{m}$ . The agreement between the computed and the measured deflections is not convincing, see Fig. 2.9. It is concluded that a *uniform*

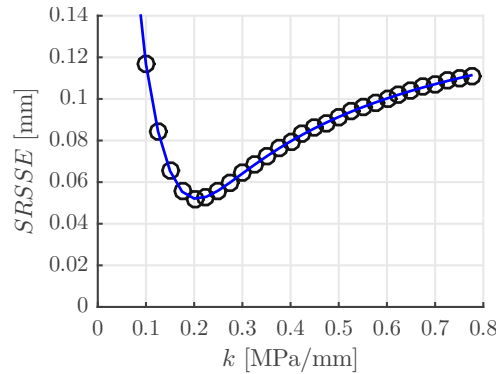


**Fig. 2.8.** Static structural analysis of the new plate: results of the optimization of the value of the modulus of subgrade reaction: square-root of sum of squared errors between measured deflections and corresponding simulation results, quantified according to Eq. (2.17).

modulus of subgrade reaction cannot explain the measured deflections in a satisfactory fashion. This calls for an extension of the structural model.

### 2.3.2 Static structural analysis: extension towards consideration of an auxiliary surface load

In order to increase the quality of reproducing the measured deflections, a uniform auxiliary load is introduced at the top-surface of the plate. Thus, Eq. (2.16) is replaced by

$$p(x, y) = \begin{cases} p_{aux} + \frac{199 \text{ kN}}{R^2 \pi} \dots \sqrt{x^2 + y^2} \leq R, \\ p_{aux} \dots \dots \dots \sqrt{x^2 + y^2} > R. \end{cases} \quad (2.18)$$

The values of the modulus of subgrade reaction *and* of the auxiliary load are optimized within the intervals  $k \in [0.05; 0.75]$  MPa/mm and  $p_{aux} \in [-0.02; +0.13]$  MPa. The values  $k = 0.65$  MPa/mm and  $p_{aux} = 0.067$  MPa allow for reproducing the measured deflections in the best-possible fashion, see Fig. 2.10. The residual error according to Eq. (2.17) amounts to  $12 \mu\text{m}$ . The agreement between the computed and the measured deflections is both qualitatively and quantitatively satisfactory, see Fig. 2.11. It is concluded that consideration of a uniform auxiliary surface load,



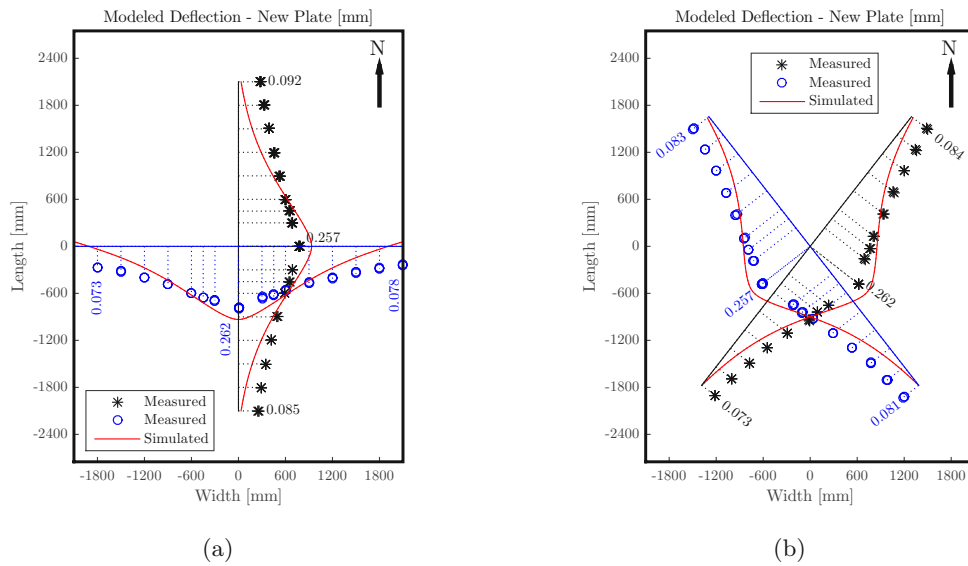


**Fig. 2.9.** Static structural analysis of the new plate: results of the optimization of the value of the modulus of subgrade reaction: measured deflections (points) and corresponding simulation results (lines) obtained with the optimal value of  $k$  amounting to 0.20 MPa/mm.

together with a uniform modulus of subgrade reaction, does allow for explaining the measured deflections in a satisfactory fashion.

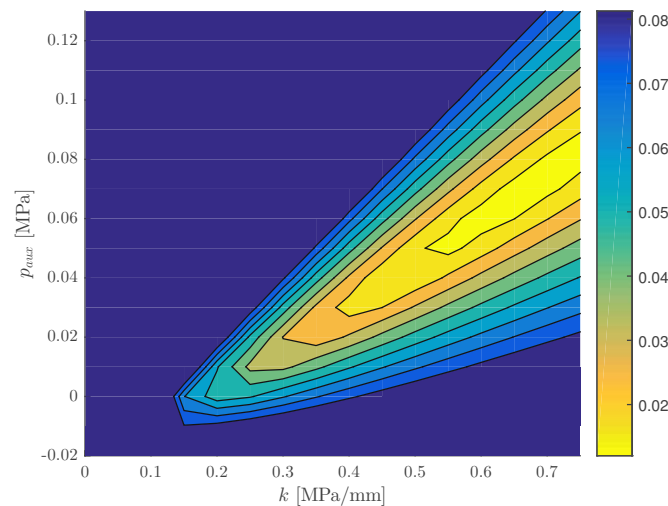


**Fig. 2.10.** Static structural analysis of the new plate: results of the optimization of the values of the uniform modulus of subgrade reaction and of the auxiliary surface load: square-root of sum of squared errors between measured deflections and corresponding simulation results, quantified according to Eq. (2.17).

It remains to be shown that the auxiliary load results in an *effective* modulus of subgrade reaction which is spatially *distributed* rather than being uniform. To this end, the plate is conceptually cut free from the Winkler foundation. In this configuration, three types of compressive normal stresses are acting on the horizontal surfaces of the plate.

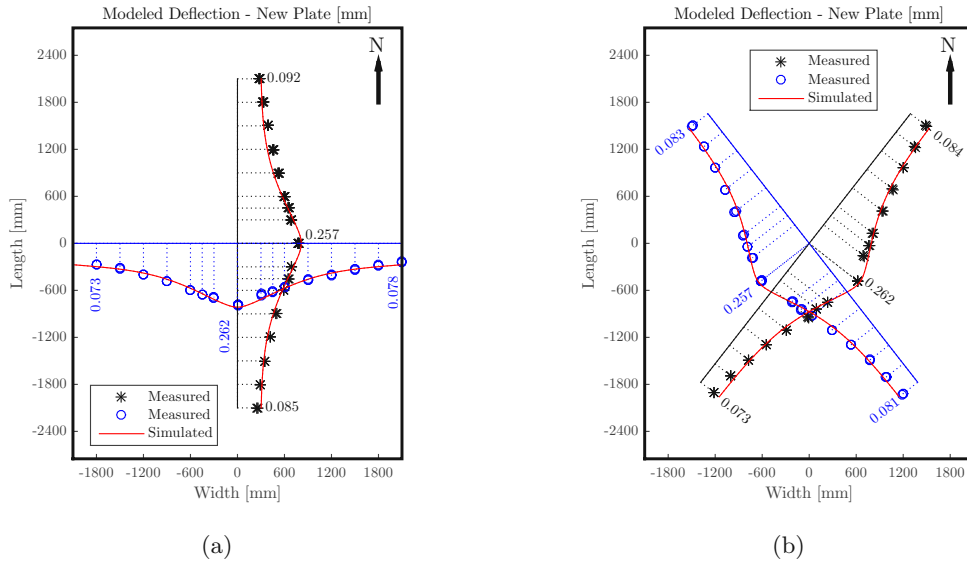


**Fig. 2.11.** Static structural analysis of the new plate: results of the optimization of the values of the uniform modulus of subgrade reaction and of the auxiliary surface load: measured deflections (points) and corresponding simulations results (lines) obtained with  $k = 0.65 \text{ MPa/mm}$  and  $p_{aux} = 0.067 \text{ MPa}$ .

- The pressure from the falling weight acts onto the top-surface of the plate, as described by Eq. (2.16).
- The pressure resulting from the springs of the Winkler foundation acts onto the bottom-surface of the plate. It reads as:  $k w(x, y)$ .
- The auxiliary pressure  $p_{aux}$  was introduced at the top-surface. This is unrealistic.

However, a *pressure* acting onto the *top*-surface of a plate is equivalent to *tensile loading* with the same absolute value, acting onto the *bottom*-surface of the plate. This way, the auxiliary loading is conceptually moved from the top to the bottom of the plate. There, it is superimposed with the stresses resulting from the springs of the Winkler foundation, see the second bullet point. The resulting pressure distribution at the bottom surface reads as  $k w(x, y) - p_{aux}$ . This is a realistic distribution of the pressure exerted from the subgrade onto the bottom-surface of the plate, because it is in equilibrium with the falling weight, and the corresponding deflection field  $w(x, y)$  satisfies the plate's field equation and boundary conditions, while reproducing the measurements in an accurate fashion.

### 2.3.3 Static structural analysis: effective modulus of subgrade reaction

The effective modulus of subgrade reaction is equal to the effective pressure  $\sigma_{zz,eff}(x, y)$  at the bottom of the plate, divided by the effective deflection field  $w_{eff}(x, y)$ :

$$k_{eff}(x, y) = \frac{\sigma_{zz,eff}(x, y)}{w_{eff}(x, y)}. \quad (2.19)$$

The load-case superposition principle applies to both the subgrade pressure and to the deflections, see the numerator and the denominator on the right-hand-side of Eq. (2.19), but not to the effective modulus of subgrade reaction, because  $k_{eff}$  is inversely proportional to  $w_{eff}$ . Thus,

Eq. (2.19) must be evaluated for the *total* load case consisting of the dead load of the plate *and* the falling weight.

The dead load represents a uniform external vertical load amounting to  $\rho gh = 5.29$  kPa, where  $g = 9.81$  m/s<sup>2</sup> denotes the gravitational acceleration. The corresponding subgrade pressure is equally large, in order to balance the external loading. The deflection resulting from the dead load,  $w_{\rho gh}$  is equal to the subgrade pressure divided by the modulus of subgrade reaction, i.e.  $w_{\rho gh} = \rho gh/k$ . Since the value of the modulus of subgrade reaction is uncertain, a sensitivity analysis is performed in the interval  $k \in [0.20; 0.30]$  MPa/mm, see Table 2.9. The chosen interval was defined in accordance with existing studies (Murthy, 2011; Nielson et al., 1969; Putri et al., 2012; Ping and Sheng, 2011; Martin et al., 2016).

**Table 2.9**

Sensitivity analysis regarding the deflection resulting from the dead load.

$\rho gh$ [MPa],	$k$ [MPa/mm]	$w_{\rho gh}$ [mm]
0.00529	0.2	0.026
0.00529	0.3	0.018

Superimposing the load cases “dead load” and “falling weight”, both in terms of the effective pressure at the bottom of the plate and in terms of the deflections, yields, after insertion into Eq. (2.19):

$$k_{eff}(x, y) = \frac{\rho gh + k w(x, y) - p_{aux}}{w_{\rho gh} + w(x, y)}. \quad (2.20)$$

The realistic distribution of the effective modulus of subgrade reaction according to Eq. (2.20) is illustrated in Fig. 2.12. The uncertainty regarding the deflection of the plate resulting from its dead load does not have a significant influence on the distribution of the effective modulus of subgrade reaction. Still, the distribution is markedly non-linear. It is reminiscent of a bell-shaped function.

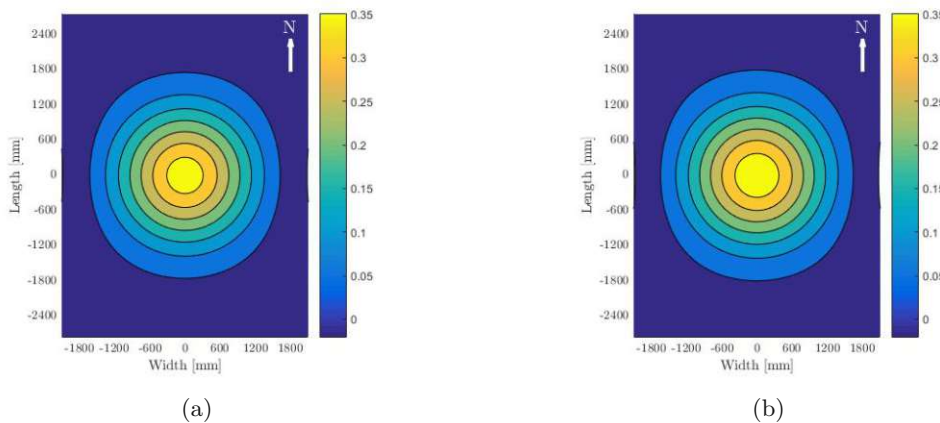


**Fig. 2.12.** Results of static structural analysis of the new plate: effective modulus of subgrade reaction, in [MPa/mm], computed according to Eq. (2.20) with (a)  $w_{\rho gh} = 0.026$  mm and (b)  $w_{\rho gh} = 0.018$  mm, see Table 2.9.

The corresponding distribution of the pressure exerted by the subgrade onto the inaccessible bottom surface of the plate reads as:  $\rho gh + k w(x, y) - p_{aux}$ , see Fig. 2.13. Because the width of the plate differs from its length, the subgrade stresses are double-symmetric with respect to the

N-S and E-W axes running through the center of the plate, rather than radial symmetric. The maximum pressure amounts to 0.115 MPa.

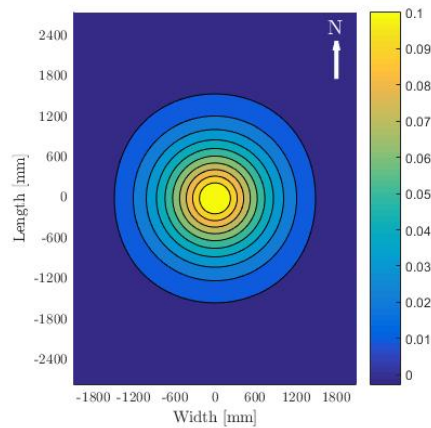


**Fig. 2.13.** Results of static structural analysis of the new plate: distribution of pressure exerted from the subgrade onto the bottom-surface of the plate:  $\rho gh + k w(x, y) - p_{aux}$ , in [MPa]

### 2.3.4 Dynamic structural analysis: effective modulus of subgrade reaction

It is of interest to quantify the influence of inertia forces  $\rho h \partial^2 w / \partial t^2$  on the effective modulus of subgrade reaction. The accelerations  $\partial^2 w / \partial t^2$  are quantified based on the readings of the geophones, see, e.g., Figs. 2.3 and 2.5. To this end, every single deflection history captured by a geophone (see the points in Fig. 2.14) is approximated, in the temporal vicinity of the maximum deflection, by means of a best-fitting polynomial, see the line in Fig. 2.14. Differentiating the

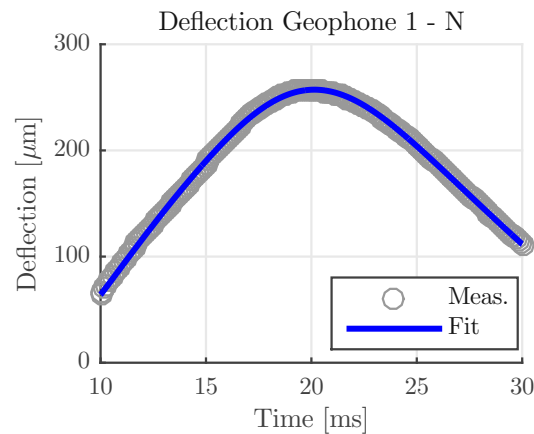


**Fig. 2.14.** Deflection history recorded by a geophone located at the center of the plate (points) and its approximation based on a polynomial (line), used to quantify the acceleration at the time instant of the maximum deflection.

polynomial twice with respect to time, and evaluating the result at the time instant of the maximum deflection delivers the sought acceleration. The acceleration is quantified for all of the 240 recordings of the geophones (Table 2.A.3 in Appendix 2.A). 240 values of the inertia forces per unit area are computed by multiplying the acceleration values with the mass density of concrete and the thickness of the plate, see the points in Fig. 2.15. These data are approximated by means of the following bell-shaped function so that a smooth and continuous description of

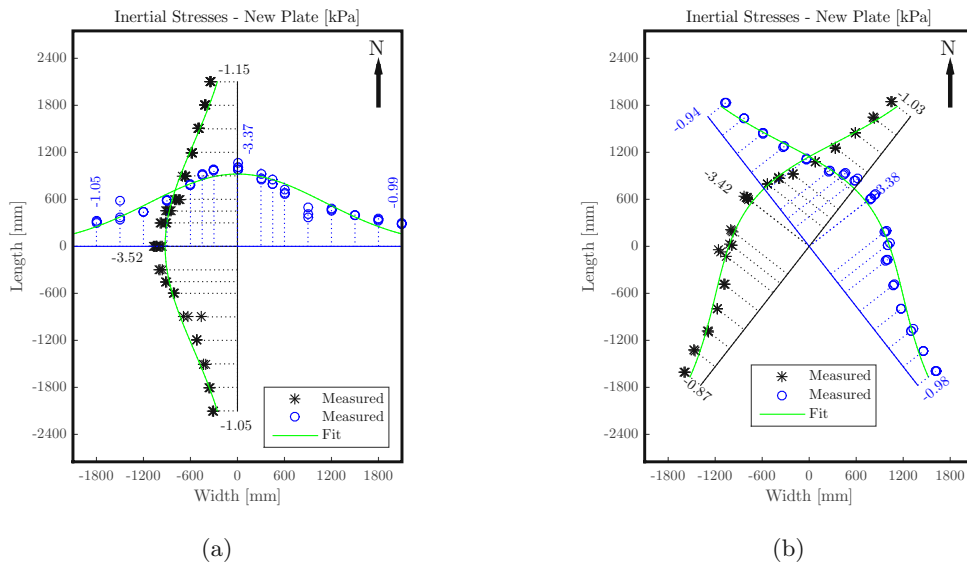


**Fig. 2.15.** Inertia forces per area of the new plate, referring to the time instants of the maximum deflections, as quantified based on the readings of the geophones, see the points, and approximation based on Eq. (2.21), see the lines.

the inertia forces is obtained:

$$p_{dyn}(x, y) = \alpha \exp \left[ - \left( \frac{x}{\beta} \right)^2 - \left( \frac{y}{\gamma} \right)^2 \right], \quad (2.21)$$

where  $\alpha$ ,  $\beta$  and  $\gamma$  are optimization variables. The optimal values read as  $\alpha = -3.077$  kPa,  $\beta = 1857$  mm and  $\gamma = 1581$  mm, see also the lines in Fig. 2.15. Finally, the expression for the effective modulus of subgrade reaction according to Eq. (2.20) is extended towards consideration of the described field of inertia forces:

$$k_{eff}(x, y) = \frac{\rho g h + k w(x, y) - p_{aux} - p_{dyn}(x, y)}{w_{\rho g h} + w(x, y)}, \quad (2.22)$$

see also Fig. 2.16. A comparison between the distribution of the modulus of subgrade reaction with and without accounting for inertia forces, compare Figs. 2.16 and 2.12, shows that consideration of inertia forces increases the effective modulus of subgrade reaction by less than 3.5%. Thus, if high precision is requested, consideration of inertia forces is recommended.

The corresponding distribution of the pressure exerted by the subgrade onto the inaccessible bottom surface of the plate is again double-symmetric and reads as:  $\rho g h + k w(x, y) - p_{aux} - p_{dyn}(x, y)$ , see Fig. 2.17. The maximum pressure amounts to 0.118 MPa. This is by 2.6% larger than the corresponding result of the static analysis, see above.

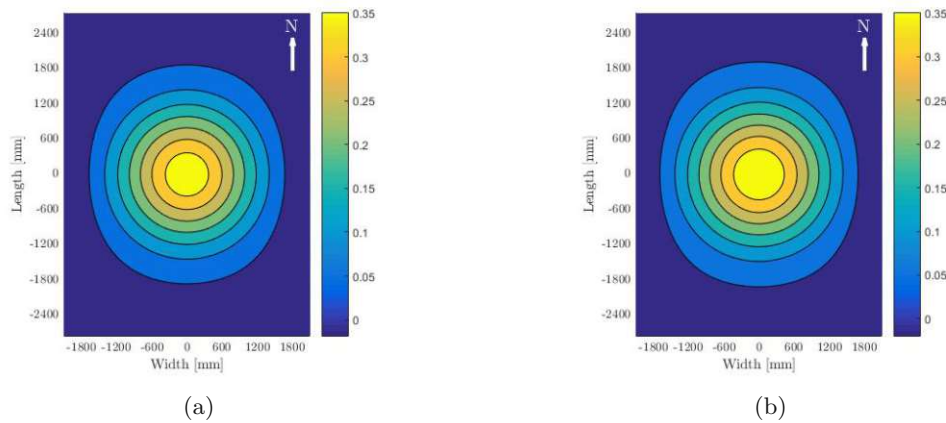


**Fig. 2.16.** Results of dynamic structural analysis of the new plate: effective modulus of subgrade reaction, in [MPa/mm], computed according to Eq. (2.22) with (a)  $w_{\rho gh} = 0.026$  mm and (b)  $w_{\rho gh} = 0.018$  mm, see Table 2.9.

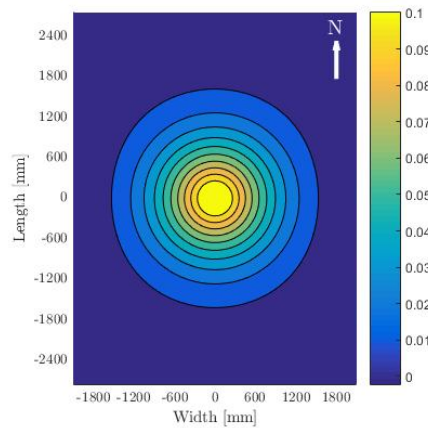


**Fig. 2.17.** Results of dynamic structural analysis of the new plate: distribution of pressure exerted from the subgrade onto the bottom-surface of the plate:  $\rho gh + k w(x, y) - p_{aux} - p_{dyn}(x, y)$ , in [MPa]

## 2.4 Conclusions

Based on the results from novel multi-directional FWD testing on two concrete plates, the following conclusions are drawn:

- Multi-directional FWD testing allows for a more detailed assessment of the state of a plate and of its directional behavior, as compared to traditional FWD tests which are limited to the driving direction.
- Insight into the non-uniform degradation of the subgrade is particularly interesting for plates subjected to long-term non-symmetric loading.
- The developed index for quantifying the asymmetry of the structural behavior, see Eq. (2.4) and Table 2.6, enriches the pool of measures available for decision-making regarding the repair of pavement plates.

- Statistical hypothesis testing corroborated the expressiveness of the index. Values of the index smaller than 5% refer to virtually symmetric behavior, values larger than 7% to asymmetric behavior.

The new plate showed a virtually double-symmetric structural behavior, although it was connected by means of dowels and tie bars to its neighbors along its Northern, Southern and Western edges, while the Eastern edge was a free boundary. The following conclusions are drawn:

- As for multi-directional FWD tests carried out at the center of a plate, values of the asymmetry index amounting to less than 5% refer to virtually double-symmetric structural behavior.
- Neither the dowels and tie bars nor potential plate-to-plate interaction had a significant influence on the FWD tests on the new plate.
- Structural analysis of such FWD tests may be carried out based on the assumption that all four edges are free boundaries.

The old plate showed significantly larger deflections than the new plate. Moreover, significant asymmetries were found. The following conclusions are drawn:

- The largest values of the asymmetry index amount to  $\geq 12\%$ . This emphasizes that the old plate presents an asymmetric behavior. If the old plate had not already been scheduled for replacement, the largest asymmetry indicators evaluated herein would suggest such a necessity for repair.
- The largest directional asymmetries were found along the E-W and the NW-SE axes. These asymmetries underline directional degradation of the subgrade of the plate resulting from long-term exposure to traffic running mainly along the Eastern edge of the plate.

Based on structural analysis of the new plate, using Kirchhoff-Love plate theory and Höller et al.'s amendment of Vlasov's approach, the following conclusions are drawn:

- The assumption of a uniform modulus of subgrade reaction is not realistic enough for reproducing deflections measured during FWD testing, see Figs. 2.8 and 2.9. Thus, it was confirmed that a multi-layered subgrade behaves in a more complex fashion than described by a Winkler foundation.
- Virtually double-symmetric deflections measured during multi-directional FWD testing were reproduced based on a uniform modulus of subgrade reaction *and* a uniform auxiliary surface load, see Figs. 2.10 and 2.11. Thus, a structural model based on a Winkler foundation is useful, provided that it is extended towards consideration of the auxiliary surface load.
- The inclusion of the auxiliary surface load allows for quantifying a realistic spatial distribution of the modulus of subgrade reaction because the subgrade pressure is in equilibrium with the dead load of the plate and the falling weight, the plate's field equation and free-edge boundary conditions are fulfilled, and the deflections obtained from multi-directional FWD testing are reproduced accurately.
- The extension of the presented mode of structural analysis towards consideration of inertia forces resulting from the dynamic nature of a FWD test was shown to be straightforward. The necessary accelerations can be computed simply from the measurements of the geophones.

- The dynamic analysis can be focused on inertia forces occurring at the same time as the deflection maxima. A transient mode of simulation is dispensable.
- Consideration of inertia forces has led to effective moduli of subgrade reaction which are by some 3.5% larger compared to those derived from static analysis. Thus, if high precision is requested, consideration of inertia forces is recommended.
- The method for quantification of double-symmetric distributions of the subgrade pressure and of the modulus of subgrade reaction is not limited to multi-directional FWD testing. It is also applicable to the evaluation of centric uni-directional FWD tests, under the assumption of a virtually double-symmetric structural behavior.

Finally, the following limitations of the study are mentioned:

- Multi-directional FWD testing requires more efforts than standard FWD tests. During standard FWD tests, operators usually stay inside their vehicle. Multi-directional FWD testing, in turn, requires hands-on work of the operators in order to position the geophone-bar in specific directions around the falling weight. Thus, also safety precautions associated with multi-directional FWD testing must be more elaborate than in the case of standard testing.
- Structural analysis was limited to the concrete plate. This allow for quantifying stresses inside the plate and at the interface between the plate and its subgrade. If properties of the individual layers underneath the plate are of interest, a multi-layered analysis is indispensable, such as the ones carried out, e.g., by (Pan, 1989a,b; Kausel and Roësset, 1981; Rahim and George, 2003; Abd El-Raof et al., 2018).

## Funding

This research received financial support by the Austrian Research Promotion Agency (FFG), the Austrian Ministry for Transport and Technology (bmvit), ÖBB-Infrastruktur AG (Vienna, Austria), and ASFINAG Bau Management GmbH (Vienna, Austria), within VIF-project 2015 “STRUKTurelle Zustandserhebung und -bewertung von Betondecke (CONcrete) auf Projektebene - ConSTRUKT” and the Bridge Project 2021 “Grundlegende Analyse von FWD-Versuchen: innovative Experimente, moderne Struktursimulationen, statistische Datenanalyse – FALLING-weight”. The authors also acknowledge the TU Wien University Library for financial support through its Open Access Funding Programme.

## Acknowledgements

Help of Pia Mandahus (TU Wien, Vienna, Austria), Marek Milcevic, Roman Oblak and Harald Aigner (Nievelt Labor GmbH, Höbersdorf, Austria) as well as interesting discussions with Wolfgang Kluger-Eigl and Luis Zelaya-Lainez (TU Wien), Martin Peyerl and Gerald Maier (Smart Minerals GmbH, Vienna, Austria) as well as Reinhard Lohmann-Pichler and Karl Gragger (ASFINAG Bau Management GmbH) are gratefully acknowledged.



## Appendix 2.A Results of multi-directional FWD testing on the new plate

**Table 2.A.1**

Maximum deflections measured during all FWD tests on the new plate [mm].

Test Direction	Test Number	Geophone								
		$g = 1$	$g = 2$	$g = 3$	$g = 4$	$g = 5$	$g = 6$	$g = 7$	$g = 8$	$g = 9$
$d = 1$ (N)	$i = 1$	0.257	0.228	0.219	0.202	0.176	0.152	0.129	0.112	0.093
$d = 1$ (N)	$i = 2$	0.259	0.229	0.221	0.203	0.178	0.153	0.129	0.112	0.093
$d = 1$ (N)	$i = 3$	0.256	0.227	0.219	0.201	0.175	0.152	0.129	0.110	0.090
$d = 2$ (NE)	$i = 1$	0.264	0.219	0.208	0.184	0.163	0.140	0.119	0.102	0.088
$d = 2$ (NE)	$i = 2$	0.260	0.216	0.206	0.189	0.162	0.138	0.118	0.097	0.082
$d = 2$ (NE)	$i = 3$	0.261	0.216	0.206	0.190	0.161	0.138	0.117	0.097	0.082
$d = 3$ (E)	$i = 1$	0.266	0.222	0.209	0.191	0.153	0.136	0.113	0.096	0.079
$d = 3$ (E)	$i = 2$	0.259	0.214	0.204	0.185	0.156	0.132	0.110	0.094	0.080
$d = 3$ (E)	$i = 3$	0.261	0.217	0.203	0.186	0.156	0.132	0.109	0.092	0.076
$d = 4$ (SE)	$i = 1$	0.258	0.206	0.203	0.182	0.152	0.126	0.100	0.093	0.078
$d = 4$ (SE)	$i = 2$	0.256	0.211	0.201	0.181	0.151	0.125	0.102	0.092	0.080
$d = 4$ (SE)	$i = 3$	0.256	0.213	0.198	0.179	0.151	0.126	0.102	0.093	0.085
$d = 5$ (S)	$i = 1$	0.261	0.231	0.218	0.198	0.165	0.142	0.118	0.096	0.086
$d = 5$ (S)	$i = 2$	0.259	0.229	0.214	0.197	0.166	0.141	0.117	0.096	0.085
$d = 5$ (S)	$i = 3$	0.261	0.230	0.215	0.197	0.169	0.141	0.117	0.097	0.085
$d = 6$ (SW)	$i = 1$	0.262	0.217	0.198	0.192	0.151	0.123	0.104	0.087	0.074
$d = 6$ (SW)	$i = 2$	0.260	0.216	0.195	0.190	0.149	0.121	0.105	0.085	0.073
$d = 6$ (SW)	$i = 3$	0.260	0.216	0.198	0.189	0.150	0.122	0.105	0.086	0.073
$d = 7$ (W)	$i = 1$	0.259	0.230	0.219	0.199	0.162	0.132	0.108	0.090	
$d = 7$ (W)	$i = 2$	0.260	0.231	0.220	0.200	0.163	0.133	0.104	0.091	
$d = 7$ (W)	$i = 3$	0.259	0.229	0.218	0.198	0.162	0.133	0.106	0.091	
$d = 8$ (NW)	$i = 1$	0.260	0.229	0.215	0.199	0.161	0.142	0.117	0.098	0.082
$d = 8$ (NW)	$i = 2$	0.259	0.228	0.217	0.198	0.168	0.142	0.118	0.099	0.082
$d = 8$ (NW)	$i = 3$	0.260	0.227	0.214	0.199	0.169	0.143	0.118	0.100	0.085
$d = 1$ (N)	$i = 4$	0.258	0.231	0.216	0.196	0.174	0.152	0.130	0.112	0.096
$d = 1$ (N)	$i = 5$	0.260	0.229	0.218	0.200	0.175	0.151	0.130	0.109	0.093
$d = 1$ (N)	$i = 6$	0.259	0.229	0.217	0.200	0.174	0.151	0.130	0.109	0.094

**Table 2.A.2**

Coefficients of variation,  $CV_{d,g}$ , of the maximum deflections measured by each geophone on the new plate, during three subsequent tests in the same direction ( $n_d = 3$ ), calculated according to Eqs. (2.1)–(2.3), see also Table 2.A.1.

Test Direction	Geophone								
	$g = 1$	$g = 2$	$g = 3$	$g = 4$	$g = 5$	$g = 6$	$g = 7$	$g = 8$	$g = 9$
d = 1 (N)	0.62%	0.51%	0.55%	0.56%	0.77%	0.42%	0.15%	0.73%	1.97%
d = 2 (NE)	0.98%	0.95%	0.44%	1.73%	0.56%	0.78%	0.53%	2.98%	4.19%
d = 3 (E)	1.48%	1.77%	1.69%	1.67%	1.00%	1.69%	1.52%	1.76%	2.62%
d = 4 (SE)	0.44%	1.56%	1.13%	1.00%	0.35%	0.68%	1.25%	0.87%	4.33%
d = 5 (S)	0.34%	0.30%	0.95%	0.35%	1.14%	0.40%	0.32%	0.74%	0.41%
d = 6 (SW)	0.43%	0.18%	0.77%	1.00%	0.65%	0.53%	0.31%	0.90%	0.55%
d = 7 (W)	0.31%	0.61%	0.46%	0.46%	0.46%	0.40%	2.09%	0.51%	
d = 8 (NW)	0.16%	0.40%	0.70%	0.31%	2.76%	0.28%	0.38%	0.72%	1.73%
d = 1 (N)	0.24%	0.34%	0.44%	1.21%	0.40%	0.34%	0.36%	1.92%	1.51%

**Table 2.A.3**

Accelerations at the time instant when the maximum deflections occurred during all FWD tests on the new plate [m/s<sup>2</sup>].

Test Direction	Test Number	Geophone								
		<i>g</i> = 1	<i>g</i> = 2	<i>g</i> = 3	<i>g</i> = 4	<i>g</i> = 5	<i>g</i> = 6	<i>g</i> = 7	<i>g</i> = 8	<i>g</i> = 9
<i>d</i> = 1 (N)	<i>i</i> = 1	-5.53	-5.10	-4.65	-4.09	-3.49	-3.02	-2.57	-2.12	-1.77
<i>d</i> = 1 (N)	<i>i</i> = 2	-5.63	-5.19	-4.81	-4.18	-3.66	-3.13	-2.66	-2.21	-1.83
<i>d</i> = 1 (N)	<i>i</i> = 3	-5.47	-5.09	-4.74	-4.15	-3.56	-3.08	-2.62	-2.17	-1.82
<i>d</i> = 2 (NE)	<i>i</i> = 1	-5.49	-4.78	-4.45	-3.83	-3.21	-2.72	-2.27	-1.95	-1.68
<i>d</i> = 2 (NE)	<i>i</i> = 2	-5.36	-4.74	-4.36	-3.84	-3.18	-2.66	-2.24	-1.91	-1.59
<i>d</i> = 2 (NE)	<i>i</i> = 3	-5.27	-4.73	-4.40	-3.83	-3.15	-2.65	-2.22	-1.82	-1.61
<i>d</i> = 3 (E)	<i>i</i> = 1	-5.63	-4.85	-4.46	-3.78	-2.61	-2.54	-2.09	-1.85	-1.52
<i>d</i> = 3 (E)	<i>i</i> = 2	-5.12	-4.50	-4.17	-3.51	-1.97	-2.44	-2.06	-1.76	-1.52
<i>d</i> = 3 (E)	<i>i</i> = 3	-5.12	-4.51	-4.15	-3.56	-2.13	-2.40	-2.09	-1.73	-1.56
<i>d</i> = 4 (SE)	<i>i</i> = 1	-5.56	-4.71	-4.35	-3.59	-2.92	-2.31	-1.85	-1.68	-1.51
<i>d</i> = 4 (SE)	<i>i</i> = 2	-5.23	-4.61	-4.21	-3.45	-2.84	-2.32	-2.07	-1.68	-1.59
<i>d</i> = 4 (SE)	<i>i</i> = 3	-5.21	-4.57	-4.16	-3.53	-2.87	-2.30	-1.86	-1.69	-1.55
<i>d</i> = 5 (S)	<i>i</i> = 1	-5.44	-5.22	-4.82	-4.26	-2.43	-2.72	-2.12	-1.88	-1.63
<i>d</i> = 5 (S)	<i>i</i> = 2	-5.37	-5.07	-4.73	-4.20	-3.61	-2.71	-2.24	-1.82	-1.63
<i>d</i> = 5 (S)	<i>i</i> = 3	-5.38	-5.20	-4.84	-4.31	-3.34	-2.73	-2.26	-1.89	-1.69
<i>d</i> = 6 (SW)	<i>i</i> = 1	-5.35	-4.78	-4.33	-3.94	-2.88	-2.26	-1.79	-1.67	-1.38
<i>d</i> = 6 (SW)	<i>i</i> = 2	-5.25	-4.73	-4.16	-4.62	-2.90	-2.31	-1.89	-1.81	-1.37
<i>d</i> = 6 (SW)	<i>i</i> = 3	-5.15	-4.65	-4.13	-4.40	-2.90	-2.30	-1.83	-1.81	-1.37
<i>d</i> = 7 (W)	<i>i</i> = 1	-5.13	-5.05	-4.74	-4.11	-3.08	-2.32	-3.02	-1.60	
<i>d</i> = 7 (W)	<i>i</i> = 2	-5.31	-5.15	-4.86	-4.16	-3.15	-2.35	-1.91	-1.62	
<i>d</i> = 7 (W)	<i>i</i> = 3	-5.32	-5.12	-4.79	-4.11	-3.07	-2.32	-1.82	-1.74	
<i>d</i> = 8 (NW)	<i>i</i> = 1	-5.64	-5.33	-4.91	-4.24	-3.45	-2.80	-2.25	-1.88	-1.50
<i>d</i> = 8 (NW)	<i>i</i> = 2	-5.13	-5.07	-4.71	-4.14	-3.43	-2.74	-2.21	-1.82	-1.52
<i>d</i> = 8 (NW)	<i>i</i> = 3	-5.21	-5.17	-4.84	-4.21	-3.48	-2.78	-2.22	-1.82	-1.47
<i>d</i> = 1 (N)	<i>i</i> = 4	-5.22	-4.85	-4.57	-3.93	-3.47	-3.03	-2.58	-2.12	-1.84
<i>d</i> = 1 (N)	<i>i</i> = 5	-5.04	-4.75	-4.45	-3.87	-3.45	-2.99	-2.54	-2.11	-1.80
<i>d</i> = 1 (N)	<i>i</i> = 6	-5.09	-4.82	-4.49	-3.93	-3.46	-2.99	-2.56	-2.22	-1.82

## Appendix 2.B Results of multi-directional FWD testing on the old plate

**Table 2.B.1**

Maximum deflections measured during all FWD tests on the old plate [mm].

Test Direction	Test Number	Geophone								
		$g = 1$	$g = 2$	$g = 3$	$g = 4$	$g = 5$	$g = 6$	$g = 7$	$g = 8$	$g = 9$
$d = 1$ (N)	$i = 1$	0.346	0.313	0.304	0.281	0.240	0.201	0.164	0.136	0.104
$d = 1$ (N)	$i = 2$	0.334	0.307	0.296	0.273	0.234	0.196	0.159	0.134	0.102
$d = 1$ (N)	$i = 3$	0.333	0.305	0.295	0.272	0.233	0.195	0.159	0.131	0.102
$d = 2$ (NE)	$i = 1$	0.342	0.311	0.302	0.283	0.247	0.209	0.171	0.138	0.105
$d = 2$ (NE)	$i = 2$	0.339	0.310	0.305	0.284	0.246	0.209	0.169	0.136	0.104
$d = 2$ (NE)	$i = 3$	0.336	0.310	0.304	0.284	0.247	0.209	0.170	0.137	0.105
$d = 3$ (E)	$i = 1$	0.339	0.318	0.311	0.291	0.258	0.217	0.172	0.135	0.104
$d = 3$ (E)	$i = 2$	0.339	0.316	0.310	0.290	0.257	0.216	0.171	0.134	0.104
$d = 3$ (E)	$i = 3$	0.337	0.315	0.309	0.289	0.256	0.215	0.171	0.133	0.104
$d = 4$ (SE)	$i = 1$	0.334	0.301	0.296	0.273	0.241	0.206	0.171	0.138	0.106
$d = 4$ (SE)	$i = 2$	0.335	0.303	0.296	0.274	0.243	0.208	0.171	0.139	0.105
$d = 4$ (SE)	$i = 3$	0.335	0.303	0.296	0.277	0.246	0.209	0.173	0.139	0.106
$d = 5$ (S)	$i = 1$	0.329	0.303	0.296	0.275	0.245	0.212	0.177	0.145	0.114
$d = 5$ (S)	$i = 2$	0.329	0.304	0.296	0.277	0.246	0.212	0.176	0.145	0.114
$d = 5$ (S)	$i = 3$	0.330	0.304	0.295	0.277	0.246	0.212	0.177	0.145	0.114
$d = 6$ (SW)	$i = 1$	0.329	0.278	0.267	0.245	0.209	0.175	0.142	0.114	0.091
$d = 6$ (SW)	$i = 2$	0.325	0.266	0.265	0.244	0.207	0.173	0.140	0.113	0.088
$d = 6$ (SW)	$i = 3$	0.327	0.271	0.266	0.244	0.208	0.174	0.142	0.113	0.089
$d = 7$ (W)	$i = 1$	0.327	0.275	0.263	0.237	0.196	0.160	0.130	0.110	
$d = 7$ (W)	$i = 2$	0.325	0.275	0.266	0.237	0.196	0.160	0.130	0.108	
$d = 7$ (W)	$i = 3$	0.325	0.274	0.262	0.236	0.194	0.159	0.128	0.106	
$d = 8$ (NW)	$i = 1$	0.329	0.286	0.270	0.247	0.207	0.171	0.139	0.115	0.091
$d = 8$ (NW)	$i = 2$	0.328	0.284	0.270	0.246	0.206	0.171	0.138	0.115	0.093
$d = 8$ (NW)	$i = 3$	0.328	0.283	0.270	0.245	0.206	0.170	0.138	0.114	0.093
$d = 1$ (N)	$i = 4$	0.329	0.302	0.288	0.266	0.228	0.188	0.151	0.120	0.093
$d = 1$ (N)	$i = 5$	0.326	0.298	0.285	0.262	0.225	0.185	0.150	0.120	0.094
$d = 1$ (N)	$i = 6$	0.328	0.298	0.286	0.263	0.226	0.187	0.152	0.123	0.095

**Table 2.B.2**

Coefficients of variation,  $CV_{d,g}$ , of the maximum deflections measured by each geophone on the old plate, during three subsequent tests in the same direction ( $n_d = 3$ ), calculated according to Eqs. (2.1)–(2.3), see also Table 2.B.1.

Test Direction	Geophone								
	$g = 1$	$g = 2$	$g = 3$	$g = 4$	$g = 5$	$g = 6$	$g = 7$	$g = 8$	$g = 9$
d = 1 (N)	2.20%	1.39%	1.67%	1.61%	1.61%	1.55%	1.73%	1.90%	1.18%
d = 2 (NE)	0.81%	0.20%	0.49%	0.22%	0.08%	0.12%	0.45%	0.77%	0.83%
d = 3 (E)	0.41%	0.56%	0.34%	0.38%	0.41%	0.49%	0.41%	0.73%	0.48%
d = 4 (SE)	0.18%	0.35%	0.14%	0.68%	1.01%	0.64%	0.50%	0.52%	0.66%
d = 5 (S)	0.22%	0.05%	0.22%	0.39%	0.15%	0.09%	0.21%	0.14%	0.43%
d = 6 (SW)	0.58%	2.31%	0.34%	0.14%	0.51%	0.69%	0.68%	0.49%	1.54%
d = 7 (W)	0.23%	0.20%	0.85%	0.32%	0.44%	0.44%	0.59%	1.92%	
d = 8 (NW)	0.21%	0.54%	0.10%	0.39%	0.39%	0.38%	0.30%	0.53%	1.16%
d = 1 (N)	0.38%	0.87%	0.58%	0.84%	0.80%	0.65%	0.53%	1.05%	1.05%

## Appendix 2.C Convergence analysis

A convergence analysis is performed for the structural simulation presented in Subsection 2.3.2. The structural analysis is repeatedly performed, whereby the number of deflection modes included in the ansatz (2.15) is progressively increased. The convergence is assessed based on the deflection referring to the center of the plate,  $w(0,0)$ , see Fig. 2.C.1. The deflections can be treated as being virtually converged, if  $\geq 256$  deflection modes are used. This is equivalent to  $N \geq 29$  in Eq. (2.15).

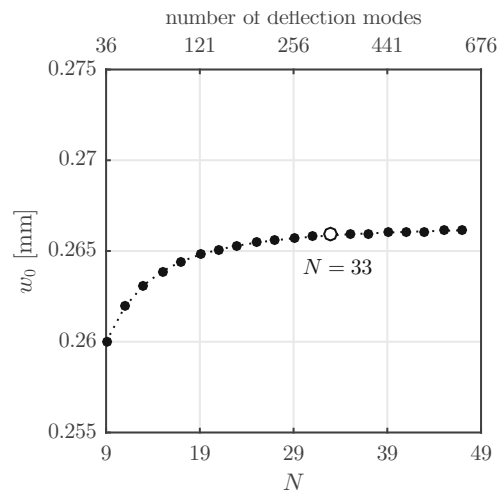


**Fig. 2.C.1.** Convergence study: computed deflection at the center of the plate, normalized with the thickness of the plate, as a function of the deflection modes included into the Fourier ansatz (2.15).

## Appendix 2.D Fourier coefficients of the deflection ansatz of Eq. (2.15), $N = 33$ .

Table 2.D.1

324 Fourier coefficients  $C_{m,n}$  describing the deflections illustrated in Fig. 2.11.

$C_{m,n}$	$n = 0$	$n = 1$	$n = 3$	$n = 5$	$n = 7$	$n = 9$
$m = 0$	-3.66969E-02	+2.01762E-02	-2.40193E-03	+3.21488E-04	-6.86965E-05	+2.48118E-05
$m = 1$	+1.55044E-02	+1.62908E-01	+3.00778E-02	+4.65923E-03	+1.36693E-03	+4.67249E-04
$m = 3$	+1.26480E-04	+5.28008E-02	+1.47846E-02	+3.51084E-03	+1.09683E-03	+4.41272E-04
$m = 5$	+1.21552E-03	+1.15046E-02	+5.91387E-03	+1.99126E-03	+8.27392E-04	+3.45888E-04
$m = 7$	-1.58940E-04	+3.76943E-03	+2.23134E-03	+1.14852E-03	+5.33703E-04	+2.75073E-04
$m = 9$	+6.32795E-05	+1.33193E-03	+1.05261E-03	+6.12921E-04	+3.56264E-04	+1.95949E-04
$m = 11$	-2.55222E-05	+6.62428E-04	+5.00935E-04	+3.62395E-04	+2.25538E-04	+1.43446E-04
$m = 13$	+1.34167E-05	+3.12863E-04	+2.89791E-04	+2.10117E-04	+1.51503E-04	+1.00226E-04
$m = 15$	-6.73579E-06	+1.95272E-04	+1.61171E-04	+1.35790E-04	+9.94418E-05	+7.31001E-05
$m = 17$	+4.65242E-06	+1.07148E-04	+1.06927E-04	+8.55991E-05	+6.97484E-05	+5.19295E-05
$m = 19$	-2.36385E-06	+7.64778E-05	+6.56069E-05	+5.97772E-05	+4.79862E-05	+3.87151E-05
$m = 21$	+2.13592E-06	+4.57650E-05	+4.78282E-05	+4.01979E-05	+3.52443E-05	+2.82695E-05
$m = 23$	-9.44815E-07	+3.57163E-05	+3.13013E-05	+2.98228E-05	+2.53043E-05	+2.16763E-05
$m = 25$	+1.18571E-06	+2.25612E-05	+2.44414E-05	+2.10463E-05	+1.93526E-05	+1.62793E-05
$m = 27$	-3.82607E-07	+1.87842E-05	+1.67200E-05	+1.63669E-05	+1.43974E-05	+1.28278E-05
$m = 29$	+7.54034E-07	+1.22894E-05	+1.37616E-05	+1.19776E-05	+1.13908E-05	+9.88162E-06
$m = 31$	-1.30748E-07	+1.07559E-05	+9.71531E-06	+9.66867E-06	+8.72420E-06	+7.97905E-06
$m = 33$	+5.28695E-07	+7.20019E-06	+8.33963E-06	+7.27497E-06	+7.09974E-06	+6.28296E-06
	$n = 11$	$n = 13$	$n = 15$	$n = 17$	$n = 19$	$n = 21$
$m = 0$	-9.06898E-06	+5.97057E-06	-1.96800E-06	+2.44791E-06	-3.76701E-07	+1.35437E-06
$m = 1$	+2.29148E-04	+1.06848E-04	+6.63279E-05	+3.58742E-05	+2.54799E-05	+1.49550E-05
$m = 3$	+2.03322E-04	+1.08816E-04	+6.12888E-05	+3.84115E-05	+2.43539E-05	+1.68463E-05
$m = 5$	+1.82667E-04	+9.34661E-05	+5.86418E-05	+3.39301E-05	+2.38882E-05	+1.49161E-05
$m = 7$	+1.44073E-04	+8.48179E-05	+5.01921E-05	+3.29411E-05	+2.13016E-05	+1.51369E-05
$m = 9$	+1.16466E-04	+6.89467E-05	+4.44435E-05	+2.84654E-05	+1.97350E-05	+1.34570E-05
$m = 11$	+8.81700E-05	+5.74266E-05	+3.71003E-05	+2.55287E-05	+1.74323E-05	+1.26426E-05
$m = 13$	+6.82444E-05	+4.51886E-05	+3.13812E-05	+2.15223E-05	+1.55319E-05	+1.10841E-05
$m = 15$	+5.09524E-05	+3.64978E-05	+2.55874E-05	+1.86407E-05	+1.34229E-05	+1.00680E-05
$m = 17$	+3.92267E-05	+2.84262E-05	+2.11976E-05	+1.54682E-05	+1.16895E-05	+8.70552E-06
$m = 19$	+2.95180E-05	+2.28144E-05	+1.71331E-05	+1.31725E-05	+9.96422E-06	+7.75119E-06
$m = 21$	+2.29974E-05	+1.78365E-05	+1.41190E-05	+1.08622E-05	+8.57647E-06	+6.64265E-06
$m = 23$	+1.76009E-05	+1.44016E-05	+1.14266E-05	+9.19774E-06	+7.26584E-06	+5.84979E-06
$m = 25$	+1.39629E-05	+1.13806E-05	+9.44933E-06	+7.58890E-06	+6.22830E-06	+4.99302E-06
$m = 27$	+1.08948E-05	+9.29490E-06	+7.70021E-06	+6.43306E-06	+5.27306E-06	+4.37592E-06
$m = 29$	+8.81044E-06	+7.44370E-06	+6.41846E-06	+5.33293E-06	+4.52371E-06	+3.73402E-06
$m = 31$	+7.00505E-06	+6.16098E-06	+5.28036E-06	+4.54289E-06	+3.84094E-06	+3.27027E-06
$m = 33$	+5.76925E-06	+5.00212E-06	+4.44497E-06	+3.79215E-06	+3.30752E-06	+2.79699E-06
	$n = 23$	$n = 25$	$n = 27$	$n = 29$	$n = 31$	$n = 33$
$m = 0$	+8.58793E-08	+8.85184E-07	+2.23834E-07	+6.32718E-07	+2.50531E-07	+4.74701E-07
$m = 1$	+1.16041E-05	+7.14584E-06	+5.91349E-06	+3.74688E-06	+3.26329E-06	+2.10117E-06
$m = 3$	+1.15454E-05	+8.53966E-06	+6.18407E-06	+4.79900E-06	+3.62090E-06	+2.91193E-06
$m = 5$	+1.13984E-05	+7.47574E-06	+6.07875E-06	+4.11862E-06	+3.51958E-06	+2.43704E-06
$m = 7$	+1.04283E-05	+7.85967E-06	+5.67144E-06	+4.47056E-06	+3.34021E-06	+2.72709E-06
$m = 9$	+9.88135E-06	+7.06729E-06	+5.42743E-06	+4.02639E-06	+3.20407E-06	+2.44578E-06
$m = 11$	+9.05298E-06	+6.86111E-06	+5.10577E-06	+4.01078E-06	+3.07836E-06	+2.48976E-06
$m = 13$	+8.31185E-06	+6.14700E-06	+4.76717E-06	+3.63332E-06	+2.89903E-06	+2.26556E-06
$m = 15$	+7.47564E-06	+5.77736E-06	+4.41429E-06	+3.50503E-06	+2.74585E-06	+2.23204E-06
$m = 17$	+6.72447E-06	+5.12684E-06	+4.05253E-06	+3.16003E-06	+2.55227E-06	+2.03088E-06
$m = 19$	+5.96155E-06	+4.72085E-06	+3.70116E-06	+2.98679E-06	+2.38595E-06	+1.96025E-06
$m = 21$	+5.29366E-06	+4.15496E-06	+3.35770E-06	+2.67629E-06	+2.19577E-06	+1.77199E-06
$m = 23$	+4.65031E-06	+3.77582E-06	+3.03560E-06	+2.49429E-06	+2.03151E-06	+1.69082E-06
$m = 25$	+4.09957E-06	+3.30536E-06	+2.73220E-06	+2.22374E-06	+1.85587E-06	+1.52697E-06
$m = 27$	+3.15042E-06	+2.97999E-06	+2.45362E-06	+2.05284E-06	+1.70397E-06	+1.43777E-06
$m = 29$	+2.75094E-06	+2.60184E-06	+2.19804E-06	+1.82404E-06	+1.54876E-06	+1.29436E-06
$m = 31$	+2.41763E-06	+2.33607E-06	+1.96642E-06	+1.67352E-06	+1.41458E-06	+1.20982E-06
$m = 33$	+2.11326E-06	+2.03883E-06	+1.75773E-06	+1.48447E-06	+1.28170E-06	+1.08686E-06





## T-shaped arrangement of geophones for rapid quantification of asymmetric behaviour of concrete slabs in central FWD tests

### 3.1 Introduction

Falling Weight Deflectometry (FWD) is frequently used for non-destructive characterisation of concrete slabs. An FWD test consists of dropping a falling weight (= standardized mass) from a defined height onto a load plate placed on top of the pavement's surface. During the impact, geophones (= displacement sensors) measure the deflection history of several points at the surface of the pavement.

During standard FWD tests, surface deflections are measured along the driving direction, see Fig. 3.1(a). Several modifications to the standard FWD testing have been developed, e.g.

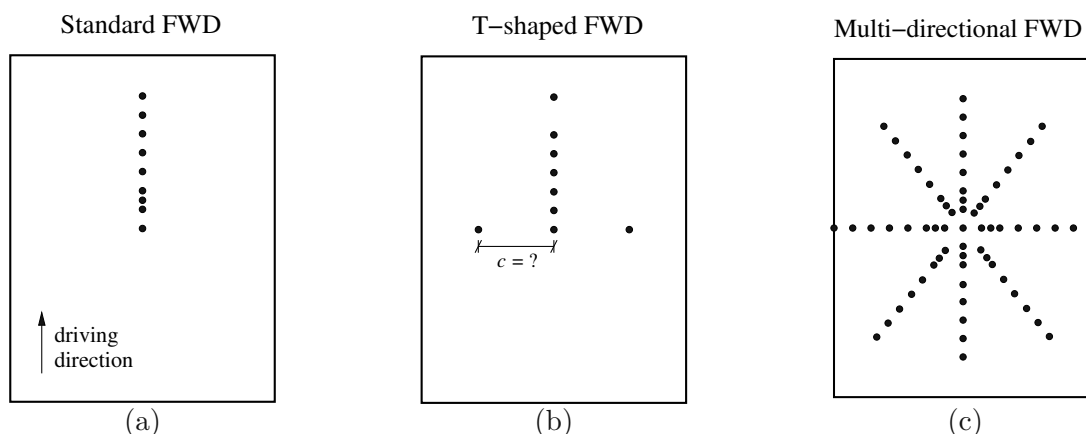


**Fig. 3.1.** Positions of geophones (see the • symbols) during central FWD testing on rigid pavements: top view onto the (a) standard approach with geophones aligned with the driving direction, (b) proposed T-shaped arrangement, where the lateral distance  $c$  is to be optimized, and (c) multi-directional testing according to Díaz Flores et al. (2021), providing input data for the aforementioned optimisation.

the Light Weight Deflectometer which is a portable device used at places inaccessible to FWD-vehicles (Fleming et al., 2007; Nazzal et al., 2007), the Rolling Weight Deflectometer which performs measurements by means of a loaded wheel running over the pavement of interest (Bay et al., 1995; Briggs et al., 2000), and the Fast Falling Weight Deflectometer which allows for carrying out a large number of tests in a short period of time (Pratelli et al., 2018; Coni et al., 2021). All these approaches have in common that deflections are measured along the driving direction. This renders the assessment of asymmetric slab behavior impossible and provides the motivation for the present paper.

Asymmetric slab behavior during central FWD tests refers to different deflections recorded at *the same* radial distance from the center of the slab, but along *different* directions, see Fig. 3.1(c) and (Díaz Flores et al., 2021). With increasing magnitude of these differences, deflections measured along the driving direction are decreasingly representative of the behavior of the slab in other directions. This is problematic, because point-symmetric deflection basins are usually assumed when it comes to back-calculation of subgrade stiffness from deflections measured along the driving direction during central FWD tests. Herein, a new T-shaped arrangement of the geophones is proposed for rapid quantification of asymmetric slab behavior in central FWD testing of concrete slabs.

One geophone is positioned at the center of impact (= center of the slab), six along the driving direction ( $N$ -direction), one right ( $E$ -direction) and one left ( $W$ -direction) of the center, see Fig. 3.1(b), where  $N$ ,  $E$ , and  $W$  refer to a local cardinal directional system. As for the quantification of asymmetric structural behavior, we here introduce a dimensionless deflection basin parameter referred to as “Lateral Asymmetry Index”:

$$\text{LASIX} = \frac{|w_E(r=c) - w_W(r=c)|}{w_N(r=c)}, \quad (3.1)$$

where  $w_E(r=c)$ ,  $w_W(r=c)$ , and  $w_N(r=c)$  refer to the deflections at the same radial distance  $r = c$  from the center of the slab, but in the  $E$ -direction (right),  $W$ -direction (left), and  $N$ -direction (driving direction), respectively, and  $|w_E(r=c) - w_W(r=c)|$  denotes the absolute value of the difference of the deflections measured in the  $E$ -direction and the  $W$ -direction, at the radial distance  $r = c$  from the center of the slab, see Fig. 3.1(b).

The main research challenge tackled herein is to optimize the radial distance  $c$  in Eq. (3.1) such as to maximize the informative content of LASIX regarding the quantification of asymmetric slab behavior. This optimisation requires the evaluation of LASIX for different values of  $c$  and, therefore, the measurement of deflections during central FWD testing on several concrete slabs (i) not only in driving direction, but also right and left of the center of the slab, and (ii) at several radial distances. The optimal value of  $c$  will be determined such that corresponding values of LASIX correlate in the best possible fashion with another newly introduced dimensionless deflection basin parameter: the effective asymmetry index  $\mathcal{A}_{28}^*$ . The latter summarizes the asymmetric behavior of every tested slab in a detailed fashion because it contains information on differences of deflections measured (i) not only in driving direction, right, and left of the center of the slab, but in *eight* different directions, and (ii) at several radial distances, see Fig. 3.1(c).

The present paper is organized as follows. Section 3.2 refers to the optimisation of the T-shaped arrangement of geophones based on experimental data from central FWD testing of ten concrete slabs, with multi-directional measurements of deflections. For all ten tested slabs, these data provide the basis for quantification (i) of the effective asymmetry index  $\mathcal{A}_{28}^*$ , and (ii) of the lateral asymmetry index LASIX for six different values of  $c$ . The optimal distance  $c$  will be identified such that associated values of LASIX exhibit the best possible correlation with  $\mathcal{A}_{28}^*$ . Section 3.3 contains a discussion regarding the sources of asymmetric slab behavior and their associated implications for the back-calculation of pavement properties from deflections

measured during FWD testing. Section 3.4 contains the conclusions drawn from the results obtained from the presented study.

## 3.2 Optimisation of a T-shaped arrangement of geophones for rapid quantification of the asymmetric behavior of concrete slabs in central FWD tests

### 3.2.1 Detailed asymmetry characterisation of ten concrete slabs subjected to central FWD testing

The development of an optimized T-shaped arrangement of geophones for central FWD testing on concrete slabs requires comprehensive insight into the asymmetries of several slabs. This provides the motivation to perform multi-directional FWD tests (Díaz Flores et al., 2021) at the centers of ten concrete slabs located on the Austrian highways “A1” and “A2”. The tests were performed early in the morning of days during which no significant temperature variations were expected. This excluded problems resulting from slab curling due to temperature gradients (Ioannides and Khazanovich, 1998; Khazanovich et al., 2001).

Five tested slabs are part of the highway “A1”. Three of them had been in service for 22 years (“old slabs”), the other two had been recently installed (“new slabs”). All slabs have a thickness of 0.22 m and a length of 5.50 m. The widths of the slabs located on the acceleration lane, the first lane, and the emergency lane, are equal to 4.20 m, 3.80 m, and 3.20 m, respectively, see Table 3.1. The maximum forces imposed during central multi-directional FWD testing range from 201 kN to 203 kN.

Another five tested slabs are part of the highway “A2”. Three of them had been in service for 33 years (“old slabs”), the other two had been recently installed (“new slabs”). All slabs have a thickness of 0.22 m. Their length ranges from 4.50 to 5.60 m, and their width from 3.10 to 4.00 m, see Table 3.1. The maximum forces imposed during central multi-directional FWD testing range from 189 kN to 193 kN.

**Table 3.1**

Properties of the ten slabs characterized by means of multi-directional FWD testing.

Slab #	Condition	Lane	Length [m]	Width [m]	Thickness [m]	Force [kN]
A1-33354	Old	Acceleration	5.50	4.20	0.22	201
A1-33360	New	Acceleration	5.50	4.20	0.22	201
A1-33868	Old	First	5.50	3.80	0.22	201
A1-33873	New	First	5.50	3.80	0.22	202
A1-33874	Old	Emergency	5.50	3.20	0.22	203
A2-47543	Old	**	4.50	4.00	0.22	193
A2-50000	Old	First	4.50	3.75	0.22	190
A2-51995	New	Emergency	5.60	3.10	0.22	191
A2-54003	Old	First	5.60	3.80	0.22	189
A2-54440	New	First	5.60	3.50	0.22	190

\*\* Transition from acceleration to emergency lane

During multi-directional FWD testing, deflections are measured along eight specific radial directions, starting with the driving direction and proceeding clockwise as described in (Díaz Flores et al., 2021), Fig. 3.2, and Table 3.2, where N, E, S, and W refer to a local cardinal directional

system with N pointing in the driving direction. Three tests are carried out immediately one after the other in every testing direction, in order to be able to assess test repeatability. After three such tests in all eight measurement directions, another final set of three tests is performed in the N direction, again for the sake of being able to assess test repeatability. Thus, the first and the ninth set of three tests correspond to the N direction.

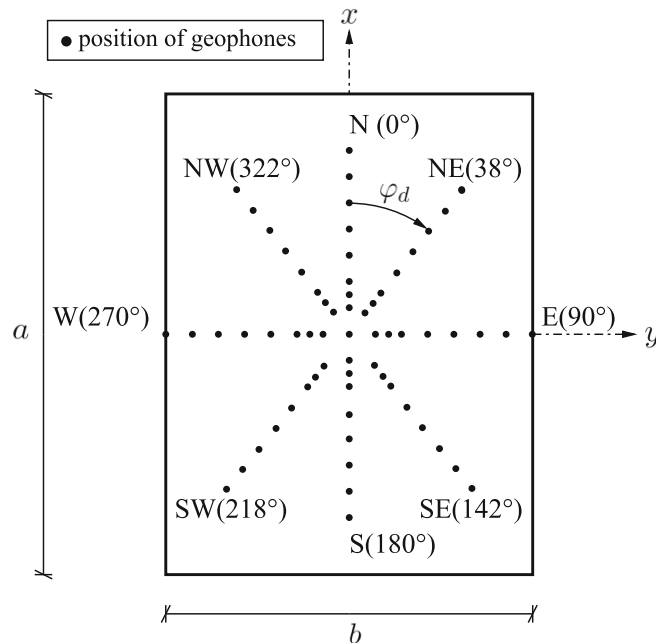


**Fig. 3.2.** Arrangement of geophones during multi-directional FWD testing according to (Díaz Flores et al., 2021) and local cardinal directional system, with N referring to the driving direction.

**Table 3.2**

Polar angles  $\varphi_d$  of the eight different measurement directions.

	Test Direction							
	N	NE	E	SE	S	SW	W	NW
	$d = 1$	$d = 2$	$d = 3$	$d = 4$	$d = 5$	$d = 6$	$d = 7$	$d = 8$
polar angle	$0^\circ$	$38^\circ$	$90^\circ$	$142^\circ$	$180^\circ$	$218^\circ$	$270^\circ$	$322^\circ$

During every single FWD test, nine geophones measure deflections of the surface of the slab. The first geophone ( $g = 1$ ) is located at the center of the slab, the other eight ( $g = 2$  to  $g = 9$ ) are fixed to a bar which ensures that the distances between them are constant. Structural constraints of the FWD-device make it necessary to move the bar 15 cm further away from the center when measuring along the SE and SW directions, as compared to all the other, see Table 3.3.

In case that the outermost geophone(s) are located on the neighboring slab or on the adjacent soil, their measurements are excluded. The number of excluded geophones are sometimes different in the E and W directions, see Table 3.4, because of small eccentricities of the FWD-device from the center of the slab, which amounted to a few single centimetres.

All deflection maxima recorded by the geophones on the ten tested slabs are listed in Tables 3.A.1 to 3.A.10. The deflection maxima measured on the slabs A2-54003 and A2-54440

**Table 3.3**

Radial distances of the geophones from the center of impact (= center of the slab),  $r_{d,g}$  [m], as functions of the measurement direction:  $d = 1$  (N),  $d = 2$  (NE),  $d = 3$  (E),  $d = 4$  (SE),  $d = 5$  (S),  $d = 6$  (SW),  $d = 7$  (W),  $d = 8$  (NW).

Test Directions	Geophone								
	$g = 1$	$g = 2$	$g = 3$	$g = 4$	$g = 5$	$g = 6$	$g = 7$	$g = 8$	$g = 9$
$d \in [1, 2, 3, 5, 7, 8]$	0.00	0.30	0.45	0.60	0.90	1.20	1.50	1.80	2.10
$d \in [4, 6]$	0.00	0.45	0.60	0.75	1.05	1.35	1.65	1.95	2.25

**Table 3.4**

Geophones which were excluded since they were located outside the tested slab.

Tested Slab	Direction	Excluded geophones
A1-33354	W	$g = 9$
A1-33360	W	$g = 9$
A1-33868	W	$g = 9$
A1-33873	E	$g \in \{8, 9\}$
	W	$g = 9$
A1-33874	E	$g \in \{8, 9\}$
	W	$g = 9$
A2-47543	E	$g \in \{8, 9\}$
	W	$g = 9$
A2-50000	E	$g \in \{8, 9\}$
	W	$g = 9$
A2-51995	E	$g \in \{8, 9\}$
	W	$g \in \{7, 8, 9\}$
A2-54003	E	$g \in \{8, 9\}$
	W	$g \in \{8, 9\}$
A2-54440	E	$g = 9$
	W	$g \in \{8, 9\}$
	E	$g = 9$

are exemplarily illustrated in Fig. 3.3. Test repeatability is satisfactory. The three (to six)<sup>1</sup> tests performed in every direction delivered very similar deflection maxima in all radial distances, see e.g. the red zoom windows in Figs. 3.3(a) and (c). In all 27 tests performed per slab, the deflection maxima measured at the center of impact are very similar, see the first columns of measured data in Tables 3.A.1 to 3.A.10. The first three tests and the last three tests, referring to the driving direction, delivered very similar results see e.g. the red zoom windows in Figs. 3.3(a) and (c) as well as data in Tables 3.A.1 to 3.A.10. This underlines that the support conditions of the ten characterized slabs were stable during the approximately 45 minutes needed to perform a complete set of multi-directional FWD tests.

<sup>1</sup>Six tests were performed in driving direction, three tests in all other directions.

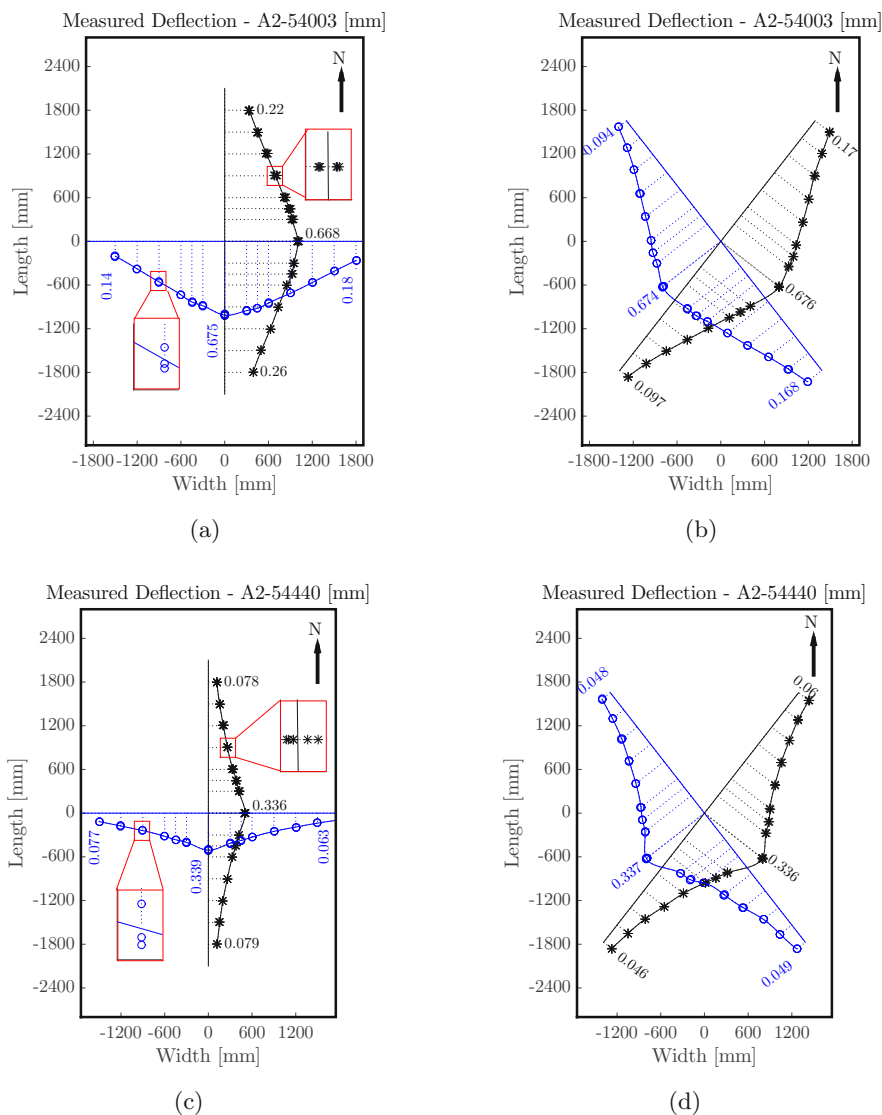


**Fig. 3.3.** Results from multi-directional FWD testing on the old slab A2-54003, see (a) and (b), as well as on the new slab A2-54440, see (c) and (d): the points refer to the deflection maxima listed in Tables 3.A.9 and 3.A.10, respectively, measured by the geophones along the N, S, E and W directions, see (a) and (c), as well as along the NE, SE, SW, and NW directions, see (b) and (d); the solid lines refer to splines interpolating between the average of the three deflections measured at each location.

### 3.2.2 Quantification of the asymmetry of the structural behavior by means of the new deflection basin parameter $\mathcal{A}_{28}^*$

The deviation of the structural behavior of the tested slabs from point symmetry with respect to the center of impact (= center of the slab) is quantified by means of the “effective asymmetry index” which is a new deflection basin parameter introduced as

$$\mathcal{A}_{28}^* = \sqrt{\frac{1}{28} \sum_{j=1}^{28} (A_{d,\delta})^2}, \quad (3.2)$$

where the relation between the summation index  $j$  and asymmetry indicators  $A_{d,\delta}$  is clarified in Table 3.5. The values of  $A_{d,\delta}$  quantify differences of deflections measured in two *different* directions  $d$  and  $\delta$ , as introduced in (Díaz Flores et al., 2021) as

$$A_{d,\delta} = \sqrt{\frac{1}{\ell} \int_0^{\ell} \left[ \frac{w_d(r)}{w_d(r=0)} - \frac{w_\delta(r)}{w_\delta(r=0)} \right]^2 dr}, \quad (3.3)$$

where both indexes  $d$  and  $\delta$  run over the eight measurement directions: N, NE, E, SE, S, SW, W, and NW. Also in Eq. (3.3),  $r$  denotes the radial coordinate, while  $w_d(r)$  and  $w_\delta(r)$  stand for splines referring to the measurement directions  $d$  and  $\delta$ , respectively. These splines (see e.g. the blue and black solid lines in Fig. 3.3) interpolate between the average of the three (to six) deflection maxima measured at each point. Finally,  $\ell$  denotes the radial length of integration. Here,  $\ell$  is equal to 2.10 m, except when comparing directions along which geophones were excluded, see Table 3.4. In these cases,  $\ell$  is equal to the distance from the center of the slab to the last geophone that was included.

For every one of the ten tested slabs, asymmetry indicators are evaluated according to Eq. (3.3) for all 28 combinations of two different directions out of the available eight measurement directions. The  $10 \times 28 = 280$  asymmetry indicators are listed in Table 3.5.

The \* symbol in  $\mathcal{A}_{28}^*$  according to Eq. (3.2) refers to multi-directional FWD testing in eight different directions, and the subscript “28” for all 28 combinations of two different directions out of the eight available measurement directions. The effective asymmetry index  $\mathcal{A}_{28}^*$  of every slab is obtained from inserting its 28 asymmetry indicators from Table 3.5 into Eq. (3.2), see Table 3.6 for the results.

The ten obtained effective asymmetry indices allow for the correct classification of the tested slabs into “old slabs” and “new slabs”, because  $\mathcal{A}_{28}^*$  of all old/new slabs is larger/smaller than 4%. This corroborates the expressiveness of  $\mathcal{A}_{28}^*$  regarding the assessment of asymmetric structural behavior.

### 3.2.3 Quantification of asymmetric structural behavior based on T-shaped testing and the deflection basin parameter LASIX

A T-shaped arrangement of geophones is proposed with the aim to combine the advantages of standard and multi-directional FWD testing: (i) rapid in situ characterisation and (ii) expressiveness regarding the assessment of asymmetric structural behavior. Surface deflections are measured by means of nine geophones: one at the center of impact (= center of the slab), six along the driving direction, one left and one right of the center of impact, see Fig. 3.1(b).

The corresponding assessment of asymmetric structural behavior is based on the deflection basin parameter LASIX, introduced in Eq. (3.1). The remaining open research question refers to optimising the radial distance  $c$  of the geophones from the center of the slab, in order to maximize

**Table 3.5**

Asymmetry indicators,  $A_{d,\delta}$  according to Eq. (3.3), quantifying the deviation of the measured structural behavior from point symmetry with respect to the center of impact (= center of the slab); evaluated for the ten tested slabs.

Slab # Condition	A1-33354 Old	A1-33360 New	A1-33868 Old	A1-33873 New	A1-33874 Old	A2-47543 Old	A2-50000 Old	A2-51995 New	A2-54003 Old	A2-54440 New
$A_{N,NE}$ $j = 1$	2.63%	5.25%	3.50%	1.55%	1.40%	3.25%	0.78%	1.13%	1.24%	0.49%
$A_{N,E}$ $j = 2$	4.18%	6.91%	8.85%	4.20%	3.73%	8.23%	1.69%	1.28%	2.97%	2.93%
$A_{N,SE}$ $j = 3$	7.48%	4.14%	1.37%	2.55%	3.72%	1.55%	8.90%	1.22%	5.99%	1.60%
$A_{N,S}$ $j = 4$	4.94%	3.98%	2.30%	1.65%	2.16%	2.41%	5.98%	0.98%	3.96%	0.68%
$A_{N,SW}$ $j = 5$	1.71%	5.25%	3.79%	2.11%	2.70%	5.33%	3.98%	3.04%	3.85%	1.56%
$A_{N,W}$ $j = 6$	9.68%	6.26%	2.26%	2.40%	3.59%	2.63%	6.10%	5.42%	14.21%	4.95%
$A_{N,NW}$ $j = 7$	6.76%	3.92%	2.87%	3.10%	3.17%	4.24%	4.87%	4.74%	9.68%	3.49%
$A_{NE,E}$ $j = 8$	1.75%	1.87%	5.44%	2.11%	2.64%	5.82%	1.67%	1.99%	3.18%	2.33%
$A_{NE,SE}$ $j = 9$	4.98%	3.09%	3.00%	1.96%	3.53%	2.29%	8.44%	1.20%	4.94%	1.84%
$A_{NE,S}$ $j = 10$	2.52%	2.54%	6.07%	2.52%	3.01%	4.98%	5.44%	1.62%	2.98%	0.98%
$A_{NE,SW}$ $j = 11$	3.01%	4.44%	7.17%	3.03%	3.99%	7.83%	3.63%	4.01%	4.88%	1.43%
$A_{NE,W}$ $j = 12$	9.75%	3.68%	3.07%	1.46%	5.48%	5.10%	6.45%	6.74%	14.70%	3.77%
$A_{NE,NW}$ $j = 13$	7.47%	2.55%	2.29%	1.24%	4.14%	2.88%	5.29%	6.08%	10.15%	3.11%
$A_{E,SE}$ $j = 14$	4.97%	3.02%	8.27%	3.66%	3.74%	6.14%	5.63%	2.37%	7.68%	4.69%
$A_{E,S}$ $j = 15$	2.62%	3.98%	10.97%	4.02%	4.46%	8.25%	3.37%	1.31%	6.14%	2.70%
$A_{E,SW}$ $j = 16$	4.54%	4.66%	12.63%	4.49%	4.69%	12.49%	3.14%	2.61%	2.93%	2.32%
$A_{E,W}$ $j = 17$	12.00%	3.49%	7.56%	2.98%	7.75%	8.60%	5.94%	5.83%	13.95%	1.78%
$A_{E,NW}$ $j = 18$	9.03%	3.65%	7.72%	1.14%	5.74%	8.01%	6.37%	5.02%	7.87%	0.89%
$A_{SE,S}$ $j = 19$	2.72%	1.14%	3.48%	2.78%	2.94%	2.90%	3.95%	1.40%	2.27%	1.71%
$A_{SE,SW}$ $j = 20$	7.34%	2.43%	4.31%	2.62%	4.35%	5.79%	5.96%	3.57%	9.67%	2.03%
$A_{SE,W}$ $j = 21$	14.88%	1.99%	1.77%	1.45%	6.91%	3.79%	14.32%	6.41%	19.11%	5.28%
$A_{SE,NW}$ $j = 22$	12.19%	1.24%	1.38%	1.63%	6.63%	1.45%	13.37%	5.98%	15.03%	4.31%
$A_{S,SW}$ $j = 23$	4.88%	2.51%	1.61%	1.85%	1.90%	2.99%	2.75%	2.63%	7.76%	1.54%
$A_{S,W}$ $j = 24$	13.53%	2.95%	4.19%	2.23%	4.00%	2.86%	11.37%	4.89%	18.06%	4.39%
$A_{S,NW}$ $j = 25$	9.58%	0.54%	3.96%	3.19%	4.28%	2.74%	10.69%	4.83%	13.00%	3.63%
$A_{SW,W}$ $j = 26$	7.58%	2.48%	5.03%	2.48%	3.24%	4.49%	9.08%	3.42%	10.67%	3.52%
$A_{SW,NW}$ $j = 27$	5.05%	2.79%	5.03%	3.57%	3.42%	5.58%	8.60%	3.15%	5.44%	2.84%
$A_{W,NW}$ $j = 28$	2.40%	2.73%	1.49%	1.60%	1.86%	3.85%	1.72%	1.41%	5.94%	1.47%

**Table 3.6**

Values of the effective asymmetry index,  $\mathcal{A}_{28}^*$  according to Eq. (3.2), calculated for the ten tested slabs; integrating the 28 asymmetry indicators of each slab (see Table 3.5) into one single value.

Slab #	Condition	$\mathcal{A}_{28}^*$
A1-33354	Old	7.68%
A1-33360	New	3.81%
A1-33868	Old	5.54%
A1-33873	New	2.73%
A1-33874	Old	4.29%
A2-47543	Old	5.52%
A2-50000	Old	7.35%
A2-51995	New	3.87%
A2-54003	Old	9.67%
A2-54440	New	2.94%

the informative content of LASIX for the quantification of asymmetric slab behavior. This optimisation requires an evaluation of LASIX for different values of  $c$ , which is possible, because multi-directional testing delivers geophone measurements at so many positions, that focusing on subsets of the available geophone positions allows for simulating T-shaped arrangements of the geophones with several different values of  $c$ . LASIX is evaluated according to Eq. (3.1) for six different values of  $c$  (0.30 m, 0.45 m, 0.60 m, 0.90 m, 1.20 m, and 1.50 m) and for all ten slabs, see Table 3.7.



**Table 3.7**

Lateral Asymmetry Index, LASIX according to Eq. (3.1), evaluated for different radial distances  $c$  of the geophones in E, W, and N directions.

Slab #	Condition	$c = 0.30$ m	$c = 0.45$ m	$c = 0.60$ m	$c = 0.90$ m	$c = 1.20$ m	$c = 1.50$ m
A1-33354	Old	12.47%	14.07%	16.11%	18.54%	<b>16.93%</b>	12.66%
A1-33360	New	4.72%	5.23%	4.51%	2.83%	<b>0.31%</b>	1.79%
A1-33868	Old	3.73%	7.27%	9.21%	10.84%	<b>8.98%</b>	5.95%
A1-33873	New	2.89%	2.72%	2.16%	0.80%	<b>0.29%</b>	2.87%
A1-33874	Old	0.74%	0.33%	1.09%	5.04%	<b>9.28%</b>	12.34%
A2-47543	Old	0.22%	2.70%	5.53%	9.09%	<b>10.43%</b>	7.79%
A2-50000	Old	1.55%	4.87%	6.58%	8.35%	<b>9.56%</b>	10.15%
A2-51995	New	3.12%	6.23%	5.98%	6.74%	<b>7.10%</b>	
A2-54003	Old	6.74%	8.60%	11.21%	15.54%	<b>18.62%</b>	20.64%
A2-54440	New	2.44%	1.92%	2.37%	2.02%	<b>2.76%</b>	4.29%

### 3.2.4 Optimal distance $c$ of the lateral geophones from the center of the slab

The optimal radial distance  $c$  of the geophones from the center of impact refers to the largest possible expressiveness of LASIX for the assessment of asymmetric structural behavior. The related optimisation problem is solved as follows. For all six different values of  $c$  (0.30 m, 0.45 m, 0.60 m, 0.90 m, 1.20 m, and 1.50 m) the following steps are performed:

1. Ten values of LASIX, referring to T-shaped testing with one specific value of  $c$ , see the respective columns in Table 3.7, are correlated with the ten corresponding values of  $\mathcal{A}_{28}^*$  derived from multi-directional testing, see Table 3.6.
2. The best linear regression function is fitted to the pairs of values of LASIX and  $\mathcal{A}_{28}^*$ , and the corresponding quadratic correlation coefficient is determined, see Table 3.8.

**Table 3.8**

Correlation between the values of LASIX in Table 3.7, referring to different values of the distance  $c$ , and values of  $\mathcal{A}_{28}^*$  listed in Table 3.6.

distance	best linear regression function	$R^2$
$c = 0.30$ m	$\mathcal{A}_{28}^* = 0.32 \times \text{LASIX} + 4.12$	25%
$c = 0.45$ m	$\mathcal{A}_{28}^* = 0.37 \times \text{LASIX} + 3.34$	42%
$c = 0.60$ m	$\mathcal{A}_{28}^* = 0.39 \times \text{LASIX} + 2.84$	61%
$c = 0.90$ m	$\mathcal{A}_{28}^* = 0.35 \times \text{LASIX} + 2.57$	78%
$c = 1.20$ m	$\mathcal{A}_{28}^* = 0.33 \times \text{LASIX} + 2.56$	82%
$c = 1.50$ m	$\mathcal{A}_{28}^* = 0.35 \times \text{LASIX} + 2.44$	74%

The best correlation between LASIX, related to T-shaped FWD testing, and  $\mathcal{A}_{28}^*$ , related to multi-directional FWD testing, is obtained for deflections measured at a distance  $c = 1.20$  m from the center of the slab, see Table 3.8. The corresponding maximum of the quadratic correlation coefficient amounts to  $R^2 = 82\%$ , see also Fig. 3.4. The values of LASIX referring to  $c = 1.20$  m allow for the correct classification of the tested slabs into “old slabs” and “new slabs”. As for all new slabs, values of LASIX referring to  $c = 1.20$  m are smaller than or equal to 7.10%. As for all old slabs, values of LASIX referring to  $c = 1.20$  m are larger than or equal to 8.98%. This underlines the expressiveness of the newly introduced deflection-basin-parameter LASIX

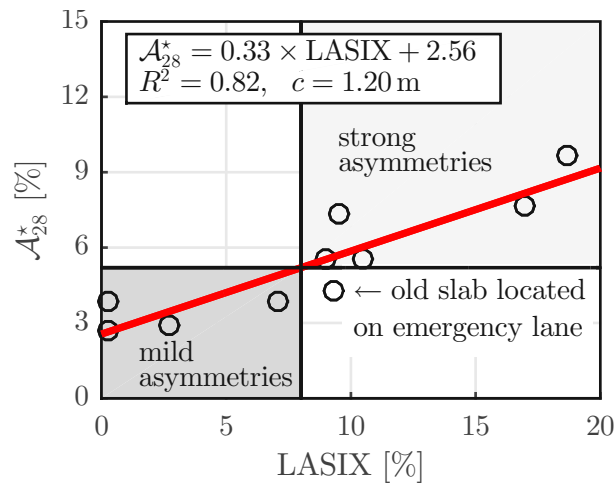


**Fig. 3.4.** Best correlation between the Lateral Asymmetry Index LASIX according to Eq. (3.1), related to T-shaped FWD testing, and the effective asymmetry index  $\mathcal{A}_{28}^*$  according to Eq. (3.2), related to multi-directional FWD testing: the deflections  $w_E$ ,  $w_W$ , and  $w_N$  used to evaluate LASIX were measured at a distance  $c = 1.20$  m from the center of impact; each symbol corresponds to one of the ten tested slabs; the horizontal and vertical black lines represent the threshold values of  $\mathcal{A}_{28}^*$  and LASIX distinguishing mild from strong asymmetries.

regarding the assessment of asymmetric structural behavior. In Fig. 3.4, the threshold value of LASIX distinguishing old from new slabs was set equal to 8.00%.

The threshold value LASIX = 8% refers, according to the red regression line in Fig. 3.4, to  $\mathcal{A}_{28}^* = 5.2\%$ . This threshold value allows for the correct classification into old and new slabs in all but one case: the old slab A1-33874 with LASIX = 10.43% ( $> 8\%$ ) and  $\mathcal{A}_{28}^* = 4.29\%$  ( $< 5.2\%$ ), see Tables 3.7 and 3.6. Notably, this slab was part of an emergency lane, see Table 3.1. Therefore, it was subjected to traffic loading only indirectly, namely, because of load transfer via tie bars connecting the tested slab to its neighbor which was part of the first lane and, therefore, directly exposed to traffic loads. This underlines that values of LASIX  $> 8\%$  call for an engineering assessment of the specific exposure of the tested slab to eccentric traffic loads.

The construction of trailers containing a fixed installation of the optimal T-shaped arrangement of geophones appears to be feasible, because the optimal distance between the two lateral geophones,  $2 \times c = 2.40$  m, is smaller than the maximum allowed width of vehicles. Such trailers will facilitate in situ data acquisition, because the operators can stay inside their vehicle, as in standard FWD testing, i.e. there is no need for the operators to get out of their vehicle and manipulate the geophones, as required for multi-directional FWD testing.

### 3.2.5 Arrangement of the geophones remaining aligned with the driving direction

As for the six geophones which remain aligned with the driving direction, it is proposed to arrange them at radial distances amounting to 0.30 m, 0.60 m, 0.90 m, 1.20 m, 1.50 m, and 2.10 m from the center of the slab. Relative to standard FWD testing, the geophones at radial distances  $r = 0.45$  m and  $r = 1.80$  m are missing in the case of T-shaped FWD testing, because they are needed right and left of the center of the slab.

The associated loss of information regarding deflections measured along the driving direction is assessed as follows. Splines are used for interpolation between the deflections measured along the driving direction during T-shaped testing, see the blue lines and the black circles

in Figs. 3.5 and 3.6. They are evaluated at the positions of the removed geophones (i.e. at  $r = 0.45$  m and  $r = 1.80$  m, respectively). The resulting spline-interpolated values are compared with deflections measured during multi-directional testing at these positions, see the red stars in Figs. 3.5 and 3.6. The relative error between spline-interpolated (index *int*) and measured (index *m*) values,  $|\frac{w_{int}(r)-w_m(r)}{w_m(r)}|$ , is smaller than 4% for all ten tested slabs and at both positions from which geophones were removed, see Table 3.9. Thus, the loss of information resulting from the re-arrangement of two geophones from the driving direction to the lateral positions is tolerable for engineering purposes.

**Table 3.9**

Values of the mean deflections measured ( $w_m(r)$ ) by the geophones at radial distances of  $r = 0.45$  m and  $r = 1.80$  m from the center of the slab, and values of the deflections ( $w_{int}(r)$ ), at the same locations, obtained from the spline interpolating between the measurements of the rest of the geophones along the driving direction, for all ten slabs, as well as the relative error between them.

Slab #	measured deflection $w_m(r = 0.45 \text{ m})$	spline-interpolated deflection $w_{int}(r = 0.45 \text{ m})$	relative error $ \frac{w_{int}-w_m}{w_m} $	measured deflection $w_m(r = 1.80 \text{ m})$	spline-interpolated deflection $w_{int}(r = 1.80 \text{ m})$	relative error $ \frac{w_{int}-w_m}{w_m} $
A1-33354	0.292 mm	0.287 mm	1.7%	0.127 mm	0.124 mm	2.4%
A1-33360	0.218 mm	0.214 mm	1.8%	0.111 mm	0.110 mm	0.9%
A1-33868	0.269 mm	0.263 mm	2.3%	0.079 mm	0.077 mm	2.5%
A1-33873	0.116 mm	0.113 mm	2.6%	0.047 mm	0.048 mm	2.1%
A1-33874	0.160 mm	0.159 mm	0.6%	0.062 mm	0.061 mm	1.6%
A2-47543	0.297 mm	0.291 mm	2.0%	0.094 mm	0.093 mm	1.1%
A2-50000	0.338 mm	0.333 mm	1.5%	0.108 mm	0.107 mm	0.9%
A2-51995	0.287 mm	0.284 mm	1.1%	0.076 mm	0.075 mm	1.3%
A2-54003	0.593 mm	0.583 mm	1.7%	0.224 mm	0.223 mm	0.5%
A2-54440	0.257 mm	0.252 mm	2.0%	0.078 mm	0.075 mm	3.8%

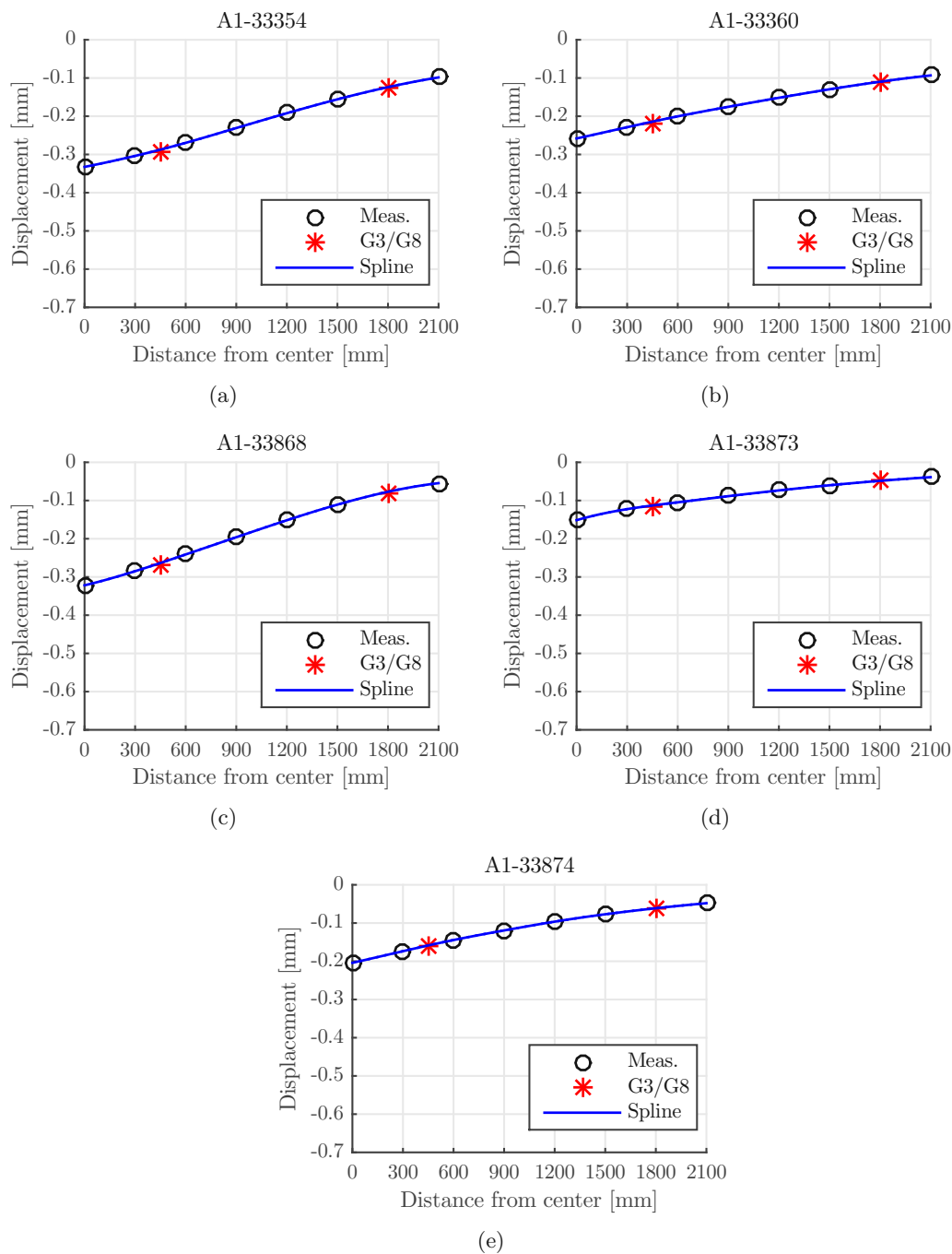


**Fig. 3.5.** Deflections measured by geophones 3 and 8 (red stars,  $r = 450$  mm and  $r = 1800$  mm, respectively), and spline (blue line) interpolating between the rest of deflections measured in the driving direction (black circles), for slabs (a) A1-33354, (b) A1-33360, (c) A1-33868, (d) A1-33873, (e) A1-33874.

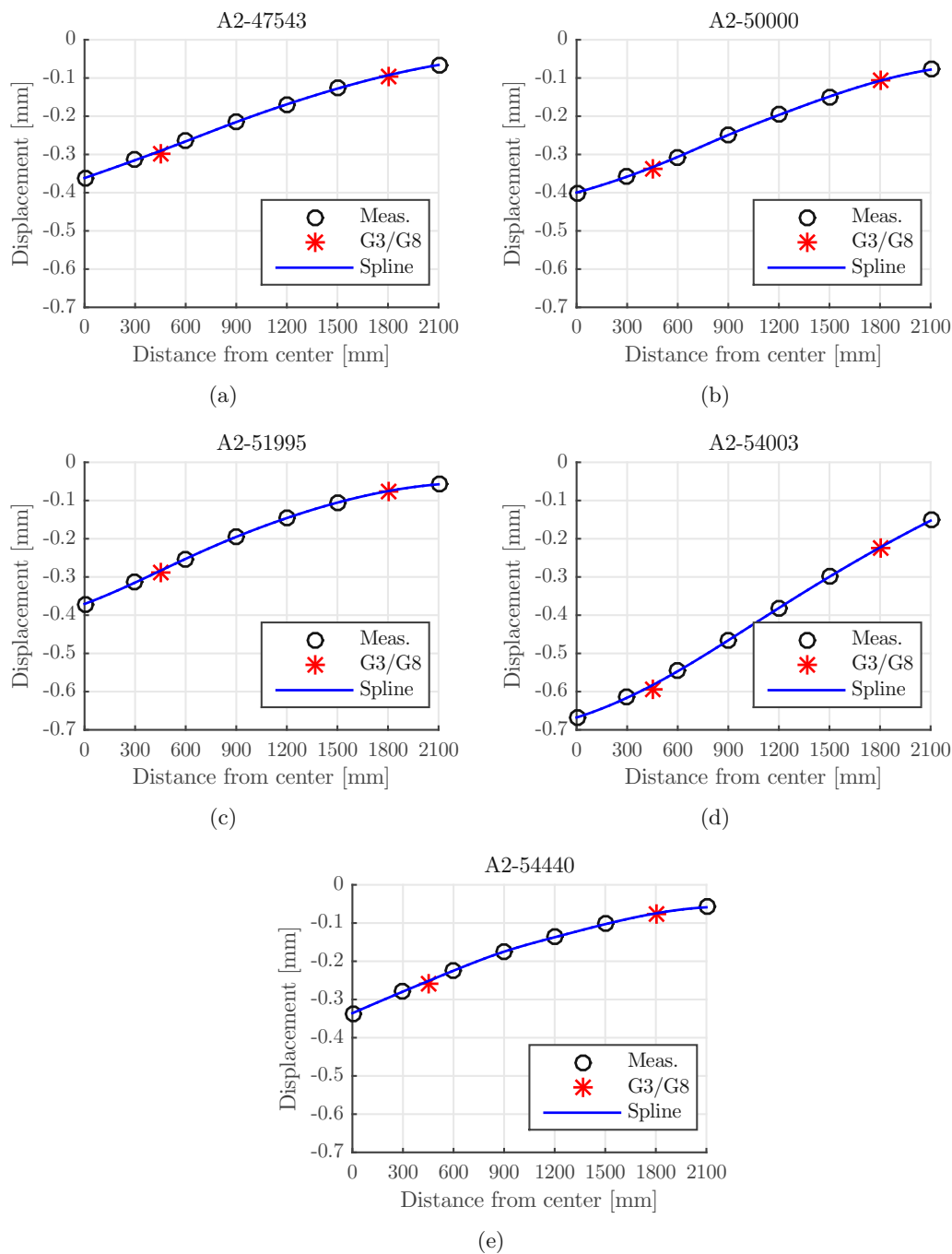


**Fig. 3.6.** Deflections measured by geophones 3 and 8 (red stars,  $r = 450$  mm and  $r = 1800$  mm, respectively), and spline (blue line) interpolating between the rest of deflections measured in the driving direction (black circles), for slabs (a) A2-47543, (b) A2-50000, (c) A2-51995, (d) A2-54003, (e) A2-54440.

### 3.3 Discussion

Central FWD tests with the developed T-shaped arrangement of geophones, and their evaluation by means of quantification of LASIX according to Eq. (3.1), was shown to provide a reliable assessment of asymmetric structural behavior of rigid pavements. The following discussion deals with the question of where do such asymmetries come from, and with implications for the back-calculation of subgrade properties.

#### 3.3.1 Reasons for asymmetric slab behavior

Values of the effective asymmetry index  $\mathcal{A}_{28}^*$  of the four new slabs range from 2.73% to 3.87%, see Table 3.6. The corresponding mean value amounts to 3.33%. Thus, even new slabs exhibit asymmetric structural behavior when subjected to central FWD testing.

The reason for an asymmetric behavior in new slabs can be explained by their *finite size* as well as *slab-to-slab interaction* through dowels and tie bars.<sup>2</sup> The dense arrangement of dowels (typical spacing: 25 to 30 cm) render slab-to-slab load transfer in driving direction effective. Dowel-connected new slabs thus almost behave as if they were continuous in driving direction. The less dense arrangement of tie bars (typical spacing: 150 cm) renders the load transfer in lateral direction less effective. In addition, many slabs are connected by means of tie bars to a neighbor on one side, while the opposite lateral edge is free. Differences in boundary conditions of the edges of the slabs, together with their rectangular (rather than quadratic) shape, render their behavior asymmetric already right after construction. The deviations from point symmetry are quantified through  $\mathcal{A}_{28}^*$ .

Values of  $\mathcal{A}_{28}^*$  of the six old slabs range from 4.29% to 9.67%, see Table 3.6. The corresponding mean value amounts to 6.67%. This underlines that the old slabs showed, on average, twice as much asymmetric structural behavior than the new slabs. Recurrent loading over many years is responsible for the increase of the asymmetries. Notably, traffic loads are *eccentric* in the standard case that tire tracks are asymmetrically arranged relative to the *N-S*-axis running through the center of the slabs, see Fig. 3.7. The corresponding asymmetric fatigue loading results in a directional deterioration of the pavement structure. This yields increasing deviations from point-symmetric behavior in central FWD testing and, therefore, increasing values of  $\mathcal{A}_{28}^*$ . As regards “eccentric” traffic loads, it is noteworthy that it is currently ensured by design that the tire tracks run as far away as possible from the free edges of the slab (those facing the shoulder). As a consequence, edge stresses are minimized and the fatigue life of the pavement is extended. In addition, some design methods include the option of installing a tied shoulder beyond the traffic lanes, with the aim of either improving service life or reducing the required slab thickness, see e.g. (Packard, 1984; Packard and Tayabji, 1985).

Imperfect positioning of the falling weight also contributes to asymmetric structural behavior. An eccentric positioning in driving direction has a smaller influence than the same eccentricity in lateral direction, because of the following two reasons:

1. Eccentricities of the falling weight are to be related to the size of the tested slab. The lateral width of slabs is smaller than their length. Thus, the same eccentricity in both directions leads to a larger effective imperfection in lateral direction. Similarly, if different slabs are tested with the same unintentional lateral eccentricity, its influence will be the larger the smaller the lateral width of the tested slab.

<sup>2</sup>It is unlikely that a *non-uniform* distribution of subgrade stiffness is responsible for asymmetric behavior of *new* slabs, because methods such as the dynamic compaction control are used during construction to ensure that all subgrade layers of pavement structure have *uniform* properties.

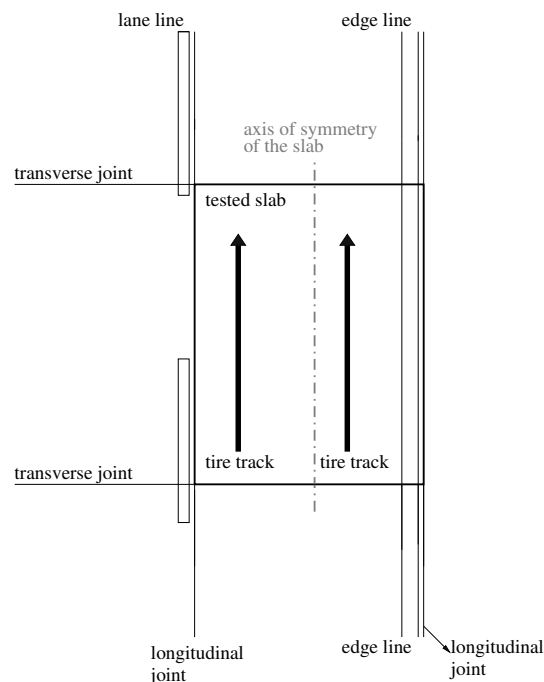


**Fig. 3.7.** Top view onto a slab subjected to eccentric long-term loading resulting from tire tracks which are asymmetrically arranged relative to the  $N$ - $S$ -axis running through the center of the slab.

2. If dowel-connected slabs almost behave as if they were continuous in driving direction, eccentricities in driving direction will not result in significant asymmetries. Lateral eccentricities, in turn, must be expected to particularly increase asymmetries of slabs which are connected by means of tie bars to a neighbor on one side, while the opposite lateral edge is free.

All described FWD tests on new plates were carried out with small eccentricities of the FWD-device from the center of the slab, amounting to a few single centimetres. The resulting asymmetries were small enough that  $A_{28}^*$  allowed for the correct classification into new and old slabs. This underlines that asymmetries arising from unintentional eccentric FWD testing are implicitly considered in the threshold value of  $A_{28}^* = 5.2\%$ , distinguishing newly built from directionally degraded pavement structures.

### 3.3.2 Back-calculation of subgrade properties based on deflections known from FWD testing

Surface deflections measured during FWD testing are functions of the loading exerted by the falling weight and of the properties of the pavement structure. Thus, it is conceptually possible to back-calculate properties of the pavement structure from known surface loading and deflections. To the best of the authors' knowledge all currently available back-calculation approaches assume a uniform distribution of subgrade stiffness and, therefore, a symmetric behavior of pavement structures. This assumption is challenged by the asymmetric structural behavior found by means of multi-directional FWD testing of old slabs. In the following, "dense liquid" models as well as the corresponding AREA and Best Fit methods will be briefly summarized. This provides the basis for subsequent correlation of LASIX with the directional variation of the deflection basin parameter AREA7, see Subsection 3.3.3.

The “dense-liquid” model (AASHTO, 2008) idealizes rigid pavements as infinite thin elastic plates on a uniform Winkler foundation (Winkler, 1867). There are two different back-calculation approaches: the AREA method and the Best Fit method. Both of them are based on closed-form solutions, which can be traced back to Westergaard (Westergaard, 1926). Back-calculation concerns identification of the radius of relative stiffness,  $l_k$ , from surface deflections measured during FWD testing.  $l_k$  is equal to  $(D/k_{sg})^{0.25}$ , where  $D$  denotes the bending stiffness of the plate and  $k_{sg}$  the modulus of subgrade reaction of the Winkler foundation. Formulae for the final transition from  $l_k$  to the modulus of subgrade reaction were proposed e.g. in (Darter et al., 1995; Hall et al., 1997). They have become part of the mechanistic-empirical design and evaluation of rigid pavements (AASHTO, 2008; Smith et al., 2017a).

The AREA method is based on the AREA parameter. It was originally introduced as the area (hence the name) under the graph showing surface deflections of the pavement structure over the radial distance from the falling weight (Hoffman and Thompson, 1980). In order to account for different amplitudes of the falling weight, which yield qualitatively similar but quantitatively different surface deflections, the latter were normalized with respect to their maximum value,  $w_1$ , measured at the position of the falling weight (Hoffman and Thompson, 1980). Therefore, the *normalized* version of the AREA parameter has the physical dimension of a length rather than an area. As for a configuration of four geophones with a uniform spacing equal to  $\Delta r$ , it reads as

$$\text{AREA} = \frac{1}{w_1} \int_0^{3\Delta r} w(r) \, dr \approx \frac{\Delta r}{2w_1} [w_1 + 2w_2 + 2w_3 + w_4], \quad (3.4)$$

where  $w_i$  (with  $i = 1, 2, 3, 4$ ) refers to surface deflections at a radial distance of  $r = (i - 1) \Delta r$ , with  $\Delta r = 300$  mm. The last expression in Eq. (3.4) refers to numerical integration using the trapezoidal rule. Inspired by a dimensionless representation of Westergaard’s solution by Losberg (1960), Ioannides (1990) used dimensional analysis for the derivation of a relation between the AREA parameter according to Eq. (3.4) and the radius of relative stiffness, see Fig. 3 in (Ioannides, 1990). Other sensor configurations were studied e.g. in (Hall and Mohseni, 1991). The method that is based on four measured deflections is referred to as “AREA4”, the one based on seven measured deflections as “AREA7”. Both of them are used for rigid pavements (Khazanovich et al., 2001).

The Best Fit method is also based on a dimensionless representation of Westergaard’s solution by Losberg (1960). A closed-form solution for surface deflections, which contains Kelvin Bessel functions, is used for fitting of measured deflections (Ioannides, 1990). The method that is based on four measured deflections is referred to as “Best Fit 4”, the one based on seven measured deflections as “Best Fit 7” (Khazanovich et al., 2001).

Depending on the number of deflection measurements used for the AREA method and the Best Fit method, respectively, the two methods deliver slightly different moduli of subgrade reaction (Khazanovich et al., 2001). Multi-layered elastic simulations performed with the DIPLOMAT program (Khazanovich, 1994; Khazanovich and Ioannides, 1995) were the basis to recommend the “Best Fit 4” method (using deflections measured in radial distances of 0, 305, 610, and 914 mm) for rigid pavements (Khazanovich et al., 2001), see also (Hall et al., 1997). Still, it is noteworthy that the “Best Fit 4” method and the “AREA7” method (integrating the deflection basin up to a radial distance of 1524 mm) are practically equivalent. Both methods deliver virtually the same back-calculated values of the modulus of subgrade reaction, see Figs. 3 and 6 in (Khazanovich et al., 2001). This provides the motivation to relate LASIX to directional variations of the deflection basin parameter AREA7.



### 3.3.3 Relation between LASIX and the coefficient of directional variation of AREA7 (“COVAREA7”)

Standard FWD tests are nowadays evaluated by means of methods that are based on the assumption of an infinite plate, uniform subgrade stiffness, and, therefore, point-symmetric slab behavior. However, multi-directional FWD testing underlined that rigid pavements which had been in service for a long time behave in a remarkable *asymmetric* fashion. Thus, back-analysing uniform slab properties from FWD tests could be questionable. In this context it is useful to categorize the asymmetric behavior of slabs into “mild asymmetries” and “strong asymmetries”. This is supported by LASIX, as will be demonstrated in the remainder of the present subsection.

The database shown in Appendix 3.A contains the deflection measurements from 27 FWD tests performed on every one of the ten tested slabs. For every slab, the following analysis is performed. The three (to six) deflections, measured by means of repeated testing in the same direction and at the same distance to the center of the falling weight, are averaged. The deflection profile between the averaged deflections is approximated, in every direction, by means of a spline. It is integrated from the center of the falling weight to a radial distance  $\ell_r = 1524$  mm:

$$\text{AREA7} = \frac{1}{w_1} \int_0^{\ell_r} w(r) \, dr. \quad (3.5)$$

This yields one value of the AREA7 parameter for every measurement direction, see Table 3.10. These eight direction-dependent AREA7 values per slab are post-processed by computing their

**Table 3.10**

Values of AREA7 [mm] obtained from the average of the three (to six) FWD tests performed along each of the eight directions for every one of the ten slabs.

Slab #	Condition	N	NE	E	SE	S	SW	W	NW
A1-33354	Old	1122.93	1158.77	1189.41	1220.18	1180.95	1122.48	1015.41	1047.43
A1-33360	New	1107.20	1028.11	1010.01	1069.03	1065.66	1077.02	1053.67	1067.07
A1-33868	Old	1020.23	969.35	899.39	1015.66	1055.42	1078.83	1019.48	1004.60
A1-33873	New	985.27	969.70	942.21	973.16	1003.82	1005.12	978.44	958.00
A1-33874	Old	993.77	995.56	1026.19	1053.00	1020.13	1007.83	959.44	953.87
A2-47543	Old	1006.91	967.51	914.17	997.75	1043.41	1090.49	1049.67	1002.81
A2-50000	Old	1042.78	1046.65	1062.54	1136.01	1120.99	1106.30	986.85	976.25
A2-51995	New	931.31	947.22	927.77	948.69	932.44	902.20	846.59	856.10
A2-54003	Old	1123.93	1141.15	1128.28	1204.03	1168.86	1087.04	953.39	1011.14
A2-54440	New	928.54	924.48	893.49	947.75	931.07	923.58	878.11	881.74

mean value,  $\mu_{\text{AREA7}}$ , and their standard deviation,  $\sigma_{\text{AREA7}}$ , see Table 3.11. Dividing the latter by the former yields the coefficient of directional variation of the AREA7 values for every slab, which is referred to as COVAREA7. It is another measure for asymmetric slab behavior.

For all slabs except the *old* slab A1-33874, the  $\mathcal{A}_{28}^*$ -value of which amounts to 4.29%, see Table 3.6, which is *smaller* than the corresponding threshold value 5.2%, see Fig. 3.4, the values of COVAREA7 from Table 3.11 are correlated with the values of LASIX from Table 3.7, see Fig. 3.8. The quadratic correlation coefficient amounts to 94%.

Values of LASIX smaller than 8% refer to values of COVAREA7 smaller than 4.6%. Such coefficients of directional variation of the AREA7 parameter are representative for new slabs. They show only mild asymmetries resulting from their finite size and slab-to-slab interaction, while the stiffness of the subgrade can be expected to be uniform. Thus, it is realistic to identify

**Table 3.11**

Mean value,  $\mu_{\text{AREA7}}$ , standard deviation,  $\sigma_{\text{AREA7}}$ , and coefficient of variation, COVAREA7, of the eight direction-dependent values of the AREA7 parameter of each slab.

Slab #	Condition	$\mu_{\text{AREA7}}$ [mm]	$\sigma_{\text{AREA7}}$ [mm]	COVAREA7 [-]
A1-33354	Old	1132.19	70.81	6.25%
A1-33360	New	1059.72	29.85	2.82%
A1-33868	Old	1007.87	54.65	5.42%
A1-33873	New	976.97	21.45	2.20%
A1-33874	Old	1001.22	33.34	3.33%
A2-47543	Old	1009.09	53.93	5.34%
A2-50000	Old	1059.80	59.14	5.58%
A2-51995	New	911.54	39.86	4.37%
A2-54003	Old	1102.23	82.94	7.52%
A2-54440	New	913.59	25.61	2.80%

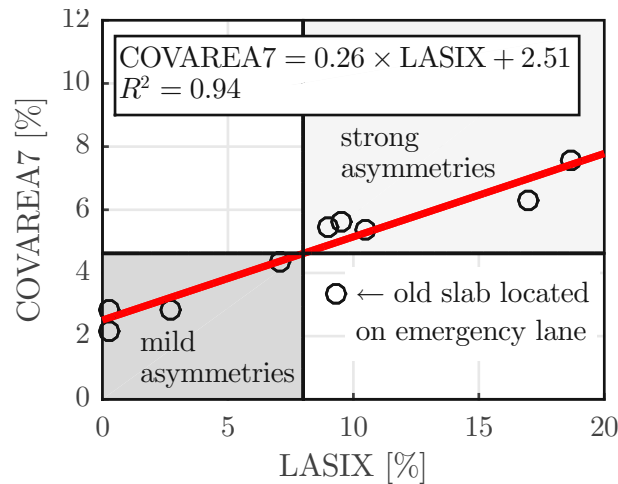


**Fig. 3.8.** Correlation between the coefficient of variation of the direction-dependent AREA7 values, COVAREA7, quantified based on results from multi-directional FWD testing over eight directions, and the Lateral Asymmetry Index LASIX according to Eq. (3.1), related to T-shaped FWD testing; each symbol corresponds to one of the ten tested slabs; the horizontal and vertical black lines represent the threshold values of COVAREA7 and LASIX distinguishing mild from strong asymmetries.

a *uniform* modulus of subgrade reaction from deflections measured in driving direction, either by the Best Fit 4 method or the AREA7 method.

Values of LASIX larger than 8% refer, according to the red regression line in Fig. 3.8, to values of COVAREA7 larger than 4.6%. Such coefficients of directional variation of the AREA7 values are representative for old slabs which show asymmetries because of directional degradation of the subgrade, resulting from eccentric traffic loads. Whether or not the identification of a *uniform* modulus of subgrade reaction, either by the Best Fit 4 method or the AREA7 method, is still realistic will be analyzed in Subsection 3.3.4.

The exposure situation explains why COVAREA7 of the *old* slab A1-33874 amounts to 3.33%, see Table 3.11, which is *smaller* than the corresponding threshold value 4.6%. This slab was part of an emergency lane, see Table 3.1. Therefore, it was subjected to traffic loading only indirectly, namely, because of load transfer via tie bars connecting the tested slab to its neighbor which was part of the first lane and, therefore, directly exposed to traffic loads.

### 3.3.4 Variation of the modulus of subgrade reaction back-calculated from eight direction-specific values of AREA7 per slab

In the AREA method, the “dense-liquid” model is used to back-calculate a uniform modulus of subgrade reaction from deflections measured in the driving direction. This model idealizes the pavement structure as a plate (finite thickness, but infinite in-plane dimensions) resting on a Winkler foundation. Assuming that deflections measured in the driving direction are axisymmetric with respect to the axis of impact of the falling weight, the AREA parameter is translated into the radius of relative stiffness  $l_k$  (Ioannides et al., 1989; Ioannides, 1990):

$$l_k \approx \left[ \ln \left( \frac{\xi_1 - \text{AREA}}{\xi_2} \right) \times \frac{1}{\xi_3} \right]^{\xi_4} \times 1 \text{ mm}, \quad (3.6)$$

where  $\xi_1$ ,  $\xi_2$ ,  $\xi_3$ , and  $\xi_4$  are coefficients that depend on the specific AREA-parameter used, see (Hall et al., 1997). The radius of relative stiffness, in turn, is equal to the fourth root of the bending stiffness of the plate,  $D$ , divided by the modulus of subgrade reaction,  $k_{sg}$ , (Westergaard, 1926):

$$l_k = \sqrt[4]{\frac{D}{k_{sg}}}. \quad (3.7)$$

The values of  $D$  and  $k_{sg}$  are usually optimized such that the model-simulated deflection basin reproduces the measured deflections in the best-possible fashion (Hall et al., 1997; Khazanovich et al., 2001). Therefore,  $D$  is not necessarily equal to the bending stiffness of the concrete slab.

If measured deflections are direction-dependent (= asymmetric), the assumption of a point-symmetric deflection basin is only useful, provided that direction-dependent values of the AREA parameter are translated, by means of Eqs. (3.6) and (3.7), into virtually the same value of  $k_{sg}$ . Whether or not this is the case, will be checked in the following.

For every slab, the following two-step procedure is performed. Step 1: The eight direction-dependent values of AREA7, see Table 3.10, are translated by means of Eq. (3.6) into eight corresponding values of  $l_k$ . Given that the AREA7-parameter is expressed in millimetres, the corresponding values of the empirical  $\xi$ -constants read as  $\xi_1 = 1524$ ,  $\xi_2 = 7358.59$ ,  $\xi_3 = -0.197868$ ,  $\xi_4 = 2.566$ , see (Hall et al., 1997) for details. With these values, Eq. (3.6) yields values of  $l_k$  in millimetres. Step 2: The eight direction-dependent values of  $l_k$  are translated by means of Eq. (3.7) into eight corresponding values of  $k_{sg}$ . Thereby, the plate stiffness  $D$  is set equal to  $D_s$  which denotes the bending stiffness of the concrete slabs:<sup>3</sup>

$$D_s = \frac{E_c h_s^3}{12(1 - \nu_c^2)}, \quad (3.8)$$

where  $E_c$  denotes the modulus of elasticity of concrete,  $h_s$  the thickness of the slab, and  $\nu_c$  Poisson’s ratio of concrete. Herein, these quantities are equal to 36500 MPa, 0.22 m, and 0.2, respectively, see also (Díaz Flores et al., 2021). Inserting these values into Eq. (3.8) yields

$$D_s = 33.74 \text{ MPa m}^3. \quad (3.9)$$

An expression for corresponding values of  $k$  is obtained by solving Eq. (3.7) for  $k_{sg}$ :

$$k_{sg} = \frac{D_s}{(l_k)^4}. \quad (3.10)$$

This completes Step 2.

<sup>3</sup>Other choices for  $D$  will be discussed at the end of the Subsection.

Applying the procedure described in the preceding paragraph to eight direction-dependent values of AREA7 per slab, allows for computing eight  $k$ -values per slab. They are the basis for computing slab-specific mean values of  $k_{sg}$ , denoted as  $\mu_k$ , as well as corresponding standard deviations,  $\sigma_k$ , and coefficients of variation,  $CV(k) = \sigma_k/\mu_k$ , see Table 3.12. The ten slab-specific values of  $CV(k)$  are finally correlated with the corresponding values of COVAREA7 from Table 3.10, see Fig. 3.9.

**Table 3.12**

Mean value,  $\mu_k$ , standard deviation,  $\sigma_k$ , and coefficient of variation,  $CV(k_{sg})$ , of the eight direction-dependent values of the modulus of subgrade reaction  $k_{sg}$  of each slab.

Slab #	Condition	$\mu_k$ [MPa/mm]	$\sigma_k$ [MPa/mm]	$CV(k_{sg})$ [-]
A1-33354	Old	0.0374	0.0249	66.58%
A1-33360	New	0.0609	0.0148	24.33%
A1-33868	Old	0.0950	0.0437	45.97%
A1-33873	New	0.1128	0.0175	15.55%
A1-33874	Old	0.0957	0.0237	24.77%
A2-47543	Old	0.0937	0.0392	41.86%
A2-50000	Old	0.0646	0.0303	46.88%
A2-51995	New	0.1814	0.0522	28.77%
A2-54003	Old	0.0505	0.0395	78.05%
A2-54440	New	0.1759	0.0309	17.57%

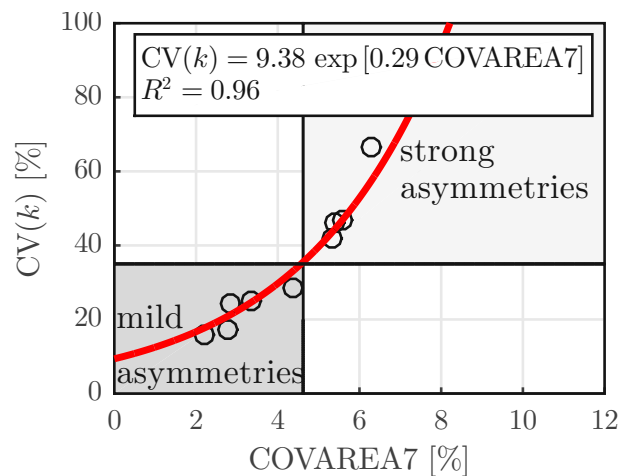


**Fig. 3.9.** Correlation between the coefficient of variation of eight values of the modulus of subgrade reaction, back-calculated from eight direction-dependent AREA7 values per slab, see  $CV(k_{sg})$  in Table 3.12, and COVAREA7, see Table 3.11; each symbol corresponds to one of the ten tested slabs; the horizontal and vertical black lines represent threshold values separating mild from strong asymmetries.

For pavement structures exhibiting mild asymmetries, as expressed by COVAREA7-values smaller than 4.6%, values of  $CV(k_{sg})$  smaller than 35% are found. In such cases, the assumptions of a *point-symmetric* deflection basin and a *uniform* modulus of subgrade reaction appear to be useful for engineering purposes. For pavement structures exhibiting strong asymmetries, as expressed by COVAREA7-values larger than 4.6%, values of  $CV(k_{sg})$  larger than 35% are found. In such cases, the assumptions of a *point-symmetric* deflection basin and a *uniform* modulus of subgrade reaction are questionable.

Finally, it is shown that the values of  $CV(k_{sg})$  listed in Table 3.12 and illustrated in Fig. 3.9 are independent of the specific choice for the plate stiffness  $D$  in Eq. (3.7). Above, the specific choice  $D = D_s$  was made. This provides the motivation to multiply  $D_s$  by a slab-specific scaling factor  $\alpha_s$ . In order to analyze the corresponding implications on  $k_{sg}$ , both sides of Eq. (3.10) are multiplied by  $\alpha_s$ :

$$\alpha_s k = \frac{\alpha_s D_s}{(l_k)^4}. \quad (3.11)$$

Eq. (3.11) underlines that scaling of  $D_s$  by a factor  $\alpha_s$  leads to  $k$ -values scaled by the same factor  $\alpha_s$ . Scaling of the eight  $k$ -values per slab by a factor of  $\alpha_s$ , in turn, leads to mean values  $\mu_k$  and standard deviations  $\sigma_k$  scaled by the same factor  $\alpha_s$ . In other words, both the  $\mu_k$ -values and  $\sigma_k$ -values in Table 3.12 are to be multiplied by  $\alpha_s$ . This underlines that the coefficient of variation,  $CV(k) = \sigma_k/\mu_k$ , is *independent* of  $\alpha_s$ . It is concluded that the last column in Table 3.12 and the ordinate values in Fig. 3.9 remain the same, even if  $D$  is optimized in order to reproduce the measured deflections (rather than setting it equal to  $D_s$ ).

### 3.3.5 Limitations and future outlook

The here-analyzed FWD experiments were carried out on slabs made from normal concrete, with a thickness of 0.22 m, lengths ranging from 4.50 m to 5.60 m, widths from 3.10 m to 4.20 m, and length-to-width ratios from 1.12 to 1.81. The optimal value of  $c$  and the threshold values of LASIX,  $\mathcal{A}_{28}^*$ , COVAREA7, and  $CV(k_{sg})$  refer to slabs with properties listed above. Otherwise, these values are questionable. In the case of bonded white-toppings featuring square slabs 1.80 m long and wide, for instance, even a new radial distance  $c$  of the lateral geophones from the center of the slabs would need to be optimized.

All non-standard FWD tests performed so far included multi-directional measurements of surface deflections. A prototype for FWD testing with a T-shaped arrangement of the geophones is in its design phase. This testing device will reduce the in-situ efforts to those known from standard FWD testing: (i) piloting the FWD trailer to the slab of interest, (ii) lowering the impact transducer and the geophones onto the surface of the slab, (iii) lifting and dropping the falling weight while recording the surface deflections, (iv) uplifting the impact transducer and the geophones, and (v) piloting the FWD trailer to the next slab of interest.

## 3.4 Conclusions

An optimal T-shaped arrangement of nine geophones was developed: one at the center of impact (= center of the slab), six along the driving direction, one right and one left of the center. The following conclusions are drawn:

- As for central FWD testing with a T-shaped arrangement of geophones, the optimal distance of the lateral geophones from the center of impact is equal to 1.20 m.
- It is possible to integrate the proposed arrangement (or an alternative similar to it) into trailers complying with the maximum allowed widths of vehicles, e.g. 2.44 m in the USA, 2.55 m in China, and 2.60 m in Europe.
- This renders highly automated and, therefore, rapid FWD testing feasible, with on-site efforts equal to those known from standard FWD testing.
- State-of-the-art evaluation of deflections measured in driving direction remains possible, as long as a suitable amount of geophones remain arranged along the driving direction (here: seven including the one at the center of the falling weight).

- The “Lateral Asymmetry Index” (LASIX) is a deflection-basin-parameter customized for T-shaped FWD testing. It enables the quantification of asymmetric slab behavior.
- Values of LASIX smaller than 8% refer to coefficients of directional variation of AREA7 smaller than 4.6%. For slabs presenting geometric and stiffness properties within the intervals studied, such values are representative for new slabs which show only mild asymmetries. The latter result from their finite size and slab-to-slab interaction, while the stiffness of the subgrade can be expected to be uniform. Thus, it is realistic to identify a *uniform* modulus of subgrade reaction, either by the Best Fit 4 method or the AREA7 method.
- Values of LASIX larger than 8% refer to coefficients of directional variation of AREA7 larger than 4.6%. For slabs presenting geometric and stiffness properties within the intervals studied, such values are representative for old slabs with directional degradation of the subgrade, resulting from eccentric traffic loads. Thus, it is questionable to identify a *uniform* modulus of subgrade reaction.

In the future, it will be interesting

- to integrate central FWD tests with a T-shaped arrangement of geophones into the monitoring strategy of pavement slabs made of concrete, i.e. to perform such tests regularly on specific slabs in order to study the evolution of LASIX as a function of the age of the slab and of the service loads to which it is exposed (traffic and hygro-thermal loads), and
- to perform such tests on slabs with different sizes and stiffness properties, in order to widen their range of applicability.

## Funding

This research received financial support by the Austrian Research Promotion Agency (FFG), the Austrian Ministry for Transport and Technology (bmvit), ÖBB-Infrastruktur AG (Vienna, Austria), and ASFINAG Bau Management GmbH (Vienna, Austria), within VIF-project 2015 “STRUKTurelle Zustandserhebung und -bewertung von Betondecke (CONcrete) auf Projektebene - ConSTRUKT” and the Bridge Project 2021 “Grundlegende Analyse von FWD-Versuchen: innovative Experimente, moderne Struktursimulationen, statistische Datenanalyse – FALLING-weight”. The authors also acknowledge the TU Wien University Library for financial support through its Open Access Funding Programme.

## Acknowledgements

The help of Pia Mandahus (TU Wien, Vienna, Austria), Marek Milcevic, Roman Oblak and Harald Aigner (Nievelt Labor GmbH, Höbersdorf, Austria) as well as interesting discussions with Wolfgang Kluger-Eigl (TU Wien), Martin Peyerl and Gerald Maier (Smart Minerals GmbH, Vienna, Austria) as well as Reinhard Lohmann-Pichler and Karl Gragger (ASFINAG Bau Management GmbH) are gratefully acknowledged.

## Disclosure Statement

No potential conflict of interest was reported by the authors

## List of symbols

$a$	length of the slab
$\mathcal{A}_{28}^*$	Effective asymmetry index
$b$	width of the slab
$c$	optimal radial distance of the lateral geophones from the center of the slab
$CV(k_{sg})$	coefficient of variation of the modulus of subgrade reaction
$d$	direction
$D$	Bending stiffness of the plate of the “dense-liquid” model
$D_s$	Bending stiffness of the tested concrete slabs
$E$	East
$E_c$	modulus of elasticity of concrete
$g$	geophones
$h_s$	thickness of the slab
$i$	Test number
$j$	Summation index for all 28 possible combinations of directions compared in $A_{d,\delta}$
$k_{sg}$	modulus of subgrade reaction of the Winkler foundation of the “dense-liquid” model
$l_k$	radius of relative stiffness
$\ell$	radial length of integration in Eq. (3.3)
$N$	North
$NE$	Northeast
$NW$	Northwest
$r$	radial coordinate
$r_{d,g}$	radial coordinate of geophone $g$ measuring deflections in the direction $d$
$R^2$	coefficient of determination
$S$	South
$SE$	Southeast
$SW$	Southwest
$w(r)$	deflection at the radial distance $r$ from the center of the slab
$w_d(r=0)$	deflection at the radial distance $r=0$ from the center of the slab measured in direction $d$
$w_\delta(r=0)$	deflection at the radial distance $r=0$ from the center of the slab measured in direction $\delta$
$w_d(r)$	deflection at the radial distance $r$ from the center of the slab measured in direction $d$
$w_\delta(r)$	deflection at the radial distance $r$ from the center of the slab measured in direction $\delta$
$w_E(r=c)$	deflection at the radial distance $r=c$ from the center of the slab measured in the direction $E$
$w_i$	deflection measured by the geophone at the radial distance of $r=(i-1)\Delta r$ , where $i=0, 1, 2$ , or $3$
$w_{int}(r)$	spline-interpolated deflection at the radial distance $r$
$w_m(r)$	measured deflection at the radial distance $r$
$w_N(r=c)$	deflection at the radial distance $r=c$ from the center of the slab measured in the direction $N$
$w_W(r=c)$	deflection at the radial distance $r=c$ from the center of the slab measured in the direction $W$

$W$	West
$\gamma$	geophone number to which the deflection $w_\gamma$ corresponds, see Eq. (3.4)
$\delta$	in $A_{d,\delta}$ , direction against which the direction $d$ is compared, $d \neq \delta$
$\Delta r$	uniform distance between two neighboring geophones
$\mu_{\text{AREA7}}$	mean value of all eight AREA7 values per slab
$\nu_c$	Poisson's ratio of concrete
$\xi_i$	empirical coefficients, with $i = 1, 2, 3, 4$
$\sigma_{\text{AREA7}}$	standard deviation of all eight AREA7 values per slab
$\varphi_d$	polar angle of the direction $d$

## List of abbreviations

AREA4	AREA value based on four measured deflections
AREA7	AREA value based on seven measured deflections
Best fit 4	best fit method based on four measured deflections
Best fit 7	best fit method based on seven measured deflections
COVAREA7	coefficient of directional variation of AREA7
FWD	Falling Weight Deflectometer
LASIX	Lateral asymmetry index



## Appendix 3.A Results of multi-directional FWD testing of all slabs

**Table 3.A.1**

Maximum deflections measured during the 27 FWD tests performed on the old slab A1-33354 [mm].

Test Direction	Test Number	Geophone								
		$g = 1$	$g = 2$	$g = 3$	$g = 4$	$g = 5$	$g = 6$	$g = 7$	$g = 8$	$g = 9$
$d = 1$ (N)	$i = 1$	0.346	0.313	0.304	0.281	0.240	0.201	0.164	0.136	0.104
$d = 1$ (N)	$i = 2$	0.334	0.307	0.296	0.273	0.234	0.196	0.159	0.134	0.102
$d = 1$ (N)	$i = 3$	0.333	0.305	0.295	0.272	0.233	0.195	0.159	0.131	0.102
$d = 2$ (NE)	$i = 1$	0.342	0.311	0.302	0.283	0.247	0.209	0.171	0.138	0.105
$d = 2$ (NE)	$i = 2$	0.339	0.310	0.305	0.284	0.246	0.209	0.169	0.136	0.104
$d = 2$ (NE)	$i = 3$	0.336	0.310	0.304	0.284	0.247	0.209	0.170	0.137	0.105
$d = 3$ (E)	$i = 1$	0.339	0.318	0.311	0.291	0.258	0.217	0.172	0.135	0.104
$d = 3$ (E)	$i = 2$	0.339	0.316	0.310	0.290	0.257	0.216	0.171	0.134	0.104
$d = 3$ (E)	$i = 3$	0.337	0.315	0.309	0.289	0.256	0.215	0.171	0.133	0.104
$d = 4$ (SE)	$i = 1$	0.334	0.301	0.296	0.273	0.241	0.206	0.171	0.138	0.106
$d = 4$ (SE)	$i = 2$	0.335	0.303	0.296	0.274	0.243	0.208	0.171	0.139	0.105
$d = 4$ (SE)	$i = 3$	0.335	0.303	0.296	0.277	0.246	0.209	0.173	0.139	0.106
$d = 5$ (S)	$i = 1$	0.329	0.303	0.296	0.275	0.245	0.212	0.177	0.145	0.114
$d = 5$ (S)	$i = 2$	0.329	0.304	0.296	0.277	0.246	0.212	0.176	0.145	0.114
$d = 5$ (S)	$i = 3$	0.330	0.304	0.295	0.277	0.246	0.212	0.177	0.145	0.114
$d = 6$ (SW)	$i = 1$	0.329	0.278	0.267	0.245	0.209	0.175	0.142	0.114	0.091
$d = 6$ (SW)	$i = 2$	0.325	0.266	0.265	0.244	0.207	0.173	0.140	0.113	0.088
$d = 6$ (SW)	$i = 3$	0.327	0.271	0.266	0.244	0.208	0.174	0.142	0.113	0.089
$d = 7$ (W)	$i = 1$	0.327	0.275	0.263	0.237	0.196	0.160	0.130	0.110	
$d = 7$ (W)	$i = 2$	0.325	0.275	0.266	0.237	0.196	0.160	0.130	0.108	
$d = 7$ (W)	$i = 3$	0.325	0.274	0.262	0.236	0.194	0.159	0.128	0.106	
$d = 8$ (NW)	$i = 1$	0.329	0.286	0.270	0.247	0.207	0.171	0.139	0.115	0.091
$d = 8$ (NW)	$i = 2$	0.328	0.284	0.270	0.246	0.206	0.171	0.138	0.115	0.093
$d = 8$ (NW)	$i = 3$	0.328	0.283	0.270	0.245	0.206	0.170	0.138	0.114	0.093
$d = 1$ (N)	$i = 4$	0.329	0.302	0.288	0.266	0.228	0.188	0.151	0.120	0.093
$d = 1$ (N)	$i = 5$	0.326	0.298	0.285	0.262	0.225	0.185	0.150	0.120	0.094
$d = 1$ (N)	$i = 6$	0.328	0.298	0.286	0.263	0.226	0.187	0.152	0.123	0.095

**Table 3.A.2**

Maximum deflections measured during the 27 FWD tests performed on the new slab A1-33360 [mm].

Test Direction	Test Number	Geophone								
		$g = 1$	$g = 2$	$g = 3$	$g = 4$	$g = 5$	$g = 6$	$g = 7$	$g = 8$	$g = 9$
$d = 1$ (N)	$i = 1$	0.257	0.228	0.219	0.202	0.176	0.152	0.129	0.112	0.093
$d = 1$ (N)	$i = 2$	0.259	0.229	0.221	0.203	0.178	0.153	0.129	0.112	0.093
$d = 1$ (N)	$i = 3$	0.256	0.227	0.219	0.201	0.175	0.152	0.129	0.110	0.090
$d = 2$ (NE)	$i = 1$	0.264	0.219	0.208	0.184	0.163	0.140	0.119	0.102	0.088
$d = 2$ (NE)	$i = 2$	0.260	0.216	0.206	0.189	0.162	0.138	0.118	0.097	0.082
$d = 2$ (NE)	$i = 3$	0.261	0.216	0.206	0.190	0.161	0.138	0.117	0.097	0.082
$d = 3$ (E)	$i = 1$	0.266	0.222	0.209	0.191	0.153	0.136	0.113	0.096	0.079
$d = 3$ (E)	$i = 2$	0.259	0.214	0.204	0.185	0.156	0.132	0.110	0.094	0.080
$d = 3$ (E)	$i = 3$	0.261	0.217	0.203	0.186	0.156	0.132	0.109	0.092	0.076
$d = 4$ (SE)	$i = 1$	0.258	0.206	0.203	0.182	0.152	0.126	0.100	0.093	0.078
$d = 4$ (SE)	$i = 2$	0.256	0.211	0.201	0.181	0.151	0.125	0.102	0.092	0.080
$d = 4$ (SE)	$i = 3$	0.256	0.213	0.198	0.179	0.151	0.126	0.102	0.093	0.085
$d = 5$ (S)	$i = 1$	0.261	0.231	0.218	0.198	0.165	0.142	0.118	0.096	0.086
$d = 5$ (S)	$i = 2$	0.259	0.229	0.214	0.197	0.166	0.141	0.117	0.096	0.085
$d = 5$ (S)	$i = 3$	0.261	0.230	0.215	0.197	0.169	0.141	0.117	0.097	0.085
$d = 6$ (SW)	$i = 1$	0.262	0.217	0.198	0.192	0.151	0.123	0.104	0.087	0.074
$d = 6$ (SW)	$i = 2$	0.260	0.216	0.195	0.190	0.149	0.121	0.105	0.085	0.073
$d = 6$ (SW)	$i = 3$	0.260	0.216	0.198	0.189	0.150	0.122	0.105	0.086	0.073
$d = 7$ (W)	$i = 1$	0.259	0.230	0.219	0.199	0.162	0.132	0.108	0.090	
$d = 7$ (W)	$i = 2$	0.260	0.231	0.220	0.200	0.163	0.133	0.104	0.091	
$d = 7$ (W)	$i = 3$	0.259	0.229	0.218	0.198	0.162	0.133	0.106	0.091	
$d = 8$ (NW)	$i = 1$	0.260	0.229	0.215	0.199	0.161	0.142	0.117	0.098	0.082
$d = 8$ (NW)	$i = 2$	0.259	0.228	0.217	0.198	0.168	0.142	0.118	0.099	0.082
$d = 8$ (NW)	$i = 3$	0.260	0.227	0.214	0.199	0.169	0.143	0.118	0.100	0.085
$d = 1$ (N)	$i = 4$	0.258	0.231	0.216	0.196	0.174	0.152	0.130	0.112	0.096
$d = 1$ (N)	$i = 5$	0.260	0.229	0.218	0.200	0.175	0.151	0.130	0.109	0.093
$d = 1$ (N)	$i = 6$	0.259	0.229	0.217	0.200	0.174	0.151	0.130	0.109	0.094

**Table 3.A.3**

Maximum deflections measured during the 27 FWD tests performed on the old slab A1-33868 [mm].

Test Direction	Test Number	Geophone								
		$g = 1$	$g = 2$	$g = 3$	$g = 4$	$g = 5$	$g = 6$	$g = 7$	$g = 8$	$g = 9$
$d = 1$ (N)	$i = 1$	0.322	0.295	0.274	0.246	0.203	0.157	0.114	0.081	0.057
$d = 1$ (N)	$i = 2$	0.329	0.292	0.277	0.250	0.204	0.155	0.114	0.079	0.052
$d = 1$ (N)	$i = 3$	0.329	0.292	0.275	0.246	0.204	0.159	0.114	0.084	0.059
$d = 2$ (NE)	$i = 1$	0.321	0.279	0.263	0.234	0.182	0.138	0.099	0.070	0.052
$d = 2$ (NE)	$i = 2$	0.326	0.280	0.266	0.235	0.183	0.137	0.099	0.070	0.046
$d = 2$ (NE)	$i = 3$	0.327	0.281	0.262	0.233	0.183	0.135	0.099	0.070	0.048
$d = 3$ (E)	$i = 1$	0.324	0.274	0.252	0.218	0.160	0.116	0.082		
$d = 3$ (E)	$i = 2$	0.323	0.268	0.250	0.216	0.159	0.115	0.080		
$d = 3$ (E)	$i = 3$	0.322	0.270	0.250	0.216	0.159	0.114	0.079		
$d = 4$ (SE)	$i = 1$	0.320	0.260	0.243	0.217	0.167	0.124	0.090	0.066	0.045
$d = 4$ (SE)	$i = 2$	0.320	0.265	0.244	0.214	0.168	0.124	0.089	0.065	0.044
$d = 4$ (SE)	$i = 3$	0.320	0.264	0.245	0.216	0.168	0.124	0.090	0.064	0.044
$d = 5$ (S)	$i = 1$	0.322	0.288	0.273	0.250	0.205	0.164	0.121	0.088	0.062
$d = 5$ (S)	$i = 2$	0.319	0.286	0.272	0.248	0.202	0.161	0.119	0.089	0.063
$d = 5$ (S)	$i = 3$	0.318	0.286	0.269	0.248	0.203	0.160	0.119	0.087	0.060
$d = 6$ (SW)	$i = 1$	0.318	0.272	0.257	0.232	0.184	0.142	0.104	0.074	0.050
$d = 6$ (SW)	$i = 2$	0.317	0.269	0.255	0.230	0.182	0.142	0.104	0.073	0.049
$d = 6$ (SW)	$i = 3$	0.317	0.270	0.255	0.230	0.182	0.142	0.104	0.073	0.049
$d = 7$ (W)	$i = 1$	0.319	0.284	0.274	0.247	0.194	0.144	0.099	0.067	
$d = 7$ (W)	$i = 2$	0.318	0.282	0.273	0.245	0.193	0.144	0.099	0.067	
$d = 7$ (W)	$i = 3$	0.321	0.283	0.275	0.247	0.195	0.145	0.101	0.064	
$d = 8$ (NW)	$i = 1$	0.314	0.274	0.261	0.236	0.189	0.141	0.102	0.073	0.046
$d = 8$ (NW)	$i = 2$	0.315	0.274	0.265	0.236	0.189	0.141	0.102	0.073	0.050
$d = 8$ (NW)	$i = 3$	0.315	0.274	0.261	0.237	0.189	0.141	0.102	0.073	0.049
$d = 1$ (N)	$i = 4$	0.317	0.276	0.262	0.235	0.188	0.146	0.108	0.078	0.053
$d = 1$ (N)	$i = 5$	0.317	0.278	0.260	0.235	0.189	0.146	0.108	0.076	0.053
$d = 1$ (N)	$i = 6$	0.317	0.277	0.263	0.235	0.188	0.147	0.108	0.077	0.054

**Table 3.A.4**

Maximum deflections measured during the 27 FWD tests performed on the new slab A1-33873 [mm].

Test Direction	Test Number	Geophone								
		$g = 1$	$g = 2$	$g = 3$	$g = 4$	$g = 5$	$g = 6$	$g = 7$	$g = 8$	$g = 9$
$d = 1$ (N)	$i = 1$	0.159	0.125	0.119	0.107	0.091	0.075	0.061	0.051	0.041
$d = 1$ (N)	$i = 2$	0.153	0.123	0.117	0.105	0.091	0.074	0.061	0.049	0.041
$d = 1$ (N)	$i = 3$	0.152	0.123	0.115	0.104	0.088	0.073	0.060	0.048	0.039
$d = 2$ (NE)	$i = 1$	0.152	0.122	0.119	0.104	0.086	0.071	0.058	0.046	0.036
$d = 2$ (NE)	$i = 2$	0.150	0.122	0.115	0.102	0.086	0.071	0.056	0.043	0.035
$d = 2$ (NE)	$i = 3$	0.151	0.122	0.115	0.102	0.086	0.071	0.056	0.044	0.033
$d = 3$ (E)	$i = 1$	0.152	0.120	0.112	0.102	0.083	0.068	0.051		
$d = 3$ (E)	$i = 2$	0.150	0.119	0.112	0.101	0.083	0.068	0.050		
$d = 3$ (E)	$i = 3$	0.150	0.118	0.113	0.102	0.083	0.068	0.051		
$d = 4$ (SE)	$i = 1$	0.152	0.112	0.111	0.097	0.076	0.063	0.051	0.040	0.030
$d = 4$ (SE)	$i = 2$	0.151	0.111	0.104	0.094	0.075	0.063	0.049	0.037	0.029
$d = 4$ (SE)	$i = 3$	0.152	0.112	0.104	0.096	0.078	0.064	0.049	0.039	0.031
$d = 5$ (S)	$i = 1$	0.150	0.125	0.115	0.106	0.091	0.072	0.056	0.047	0.037
$d = 5$ (S)	$i = 2$	0.148	0.121	0.117	0.108	0.091	0.071	0.059	0.047	0.037
$d = 5$ (S)	$i = 3$	0.149	0.123	0.116	0.108	0.090	0.071	0.059	0.047	0.039
$d = 6$ (SW)	$i = 1$	0.149	0.112	0.106	0.095	0.079	0.065	0.052	0.044	0.038
$d = 6$ (SW)	$i = 2$	0.147	0.110	0.106	0.095	0.079	0.067	0.052	0.044	0.038
$d = 6$ (SW)	$i = 3$	0.147	0.110	0.106	0.095	0.079	0.067	0.052	0.044	0.038
$d = 7$ (W)	$i = 1$	0.148	0.123	0.117	0.105	0.084	0.068	0.055	0.044	
$d = 7$ (W)	$i = 2$	0.149	0.123	0.115	0.105	0.083	0.068	0.054	0.044	
$d = 7$ (W)	$i = 3$	0.149	0.124	0.117	0.105	0.085	0.068	0.055	0.044	
$d = 8$ (NW)	$i = 1$	0.148	0.118	0.113	0.101	0.083	0.068	0.053	0.043	0.033
$d = 8$ (NW)	$i = 2$	0.148	0.118	0.113	0.101	0.083	0.067	0.053	0.043	0.032
$d = 8$ (NW)	$i = 3$	0.149	0.121	0.109	0.101	0.084	0.067	0.055	0.043	0.033
$d = 1$ (N)	$i = 4$	0.148	0.120	0.115	0.104	0.086	0.072	0.059	0.049	0.037
$d = 1$ (N)	$i = 5$	0.148	0.122	0.115	0.103	0.087	0.073	0.059	0.047	0.038
$d = 1$ (N)	$i = 6$	0.149	0.122	0.116	0.106	0.088	0.074	0.060	0.043	0.039

**Table 3.A.5**

Maximum deflections measured during the 27 FWD tests performed on the old slab A1-33874 [mm].

Test Direction	Test Number	Geophone								
		$g = 1$	$g = 2$	$g = 3$	$g = 4$	$g = 5$	$g = 6$	$g = 7$	$g = 8$	$g = 9$
$d = 1$ (N)	$i = 1$	0.204	0.174	0.159	0.145	0.119	0.096	0.077	0.063	0.048
$d = 1$ (N)	$i = 2$	0.205	0.174	0.163	0.147	0.121	0.098	0.079	0.061	0.050
$d = 1$ (N)	$i = 3$	0.204	0.174	0.162	0.146	0.119	0.096	0.077	0.059	0.047
$d = 2$ (NE)	$i = 1$	0.200	0.168	0.159	0.143	0.119	0.098	0.079	0.066	0.050
$d = 2$ (NE)	$i = 2$	0.203	0.171	0.158	0.142	0.118	0.099	0.080	0.067	0.052
$d = 2$ (NE)	$i = 3$	0.204	0.173	0.159	0.141	0.118	0.097	0.080	0.066	0.052
$d = 3$ (E)	$i = 1$	0.198	0.169	0.159	0.142	0.120	0.103	0.089		
$d = 3$ (E)	$i = 2$	0.202	0.173	0.159	0.144	0.123	0.107	0.092		
$d = 3$ (E)	$i = 3$	0.206	0.172	0.161	0.144	0.123	0.107	0.091		
$d = 4$ (SE)	$i = 1$	0.205	0.169	0.152	0.141	0.116	0.095	0.075	0.061	0.048
$d = 4$ (SE)	$i = 2$	0.205	0.165	0.155	0.140	0.113	0.093	0.074	0.060	0.048
$d = 4$ (SE)	$i = 3$	0.204	0.170	0.153	0.140	0.115	0.093	0.074	0.060	0.048
$d = 5$ (S)	$i = 1$	0.203	0.179	0.171	0.151	0.127	0.099	0.076	0.059	0.045
$d = 5$ (S)	$i = 2$	0.204	0.185	0.168	0.150	0.117	0.098	0.076	0.059	0.046
$d = 5$ (S)	$i = 3$	0.204	0.183	0.169	0.151	0.113	0.097	0.076	0.059	0.045
$d = 6$ (SW)	$i = 1$	0.200	0.160	0.145	0.131	0.105	0.081	0.061	0.047	0.035
$d = 6$ (SW)	$i = 2$	0.201	0.161	0.147	0.132	0.105	0.081	0.061	0.047	0.033
$d = 6$ (SW)	$i = 3$	0.202	0.161	0.148	0.133	0.106	0.081	0.061	0.047	0.035
$d = 7$ (W)	$i = 1$	0.205	0.172	0.167	0.144	0.112	0.089	0.066	0.048	
$d = 7$ (W)	$i = 2$	0.201	0.173	0.156	0.139	0.112	0.085	0.065	0.048	
$d = 7$ (W)	$i = 3$	0.202	0.173	0.158	0.140	0.112	0.086	0.066	0.048	
$d = 8$ (NW)	$i = 1$	0.201	0.166	0.152	0.136	0.111	0.089	0.069	0.053	0.041
$d = 8$ (NW)	$i = 2$	0.203	0.168	0.152	0.137	0.112	0.089	0.069	0.054	0.041
$d = 8$ (NW)	$i = 3$	0.203	0.168	0.154	0.137	0.112	0.089	0.070	0.054	0.041
$d = 1$ (N)	$i = 4$	0.203	0.172	0.161	0.144	0.118	0.096	0.077	0.061	0.047
$d = 1$ (N)	$i = 5$	0.204	0.174	0.159	0.143	0.119	0.096	0.077	0.064	0.048
$d = 1$ (N)	$i = 6$	0.205	0.175	0.158	0.142	0.119	0.096	0.077	0.064	0.049

**Table 3.A.6**

Maximum deflections measured during the 27 FWD tests performed on the old slab A2-47543 [mm].

Test Direction	Test Number	Geophone								
		$g = 1$	$g = 2$	$g = 3$	$g = 4$	$g = 5$	$g = 6$	$g = 7$	$g = 8$	$g = 9$
$d = 1$ (N)	$i = 1$	0.389	0.338	0.319	0.285	0.233	0.183	0.139	0.103	0.075
$d = 1$ (N)	$i = 2$	0.384	0.333	0.316	0.283	0.230	0.181	0.137	0.102	0.070
$d = 1$ (N)	$i = 3$	0.381	0.329	0.312	0.279	0.227	0.178	0.135	0.099	0.070
$d = 2$ (NE)	$i = 1$	0.371	0.323	0.295	0.263	0.205	0.157	0.117	0.082	0.059
$d = 2$ (NE)	$i = 2$	0.372	0.323	0.298	0.264	0.206	0.158	0.118	0.082	0.061
$d = 2$ (NE)	$i = 3$	0.372	0.323	0.298	0.264	0.207	0.159	0.119	0.083	0.061
$d = 3$ (E)	$i = 1$	0.364	0.311	0.287	0.249	0.187	0.132	0.088	0.053	
$d = 3$ (E)	$i = 2$	0.365	0.314	0.290	0.251	0.188	0.131	0.088	0.052	
$d = 3$ (E)	$i = 3$	0.363	0.308	0.283	0.247	0.185	0.131	0.087	0.053	
$d = 4$ (SE)	$i = 1$	0.342	0.280	0.256	0.218	0.174	0.131	0.097	0.069	0.045
$d = 4$ (SE)	$i = 2$	0.344	0.279	0.259	0.225	0.176	0.133	0.101	0.074	0.051
$d = 4$ (SE)	$i = 3$	0.342	0.275	0.259	0.225	0.175	0.133	0.101	0.074	0.054
$d = 5$ (S)	$i = 1$	0.350	0.319	0.300	0.268	0.213	0.167	0.127	0.094	0.072
$d = 5$ (S)	$i = 2$	0.352	0.324	0.297	0.269	0.214	0.169	0.130	0.094	0.072
$d = 5$ (S)	$i = 3$	0.351	0.322	0.296	0.268	0.214	0.168	0.128	0.095	0.072
$d = 6$ (SW)	$i = 1$	0.347	0.301	0.274	0.244	0.197	0.154	0.117	0.089	0.061
$d = 6$ (SW)	$i = 2$	0.347	0.304	0.273	0.245	0.198	0.154	0.116	0.086	0.059
$d = 6$ (SW)	$i = 3$	0.348	0.303	0.274	0.246	0.199	0.156	0.117	0.087	0.059
$d = 7$ (W)	$i = 1$	0.346	0.309	0.295	0.268	0.218	0.168	0.114	0.068	
$d = 7$ (W)	$i = 2$	0.348	0.312	0.297	0.269	0.220	0.168	0.116	0.067	
$d = 7$ (W)	$i = 3$	0.348	0.314	0.297	0.270	0.220	0.169	0.116	0.067	
$d = 8$ (NW)	$i = 1$	0.348	0.307	0.280	0.251	0.204	0.162	0.121	0.088	0.053
$d = 8$ (NW)	$i = 2$	0.349	0.306	0.281	0.253	0.206	0.163	0.124	0.090	0.057
$d = 8$ (NW)	$i = 3$	0.346	0.308	0.281	0.252	0.205	0.162	0.123	0.090	0.056
$d = 1$ (N)	$i = 4$	0.340	0.298	0.280	0.251	0.201	0.157	0.119	0.089	0.059
$d = 1$ (N)	$i = 5$	0.337	0.296	0.277	0.248	0.200	0.157	0.118	0.087	0.056
$d = 1$ (N)	$i = 6$	0.339	0.295	0.278	0.249	0.200	0.158	0.119	0.089	0.066

**Table 3.A.7**

Maximum deflections measured during the 27 FWD tests performed on the old slab A2-50000 [mm].

Test Direction	Test Number	Geophone								
		$g = 1$	$g = 2$	$g = 3$	$g = 4$	$g = 5$	$g = 6$	$g = 7$	$g = 8$	$g = 9$
$d = 1$ (N)	$i = 1$	0.407	0.369	0.346	0.315	0.255	0.202	0.155	0.112	0.081
$d = 1$ (N)	$i = 2$	0.402	0.360	0.341	0.310	0.253	0.199	0.151	0.109	0.084
$d = 1$ (N)	$i = 3$	0.402	0.358	0.339	0.309	0.252	0.198	0.151	0.109	0.084
$d = 2$ (NE)	$i = 1$	0.395	0.356	0.335	0.303	0.251	0.200	0.150	0.111	0.080
$d = 2$ (NE)	$i = 2$	0.397	0.354	0.335	0.301	0.250	0.200	0.150	0.112	0.084
$d = 2$ (NE)	$i = 3$	0.399	0.356	0.336	0.302	0.251	0.200	0.150	0.110	0.082
$d = 3$ (E)	$i = 1$	0.398	0.358	0.339	0.310	0.254	0.205	0.156		
$d = 3$ (E)	$i = 2$	0.401	0.357	0.344	0.311	0.258	0.206	0.158		
$d = 3$ (E)	$i = 3$	0.400	0.358	0.340	0.311	0.255	0.207	0.158		
$d = 4$ (SE)	$i = 1$	0.396	0.345	0.338	0.310	0.250	0.200	0.275	0.112	0.074
$d = 4$ (SE)	$i = 2$	0.397	0.347	0.330	0.304	0.246	0.203	0.157	0.113	0.081
$d = 4$ (SE)	$i = 3$	0.398	0.351	0.332	0.306	0.263	0.203	0.158	0.114	0.080
$d = 5$ (S)	$i = 1$	0.394	0.365	0.348	0.323	0.276	0.221	0.175	0.134	0.096
$d = 5$ (S)	$i = 2$	0.394	0.360	0.347	0.323	0.273	0.222	0.172	0.137	0.088
$d = 5$ (S)	$i = 3$	0.398	0.368	0.349	0.323	0.275	0.225	0.174	0.138	0.092
$d = 6$ (SW)	$i = 1$	0.393	0.344	0.317	0.287	0.236	0.184	0.136	0.098	0.070
$d = 6$ (SW)	$i = 2$	0.391	0.344	0.317	0.287	0.236	0.186	0.140	0.101	0.074
$d = 6$ (SW)	$i = 3$	0.391	0.344	0.319	0.287	0.236	0.187	0.139	0.100	0.072
$d = 7$ (W)	$i = 1$	0.389	0.346	0.325	0.284	0.222	0.169	0.117	0.077	
$d = 7$ (W)	$i = 2$	0.393	0.359	0.319	0.286	0.224	0.166	0.117	0.075	
$d = 7$ (W)	$i = 3$	0.394	0.348	0.321	0.285	0.223	0.169	0.118	0.075	
$d = 8$ (NW)	$i = 1$	0.398	0.345	0.318	0.284	0.225	0.173	0.125	0.091	0.065
$d = 8$ (NW)	$i = 2$	0.396	0.344	0.318	0.284	0.225	0.172	0.122	0.088	0.061
$d = 8$ (NW)	$i = 3$	0.394	0.344	0.318	0.284	0.225	0.172	0.124	0.088	0.063
$d = 1$ (N)	$i = 4$	0.395	0.353	0.333	0.301	0.244	0.193	0.145	0.106	0.075
$d = 1$ (N)	$i = 5$	0.397	0.354	0.333	0.302	0.245	0.194	0.146	0.106	0.073
$d = 1$ (N)	$i = 6$	0.396	0.354	0.334	0.302	0.245	0.194	0.144	0.106	0.072

**Table 3.A.8**

Maximum deflections measured during the 27 FWD tests performed on the new slab A2-51995 [mm].

Test Direction	Test Number	Geophone								
		$g = 1$	$g = 2$	$g = 3$	$g = 4$	$g = 5$	$g = 6$	$g = 7$	$g = 8$	$g = 9$
$d = 1$ (N)	$i = 1$	0.370	0.316	0.289	0.256	0.200	0.150	0.109	0.079	0.060
$d = 1$ (N)	$i = 2$	0.370	0.311	0.283	0.249	0.194	0.143	0.105	0.075	0.062
$d = 1$ (N)	$i = 3$	0.366	0.312	0.289	0.254	0.196	0.146	0.106	0.075	0.058
$d = 2$ (NE)	$i = 1$	0.367	0.313	0.291	0.256	0.199	0.151	0.108	0.078	0.055
$d = 2$ (NE)	$i = 2$	0.368	0.314	0.289	0.256	0.199	0.151	0.107	0.077	0.054
$d = 2$ (NE)	$i = 3$	0.369	0.315	0.290	0.257	0.200	0.152	0.109	0.076	0.057
$d = 3$ (E)	$i = 1$	0.368	0.316	0.290	0.254	0.193	0.139	0.094		
$d = 3$ (E)	$i = 2$	0.371	0.318	0.292	0.257	0.193	0.140	0.095		
$d = 3$ (E)	$i = 3$	0.372	0.318	0.294	0.257	0.195	0.142	0.093		
$d = 4$ (SE)	$i = 1$	0.370	0.283	0.262	0.224	0.173	0.128	0.091	0.066	0.046
$d = 4$ (SE)	$i = 2$	0.371	0.287	0.254	0.226	0.174	0.130	0.092	0.065	0.048
$d = 4$ (SE)	$i = 3$	0.370	0.286	0.257	0.226	0.173	0.128	0.091	0.066	0.047
$d = 5$ (S)	$i = 1$	0.367	0.315	0.281	0.252	0.193	0.143	0.103	0.072	0.050
$d = 5$ (S)	$i = 2$	0.369	0.313	0.283	0.255	0.190	0.144	0.106	0.071	0.048
$d = 5$ (S)	$i = 3$	0.368	0.313	0.284	0.255	0.191	0.143	0.106	0.071	0.044
$d = 6$ (SW)	$i = 1$	0.372	0.277	0.247	0.213	0.156	0.113	0.079	0.055	0.043
$d = 6$ (SW)	$i = 2$	0.372	0.289	0.248	0.213	0.153	0.113	0.079	0.056	0.046
$d = 6$ (SW)	$i = 3$	0.373	0.287	0.249	0.211	0.146	0.114	0.079	0.055	0.044
$d = 7$ (W)	$i = 1$	0.370	0.305	0.272	0.233	0.168	0.114			
$d = 7$ (W)	$i = 2$	0.372	0.306	0.268	0.233	0.168	0.114			
$d = 7$ (W)	$i = 3$	0.370	0.305	0.267	0.235	0.169	0.114			
$d = 8$ (NW)	$i = 1$	0.370	0.297	0.267	0.232	0.172	0.123	0.086	0.059	0.041
$d = 8$ (NW)	$i = 2$	0.371	0.299	0.271	0.233	0.173	0.124	0.086	0.060	0.042
$d = 8$ (NW)	$i = 3$	0.372	0.300	0.269	0.233	0.174	0.125	0.086	0.059	0.041
$d = 1$ (N)	$i = 4$	0.370	0.315	0.286	0.252	0.194	0.147	0.104	0.075	0.055
$d = 1$ (N)	$i = 5$	0.373	0.315	0.287	0.252	0.193	0.145	0.104	0.076	0.055
$d = 1$ (N)	$i = 6$	0.374	0.319	0.285	0.252	0.193	0.144	0.105	0.077	0.055



**Table 3.A.9**

Maximum deflections measured during the 27 FWD tests performed on the old slab A2-54003 [mm].

Test Direction	Test Number	Geophone								
		$g = 1$	$g = 2$	$g = 3$	$g = 4$	$g = 5$	$g = 6$	$g = 7$	$g = 8$	$g = 9$
$d = 1$ (N)	$i = 1$	0.671	0.624	0.596	0.552	0.473	0.388	0.303	0.228	0.156
$d = 1$ (N)	$i = 2$	0.676	0.624	0.603	0.556	0.476	0.389	0.304	0.227	0.157
$d = 1$ (N)	$i = 3$	0.676	0.621	0.604	0.557	0.474	0.391	0.305	0.229	0.156
$d = 2$ (NE)	$i = 1$	0.676	0.630	0.607	0.563	0.482	0.396	0.299	0.233	0.166
$d = 2$ (NE)	$i = 2$	0.677	0.630	0.609	0.565	0.484	0.398	0.300	0.235	0.167
$d = 2$ (NE)	$i = 3$	0.676	0.634	0.607	0.564	0.481	0.396	0.312	0.234	0.167
$d = 3$ (E)	$i = 1$	0.670	0.630	0.610	0.564	0.475	0.376	0.273	0.174	
$d = 3$ (E)	$i = 2$	0.676	0.636	0.613	0.566	0.476	0.377	0.274	0.176	
$d = 3$ (E)	$i = 3$	0.680	0.638	0.614	0.566	0.476	0.378	0.275	0.176	
$d = 4$ (SE)	$i = 1$	0.670	0.621	0.595	0.548	0.470	0.392	0.310	0.235	0.169
$d = 4$ (SE)	$i = 2$	0.676	0.617	0.596	0.550	0.471	0.394	0.309	0.233	0.168
$d = 4$ (SE)	$i = 3$	0.676	0.620	0.596	0.549	0.472	0.394	0.311	0.234	0.168
$d = 5$ (S)	$i = 1$	0.672	0.634	0.610	0.569	0.490	0.416	0.333	0.258	0.193
$d = 5$ (S)	$i = 2$	0.673	0.632	0.616	0.570	0.493	0.418	0.334	0.260	0.191
$d = 5$ (S)	$i = 3$	0.674	0.632	0.616	0.571	0.493	0.418	0.335	0.261	0.192
$d = 6$ (SW)	$i = 1$	0.672	0.579	0.539	0.491	0.400	0.312	0.228	0.151	0.096
$d = 6$ (SW)	$i = 2$	0.675	0.578	0.540	0.491	0.399	0.314	0.229	0.154	0.097
$d = 6$ (SW)	$i = 3$	0.674	0.577	0.541	0.491	0.401	0.314	0.228	0.155	0.096
$d = 7$ (W)	$i = 1$	0.663	0.586	0.552	0.487	0.369	0.251	0.133		
$d = 7$ (W)	$i = 2$	0.668	0.590	0.556	0.491	0.372	0.252	0.136		
$d = 7$ (W)	$i = 3$	0.669	0.592	0.556	0.492	0.373	0.253	0.138		
$d = 8$ (NW)	$i = 1$	0.665	0.583	0.551	0.495	0.401	0.310	0.222	0.149	0.094
$d = 8$ (NW)	$i = 2$	0.668	0.584	0.554	0.497	0.402	0.312	0.222	0.149	0.094
$d = 8$ (NW)	$i = 3$	0.668	0.585	0.554	0.498	0.403	0.312	0.221	0.149	0.094
$d = 1$ (N)	$i = 4$	0.660	0.607	0.583	0.538	0.457	0.373	0.297	0.220	0.147
$d = 1$ (N)	$i = 5$	0.661	0.609	0.587	0.538	0.457	0.372	0.294	0.220	0.150
$d = 1$ (N)	$i = 6$	0.663	0.609	0.586	0.538	0.458	0.374	0.295	0.219	0.150

**Table 3.A.10**

Maximum deflections measured during the 27 FWD tests performed on the new slab A2-54440 [mm].

Test Direction	Test Number	Geophone								
		$g = 1$	$g = 2$	$g = 3$	$g = 4$	$g = 5$	$g = 6$	$g = 7$	$g = 8$	$g = 9$
$d = 1$ (N)	$i = 1$	0.336	0.284	0.259	0.229	0.178	0.138	0.105	0.078	0.060
$d = 1$ (N)	$i = 2$	0.337	0.281	0.257	0.227	0.176	0.136	0.106	0.080	0.057
$d = 1$ (N)	$i = 3$	0.338	0.282	0.257	0.227	0.174	0.136	0.101	0.077	0.060
$d = 2$ (NE)	$i = 1$	0.334	0.278	0.257	0.224	0.174	0.133	0.101	0.075	0.061
$d = 2$ (NE)	$i = 2$	0.336	0.279	0.259	0.225	0.176	0.134	0.102	0.076	0.060
$d = 2$ (NE)	$i = 3$	0.337	0.280	0.257	0.225	0.175	0.135	0.102	0.076	0.060
$d = 3$ (E)	$i = 1$	0.339	0.275	0.249	0.219	0.167	0.127	0.091	0.063	
$d = 3$ (E)	$i = 2$	0.340	0.276	0.251	0.220	0.167	0.127	0.092	0.063	
$d = 3$ (E)	$i = 3$	0.338	0.276	0.251	0.221	0.167	0.127	0.091	0.063	
$d = 4$ (SE)	$i = 1$	0.336	0.254	0.235	0.197	0.158	0.125	0.087	0.067	0.050
$d = 4$ (SE)	$i = 2$	0.338	0.256	0.239	0.201	0.159	0.128	0.085	0.068	0.049
$d = 4$ (SE)	$i = 3$	0.338	0.254	0.242	0.200	0.160	0.127	0.088	0.068	0.049
$d = 5$ (S)	$i = 1$	0.329	0.276	0.253	0.220	0.179	0.134	0.099	0.081	0.057
$d = 5$ (S)	$i = 2$	0.334	0.279	0.250	0.221	0.171	0.135	0.109	0.077	0.058
$d = 5$ (S)	$i = 3$	0.333	0.280	0.249	0.221	0.172	0.132	0.105	0.079	0.058
$d = 6$ (SW)	$i = 1$	0.338	0.251	0.226	0.199	0.150	0.117	0.085	0.063	0.046
$d = 6$ (SW)	$i = 2$	0.338	0.251	0.225	0.199	0.151	0.117	0.084	0.063	0.045
$d = 6$ (SW)	$i = 3$	0.338	0.252	0.224	0.199	0.149	0.117	0.084	0.063	0.045
$d = 7$ (W)	$i = 1$	0.331	0.266	0.241	0.211	0.160	0.117	0.077		
$d = 7$ (W)	$i = 2$	0.333	0.269	0.244	0.213	0.161	0.120	0.079		
$d = 7$ (W)	$i = 3$	0.331	0.268	0.246	0.212	0.160	0.116	0.075		
$d = 8$ (NW)	$i = 1$	0.334	0.266	0.243	0.213	0.163	0.124	0.089	0.066	0.049
$d = 8$ (NW)	$i = 2$	0.335	0.268	0.243	0.214	0.164	0.126	0.090	0.067	0.049
$d = 8$ (NW)	$i = 3$	0.337	0.269	0.241	0.211	0.165	0.125	0.090	0.064	0.047
$d = 1$ (N)	$i = 4$	0.334	0.276	0.254	0.221	0.173	0.135	0.102	0.077	0.060
$d = 1$ (N)	$i = 5$	0.335	0.276	0.257	0.222	0.174	0.139	0.102	0.079	0.059
$d = 1$ (N)	$i = 6$	0.335	0.277	0.255	0.223	0.174	0.140	0.102	0.079	0.058

## Instrumentation of field-testing sites for dynamic characterization of the temperature-dependent stiffness of pavements and their layers

### 4.1 Introduction

Roads are exposed to variable atmospheric conditions. The corresponding changes of temperature have a significant influence on the stiffness of rigid and flexible pavement structures.

- Flexible pavements include layers of asphalt. The stiffness of bituminous asphalt materials decreases with increasing temperature (Olard and Di Benedetto, 2003; Khabaz and Khare, 2018).
- Rigid pavements include concrete slabs. Their temperature-gradient-induced curling (= partial loss of full-face contact along one of the layer interfaces) reduces the structural stiffness of concrete roads (Khazanovich et al., 2001; Vandenbossche, 2003).
- Many pavement structures include unbound granular layers. Their stiffness was shown to be a function of the temperature and moisture (Salour and Erlingsson, 2013; Bayat, 2009).

Consequently, it is challenging to interpret *different* surface deflections measured during nominally *identical* Falling Weight Deflectometer (FWD) tests performed on *the same* pavement structure at *different* temperatures. The described situation provides the motivation to gain (i) more insight into the load-carrying behavior of multi-layered pavement structures subjected to dynamic loading, and (ii) direct access to the stiffness of individual layers of interest. To this end, one rigid and two flexible pavement structures are equipped with three types of sensors: (i) Pt100 sensors in order to measure the temperature at specific depths of the pavement structure, (ii) strain gauges in order to quantify the deformation of asphalt layers during FWD testing, and (iii) acceleration sensors in order to analyze how dynamic loads propagate through pavement structures.

FWD testing is a worldwide-popular non-destructive method for the assessment of the health of pavement structures. FWD tests consist of dropping a standardized weight onto a damped spring system placed over a circular load plate that transmits the dynamic load to the pavement structure. The force history is measured using an integrated load cell. Several displacement

sensors (so-called geophones) measure the vertical deflection history at specific distances from the center of the falling weight (COST, 2005; Smith et al., 2017a).

Surface deflections measured during FWD tests are usually evaluated using one of two popular conceptual approaches. The first one refers to the quantification and interpretation of *deflection basin parameters* such as the surface curvature index (SCI) or the AREA parameter, see e.g. (COST, 2005; Hossain and Zaniewski, 1991; Xu et al., 2002; Rada et al., 2016; Rabbi and Mishra, 2021; Hoffman and Thompson, 1980). Similar indexes have been developed for quantification of asymmetric behavior of concrete slabs subjected to central FWD testing (Díaz Flores et al., 2021, 2023, 2022). The second approach for evaluation of FWD tests refers to back-calculation of properties of the tested pavement structure, in order to minimize the difference between measured and simulated deflections. Two types of static structural simulation models are frequently used: multi-layered elastic half-space models and dense-liquid models. The former models explicitly resolve the individual layers of pavement structures (Burmister, 1945a). Back-calculation is aimed at quantifying the thickness and stiffness of the individual layers. Different commercial programs frequently produce different results even when fed with same input data (Romeo et al., 2023), because different combinations of layer moduli and thicknesses produce (virtually) the same deflections (Smith et al., 2017b; Tarefder and Ahmed, 2013). The second type of structural models (“dense-liquid models”) idealize pavement structures as an elastic plate resting on a Winkler foundation (Westergaard, 1926, 1948). Back-calculation is aimed at quantifying the bending stiffness of the plate and the modulus of subgrade reaction of the Winkler foundation. Analytical formulae facilitate the back-calculation procedure, see e.g. (Ioannides et al., 1989; Ioannides, 1990; Hall et al., 1997; Khazanovich et al., 2001). Notably, back-calculations were also carried out in the context of dynamic analyses with the aid of Finite Element (FE) simulations (Zaghloul, 1993; Li, 2017; Assogba et al., 2020, 2021).

The present study builds on experience from FWD research approaches which consisted of equipping road sections and pavement testing facilities with different types of measurement sensors. A variety of strain gauges, pressure cells, deflection and temperature sensors were installed into a flexible pavement, and recommendations were given regarding their selection and use (Tabatabaee and Sebaaly, 1990). The readings of embedded strain gauges and pressure cells were compared with back-calculated stresses (Solanki et al., 2009; Yin, 2012; Mateos et al., 2013) and strains (Lenngren, 1991; Shafiee et al., 2018; Barriera et al., 2021). Multi-depth deflectometer sensors have been installed to improve the interpretation of FWD data with respect to base and subgrade damage (Donovan and Tutumluer, 2009). Moisture and ground water sensors allowed for assessing the influence of moisture content and depth of the groundwater table on FWD deflections and back-calculated stiffness of the unbound layers (Salour and Erlingsson, 2013). The recorded time history of the deflections measured during an FWD test, together with strain sensor readings, were exploited to study the cross-anisotropic viscoelastic properties of asphalt concrete (Khan et al., 2020). MEMS accelerometers have been installed (i) to compute displacement histories either by means of double time-integration or by constrained least-squares estimation, and (ii) to compare the resulting data with surface displacements measured by FWD geophones (Bajwa et al., 2020).

The present study serves two main purposes. (i) Experience with instrumentation of rigid and flexible pavements during their new construction will be gained and shared. This concerns particularly the installation of the strain gauges into asphalt layers. Three different methods will be compared: “Method A: Cut, install, and cover after asphalt placement”, “Method B: Installation in a fixation tool, before asphalt placement”, and “Method C: Use of steel dummy place-holders for the real sensors”. (ii) First data from dynamic testing at the innovatively equipped field-testing sites will be presented and discussed. This includes data from both FWD tests and a newly proposed “sledgehammer test”. It consists of sledgehammer strokes onto a metal

plate, transmitted to the pavement via a rubber pad. The sledgehammer test is performed in order to obtain accelerometer readings that allow for quantification of the runtime of longitudinal waves through asphalt, cement-stabilized, and unbound layers, such that their stiffness can be quantified using the theory of elastic wave propagation through isotropic media. To this end, acceleration sensors are installed both at the top and the bottom of layers of interest.

The present manuscript is organized as follows. Section 4.2 describes the three specific field-testing sites together with the corresponding instrumentation layouts. Section 4.3 refers to the accelerometers: it presents the theoretical foundations for quantification of layer stiffnesses, the criteria for sensor selection, and the experience gained from the installation of the sensors. Section 2.4 refers to the asphalt strain gauges: it presents the criteria for sensor selection, three different approaches for the installation of the sensors, and the experience gained with them. Section 4.5 discusses exemplary data from FWD testing of rigid and flexible pavements, together with results from the sledgehammer tests. Section 4.6 closes the paper with conclusions drawn from the presented results.

## 4.2 Overview of the three field-testing sites

One rigid and two flexible pavement structures were instrumented to become field-testing sites for FWD experiments. They were equipped with temperature sensors, accelerometers (Section 4.3), and asphalt strain gauges (Section 4.4), see Fig. 4.1.



**Fig. 4.1.** Accelerometers, strain gauges, temperature sensors, and data acquisition system.

As for temperature measurements, platinum-based detectors with an electrical resistance of 100 Ohm, see the Pt100 in Fig. 4.1, were installed in asphalt, concrete, cement-stabilized, and unbound layers. The sensors were connected by means of 4-wires running through Perfluoroalkoxy cables to a Lemo connector. The cables were protected by a  $\varnothing 5 \times 40$  mm stainless steel sleeve, a 300 mm heat shrink sleeve, and a waterproof corrugated plastic tube.

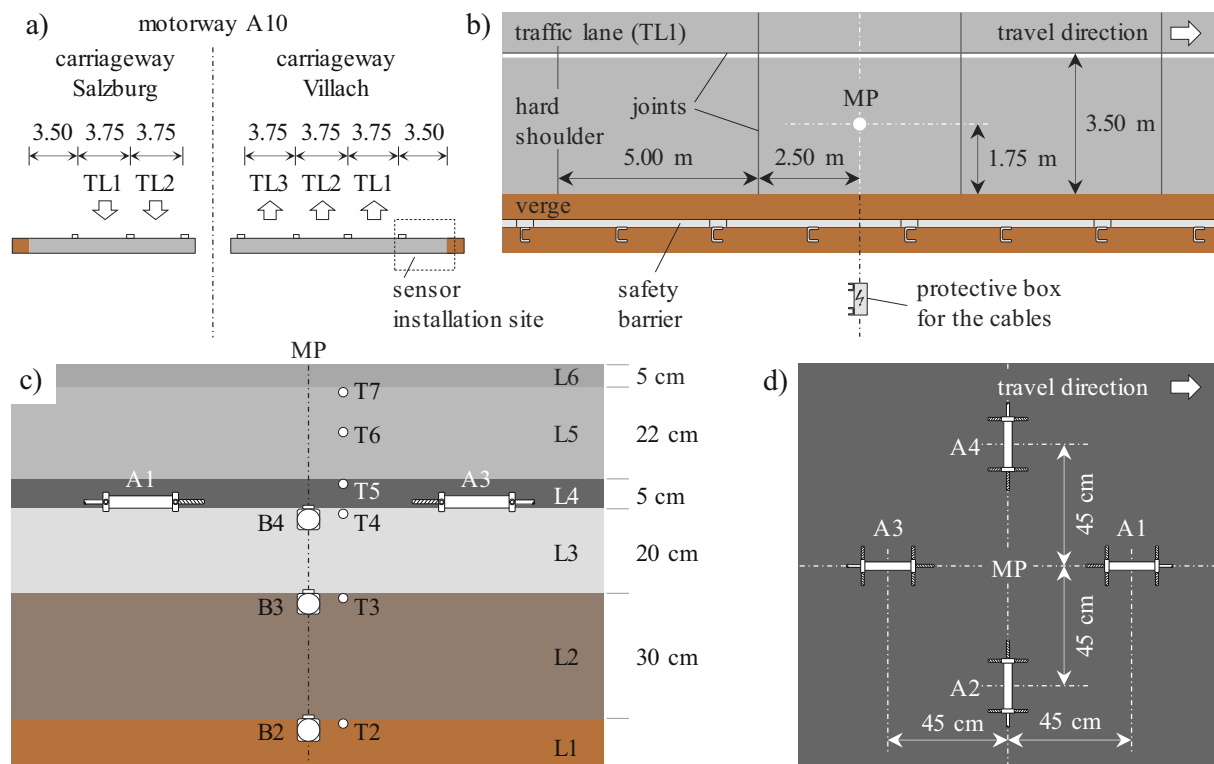
Signals of all installed sensors were recorded during dynamic testing by means of the mobile data acquisition systems DEWE-43-A (strain gauges and accelerometers) and KRYPTONi-8xRTD (temperature sensors) by DEWESoft, see Fig. 4.1. These systems are suitable for measurements at multiple unsheltered field-testing sites, because it is water-, dust-, and shockproof, and it is capable of operation within the temperature range from  $-40^{\circ}\text{C}$  to  $85^{\circ}\text{C}$ . The required electricity was provided by a portable powerbank Novoo 230 Wh, see Fig. 4.1. Between successive measurement days, the connector-ends of all sensor cables were stored inside a stainless steel box

near the verge.

Three different types of pavement structures, frequently used on the Austrian motor- and expressways, were instrumented: (i) a rigid pavement consisting of jointed plain concrete slabs connected to their neighbors through dowels and tie bars, (ii) a flexible pavement consisting of asphalt concrete layers placed over a cement-stabilized granular layer, and (iii) a flexible pavement consisting of asphalt concrete layers over two unbound granular layers. All three field-testing sites were installed in the course of major rehabilitation treatments.

#### 4.2.1 Field-testing site #1 on motorway A10

Field-testing site #1 is a concrete slab on the motorway A10, south of Salzburg. A slab of the emergency lane was selected, see Fig. 4.2(a). It has the same pavement structure as the traffic



Note: The size of the sensors is exaggerated. MP, B, T and A stand for measuring point, accelerometer, temperature sensor and asphalt strain gauge.

**Fig. 4.2.** Field-testing site #1 on motorway A10: (a) cross section through the motorway, (b) plan view onto the instrumented slab which was part of the emergency lane, MP = measurement point for FWD testing, (c) cross-section of the pavement structure, nominal thicknesses of the layers, and depths of the installed sensors, (d) plan view showing the in-plane positions and orientations of the strain gauges around the MP.

lanes, see Fig. 4.2(c), and it can be closed for FWD measurements without interrupting the traffic. The width and the length of the slab amount to 3.50 m and 5.00 m, respectively, see Fig. 4.2(b). The measurement sensors were installed during the rehabilitation of the motorway. It included the following steps. The existing asphalt and concrete layers were removed such that the subgrade was covered by two unbound granular layers only. The upper unbound granular layer was mixed in-place with cement and water, followed by compaction, in order to transform it into a cement-stabilized layer (L3). A separation layer made of asphalt (L4) was installed. Two concrete layers (L5 and L6) were laid in one pass using a train of two slipform pavers. This

completed the new pavement structure, see Fig. 4.2(c).

Measurement sensors were embedded at several depths. Six temperature sensors (T2-T7) were placed at all interfaces between neighboring layers as well as in the middle of the lower concrete layer, see Fig. 4.2(c). Three accelerometers (B2-B4) were installed along a vertical axis running through the central measurement point (MP) for FWD testing, at the interfaces between the subgrade (L1), the unbound layer (L2), the cement-stabilized layer (L3), and the asphalt layer (L4), see Fig. 4.2(b) and (c). Four strain gauges (A1-A4) were installed at the bottom of the asphalt layer, see Fig. 4.2(d) for the symmetric crosswise arrangement relative to the measuring point.

As regards the sequence of sensor installation, sensors B2 and T2 were put in place before the cement-stabilization of L3. Immediately after the stabilization, a trench was cut with an excavator down to the interface between layers L2 and L3. There, the sensors B3 and T3 were installed, the trench was refilled with the excavation material, and the layer was compacted. These works were completed before the start of the main phase of the cement hardening process. Sensors B4 and T4 were installed shortly before the placement of the asphalt concrete. The strain gauges and the temperature sensors T5, T6, and T7 were installed immediately after the construction of the asphalt layer and the lower concrete layer, respectively. Details regarding the selection of the accelerometers and the strain gauges, the design of their positions, and the used installation procedures are described in Sections 4.3 and 4.4, respectively.

The thicknesses and mass densities of the layers were determined as follows. A precision laser was used to measure the actual layer thicknesses, see Table 4.1. They slightly deviate from

**Table 4.1**

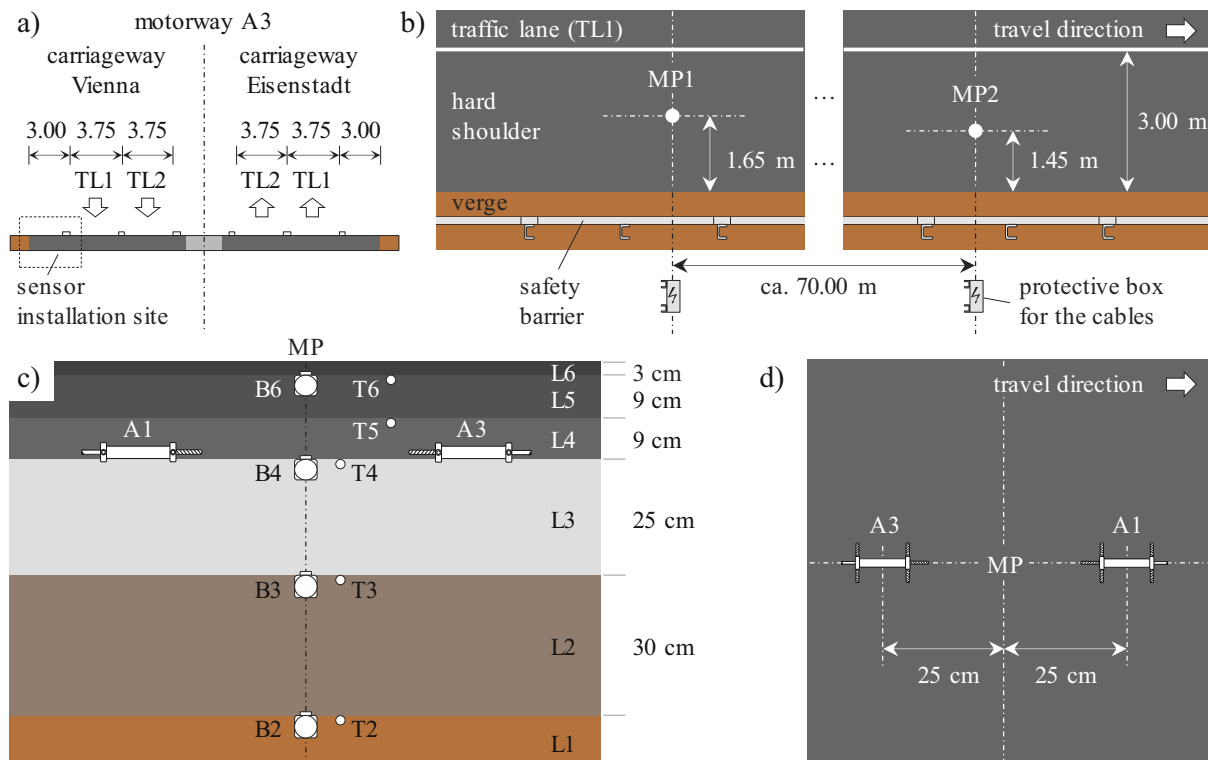
Field-testing site #1: Properties of the layers of the pavement structure, including nominal and actual measured thicknesses,  $h_{nom}$  and  $h_{meas}$ , respectively.

Layer	Name	Material	Binder [mass%]	$h_{nom}$ [cm]	$h_{meas}$ [cm]	Density [kg/m <sup>3</sup> ]
L6	Top-layer concrete	OB GK 8 (CEM II/B-S 42.5 N)	19.2	5.0	5.0	2305
L5	Bottom-layer concrete	UB GK 32 (CEM II/B-S 42.5 N)	15.6	22.0	22.0	2390
L4	Asphalt base course	AC 16 trag 70/100	4.7	5.0	8.2	2514
L3	Cement-stabilized granular layer	Cement & angular aggregates	–	20.0	17.6	2568
L2	Lower unbound granular layer	Angular aggregates	–	30.0	31.4	2595
L1	Subgrade	–	–	–	–	–

the nominal values of Fig. 4.2, because of execution tolerances. The mass densities of the two granular layers L2 and L3 were quantified in situ using the water replacement method. After digging a hole into the layer of interest, the excavated mass (measured by means of a portable digital scale) was divided by the volume of the hole. The volume was determined by laying a thin sheet of plastic into the hole, pouring water into it until the hole was filled, and then measuring the volume of the water with a graduated cylinder. For both layers L2 and L3, the water replacement method was performed three times each, resulting in the mean values of the mass densities listed in Table 4.1. As for the layers L4, L5, and L6, samples of the three materials were collected during construction, see Table 4.1 for the mean values of the mass densities determined in the laboratory.

#### 4.2.2 Field-testing site #2 on motorway A3

Field-testing site #2 is a flexible pavement on the motorway A3, south of Vienna. Two nominally identical FWD measuring points were instrumented at a distance of approximately 70 m from each other, see Fig. 4.3(b). Both measuring points are located in the middle of the hard shoulder which has the same design as the rest of the carriageway. The road section was rehabilitated as follows. The existing asphalt layers were removed. The existing cement-stabilized layer (L3) was



Note: The size of the sensors is exaggerated. MP, B, T and A stand for measuring point, accelerometer, temperature sensor and asphalt strain gauge.

**Fig. 4.3.** Field-testing site #2 on motorway A3: (a) cross section through the motorway, (b) plan view onto the instrumented slab which was part of the emergency lane, MP1 and MP2 denote measurement points for FWD testing, (c) cross-section of the pavement structure, nominal thicknesses of the layers, and depths of the installed sensors, (d) plan view showing the in-plane positions and orientations of the strain gauges around the MPs.

relaxed using a guillotine-type breaker followed by re-compaction with a roller. This two-step treatment reduced the potential for reflective cracking of three newly constructed asphalt layers. They are referred to as “base course L4”, “binder course L5”, and “surface course L6”.

Measurement sensors were embedded at several depths. Five temperature sensors (T2-T6) were placed at all interfaces between neighboring layers, see Fig. 4.3(c). Four accelerometers (B2-B4 and B6) each were installed along a vertical axes running through the measurement points (MP) for FWD testing, at the interfaces between the subgrade (L1), the unbound layer (L2), the cement-stabilized layer (L3), and the base course (L4), as well as between the binder course (L5) and the surface course (L6), see Fig. 4.3(b) and (c). Two asphalt strain gauges (A1, A3) each were installed at the bottom of the base course, see Fig. 4.3(d) for their symmetric arrangement relative to the measurement points. Two rather than four strain gauges were installed in order to reduce the number of embedded inhomogeneities, accounting for the fact that the asphalt layers have a significant load-carrying function in the pavement structure.

For the installation of sensors B2, T2, B3, and T3, rectangular areas with dimensions of  $2.50 \times 2.50 \times 0.25$  m were excavated from the cement-stabilized layer L3, symmetrically with respect to the FWD measuring points, down to the surface of the unbound layer L2, see Fig. 4.4. A smaller trench was excavated from the unbound layer L2 down to the surface of the subgrade L1, so that B2 and T2 could be installed. The material excavated from L2 was then reinserted and compacted with a vibrating plate compactor. The sensors B3 and T3 were installed. The volume excavated from L3 was filled with lean concrete rather than with the excavated material,





**Fig. 4.4.** Installation of accelerometers in unbound granular layers on the motorway A3: (a) excavation of the cement-stabilized layer, (b) smaller excavation of the unbound layer down to its boundary with the subgrade, (c) installation of sensors at the surface of the subgrade, (d) refilling and compaction of granular material, (e) installation of sensors at the surface of the unbound layer, and (f) placement of lean concrete.

because it was impossible to reinsert the excavated material in a way that would have led to properties similar to those of the relaxed cement-stabilized layer. Sensors B4 and T4, as well as the strain gauges were installed shortly before the placement of the base course L4. The temperature sensor T5 was installed immediately after the construction of the base course L4. The sensors T6 and B6 followed immediately after the construction of the binder course L5. Details regarding the selection of the accelerometers and the strain gauges, the design of their positions, and the used installation procedures are described in Sections 4.3 and 4.4, respectively.

The thicknesses of the layers and the mass-density of the unbound layer L2, see Table 4.2 was determined using the same methods as described for field-testing site #1. In situ cast cubes

**Table 4.2**

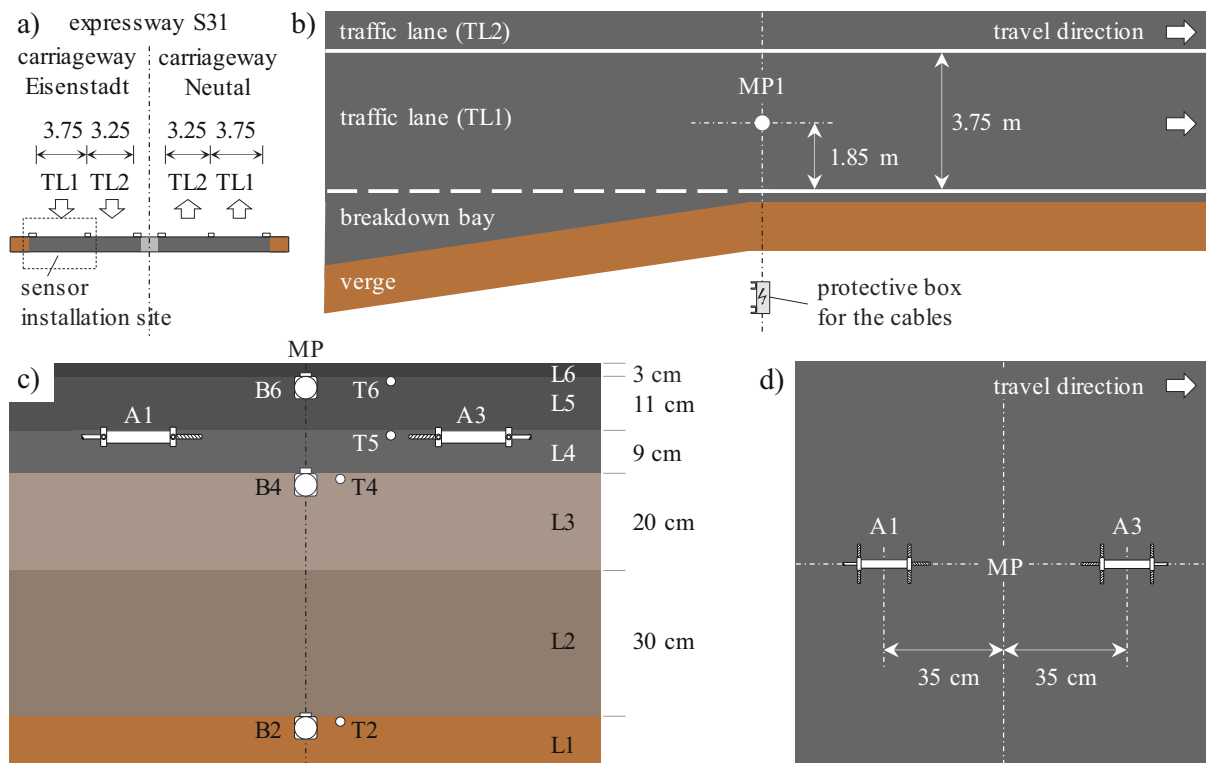
Field-testing site #2: Properties of the layers of the pavement structure, including nominal and actual measured thicknesses for both measuring points,  $h_{nom}$ ,  $h_{meas}^{MP1}$  and  $h_{meas}^{MP2}$ , respectively.

Layer	Name	Material	Binder [mass%]	$h_{nom}$ [cm]	$h_{meas}^{MP1}$ [cm]	$h_{meas}^{MP2}$ [cm]	Density [kg/m <sup>3</sup> ]
L6	Asphalt surface course	SMA 11 deck PmB 45/80-75	5.8	3.0	3.7	3.7	2515
L5	Asphalt binder course	AC 22 bin PmB 25/55-65	4.3	9.0	8.6	8.7	2420
L4	Asphalt base course	AC 22 bin PmB 45/80-65	4.2	9.0	8.8	8.3	2500
L3	Cement-stabilized granular layer (lean concrete)	C8/10 GK16 (CEM II/A-M 42.5 N)	–	25.0	23.0	33.0	2165
L2	Unbound granular layer	Angular aggregates	–	30.0	30.0	33.0	2455
L1	Subgrade	–	–	–	–	–	–

of lean concrete (L3) and fresh-mix samples of all three asphalt layers (L4-L6) were collected for laboratory testing. The mass-densities of these materials are listed in Table 4.2.

### 4.2.3 Field-testing site #3 on expressway S31

Field-testing site #3 is a flexible pavement on the expressway S31 in the federal state Burgenland. In the absence of a hard shoulder, the FWD measuring point was installed in the middle of the right lane (TL1), see Fig. 4.5 There, predominantly heavy-vehicle traffic is expected. In the longitudinal direction, the instrumented site is located after a breakdown bay. This position



Note: The size of the sensors is exaggerated. MP, B, T and A stand for measuring point, accelerometer, temperature sensor and asphalt strain gauge.

**Fig. 4.5.** Field-testing site #3 on expressway S31: (a) cross section through the motorway, (b) plan view onto the instrumented slab which was part of the emergency lane, MP = measurement point for FWD testing, (c) cross-section of the pavement structure, nominal thicknesses of the layers, and depths of the installed sensors, (d) plan view showing the in-plane positions and orientations of the strain gauges around the MP.

(i) facilitated the installation of sensors and (ii) renders in-situ testing convenient and safe for the experimenters. The rehabilitation treatment comprised (i) the renewal of the asphalt pavement, and (ii) widening of the carriageways including the introduction of a central reserve. The instrumented pavement structure consists of three asphalt layers resting on two unbound layers which are so similar that the interface between them could not be identified.

Measurement sensors were embedded at several depths. Three temperature sensors (T2, T4, and T6) were placed at the interfaces between (i) the subgrade (L1) and the lower unbound layer (L2), (ii) the upper unbound layer (L3) and the base course (L4), as well as (iii) the binder course (L5) and the surface course (L6), see Fig. 4.5 (b) and (c). Temperature sensor T5 was installed at the interface between the base and binder courses. Three accelerometers (B2, B4, and B6) were installed along a vertical axis running through the central measurement point (MP) for FWD testing, at the same interfaces as T2, T4, and T6. Two asphalt strain gauges (A1, A3) were installed into the base course, see Fig. 4.3(d) for their symmetric arrangement relative to the measurement point. Again two rather than four strain gauges were installed in order to keep the number of embedded inhomogeneities at a reasonable minimum.

The sequence of installation of the sensors B2-B4, T2, and T4-T6 was the same as in the other field-testing sites. The asphalt strain gauges, however, were installed at the *top* of the base course. This was part of an installation strategy which was specifically aimed at ensuring the position accuracy of the strain gauges. Details regarding the selection of the accelerometers and the strain gauges, the design of their positions, and the used installation procedures are

described in Sections 4.3 and 4.4, respectively.

The thicknesses of the layers and the mass-density of the unbound layers L2 and L3 were determined using the same methods as described for field-testing site #1. Samples from all three

**Table 4.3**

Field-testing site #3: Properties of the layers of the pavement structure, including nominal and actual measured thicknesses,  $h_{nom}$  and  $h_{meas}$ , respectively.

Layer	Name	Material	Binder [mass%]	$h_{nom}$ [cm]	$h_{meas}$ [cm]	Density [kg/m <sup>3</sup> ]
L6	Asphalt surface course	SMA 11 deck PmB 45/80-65	5.8	3.0	4.0	2515
L5	Asphalt binder course	AC 32 bin PmB 45/80-65	4	11.0	11.9	2413
L4	Asphalt base course	AC 22 bin PmB 45/80-65	4.3	9.0	11.0	2416
L3	Upper unbound granular layer	Angular aggregates (basalt)	-	20.0	*	2590
L2	Lower unbound granular layer	Rounded aggregates	-	30.0	*	2720
L1	Subgrade	-	-	-	-	-

\* No clear division was found between layers L2 and L3. Only a total thickness of  $h_{meas} = 55.4$  cm was reported.

asphalt layers (L4-L6, fresh mix) were collected for laboratory testing. The mass-densities of these materials are listed in Table 4.3.

## 4.3 Installation of the accelerometers

### 4.3.1 State-of-the-art applications

Two types of accelerometers have been mainly used in past pavement applications: integrated electronics piezoelectric (IEPE) and micro-electro-mechanical system (MEMS) accelerometers. IEPE sensors are mainly used to capture dynamic events, exhibiting a frequency range of some 0.3 Hz-10 kHz. They consist of a fixed mass, a piezoelectric material (e.g. quartz or a piezoceramic), and an integrated signal amplifier to reduce noise (Wilson, 2004; Levinzon, 2015). If an acceleration is imposed on the sensor, the mass will be pressed against the piezoelectric element. The generated electric charge can be measured and correlated to the acceleration. MEMS sensors, in turn, are used for dynamic and low-frequency measurements, and are also applicable for frequencies smaller than 0.3 Hz. MEMS accelerometers are either based on measurements of changes in electrical capacitance (capacitive sensors), or they use strain gauges (piezoresistive sensors), see e.g. (Wilson, 2004; De Silva et al., 2015).

Accelerometers were mounted in several studies to the *surface* of pavement structures in order to measure acceleration histories either caused by real traffic or by load simulators. The measured acceleration histories were used as reference values for the optimization of dynamic simulations of the behavior of pavement structures (Levenberg, 2012; Nielsen et al., 2020). Measured acceleration histories were also converted, by means of double time-integration, into deflection histories, see e.g. (Bohn et al., 1972; Arraigada et al., 2007; Rynänen et al., 2010; Rada et al., 2016; Bahrani et al., 2020; Bajwa et al., 2020). The deflections were then used for back-calculation of layer properties. Accelerometers positioned on the pavement surface have also been used in the context of surface wave testing, see e.g. (Nazarian et al., 1999; Gucunski and Maher, 2002; Tawfiq et al., 2002; Rydén, 2004; Kumar and Rakaraddi, 2013; du Tertre et al., 2022). Depending on the used technique, surface wave pavement testing allows either for direct determination of the modulus of the top paving layer or for the estimation of the modulus of each layer through a back-calculation analysis.

In this study, accelerometers are used to determine the time of flight of longitudinal waves propagating vertically through these layers. This way, the theory of elastic wave propagation

trough isotropic elastic media can be used for the direct quantification of layer moduli. Back-calculation procedures become obsolete.

### 4.3.2 Theoretical fundamentals

Three types of stress waves are generated when hitting a pavement structure vertically at its surface. Longitudinal waves mainly propagate vertically downwards. They are also referred to as compression or P-waves. Particle displacements are aligned with the direction of wave propagation. Transversal waves mainly propagate diagonally downwards. They are also referred to as shear or S-waves. Particle displacements are normal to the direction of wave propagation. Longitudinal and transversal waves are partly reflected and refracted at the interfaces between different layers (Chatti et al., 2017). Rayleigh waves travel along the surface. They are also referred to as surface or R-waves. Herein, the focus rests on longitudinal waves.

Depending on the amplitude of stress waves, they may be either *elastic*, provided that they induce *reversible* deformation only, or *inelastic*, provided that also irreversible deformations take place. The wave propagation front, in turn, always refers to an elastic wave, because it is faster than inelastic waves (Kolsky, 1953). The present study takes advantage of this property.

Herein, accelerometers are installed both at the top and at the bottom of layers of interest, in order used to determine the time of flight,  $\Delta t$ , of the front of a longitudinal wave which propagates vertically through these layers. Based on measured values of  $\Delta t$ , the velocity of the longitudinal wave,  $v_L$ , can be quantified as

$$v_L = \frac{h}{\Delta t}, \quad (4.1)$$

where  $h$  denotes the thickness of the layer of interest.

Quantification of the elastic stiffness of the layer based on its longitudinal wave velocity is facilitated by two realistic assumptions: (i) the layer is idealized as a macrohomogeneous material, and (ii) the longitudinal wave is considered to be a bulk (rather than a bar) wave, meaning that the lateral deformation is prevented (rather than free). Under these premises, the theory of elastic waves propagating through isotropic media delivers the following relation between the component  $C_{1111}$  of the elastic stiffness tensor, the mass density  $\rho$  of the material, and  $v_L$  of Eq. (4.1):

$$C_{1111} = \rho v_L^2. \quad (4.2)$$

Assuming the layer material to be isotropic, and its Poisson's ratio  $\nu$  to be known, the following standard relation of isotropic elasticity allows for quantification of the modulus of elasticity  $E$

$$E = C_{1111} \frac{(1 + \nu)(1 - 2\nu)}{1 - \nu}. \quad (4.3)$$

### 4.3.3 Sensor selection

IEPE accelerometers 602D61 and HT602D61 by PCB with a stainless steel housing and a ceramic sensing element, see Fig. 4.1, comply with the requirements of the present study. They are suitable in terms of measurement range and resolution, they are reasonably small, and they have a sufficient resistance against (i) mechanical impact during compaction and (ii) high temperatures during construction of asphalt layers. The side exit of the sensors together with a 3 m armored jacketed sleeve provide the high level of protection for the connector and the cable, which is required in the present geotechnical application. In more detail, the sensors 602D61 have dimensions of 25.4 mm  $\times$  18.8 mm  $\times$  25.4 mm ( $L \times W \times H$ ), a temperature range of  $-54$  to  $+121^\circ\text{C}$ , and a frequency range of 0.5 Hz to 8000 Hz. The high-temperature sensors HT602D61

have dimensions of 26.9 mm × 25.4 mm × 30.2 mm, a temperature range of −54 to +162°C, and a frequency range of 0.8 Hz to 8000 Hz. The sensitivity and the amplitude range of both sensors amount to 10.2 mV/(m/s<sup>2</sup>) and to ± 490 m/s<sup>2</sup>, respectively.

#### 4.3.4 Data acquisition rate and system

A suitable data acquisition rate had to be selected, in order to ensure that the time of flight of a longitudinal wave propagating through a layer of interest can be determined with acceptable accuracy. In order to achieve a measurement accuracy of at least 10%, it is necessary to record at least 10 acceleration values while a longitudinal wave travels from the accelerometer at the top of a layer to the accelerometer at the bottom of the same layer. This calls for the data acquisition rate which is by factor of at least 10 larger than the inverse of the estimated time of flight of the elastic wave through the layer of interest. In order to estimate times of flight a priori, Eqs. (4.1)-(4.3) were evaluated for the designed thicknesses of the layers, see Tables 4.1-4.3, and values of the elastic modulus, Poisson's ratio, and mass density of each layer of interest were taken from the literature (BMVIT, 2018; Park and Lytton, 2004; Nguyen et al., 2021; Liu and Luo, 2017; Omine et al., 1999a), see Table 4.4. For asphalt and unbound materials, upper and lower bounds of the elastic modulus, representative for winter and summer conditions, respectively, were taken into account. The stiffness properties of the concrete and cement-stabilized layers were assumed to remain virtually constant within the temperature range investigated (Binder et al., 2023). The estimated times of flight are listed in Table 4.4.

**Table 4.4**

Design calculations: data acquisition rates theoretical required for reliable measurements of the times of flight of elastic waves passing vertically through individual layers of all three field-testing sites; note: actual times of flight were measured with a data acquisition rate = 200 kHz for the layers printed in bold face.

Layer	Thickness [cm]	E-Modulus [MPa]	Poisson's ratio [-]	Density [kg/m <sup>3</sup> ]	Velocity [m/s]	Time of flight $\Delta t$ [s]	1/ $\Delta t$ [s <sup>-1</sup> ]	Requ. rate of data acquisition [kHz]
Field-testing site #1 on motorway A10								
L6	5	30,000	0.20	2,305	3,803	1.31E-05	76,056	761
L5	22	30,000	0.20	2,390	3,735	5.89E-05	16,975	170
L4 (W)	5	16,000	0.30	2,514	2,927	1.71E-05	58,540	585
L4 (S)	5	1,300	0.30	2,514	834	5.99E-05	16,687	167
<b>L3</b>	20	5,000	0.20	2,568	1,471	1.36E-04	7,354	74
<b>L2 (W)</b>	30	800	0.35	2,595	703	4.27E-04	2,345	23
<b>L2 (S)</b>	30	200	0.35	2,595	352	8.53E-04	1,172	12
Field-testing site #2 on motorway A3								
L6 (W)	3	18,000	0.30	2,515	3,104	9.70E-06	103,465	1,035
L6 (S)	3	2,400	0.30	2,515	1,133	2.65E-05	37,780	378
<b>L5 + L4 (W)</b>	18	17,000	0.30	2,459	3,051	5.90E-05	16,948	169
<b>L5 + L4 (S)</b>	18	1,850	0.30	2,459	1,006	1.79E-04	5,591	56
<b>L3</b>	25	5,000	0.20	2,165	1,602	1.56E-04	6,408	64
Field-testing site #3 on expressway S31								
<b>L5 + L4 (W)</b>	20	17,000	0.30	2,414	3,079	6.50E-05	15,395	154
<b>L5 + L4 (S)</b>	20	1,850	0.30	2,414	1,016	1.97E-04	5,078	51
<b>L3 + L2 (W)</b>	50	915	0.35	2,655	744	6.72E-04	1,487	15
<b>L3 + L2 (S)</b>	50	220	0.35	2,655	365	1.37E-03	729	7

Notes: L2 of A3 is equal to L2 of A10; L6 of S31 is equal to L6 of A3; (W) = Winter; (S) = Summer.

- At the field-testing site #1 on the A10, three accelerometers were installed: at the bottom

of the unbound layer L2, at the interface between L2 and the cement-stabilized layer L3, and at the top of L3, see Fig. 4.2. This allows for in-situ stiffness characterization of layers L2 and L3. The required data acquisition rate required is equal to 77 kHz, see Table 4.4.<sup>1</sup>

- At the field-testing site #2 on the A3, four accelerometers were installed: at the bottom of the unbound layer L2, at the interface between L2 and the lean concrete layer L3, at the interface between L3 and the asphalt base course L4, and at the top of the asphalt binder course L5, see Fig. 4.3. This allows for in-situ stiffness characterization of layers L2 and L3 as well as of the sandwich layer consisting of the asphalt base and binder courses (L4 and L5). The required data acquisition rate required is related to the high stiffness of asphalt exposed to winter temperatures. It is equal to 180 kHz, see Table 4.4.
- At the field-testing site #3 on the S31, three accelerometers were installed: at the bottom of the lower unbound layer L2, at the interface between the upper unbound layer L3 and the asphalt base course L4, and at the top of the asphalt binder course L5, see Fig. 4.3. This allows for in-situ stiffness characterization of two sandwich layers. They consist of the unbound materials (L2 and L3) and of the asphalt base and binder courses (L4 and L5), respectively. The required data acquisition rate is equal to 162 kHz, see Table 4.4.

The USB data acquisition system DEWE-43-A, see Fig. 4.1, with a data acquisition rate of 200 kHz and eight fully synchronized channels complies with the requirements of all three field-testing sites. DEWE-43-A supports voltage and full-bridge signals without additional adapters, as well as IEPE, charge, thermocouples, half-bridge, quarter bridge, RTD, current, resistance, and LVDT signals with the help of DSI adapters. Thus, the DEWE-43-A is capable of simultaneously acquiring data from four strain gauges and four accelerometers. DSI-ACC adapters were required for the powering the IEPE accelerometers with the required directed current. As for the ACC, a BNC adapter RS 124-2521 was used.

#### 4.3.5 Sensor installation

Installing accelerometers at *multiple depths during the construction* of the pavement represented a novel challenge, differing from the installation at a *single depth* and *after* construction as described e.g. in (Arraigada et al., 2007; Levenberg, 2012; Rada et al., 2016; Bahrani et al., 2020). As for the present study, the following two requirements had to be fulfilled:

- the sensors must remain in place and deliver a reliable signal after the installation and compaction of subsequent layers of the pavement structures, and
- the sensors must be aligned along a vertical axis, such that the longitudinal wave, produced by hitting the surface of the completed pavement right above the sensors, propagates downwards along this axis.

The installation of the accelerometers in unbound granular layers (B2 and B3) was conducted as follows, see also Fig. 4.4. The starting level was that of the unbound layers, given that they remained in place during the rehabilitation works on all three field-testing sites. For the installation of the lowest sensors B2 and T2, an excavator was used to reach the boundary between the unbound layer L2 and the subgrade L1. Layer-wise excavation allowed for separating different materials, in order to refill the trenches later with the right excavation materials. In a first step, the excavation reached the boundary between L2 and L3, see Fig. 4.4(a). In a second

<sup>1</sup>As for quantification of the stiffness properties of the concrete and asphalt layers, samples were taken for laboratory testing.

step a smaller trench was created reaching the boundary between L2 and L1, see Fig. 4.4(b). At this level, sensors B2 and T2 were embedded using a quick-setting cement mortar that served two goals: (i) to prevent a displacement of the sensor or a disconnection of the cable, and (ii) to protect the sensor from direct contact with (tips of) large aggregates, since concentrated loads could damage the sensors, see Fig. 4.4(c). The exact horizontal and vertical position of all sensors was determined using a measuring tape and a precision laser, respectively. Two independent permanent reference points were used. The cables from both sensors were placed in a protection tube starting approximately 30 cm away from the sensors. In the next step, the excavation material from layer L2 was reinserted in the smaller trench and the layer was compacted using a vibrating plate, see Fig. 4.4(d). At the interface between L2 and L3, sensors B3 and T3 were installed similarly, see Fig. 4.4(e). Finally, the remaining trench was closed with the excavation material from L3 and compacted. Only in the case of the second field-testing site on the A3 motorway, as described in Section 4.2, new material was inserted, see Fig. 4.4(f).

High-temperature accelerometers were installed at the interfaces between asphalt layers and the cement-stabilized or lean concrete layers (B4 and B6). The procedure is illustrated in Fig. 4.6 and described next. First, openings for the sensors and grooves for the cables were cut in the

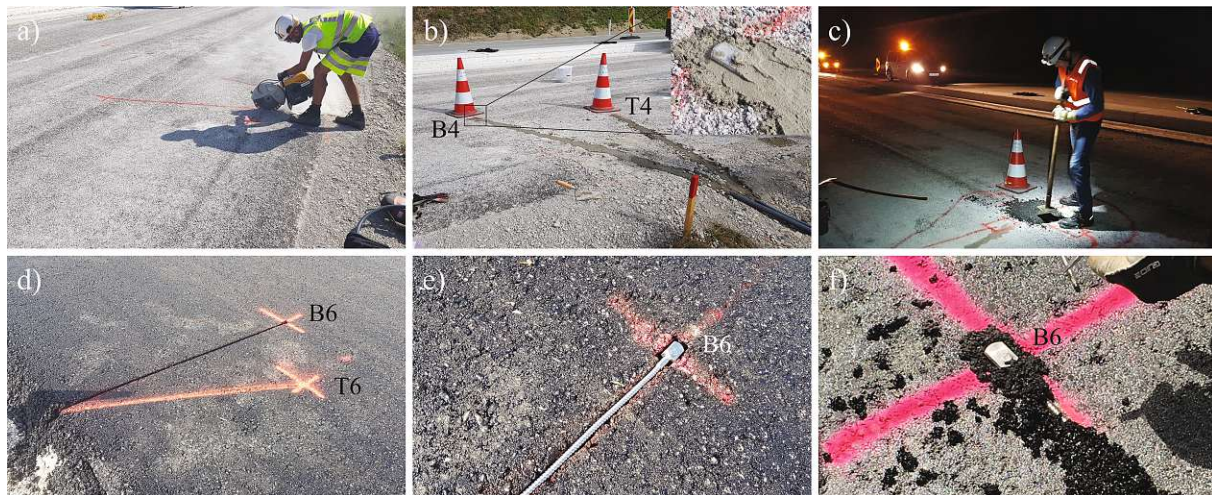


**Fig. 4.6.** Installation of accelerometers on top of the cement-stabilized layer of motorway A10, see (a)-(c), and on top of an asphalt layer of motorway A3, see (d)-(f), respectively: (a) groove cutting for sensors and cables, (b) installation with quick-setting cement mortar, (c) hand compaction of small asphalt sample as protection prior to paving, (d) groove for sensor and cable, (e) placement of accelerometer in the groove, (f) compaction with fine-grained asphalt material.

cement-stabilized or lean concrete, see Fig. 4.6(a) layers. Then, the sensors were fixed and the cables were covered using quick-setting mortar, see Fig. 4.6(b). Right before paving, the sensors were first covered with loose asphalt mixture, followed by careful compaction with a hand tamper, see Fig. 4.6(c). This provided protection to the sensor against high compaction forces, and slightly reduced the temperature of the material in contact with the sensor. Special care was taken so that delivery trucks and, especially, the track chain of the paver did not drive over the positions of the sensors. The plastic tubes protecting the cables were used only outside of the bound layers (starting from the edge of the pavement) in order to minimize potential weak spots and cavities.

For the installation of the accelerometers between two asphalt layers (B6), the opening for the sensor and the groove for the cable were produced *during* the construction of the lower asphalt layer. This was achieved by pushing a steel dummy of the sensor and a steel pipe as

place holders for sensor and the cable into the surface of the freshly placed asphalt, followed by regular compaction with rollers. Later, the dummy and the pipe were removed, and the sensor together with its cable could be simply inserted into the opening and the groove, see Fig. 4.6(d,e). Before the construction of the next layer, a small quantity of loose asphalt was sieved using a standard sieve to obtain material with a grain size smaller than 8 mm. The sieved material was used to fill remaining cavities and to cover the accelerometer with approximately 1 cm of asphalt as a protective measure, see Fig. 4.6(f). Next, unsieved material was piled on the sensors and compacted manually, as shown in Fig. 4.6(c). The new asphalt layer was afterwards paved as usual.

All but two of the installed accelerometers deliver reliable signals under dynamic loads. The exact reason why sensors B2 on the A10 and B6 of the S31 do not work remains unknown. It is speculated that either the sensor, and/or the sensor-cable connection, and/or the cable was/were mechanically damaged during construction.

## 4.4 Installation of the asphalt strain gauges

### 4.4.1 State of the art applications

Asphalt strain gauge have been successfully employed in the context of pavement testing (Elseifi et al., 2009; FDOT, 2011; Rizvi et al., 2017), monitoring of instrumented sections (Pouteau et al., 2016; Duong et al., 2019), studies of stiffness properties of layers (Chun et al., 2015; Cheng et al., 2019), and to compare vehicle loads with FWD tests (Yang et al., 2020). The performance of KM-100HAS and other asphalt strain gauges has been compared in full-scale experiments under controlled loading and temperature conditions (Chenevière et al., 2005). Different installation methods have been studied in a project involving 374 strain gauges which were used to monitor pavements over a period of four years (Seo and Lee, 2012).

### 4.4.2 Sensor selection

KM-100HAS asphalt strain gauges by Tokyo Measuring Instruments were installed, see Fig. 4.1. They have a temperature range from  $-20^{\circ}\text{C}$  to  $+180^{\circ}\text{C}$ , an amplitude range of  $\pm 5000 \mu\text{m/m}$ , and a measurement length of 100 mm. These sensor have reinforcing bars at both ends, see Fig. 4.1. They ensure a firm embedment in asphalt. The used data acquisition system, DEWE-43-A, provides a 5 V ( $350 \Omega$ ) excitation for full bridge sensors. This is larger than the recommended voltage (2 V) but smaller than the allowable bridge excitation for KM-100HAS (10 V).

### 4.4.3 Design of the installation position of the strain gauges

The installation positions of the strain gauges was decided based on the results of linear elastic, static, and radial symmetric finite element (FE) simulations of an FWD experiment on multi-layered pavement structures, performed with ABAQUS (Smith, 2009). For each one of the three field-testing sites, a customized simulation was performed. The elastic properties of the layers were taken from Table 4.4. The imposed FWD forces were set equal to 200 kN for field-testing site #1 and to 150 kN otherwise. Exemplary FE results for the field-testing site #3 (winter-simulation) are shown in terms of the vertical displacements in Fig. 4.7(a), whereby the horizontal and vertical length scales are identical and the magnification factor amounts to 3969.

The essential results from the FE simulations are the radial normal strains of asphalt, as a function of the distance from the center of the falling weight, in the specific depths from the surface of the pavement structures, in which the sensors were installed, see Fig. 4.7(b,c,d). The horizontal distance of the asphalt strain gauges from the center of the falling weight was



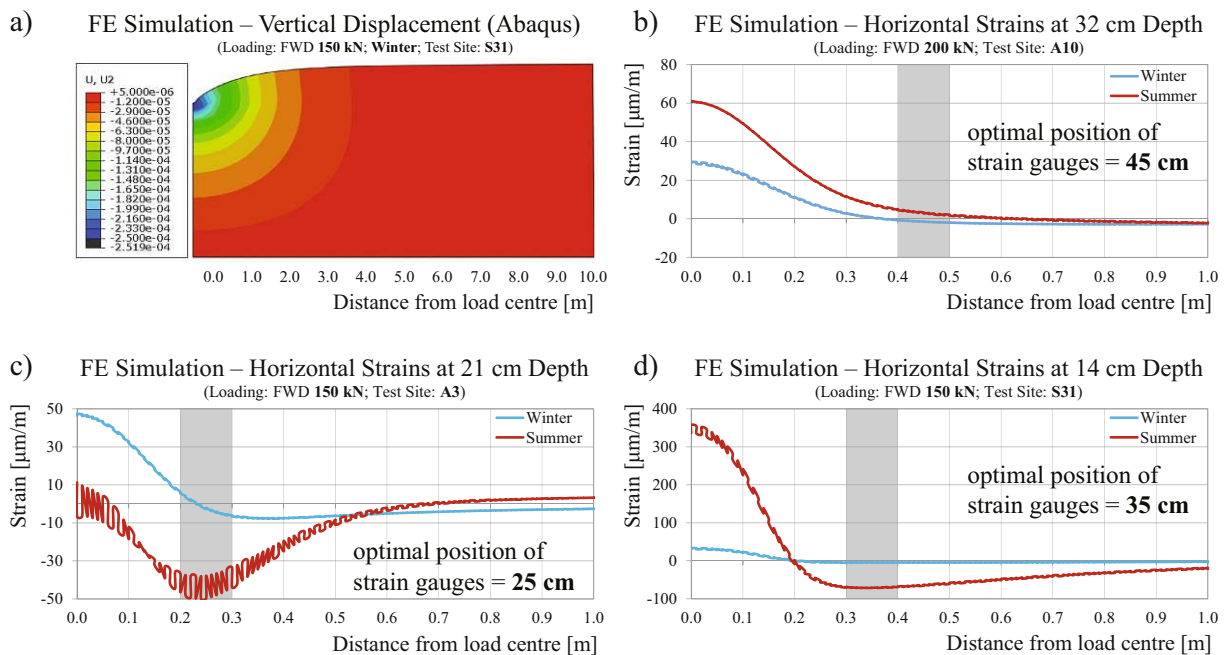


**Fig. 4.7.** Results of radial-symmetric FE simulations providing input for the decision making process regarding the installation positions of the asphalt strain gauges: (a): vertical displacement field of testing site #3 on the S31, as well as radial normal strains as a function of the distance from the center of the falling weight in specific depths of the pavement structures of field-testing sites (b) #1 on the A10, (c) #2 on the A3, and (d) #3 on the S31.

determined based on the following three considerations: (i) the strain shall be sufficiently large to obtain reliable measurements; (ii) the strain gradients at the position of the sensors should be reasonably small, such that the measurements are easy to interpret; and (iii) the difference between the simulated strain during summer and winter should be sufficiently large, such that the measurements will capture seasonal variations. Based on these considerations, it was decided to install the strain gauges in horizontal distance from the center of the falling weight amounting to 45 cm for testing site #2 on the A3, and to 35 cm for testing site #3 on the S31.

#### 4.4.4 Installation method A: Cut, install, and cover after asphalt placement

Installation method A was applied at the field-testing site #1 on the A10, see the schematic overview in Fig. 4.8(a). The installation method is similar to the trench-cut method described in (Seo and Lee, 2012), with the difference that we used the *the same* asphalt mixture to fill the holes which were excavated in order place the sensors (rather than a different material as in (Seo and Lee, 2012)). The installation began immediately after the placement of the asphalt mixture and the first roller pass, see Figs. 4.8 (a)-I and Fig. 4.9 (a). The position of the four strain gauges were marked, see Fig. 4.9 (b). The openings for the sensors and grooves for the cables were excavated using a pickaxe, a geological hammer, and a shovel, see Fig. 4.9(c). These openings reached down to the cement-stabilized layer on top of which the asphalt layer was constructed, Fig. 4.8(a)-II. The manufacturer of the strain gauges recommends to cover the sensors with asphalt having a maximum aggregate size of 5 mm. Therefore, a standard sieve was used to decrease the maximum aggregate size of hot asphalt, directly taken from the auger of the paver, from 16 mm to smaller than 8 mm, see Fig. 4.9(d). Sieving worked best when using a short wooden plank to press the material through the sieve. From the sieved material, 1 cm thick

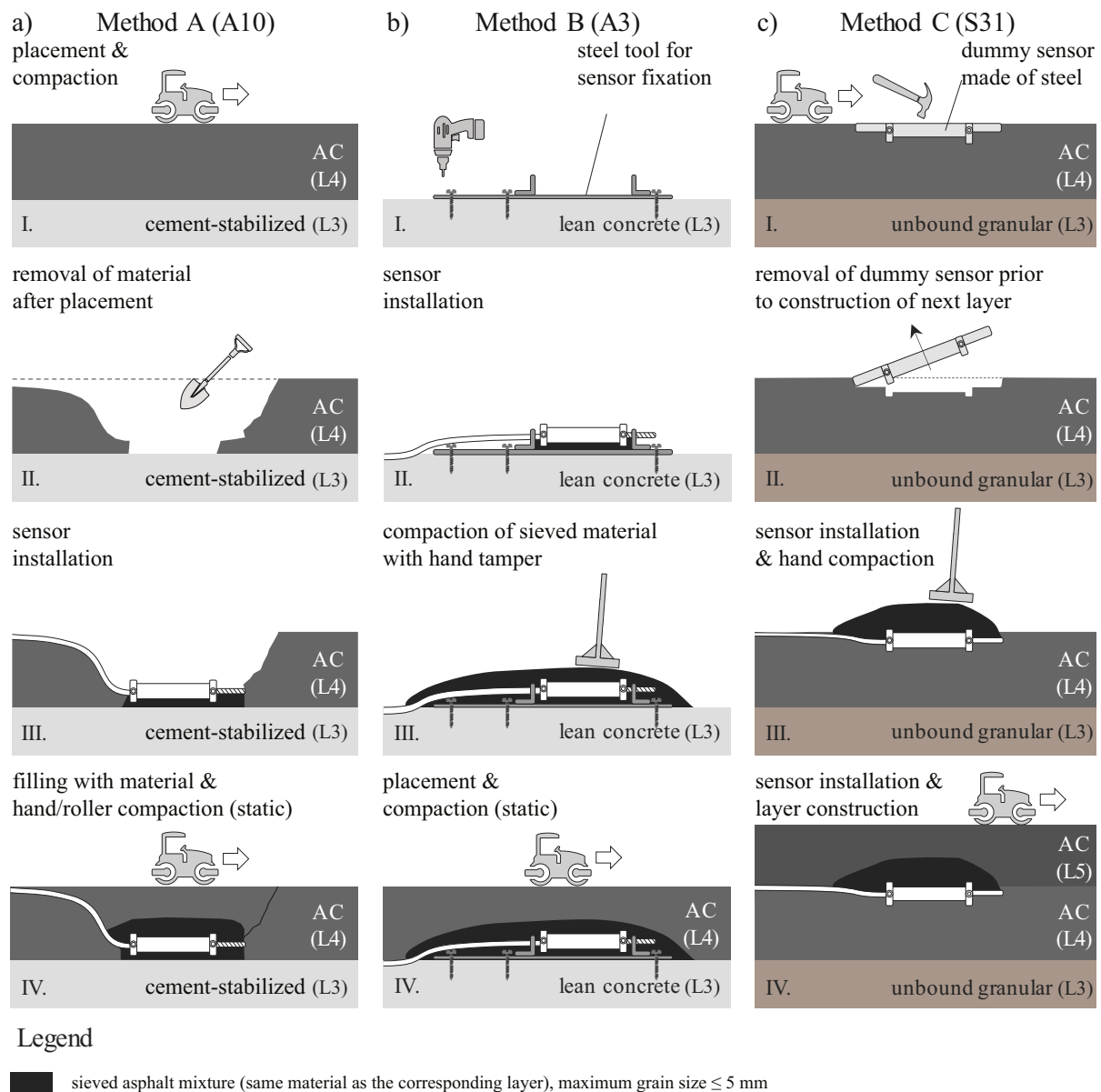


**Fig. 4.8.** Overview of the three methods used for installation of asphalt strain gauges.

asphalt beds were produced, the strain gauges were placed on top, and their vertical position was measured, see Figs. 4.8(a)-II and 4.9(e). The sensors were covered with another 1 cm thick layer of sieved material. Finally, the opening was closed using the regular asphalt with maximum aggregate size of 16 mm. Compaction was started by hand with a tamper and continued with a roller, see Figs. 4.8(a)-IV. In the immediate vicinity of the installed strain gauges, the roller was operated in static rather than in vibrating mode.

The following experience was gained with installation method A. Its main advantages are the position accuracy of the sensors and the low potential for damage during construction. The main disadvantage are problems related to the rather fast cooling of the asphalt. It made the installation process quite stressful, and it got progressively more difficult to work with the material. These problems manifest themselves in visible imperfections regarding the uniformity of the asphalt layer in the region of the field-testing site, see Fig. 4.9(f). While these imperfections are most probably the result of delayed compaction, they are rather unproblematic in the case of



**Fig. 4.9.** Installation of asphalt strain gauges at field-testing site #1 on the A10 using method A: Cut, install, and cover after asphalt placement.

field-testing site #1, since a concrete slab was later placed on top of the asphalt layer. At the field-testing sites #2 and #3, however, the asphalt base course serves a much more important role in the behavior of the pavement structures. Therefore, installation method B was designed and used for field-testing site #2.

#### 4.4.5 Installation method B: Installation in a fixation tool, before asphalt placement

Installation method B was applied at both measuring points of the field-testing site #2 on the A3, see Fig. 4.8(b). The installation method is an extension of the mound method described in (Seo and Lee, 2012). A device was developed and produced to ensure the position stability of the strain gauges during construction, see Fig. 4.10(a). The device consisted of two L-shaped

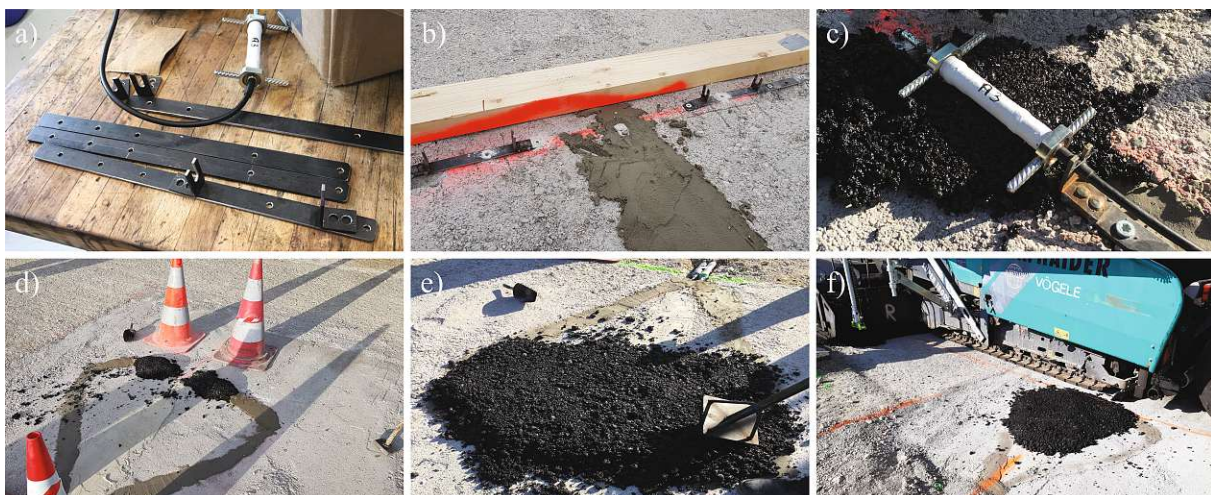


**Fig. 4.10.** Installation of asphalt strain gauges at field-testing site #2 on the A3 using method B: Installation in a fixation tool, before asphalt placement.

metal bars that were fixed to a 30 cm flat stainless steel flat bar. Cuts in the vertical parts of the L-shaped bars ensured that an asphalt strain gauge fitted into the fixation device. The distance

between the two L-shaped bars was designed to be slightly longer than the length of the sensor, leaving room in longitudinal direction for the strain gauge to operate without constraints. The vertical parts of the L-shaped bars had openings for the cable and the axial reinforcing bar of the sensor, respectively. One day before the asphalt paving, the device was screwed onto the underlying lean concrete layer, see Figs. 4.8(b)-I and 4.10(b). Wooden planks were installed temporarily to prevent construction vehicles from accidentally driving over the device. Right before asphalt placement, a 1 cm thick bed made of sieved asphalt (see also Subsection 4.4.4) was placed on the device, and the strain gauge was installed on top of it, see Figs. 4.8(b)-II. The openings of the vertical parts of the L-shaped bars were closed with wire in order to prevent possible vertical movements of the sensors, see Fig. 4.10(c). Thus, the fixation device prevented rigid body motions of the asphalt strain gauge, but in a way which allows the sensor to operate without constraints. The sensors were covered, first with sieved material, see Figs. 4.8(b)-III and 4.10(d), and then with loose asphalt mixture around a larger area in order to protect the sensors from damage associated with laydown and compaction, see Fig. 4.10(e). During the paving process, care was taken to ensure that the construction machines did not drive over the sensors, see Fig. 4.10(f). Roller compaction in the area near the sensors was conducted in static than in vibrating mode, see Fig. 4.8(b)-IV.

The following experience was gained with installation method B. Its main advantage is that the asphalt strain gauges remained in their desired positions during installation and compaction of the asphalt layer. The main disadvantage is that, despite the numerous steps taken to protect the asphalt strain gauges, only two out of four sensors work now that the construction work is finished. Therefore, installation method C was designed and used for field-testing site #3, with the aim to protect strain gauges from damage during compaction.

#### 4.4.6 Installation method C: Use of steel dummy place-holders for the real sensors

Installation method C resembles the installation of accelerometers in asphalt layers, see Subsection 4.3.5 and Fig. 4.8(c). Before installation, steel dummy sensors were produced, see Fig. 4.11(a). They had the same dimensions as the actual strain gauges. The installation method works only

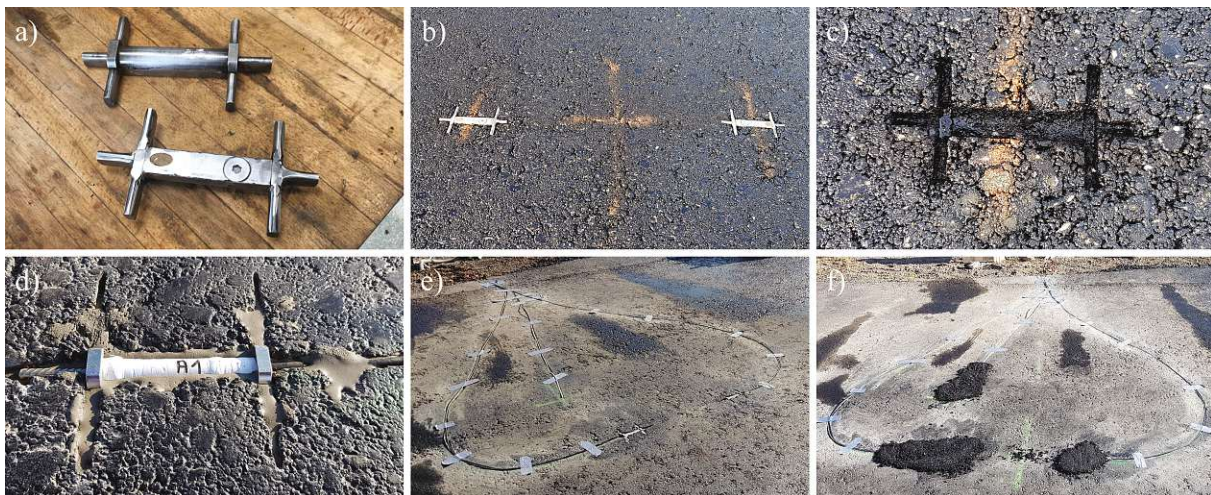


**Fig. 4.11.** Installation of asphalt strain gauges at field-testing site #3 on the S31 using method C: Use of steel dummy place-holders for the real sensors.

if the strain gauges are installed at the top of a freshly built asphalt layer, rather than at the bottom (as done at the field-testing sites #1 and #2). The installation process began right after

the placement of the asphalt base layer, but before its compaction. The steel dummies were hammered into the asphalt at the positions where the strain gauges should be finally located, see Figs. 4.8(c)-I and 4.11(b). Then the rollers compacted the asphalt in vibrating mode, without paying special attention to the steel dummies, see Fig. 4.8(c)-I. One day before placement of the next asphalt layer (= asphalt binder course), the steel dummies were removed, see Figs. 4.8(c)-II and 4.11(c), and grooves for the cables of the sensor were cut into the surface by means of an angle grinder. The sensor were installed, see Fig. 4.11(e), whereby the small gaps to the surrounding asphalt were filled with cement paste in order to ensure firm bond, see Fig. 4.11(d). The strain gauges were covered with sieved asphalt binder course material, followed by manual compaction, see Fig. 4.8(c)-III, in order to protect the sensors from damage associated with laydown and compaction.

The following experience was gained with installation method C. Its main advantage is that the dummy place-holders allow for installing the strain gauges at the intended positions, without exposing the real sensors to overly high loads during compaction. Compaction of the asphalt layer into which the sensors are now embedded did not result in loading of the sensors, because the compaction loads were carried by the dummy place-holders. Compaction of the next asphalt layer on top of the installed sensors did not damage the sensors either, because the sensors did not protrude from the surface onto which the next asphalt layer was constructed, and because compaction of the new layer resulted in considerable strains in this layer, but not in the much cooler layer underneath, in which the sensors are embedded. The main limitation of this method is that it can only be used, at least in the presented form, for installation of strain gauges at the top of an asphalt layer. Both strain gauges installed at field-testing site #3 on the S31 deliver realistic measurements.

## 4.5 First data from dynamic testing at the field-testing sites

### 4.5.1 Results from dynamic field testing on the rigid pavement

Experiments at field-testing site #1 were performed over four days from March 2021 until January 2022. The FWD tests were performed with a maximum force of 200 kN. The number of FWD tests performed immediately one after the other and the corresponding average values of the maximum deflections measured by the geophones and of the maximum strains measured by the asphalt strain gauges are given in Table 4.5. The deflections measured in September,

**Table 4.5**

Experimental results from FWD experiments on field-testing site #1: Average values (from  $n_{FWD}$  tests) of the maximum deflections measured by geophones at different distances from the center of the slab ( $w(r)$ ) and of the maximum strain obtained by the asphalt strain gauges ( $\varepsilon_{ASG}$ ).

Date	$n_{FWD}$	Deflections [mm] measured at a radial distance of:								strain $\varepsilon_{ASG}$ [-]
		$r=0.00$ m	$r=0.30$ m	$r=0.60$ m	$r=0.90$ m	$r=1.20$ m	$r=1.50$ m	$r=1.80$ m	$r=2.10$ m	
Mar 21	23	0.286	0.256	0.225	0.190	0.157	0.124	0.096	0.075	$16.6 \times 10^{-6}$
Sep 21	15	0.176	0.157	0.135	0.115	0.099	0.081	0.068	0.055	$4.9 \times 10^{-6}$
Oct 21	17	0.169	0.150	0.131	0.110	0.092	0.075	0.062	0.052	$4.6 \times 10^{-6}$
Jan 22	12	0.166	0.147	0.129	0.109	0.091	0.076	0.061	0.052	$6.6 \times 10^{-6}$

October, and January are similarly large, while those measured in March are significantly larger. This underlines the challenges associated with the interpretation of FWD test results. Also the measured asphalt strains underline the outstanding nature of the tests performed in March. The

strain measured in spring is equal to  $16.6 \times 10^{-6}$ . This is significantly larger than the strains measured in fall and winter, which range from  $4.6 \times 10^{-6}$  to  $6.6 \times 10^{-6}$ .

The temperatures measured by means of a digital infrared thermometer at the surface of the slab, and by means of the Pt100 sensors inside the pavement structure are listed in Table 4.6. The asphalt temperature amounted to some 6°C in March, some 18°C in September, some 9°C

**Table 4.6**

Experimental results from field-testing site #1: temperature measured at the surface of the slab ( $T_{surf}$ ), the top and mid-depth of the bottom concrete layer ( $T_7$  and  $T_6$  respectively), the interface between concrete and asphalt ( $T_5$ ), the interface between asphalt and the cement-stabilized layer ( $T_4$ ), the interface between the cement-stabilized layer and the unbound layer ( $T_3$ ), and the interface between the unbound layer and the subgrade ( $T_2$ ), see also Fig. 4.2.

Date	$T_{surf}$ [°C]	$T_7$ [°C]	$T_6$ [°C]	$T_5$ [°C]	$T_4$ [°C]	$T_3$ [°C]	$T_2$ [°C]
Mar 21	23.4	18.0	12.2	6.6	5.6	5.2	4.7
Sep 21	20.5	19.2	17.3	17.6	18.2	18.9	18.3
Oct 21	10.5	10.5	8.8	9.0	9.6	11.0	12.7
Jan 22	-0.5	-0.6	-0.7	-0.3	0.1	0.7	1.5

in October, and some 0°C in January, see values of  $T_5$  and  $T_4$  in Table 4.6. It is concluded that stiffness changes of the asphalt layer must have influenced the behavior of the pavement structure. However, the temperature of asphalt alone cannot explain the significant differences of FWD tests performed in March and in the other months.<sup>2</sup> This provides the motivation to discuss, for the results obtained in March, indicators for temperature-induced curling (= partial loss of contact along an interface between two adjacent layers of the pavement structure). This type of slab curling is driven by the temperature difference between the top and the bottom of the slab Yu et al. (1998).

The first indicator for slab curling in March is provided by the temperatures measured across the depth of the concrete slab, see  $T_{surf}$ ,  $T_7$ ,  $T_6$ , and  $T_5$  in Table 4.6. In January, the temperature of the concrete slab was almost uniform. In March, September, and October, the temperature at the top of the concrete slab was larger than that at its bottom, i.e.  $T_{surf} > T_5$ . The corresponding temperature difference,  $T_{surf} - T_5$ , amounted to 16.8°C in March, 2.9°C in September, 1.5°C in October, and -0.2°C in January, see Table 4.6. Thus, the temperature gradient experienced by the concrete slab in March was significantly larger compared to those in the other months.

The second indicator for slab curling in March is provided by the measured asphalt strains. In this context, it is recalled that the readings of the strain gauges were set to zero before the first FWD test of the day. In an FWD test on a curling-free pavement, the structure responds to the dynamic loading with the stiffness of a firmly bonded multilayered half-space. This results in tensile strains at the positions of the asphalt strain gauges, as indicated by strains measured during the curling-free FWD tests performed in September, October, and January. An FWD test on a curled pavement structure can be subdivided into two phases. During the first phase, the curled part of the pavement structure is pushed down until full-face contact is re-established along all interfaces. During the second phase, the pavement structure responds to the continued dynamic loading with the stiffness of a firmly bonded multilayered half-space. Let us consider that loss of contact occurred, in March, in the interface between the asphalt and the cement-stabilized layer, i.e. that the asphalt was well bonded to the concrete slab and curled up together with it. During the first phase of the FWD tests, the sandwich structure consisting of concrete and asphalt layers was pushed from the convexly curved initial configuration down to a

<sup>2</sup>Note that the asphalt temperatures were quite similar in March and October.

plane state. This resulted in a significant tensile strain experienced by the asphalt strain gauges. During the second phase of the FWD tests, the tensile strain increased, similar to the situations in the curling-free FWD tests performed in September, October, and January.

The third indicator for slab curling in March is provided by the results of the sledgehammer tests, see Table 4.7 for the number of tests performed, corresponding results, and the derived values of the modulus of elasticity of the cement-stabilized layer. The tests performed in September, October, and January delivered stiffness moduli in the overlapping intervals from  $9.16 \text{ GPa} \pm 1.24 \text{ GPa}$  to  $7.70 \text{ GPa} \pm 1.62 \text{ GPa}$ . The accelerometer readings recorded in March, in

**Table 4.7**

Experimental results from sledgehammer experiments on field-testing site #1: mean values  $\pm$  standard deviation (from  $n_{slh}$  tests) of the time of flight through the cement-stabilized layer ( $\Delta t$ ), its wave speed ( $v_L$ ), and its modulus of elasticity ( $E$ ), see Table 4.1 for layer thickness  $h = 17.6 \text{ cm}$  and mass density  $\rho = 2568 \text{ kg/m}^3$  as well as Table 4.4 for Poisson's ratio  $\nu = 0.20$ .

Date	$n_{slh}$	$\Delta t$ [ $\mu\text{s}$ ]	$v_L$ [m/s]	$E$ [GPa]
Mar 21	67	—*	—*	—*
Sep 21	49	$89.2 \pm 7.3$	$1973 \pm 161$	$9.16 \pm 1.24$
Oct 21	38	$94.2 \pm 3.9$	$1871 \pm 77$	$8.05 \pm 0.54$
Jan 22	43	$98.3 \pm 9.7$	$1809 \pm 186$	$7.70 \pm 1.62$

\* results affected by curling of the concrete slab

turn, could not be evaluated, because the signal arrived at both acceleration sensors at virtually the same time, see Fig. 4.12(a). In addition, the amplitude of the signals captured in March was

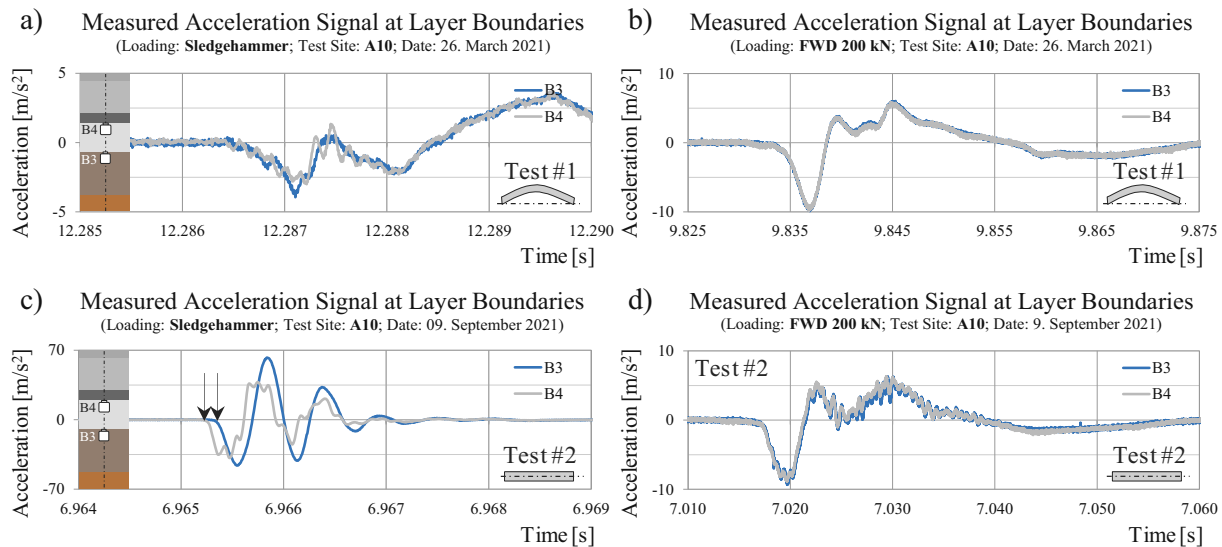


**Fig. 4.12.** Accelerometer readings from dynamic experiments at field-testing site #1 on the A10: (a) and (b) show readings from March 2021 when slab curling occurred; (c) and (d) show readings from September 2021 when full-face contact prevailed at all layer interfaces; (a) and (c) show results from sledgehammer tests; (b) and (d) show results from FWD tests.

one order of magnitude smaller compared to the other months, compare Figs. 4.12(a) and (c). These results can be explained as follows.

The sledgehammer strokes were not strong enough to close the curling-induced gap between the asphalt and the cement-stabilized layer. The front of the longitudinal wave propagating

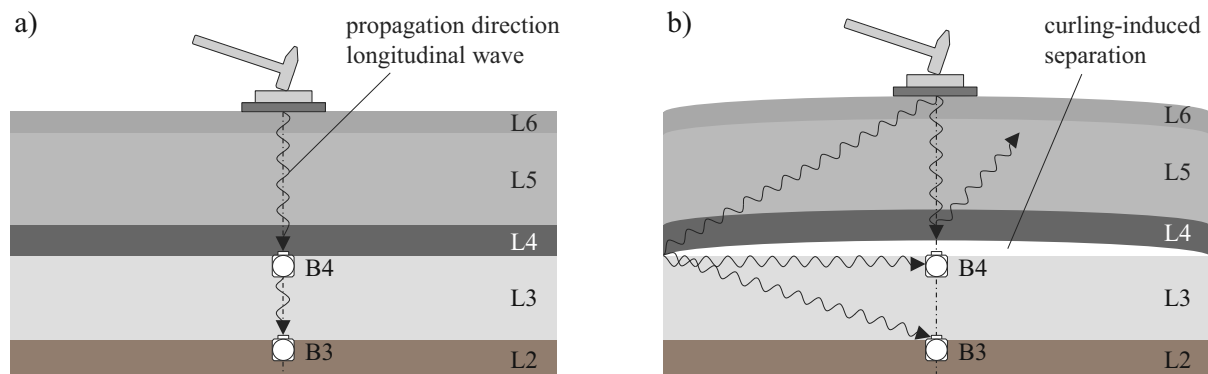


**Fig. 4.13.** Traveling paths of fronts of elastic waves produced with sledgehammer strokes: (a) situation with full-face contact along all layer interfaces, and (b) situation with slab curling.

vertically downwards was reflected at the upper free surface of the separated interface. Therefore, it did not arrive at the accelerometers below. The wave resulting in the first signals of the accelerometers had to travel *around* the separated interface. This wave was initially traveling diagonally downwards, away from the vertical axis through the accelerometers, towards the edge between the separated region and the contact region of the interface. There, the wave had to change direction and continued to propagate diagonally downwards, but this time underneath the separated region and towards the accelerometers, see Fig. 4.13. The effective propagation distances from the hit surface around the separated interface to the two accelerometers were similarly large. This explains why the wavefront arrived virtually at the same time at the two accelerometers, although they are buried at different depths. The change of the traveling direction of the wavefront at the edge of the separated region, in turn, explains why the recorded accelerations were much smaller in March compared to the curling-free cases of the other months.

It is very likely that full-face contact prevailed along all layer interfaces in September, October, and January. Thus, the dynamic wave created by sledgehammer strokes propagated vertically downwards, reaching accelerometer B4 first and accelerometer B3 by some  $95\ \mu\text{s}$  later, see Table 4.7. The difference between the wave arrival times at B4 and B3 could be measured in a straightforward fashion, see Fig. 4.12(c). The accurateness of the results is underlined by the standard deviations of the time of flight, ranging from 4 to  $10\ \mu\text{s}$ , see Table 4.7. This interval is virtually one- to two-times the resolution of the accelerometer readings which were captured with a data acquisition rate of 200 kHz, i.e. every  $5\ \mu\text{s}$ .

The accelerometer readings captured during FWD testing, in turn, do not allow for reliable determination of the time of flight through the cement-stabilized layer, see Fig. 4.12(b) and (d). The reason will be explained in the next subsection where accelerometer readings are available at four rather than two different depths.

#### 4.5.2 Results from dynamic field testing on a flexible pavement

Experiments at measurement point MP2 of field-testing site #2 were performed over two days in July 2021 and April 2022, respectively. The FWD tests were performed with a maximum force of 150 kN. The number of FWD tests performed immediately one after the other and the corresponding average values of the maximum deflections measured by the geophones are given in Table 4.8. The strains gauges did not yield readings because they were damaged during installation. The deflections measured in July and April, respectively, are the same ( $= 0.062\ \text{mm}$ ) in a distance of 2.1 m from the center of the falling weight. This indicates that the subgrade



**Table 4.8**

Experimental results from FWD experiments on field-testing site #2: Average values (from  $n_{FWD}$  tests) of the maximum deflections measured by geophones at different distances from the center of the slab ( $w(r)$ ).

Date	$n_{FWD}$	Deflections [mm] measured at a radial distance of:							
		$r=0.00$ m	$r=0.30$ m	$r=0.60$ m	$r=0.90$ m	$r=1.20$ m	$r=1.50$ m	$r=1.80$ m	$r=2.10$ m
Jul 21	5	0.458	0.239	0.205	0.176	0.140	0.103	0.078	0.062
Apr 22	13	0.256	0.200	0.170	0.145	0.121	0.097	0.076	0.062

and the bottommost layers of the pavement structure had the same stiffness. With increasing proximity to the center of the falling weight, however, the differences between deflections measured in July and April increase both in absolute and in relative terms. At the center of the falling weight, the absolute difference is equal to 0.202 mm, and this equal to 79% of the deflection measured in April. This indicates that the stiffness of the topmost layers of the pavement structure were significantly different in July and April.

The temperatures measured by means of a digital infrared thermometer at the surface of the expressway, and by means of the Pt100 sensors inside the pavement structure are listed in Table 4.9. Both times, the temperature in the lean concrete layer was virtually constant. The

**Table 4.9**

Experimental results from measurement point MP2 of field-testing site #2: temperature measured at the surface of the slab ( $T_{surf}$ ), the interface between surface and binder courses ( $T_6$ ), between binder and base courses ( $T_5$ ), binder course and lean concrete ( $T_4$ ), lean concrete and unbound layer ( $T_3$ ), as well as between unbound layer und subgrade ( $T_2$ ), see Fig. 4.3.

Date	$T_{surf}$ [°C]	$T_6$ [°C]	$T_5$ [°C]	$T_4$ [°C]	$T_3$ [°C]	$T_2$ [°C]
Jul 21	48.7	36.8	31.9	31.4	31.5	30.3
Apr 22	18.8	14.3	12.6	13.2	12.6	11.1

temperature difference across this layer,  $T_4 - T_3$ , was as small as  $-0.1^\circ\text{C}$  in July and  $+0.6^\circ\text{C}$  in April. This underlines that (i) curling of the lean concrete slab is very unlikely, and (ii) the seasonal differences of the measured surface deflections must have a different origin. Averaging the temperatures measured at the top and the bottom of each one of the three asphalt courses, yields  $42.8^\circ\text{C}$  (surface course),  $34.4^\circ\text{C}$  (binder course),  $31.7^\circ\text{C}$  (base course) in July, and  $16.6^\circ\text{C}$  (surface course),  $13.5^\circ\text{C}$  (binder course),  $12.9^\circ\text{C}$  (base course) in April. The seasonal temperature differences have resulted in significant stiffness changes of all three asphalt layers. This provides the motivation to discuss layer stiffnesses quantified from sledgehammer tests.

The number of sledgehammer tests performed, corresponding results, and the derived values of moduli of elasticity are listed in Table 4.10. The values of the thickness, the mass density, and Poisson's ratio of the lean concrete and unbound layers were taken from Tables 4.2 and 4.4. As for asphalt, the measured time of flight refers to a sandwich structure consisting of the binder and base courses, see Fig. 4.3. Its thickness is equal to 17.0 cm, its average mass density to  $2,459\text{ kg/m}^3$ , and its Poisson's ratio to 0.3, see Tables 4.2 and 4.4.

The seasonal difference of stiffness of the sandwich asphalt layer is significantly larger than that of the lean and unbound layers. For all three layers, the determined stiffness was smaller in July than in April. It was by 54% smaller for sandwich asphalt layer, by 6.6% smaller for the lean concrete layer, and by 2.5% smaller for the unbound layer.

Both in July and in April, the accelerometer readings from sledgehammer tests could be

**Table 4.10**

Experimental results from sledgehammer experiments on measurement point MP2 of field-testing site #2: mean values  $\pm$  standard deviation (from  $n_{slh}$  tests) of the time of flight ( $\Delta t$ ), the wave speed ( $v_L$ ), and the modulus of elasticity ( $E$ ).

Date	Layer	$n_{slh}$	$\Delta t$ [ $\mu$ s]	$v_L$ [m/s]	$E$ [GPa]
Jul 21	Asphalt	40	$119.6 \pm 11.8$	$1434 \pm 136$	$3.95 \pm 1.35$
	Lean concrete	40	$156.5 \pm 2.7$	$2109 \pm 36$	$8.67 \pm 0.30$
	Unbound	40	$655.8 \pm 12.3$	$503 \pm 9$	$0.39 \pm 0.01$
Apr 22	Asphalt	47	$93.0 \pm 35.5$	$1997 \pm 473$	$8.63 \pm 1.97$
	Lean concrete	47	$151.4 \pm 3.7$	$2181 \pm 53$	$9.28 \pm 0.45$
	Unbound	47	$643.6 \pm 18.0$	$513 \pm 14$	$0.40 \pm 0.02$

evaluated in a straightforward fashion, in order to compute times of flight, see Fig. 4.14(c), while determination of the time of flight was impossible based on the accelerometer readings from FWD tests, see Fig. 4.14(d). This can be explained as follows. The maximum force of the falling weight is much larger than that of the sledgehammer tests. In order to ensure that the pavement structure is not damaged during dynamic testing, the impact of the falling weight must be damped much more than that of the sledgehammer. The wave front of a sledgehammer test is, therefore, much sharper than that of a FWD test, compare Figs. 4.14(e) and (f).

When comparing the accelerations recorded during the sledgehammer and FWD tests, see Figs. 4.14(c) and (d), the following additional points appear to be interesting:

- The peak accelerations produced by the sledgehammer test near the surface are much larger than those obtained during FWD tests, but decrease much more rapidly with increasing depth. In the exemplary sledgehammer test of Fig. 4.14(c), peak accelerations recorded by the sensor closest to the surface and by the deepest sensor amounted to some  $\pm 400 \text{ m/s}^2$  and some  $\pm 10 \text{ m/s}^2$ , respectively. In the exemplary FWD test of Fig. 4.14(d), in turn, the same sensors recorded peak accelerations of some  $\pm 20 \text{ m/s}^2$  and  $\pm 8 \text{ m/s}^2$ .
- The waves caused by the sledgehammer had a base-frequency of 1 kHz to 2 kHz. This is by two orders of magnitude larger than the base-frequency of the waves caused by the falling weight. It ranges from 0.01 kHz to 0.03 kHz. Note the different scales of the abscissas of Figs. 4.14(c) and (d).

It is concluded that sledgehammer tests are significantly better suited for determination of layer stiffnesses, based on measured times of flight and the theory of elastic wave propagation through isotropic media. In addition, several dozens of sledgehammer tests can be performed with a few minutes, because they can be repeated within seconds. This is very beneficial for the statistical evaluation of the test results.

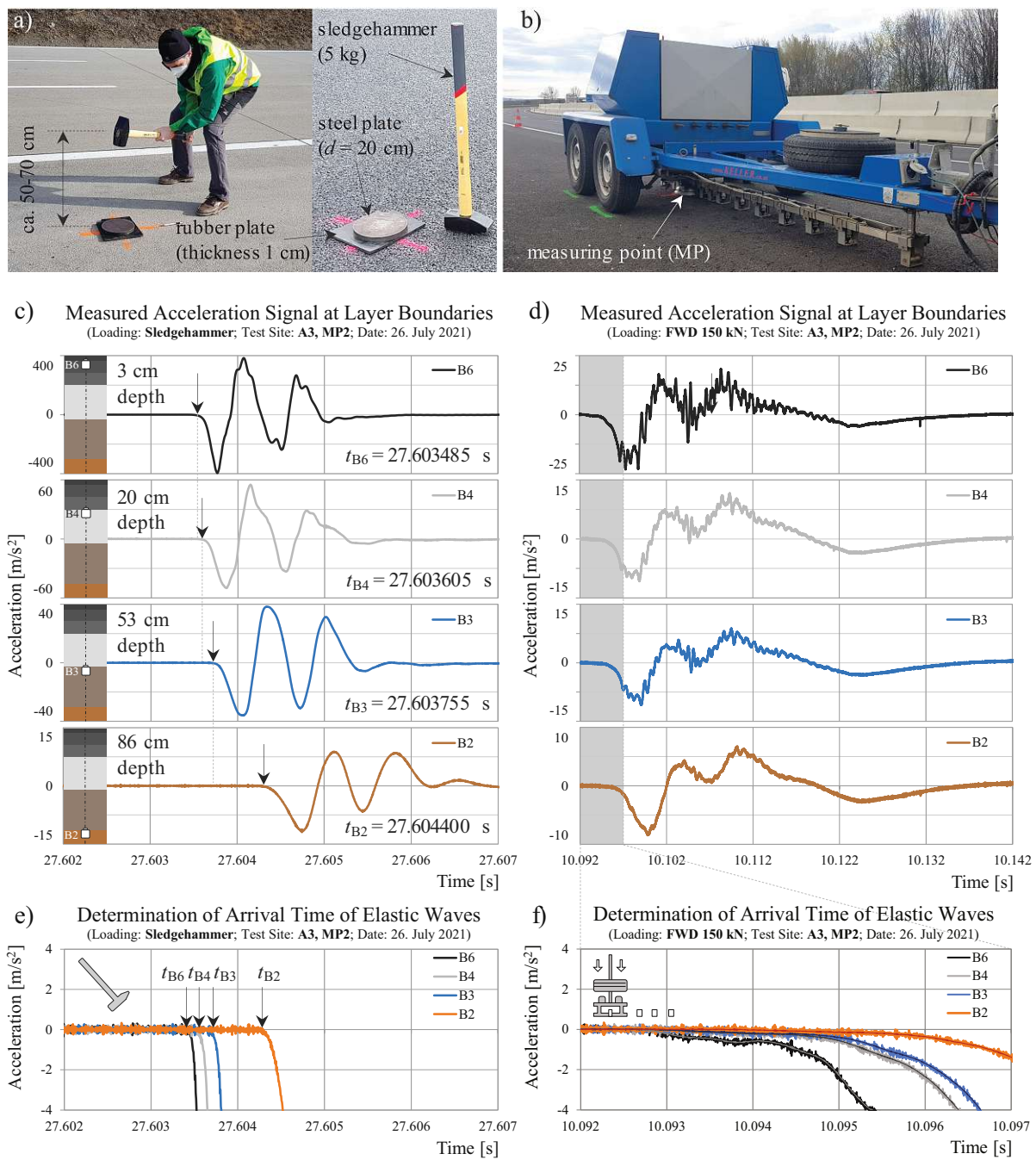


**Fig. 4.14.** Dynamic experiments at measurement point MP2 of field-testing site #2 on the A3: (a), (c), and (e) refer to sledgehammer tests, (b), (d), and (f) refer to FWD tests: (a) and (b) show photos from in-situ testing, (c) and (d) show the accelerations recorded in one test, (e) and (f) show details of the measured accelerations recorded around the arrival of the wave front; the depths of the sensors given in (c) refer to the ones measured in-situ.

## 4.6 Conclusions and future outlook

One rigid and two flexible pavement structures were equipped, during their construction, with temperature sensors, accelerometers, and strain gauges. The following conclusions are drawn from the experience gained with the installation of the sensors:

- The used Pt100 temperature sensors and IEPE accelerometers are suitable for installation in all types of pavement layers. They particularly withstood high temperatures and compaction forces during construction of asphalt layers.
- Sensor overload during hot-state roller compaction of asphalt layers was the main problem encountered with the strain gauges. In order to avoid such problems, it is recommended to install a steel dummy as a place-holder into hot asphalt layers, immediately *after* their construction and right *before* their compaction, to replace the dummy by the actual sensor right before the installation of the next layer, and to fill small gaps between the sensor and the asphalt by cement paste, see Subsection 4.4.6.

The following conclusions are drawn from results of newly proposed sledgehammer tests and FWD experiments performed at the three field-testing sites:

- Strokes with a sledgehammer onto a metal plate, transmitted to the pavement structure via a rubber pad, are well suited for quantification of the time of flight of elastic waves through asphalt, cement-stabilized, and unbound aggregate layers, as long as the individual layers directly underneath the hit surface position are in full-face contact. In such cases, stiffness quantification of individual layers is possible using the theory of propagation of elastic longitudinal waves through isotropic media.
- As regards rigid pavements, sledgehammer tests are capable of detecting curling-induced partial loss of contact of concrete slabs from lower layers by which they are supported. Loss of layer-to-layer contact underneath the falling weight significantly increases measured deflections during FWD testing.
- As regards flexible pavements, seasonal variations of FWD results can be primarily traced back to temperature-induced stiffness variations of asphalt layers. The other unbound and bound layers were found to exhibit significantly smaller stiffness variations.

These conclusions provide motivation for the following future studies:

- Data from field testing together with results from laboratory characterization of the stiffness of bound layers of pavement structures will provide a valuable database for the assessment of software which is designed to back-calculate layer stiffnesses from deflections measured during FWD tests.
- Performing sledgehammer tests and FWD experiments repeatedly at the first field-testing site, during the morning of a day with significant solar heating of the surface of the concrete slab, will allow for studying the evolution of slab curling and its influence on surface deflections measured during FWD testing.

## Funding

This research received financial support by the Österreichische Forschungsförderungsgesellschaft (FFG, Austrian Research Promotion Agency) within the BRIDGE-project “Grundlegende Analyse von FWD-Versuchen: Innovative Experimente, moderne Struktursimulationen, statistische Datenanalyse – FALLINGweight”. The authors are grateful to the Austrian motorway and expressway operator ASFINAG for the support regarding the selection and instrumentation of the field-testing sites as well as for providing traffic control during in-situ measurements. Financial support through the Open Access Funding Programme of TU Wien’s University Library is also gratefully acknowledged.

## Acknowledgements

The authors gratefully acknowledge the help of Mehdi Aminbaghai, Stefan Hofbauer, Wolfgang Dörner, Dominic Hassan, Constantin Kreil, and Michael Haminger (TU Wien, Austria) during the instrumentation of the field-testing sites. Michael Celadnik and Harald Aigner (Nievelt Labor GmbH, Austria) are also acknowledged for conducting FWD measurements and interesting discussions.

## Disclosure Statement

No potential conflict of interest was reported by the authors



## Asphalt-related temperature correction of deflections measured in central FWD tests on a concrete-over-asphalt composite pavement

### 5.1 Introduction

The assessment of the health of pavement structures and the design of rehabilitation measures requires knowledge of the mechanical properties of the pavement layers, with a particular focus on the stiffness of the subgrade. One of the most widely used deflection testing devices for quantification of such mechanical properties is the Falling Weight Deflectometer (FWD). During FWD tests, geophones measure the deflections caused by the impact of a standardized weight that freely falls on the surface of the pavement. The evaluation of FWD tests performed on composite pavements is challenging, because measured deflections are influenced by both the temperature-dependent stiffness of asphalt and seasonal variations of the stiffness of the subgrade. To separate these two contributions is the aim of the present paper. To this end, comprehensive structural field-testing and material laboratory characterisation methods are combined with multi-layered modeling of the composite pavement structure.

Multi-layered models are frequently used for back-calculation of the thickness and the stiffness of every layer to best fit the deflections measured during FWD testing. Such models assume an axisymmetric behavior of the pavement structure. Despite recent challenges to this assumption (Díaz Flores et al., 2021, 2022, 2023), they still constitute the most accurate description of the problem. The theoretical origin of multi-layered models is Boussinesq's theory (Boussinesq, 1885). They were first applied to pavement structures by Burmister (1945a,b). The introduction of layer stiffness matrices was a significant step ahead in the continuous development of these methods (Thomson, 1950; Haskell, 1953; Kausel and Roësset, 1981). Explicit solutions for general surface and dislocation loads acting on a transversely isotropic half-space are available since the late 1980s (Pan, 1989a,b). Much of the recent work refers to the development of modern computational methods to improve the accuracy of the back-calculation, e.g. by using artificial neural networks to obtain elastic (Sharma and Das, 2008; Ghanizadeh et al., 2020; Wang et al., 2021) or viscoelastic properties (Varma and Emin Kutay, 2016; Chatti et al., 2017),

a combination of artificial neural networks with genetic algorithms (Rakesh et al., 2006; Li and Wang, 2019), a hybrid neural network structure (Han et al., 2021), as well as knowledge discovery and data mining (Gopalakrishnan et al., 2013) to obtain the mechanical properties of every layer. Still, despite the remarkable achievements of multi-layered models, their use for back-calculation methods is computationally rather expensive (Chatti et al., 2017). Furthermore, much care and experience is recommended when it comes to the definition of search intervals and to the interpretation of results, as the nature of the mathematical problem is ill-posed (Romeo et al., 2023), i.e. that different sets of thicknesses and stiffnesses reproduce (virtually) the same deflections.

The importance of correcting FWD results for seasonal variations of temperature and moisture and, therefore, for changes of the stiffness of individual layers has been pointed out in (Bohn et al., 1972; Khazanovich et al., 2001). Most corrections have been developed for flexible pavements. Deflections have been adjusted to different temperatures, for instance by developing deflection curves from synthetic databases for temperatures in the asphalt, e.g. between 5°C and 30°C (Bohn et al., 1972), and then adjusting the deflection at each geophone through linear (Chen et al., 2000), quadratic (García and Castro, 2011; Chou et al., 2017; Zheng et al., 2019), and logarithmic (Kim et al., 1995) relations of deflections vs. temperature. Back-calculated moduli have been corrected by making use of the time-temperature superposition principle for the asphalt layers (Park and Kim, 1997; Le et al., 2022), e.g. through correction factors that present a logarithmic relation with temperature (Park et al., 2001). In the case of rigid and concrete-over-asphalt composite pavements, commonly evaluated with the “dense-liquid model” (Westergaard, 1926, 1948; Ioannides, 1990), correction approaches have been mostly focused on the influence of temperature gradients, because the corresponding curling of slabs influences (i) the stresses experienced by the slab and by the subgrade (Ioannides and Khazanovich, 1998; Schmid et al., 2022), (ii) the load transfer efficiency of the joints (Shoukry et al., 2005; Vandenbossche, 2007; Muslim et al., 2021), and (iii) the accuracy of the back-calculation (Khazanovich et al., 2001). Few recommendations have been given regarding the correction of seasonal variations of the properties of individual layers. Concrete-over-asphalt structures were idealized as a thin composite plate with either a bonded or an unbonded interface between the two layers (Khazanovich et al., 2001). A modular ratio was prescribed, defined as the ratio between the moduli of the asphalt and the concrete layers (Ioannides and Khazanovich, 1994; Smith et al., 2017a). The back-calculated moduli are significantly influenced by the choice of the modular ratio (Smith et al., 2017a), and identification of a realistic ratio is difficult. Furthermore, if the thickness of the asphalt layer is so large that the assumptions used in the theory of thin plates become unrealistic, less accurate results will be obtained (Khazanovich et al., 2001; Smith et al., 2017a), especially when dealing with hot temperatures that cause the stiffness of asphalt to decrease significantly.

This study contains two main innovations: (i) A multi-layered model is used to simulate the results of five FWD tests performed (in summer, winter, and transitional periods) on an innovatively-equipped slab of a concrete-over-asphalt composite pavement structure (Donev et al., 2023). The field-testing site is equipped with temperature sensors, acceleration sensors, and asphalt strain gauges (Donev et al., 2023). Laboratory and in situ characterisation provides access to the constant, temperature-dependent, and seasonally varying stiffnesses of concrete, asphalt, and a cement-stabilized granular material, respectively. Only two unknowns are left for back-calculation: the constant thickness and the seasonally varying stiffness of the subgrade. (ii) In order to separate the influence of the temperature-dependent stiffness of asphalt on the deflections measured during FWD testing, a temperature-correction approach is developed. It allows for translating deflections measured at any temperature of asphalt into deflections which refer to an asphalt temperature of 20°C. The corrected deflections still contain the influence of the seasonal changes of the stiffness of the subgrade. This provides the motivation to use



corrected deflections in order to compute  $k$ -values of the dense-liquid model by means of the AREA method. In order to assess the quality of the temperature corrections approach, it will be checked whether or not the seasonally varying  $k$ -values correlate with the seasonally varying elastic stiffness moduli of the subgrade. Finally, an alternative correction approach will be proposed, which does not require more information than just measured deflections.

The paper is structured as follows. Section 5.2 presents experimental data from structural testing at the field testing site and from material testing of concrete and asphalt performed in the laboratory. Section 5.3 refers to the multi-layered elastostatic simulations of the pavement structure. They are used (i) to back-calculate properties of the subgrade, and (ii) for the development of the asphalt-related temperature correction of measured deflections.  $k$ -values of the dense-liquid model are quantified from corrected deflections, and the correlation of these  $k$ -values with elastic moduli of the subgrade is demonstrated. Section 5.4 contains the alternative correction approach which does not require more information than just measured deflections. Finally, in Section 5.5, conclusions are drawn.

## 5.2 In situ and laboratory characterisation of the temperature-dependent stiffness of a composite pavement and its layers

### 5.2.1 Field-testing site equipped with temperature sensors, strain gauges, and accelerometers (Donev et al., 2023)

Field data were measured at an innovatively-equipped field-testing site on the motorway A10, south of Salzburg (Donev et al., 2023). The concrete-over-asphalt composite pavement structure consists of six layers. The top concrete (index = tc) layer has a thickness  $h_{tc} = 5.0$  cm, see Fig. 5.1. It rests on a bottom concrete (bc) layer,  $h_{bc} = 22.0$  cm, an asphalt (a) layer,  $h_a = 8.2$  cm, a cement-

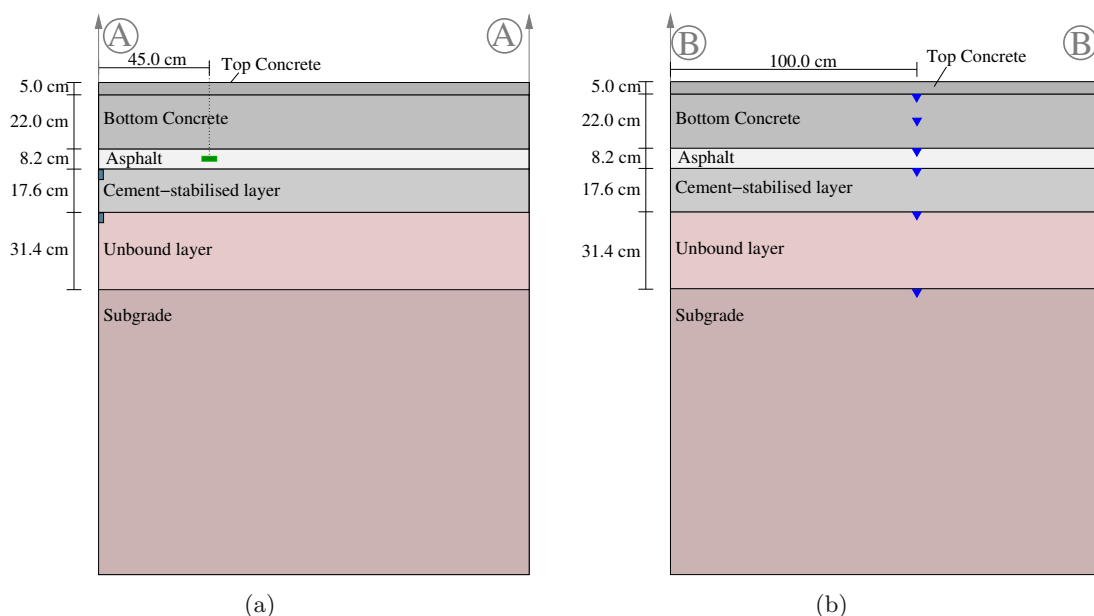


**Fig. 5.1.** Cross-section of the investigated pavement structure and positions of (a) the accelerometers (light-blue rectangles) and asphalt strain gauges (green lines), and (b) the temperature sensors (dark-blue triangles).

stabilized (cs) granular layer,  $h_{cs} = 17.6$  cm, an unbound (ub) granular layer,  $h_{ub} = 31.4$  cm, and

the local subgrade (sb).

One concrete slab of the emergency lane is equipped with temperature sensors, asphalt strain gauges, and accelerometers.

- Six Pt100 temperature sensors are positioned along a vertical axis, see the dark-blue triangles in Fig. 5.1(b). This axis has an in-plane distance from the center of the slab, which amounts to 1.40 m in driving direction and to 1.00 m in lateral direction, see Fig. 5.2. This eccentric arrangement minimizes the influence of the sensors on the structural behavior of the pavement structure when subjected to dynamic loading. Five Pt100 sensors are installed at the interfaces between neighboring layers, while the sixth sensor is located at mid-depth of the bottom concrete layer, see Fig. 5.1(b). The temperature at the surface of the pavement was measured by means of a digital infrared thermometer.
- Four KM-100HAS strain gauges by Tokyo Measuring Instruments are installed at the bottom of the asphalt layer, at a depth of 33.0 cm and a radial distance of 45.0 cm from the center of the slab, in symmetric crosswise arrangement, see the green lines in Figs. 5.1(a) and 5.2. The right strain gauge was damaged during installation. Measurements from the remaining three sensors will be analyzed in the present study.
- Two acceleration sensors are installed, one each at the top and at the bottom of the cement-stabilized granular layer, at depths of 35.2 cm and 50.8 cm, respectively, see the light-blue rectangles at the left boundary of Fig. 5.1(a).

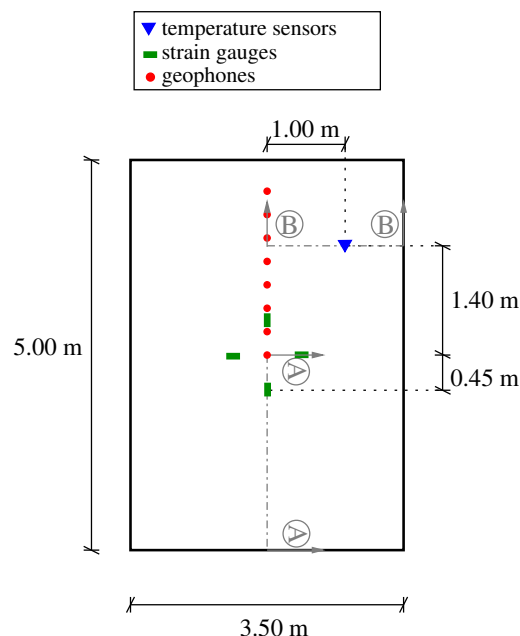


**Fig. 5.2.** Top view of the investigated slab and positions of the temperature sensors (dark-blue triangles), the asphalt strain gauges (green lines), and the geophones (red dots).

The length and width of the instrumented slab amount to 5.00 m and 3.50 m, respectively, see Fig. 5.2.

### 5.2.2 In situ stiffness characterisation of the composite pavement structure by means of FWD testing

FWD tests were performed at the field-testing site over five days from July 2021 until March 2022. The measured temperatures are representative for summer (Jul and Sep), winter (Jan), and the transitional period (Oct and Mar), see Table 5.1.

**Table 5.1**

Temperatures measured at the field testing site on five FWD testing days: at the surface ( $T_{top-tc}$ ), at mid-depth of the bottom concrete layer ( $T_{mid-bc}$ ), and at the interfaces between neighboring layers, e.g.  $T_{tc-bc}$  denotes the temperature at the interface between the top concrete (tc) and the bottom concrete (bc) layers, see also Fig. 5.1(b).

Date	$T_{top-tc}$ [°C]	$T_{tc-bc}$ [°C]	$T_{mid-bc}$ [°C]	$T_{bc-a}$ [°C]	$T_{a-cs}$ [°C]	$T_{cs-ub}$ [°C]	$T_{ub-sb}$ [°C]
Jul 21	25.5	24.7	22.4	22.1	22.4	21.1	19.6
Sep 21	20.5	19.2	17.3	17.6	18.2	18.9	18.3
Oct 21	10.5	10.5	8.8	9.0	9.6	11.0	12.7
Jan 22	-0.5	-0.6	-0.7	-0.3	0.1	0.7	1.5
Mar 22	8.5	8.7	8.5	9.2	9.7	9.8	8.4

tc = top concrete, bc = bottom concrete, a = asphalt, cs = cement-stabilized layer, ub = unbound layer, sb = subgrade

All FWD tests were performed with a maximum force of 200 kN. The number of FWD tests performed immediately one after the other, and the corresponding average values of the maximum deflections measured by the eight geophones as well as of the maximum strains measured by the three functional asphalt strain gauges are listed in Table 5.2. The measured deflections show

**Table 5.2**

Measurements from FWD experiments on the field-testing site, performed on five days: Average values (from  $n_{FWD}$  tests) of the maximum deflections measured by geophones at radial distances from the center of the slab, ranging from 0 to 2.1 m, and of the maximum strain obtained by the asphalt strain gauges ( $\varepsilon_{ASG}$ ).

Date	$n_{FWD}$	Deflections [mm] measured at a radial distance of:								$\varepsilon_{ASG}$ [ $10^{-6}$ ]
		$r_1=0.0$ m	$r_2=0.3$ m	$r_3=0.6$ m	$r_4=0.9$ m	$r_5=1.2$ m	$r_6=1.5$ m	$r_7=1.8$ m	$r_8=2.1$ m	
$t_1 =$ Jul 21	15	0.186	0.167	0.144	0.122	0.103	0.086	0.072	0.061	5.20
$t_2 =$ Sep 21	15	0.176	0.157	0.135	0.115	0.099	0.081	0.068	0.055	4.94
$t_3 =$ Oct 21	15	0.169	0.150	0.131	0.110	0.092	0.075	0.062	0.052	4.64
$t_4 =$ Jan 22	12	0.166	0.147	0.129	0.109	0.091	0.076	0.061	0.052	6.58
$t_5 =$ Mar 22	12	0.171	0.152	0.130	0.109	0.095	0.076	0.066	0.052	5.85

a considerable seasonal variation. The largest deflections were measured on the hottest FWD testing day in July 2021. They are by some 12% larger than the smallest deflections, which were recorded on the coldest field-testing day in January 2022. As regards days with similar temperature profiles, see October 2021 and March 2022, similar deflections (with difference of up to 3  $\mu\text{m}$  only) were measured. The measured strains range from  $4.64 \times 10^{-6}$  to  $6.58 \times 10^{-6}$  and show a less clear trend with temperature. The largest strain was measured in January 2022, when icy conditions prevailed in the depth of the asphalt layer. These conditions may have affected the experimental results.

### 5.2.3 Laboratory stiffness characterisation of concrete by means of uniaxial compression tests

The stiffnesses of the top and bottom concrete layers were quantified in the laboratory. Three cylindrical specimens and three cubic specimens of each of the two types of concrete were cast in situ from the same batches that were used to produce the slab. The cubic specimens had a side length of 0.15 m. The cylindrical specimens had a diameter of 0.07 m and a height of 0.34 m. They cured, sealed inside their molds, until testing at an age of 30 weeks.

The strength of each of the two concretes was determined by subjecting the cubic specimens to destructive uniaxial compression tests with a stress rate of 1 MPa/s. The cube compressive strength of the top and bottom concrete layer amounted to 65.4 MPa and 59.7 MPa, respectively, see Table 5.3.

**Table 5.3**

Cube compressive strength and unloading modulus of the top and bottom concrete.

Property	Top concrete	Bottom concrete
Cube compressive strength [MPa]	65.4	59.7
Unloading modulus [GPa]	34.1	46.3

The stiffness of each of the two concretes was determined by subjecting three cylindrical specimens to a series of nondestructive loading and unloading cycles, see also (Karte et al., 2015; Irfan-ul Hassan et al., 2016). Six loading-unloading cycles were performed for each specimen, three with a loading rate of 1 kN/s, and three with a loading rate of 20 kN/s. The maximum load was held constant for 10 s before the unloading began with the same speed as used for the loading. In order to avoid damage of the specimens, the maximum load was limited to 15% of the cube compressive strength. The unloading modulus was quantified as the secant modulus in the unloading branch between 20% and 80% of the maximum load. The average of the 18 unloading moduli (six cycles and three specimens) amounted to 34.1 GPa for the concrete of the top layer and to 46.3 GPa for the concrete of the bottom layer, see Table 5.3.

All tests were performed at 20°C. The elastic modulus of cementitious materials remains virtually constant in the temperature range from 0 to 25°C (Vidal et al., 2015; Binder et al., 2023). During field-testing, the temperature of concrete ranged in this interval, see Table 5.1. Therefore, temperature-independent stiffness properties of concrete will be assumed throughout the rest of this study.

### 5.2.4 Laboratory stiffness characterisation of asphalt by means of cyclic uniaxial tension-compression tests

The viscoelastic properties of the asphalt were determined in the laboratory. Cylindrical specimens with height  $h = 0.20$  m and diameter  $d = 0.05$  m were manufactured using the asphalt that was placed in situ. At temperatures  $T \in \{-10, -2.5, 2.5, 5, 10, 20, 30\}$  °C, the specimens were subjected to sinusoidal uniaxial tension-compression cycles imposed with frequencies  $f \in \{0.1, 1, 3, 5, 8, 10\}$  Hz.

Dynamic Mechanical Analysis (Planche et al., 1998; Chehab et al., 2002) is used for the evaluation of the test results. In the context of displacement-driven testing, sinusoidal strain histories were prescribed as a function of time  $t$ :

$$\varepsilon(t) = \varepsilon_0 \sin(\omega t), \quad (5.1)$$

where  $\varepsilon_0 = 95 \times 10^{-6}$  denotes the strain amplitude and  $\omega = 2\pi f$  the angular frequency. The measured stress histories are approximated as sinusoidal evolutions by optimizing the stress amplitude  $\sigma_0$  and phase lag  $\delta$ :

$$\sigma(t) = \sigma_0 \sin(\omega t + \varphi). \quad (5.2)$$

Known values of the phase-lag and the stress/strain amplitudes allow for computing the storage modulus  $E'_a$  and the loss modulus  $E''_a$  as

$$E'_a = \frac{\sigma_0}{\varepsilon_0} \cos \varphi, \quad (5.3)$$

$$E''_a = \frac{\sigma_0}{\varepsilon_0} \sin \varphi,$$

see also Fig. 5.3(a). Notably,  $E'_a$  is associated with the elastic response of the material, and  $E''_a$  with its viscous response. Both of them are used to quantify the complex modulus,  $E_a^*$ , which is defined as

$$E_a^* = E'_a + i E''_a, \quad (5.4)$$

where  $i$  denotes the imaginary unit. The norm of  $E_a^*$  is also referred to as “dynamic modulus”, see Fig. 5.3(b).

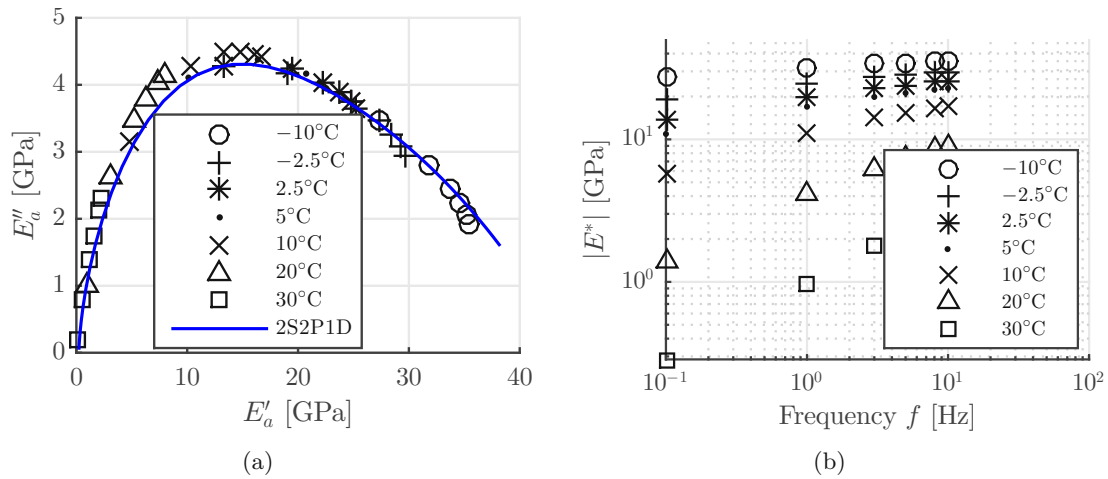


**Fig. 5.3.** Results of Dynamic Mechanical Analysis: (a) loss modulus  $E''_a$  over storage modulus  $E'_a$  (“Cole-Cole diagram”), the solid line represents the 2S2P1D model of Eq. (5.7), and (b) dynamic modulus,  $|E_a^*|$ , as a function of test frequency and temperature.

The time-temperature superposition principle (Williams et al., 1955; Ferry, 1980) is used for quantification of the dynamic modulus at temperatures and frequencies beyond the tested ones. The temperature- and frequency-dependent dynamic moduli,  $|E_a^*|(T, \omega)$ , are plotted in a double logarithmic diagram as a function of the angular frequency. All data points referring to the same testing temperature are shifted along the abscissa, such as to obtain a chain of data points which can be approximated by a master curve, see Fig. 5.4(a). The latter is associated with a reference temperature, here:  $T_0 = 20^\circ\text{C}$ . Mathematically, this is expressed as

$$|E_a^*|(T, \omega) = |E_a^*|(T_0, \omega_r), \quad (5.5)$$

where  $\omega_r = \alpha_T \omega$  denotes the “reduced” angular frequency, with  $\alpha_T$  standing for the shift factor, which is a non-linear function of temperature, see Fig. 5.4(b). The relation between the shift

factor and the temperature is fitted using the Williams-Landel-Ferry equation (Williams et al., 1955):

$$\log(\alpha_T) = -\frac{C_1(T - T_0)}{C_2 + (T - T_0)}, \quad (5.6)$$

where  $C_1 = 26.1$  and  $C_2 = 181.3^\circ\text{C}$  are optimal parameters for the here-investigated asphalt, see Fig. 5.4(b).

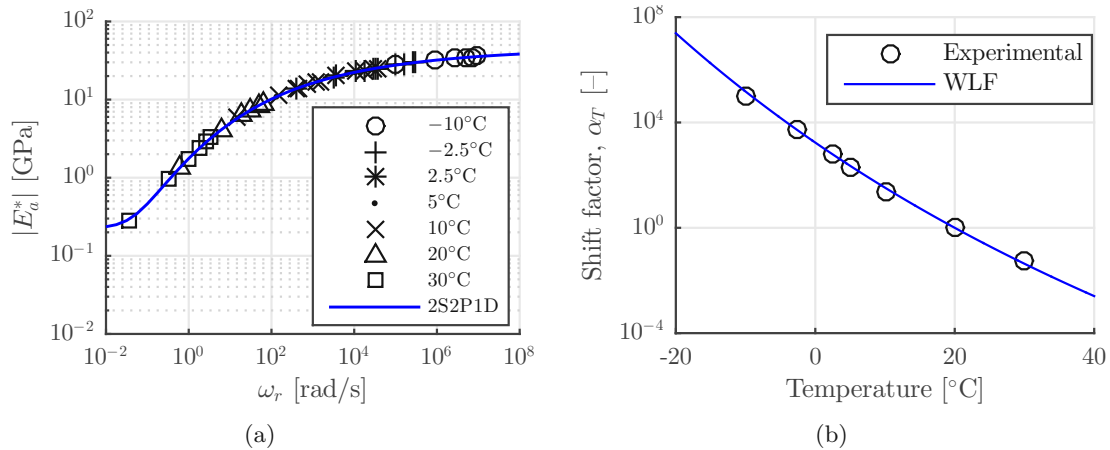


**Fig. 5.4.** Viscoelastic properties of asphalt: (a) master curve for the dynamic modulus,  $|E_a^*|$ , as a function of the “reduced” angular frequency  $\omega_r = \alpha_T \omega$ , and (b) horizontal shift factor,  $\alpha_T$ , approximated by the Williams-Landel-Ferry equation (5.6).

In order to express the complex moduli as a continuous function of the reduced frequency, the rheological model 2S2P1D is used (Olard and Di Benedetto, 2003; Di Benedetto et al., 2004). Introducing two springs, two parabolic dashpots, and one linear dashpot, the mathematical formulation of the model reads as

$$E_a^*(\omega_r) = E_0 + \frac{E_\infty - E_0}{1 + \delta(i\omega_r \tau_0)^{-k} + (i\omega_r \tau_0)^{-h} + (i\beta\omega_r \tau_0)^{-1}}. \quad (5.7)$$

Eq. (5.7) contains seven fitting parameters.  $E_0$  is the static modulus. It is the limit case of  $E_a^*$  when  $\omega_r$  tends to zero.  $E_\infty$  is the glassy modulus. It is the limit case of  $E_a^*$  when  $\omega_r$  tends to infinity.  $k$  and  $h$  are exponents with numerical values between zero and one,  $\delta$  and  $\beta$  are constants, and  $\tau_0$  is a characteristic time referring to the reference temperature. These parameters are optimized (see Table 5.4) such as to reproduce the shifted data points, see the solid line in Fig. 5.4(a).

**Table 5.4**

Parameters of the 2S2P1D model (Olard and Di Benedetto, 2003; Di Benedetto et al., 2004) and the Williams-Landel-Ferry equation used in this study.

$E_0$ [MPa]	$E_\infty$ [MPa]	$\delta$ [-]	$h$ [-]	$k$ [-]	$\tau_0$ [s]	$\beta$ [-]	$C_1$ [-]	$C_2$ [-]
225.2	44480	1.843	0.5174	0.1837	0.004544	26.48	26.1	181.3

16.7 Hz is the characteristic frequency of the dynamic load resulting from a falling weight in an FWD test, see e.g. (Ullidtz and Stubstad, 1985; Zhang et al., 2022; Fu et al., 2020; Tutumluer et al., 2009; Díaz Flores et al., 2021; Roesset and Shao, 1985). The temperature-dependent

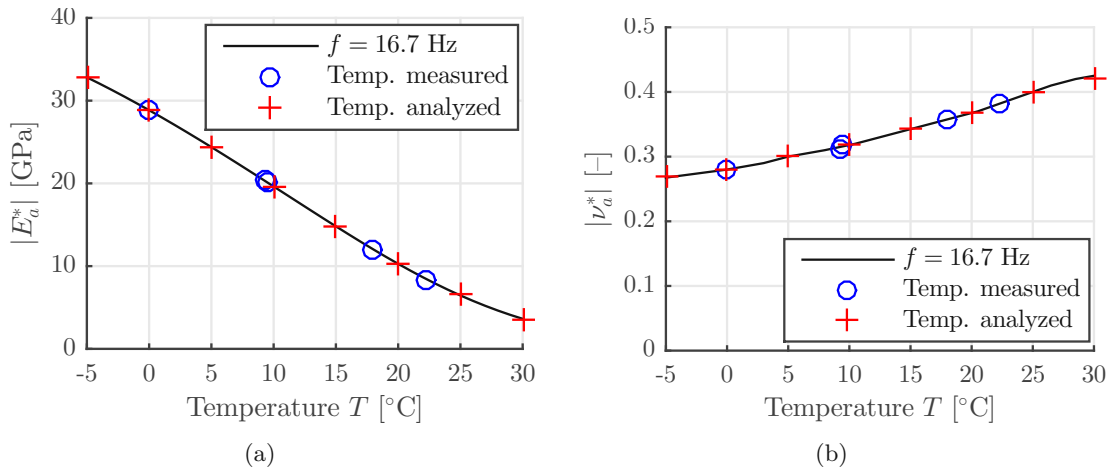


**Fig. 5.5.** Temperature-dependent stiffness properties of asphalt at the FWD frequency of  $f = 16.7$  Hz: (a) the dynamic modulus, as obtained from direct tension-compression tests,  $|E_a^*|$ , and (b) the norm of complex Poisson's ratio, which is set equal to the mean of the results suggested in (Nguyen et al., 2021; Graziani et al., 2014; Gudmarsson et al., 2014; Islam et al., 2015),  $|\nu_a^*|$ ; the solid line refers to the model, the circles to temperatures of asphalt measured during FWD testing, and the crosses to temperatures of asphalt considered during structural analysis.

dynamic modulus at 16.7 Hz is used as the elastic modulus of asphalt, required for elastostatic analysis of FWD tests, see Fig. 5.5(a).

Poisson's ratio of asphalt is also temperature- and frequency-dependent (Benedetto et al., 2007; Gudmarsson et al., 2015), rather than being constant (Aurangzeb et al., 2017; Lee and Kim, 2009). In order to account for the influence of temperature, we use average values suggested in four studies, see (Graziani et al., 2014; Gudmarsson et al., 2014; Nguyen et al., 2021; Islam et al., 2015) and Fig. 5.5(b).

### 5.2.5 In situ stiffness characterisation of the cement-stabilized layer by means of accelerometer measurements recorded during sledgehammer tests

The stiffness of the cement-stabilized layer was quantified based on “sledgehammer tests” performed at the center of the instrumented slab (Donev et al., 2023). A rubber pad was put at the surface of the slab to ensure that it remained undamaged during the sledgehammer tests. A metal plate was put on top of the pad and hit by a sledgehammer to generate an elastic wave. The accelerometers described in Section 3.4 collected readings with a sampling rate of 200 kHz. Their signals are used to determine the time of arrival of the elastic wave both at the top and the bottom of the cement-stabilized layer. The time of arrival at each sensor is set equal to the time at which the first acceleration measurement is recorded outside the interval of white noise of the sensor. The difference of the two arrival times is equal to the time of flight,  $\Delta t$ , of the wave through the layer. Dividing the thickness of the layer (17.6 cm) by the time of flight delivers the speed  $v_L$  of the elastic wave. Using the theory of propagation of waves through elastic media, see e.g. (Biot, 1956; Bedford and Drumheller, 1994), the elastic modulus of the cement-stabilized layer is quantified as

$$E_{cs} = \rho_{cs} v_L^2 \frac{(1 + \nu_{cs})(1 - 2\nu_{cs})}{1 - \nu_{cs}}, \quad (5.8)$$

where  $\nu_{cs} = 0.20$  is the value of Poisson's ratio assigned to the cement-stabilized layer. Its mass density  $\rho_{cs}$  was determined in situ by excavating a hole, and by dividing the excavated mass (measured by means of a scale) by the volume of the hole. The volume was determined by laying a thin sheet of plastic into the hole, pouring water into it until the hole was filled, and then measuring the volume of water with a graduated cylinder. This process was performed three times, resulting in a mean mass density  $\rho_{cs} = 2568 \text{ kg/m}^3$ .

Since one sledgehammer test takes a few seconds only, several dozens of tests were performed every time shortly before an FWD test was carried out, see Table 5.5. The resulting database of times of flight, wave speeds, and stiffness moduli was evaluated statistically, see the mean values and standard deviations listed in Table 5.5. The elastic moduli determined from five sets of measurements, carried out between July 2021 and March 2022, range from 7.7 to 9.2 GPa. This underlines a satisfactory degree of test repeatability and an only moderate seasonal (temperature and moisture) dependence.

**Table 5.5**

Results from  $n_{slh}$  sledgehammer tests performed on the instrumented slab:  $\Delta t$  denotes the time of flight through the cement-stabilized layer,  $v_L$  the speed of the wave passing through that layer, and  $E_{cs}$  its modulus of elasticity.

Date	$n_{slh}$	$\Delta t$ [ $\mu\text{s}$ ]	$v_L$ [m/s]	$E_{cs}$ [GPa]
Jul 21	51	$91.2 \pm 7.3$	$1942 \pm 150$	$8.74 \pm 1.21$
Sep 21	49	$89.2 \pm 7.3$	$1973 \pm 161$	$9.16 \pm 1.24$
Oct 21	38	$94.2 \pm 3.9$	$1871 \pm 77$	$8.05 \pm 0.54$
Jan 22	50	$94.5 \pm 4.7$	$1862 \pm 93$	$8.08 \pm 0.80$
Mar 22	43	$98.3 \pm 9.7$	$1809 \pm 186$	$7.70 \pm 1.62$

## 5.3 Elastostatic simulations of the multi-layered pavement structure allowing for the derivation of an asphalt-related temperature correction of deflections measured during FWD testing

### 5.3.1 Multi-layered simulations: a boundary value problem

Five datasets from FWD testing are analyzed by means of radial-symmetric structural simulations following Pan (1989a,b), see also Appendix 5.A. The pavement structure is represented as a body consisting of six layers with finite thickness and infinite in-plane dimensions, see Fig. 5.6: top-concrete, bottom-concrete, asphalt, cement-stabilized layer, the unbound layer, and the subgrade. A cylindrical coordinate system with base vectors  $\underline{e}_r$ ,  $\underline{e}_\vartheta$ , and  $\underline{e}_z$  is introduced. The  $z$ -axis coincides with the axis of the falling weight. It is zero at the surface of the pavement, and increases with increasing depth, see Fig. 5.6.

The boundary value problem at hand represents a problem of three-dimensional, static, linear elasticity. Because the problem is radial-symmetric, all quantities are constant along the circumferential coordinate  $\vartheta$ . Three types of field equations are to be fulfilled at all positions  $\underline{x}$  inside the volume of the structure:

- The static equilibrium conditions read as

$$\text{div } \boldsymbol{\sigma}(r, z) = 0, \quad (5.9)$$



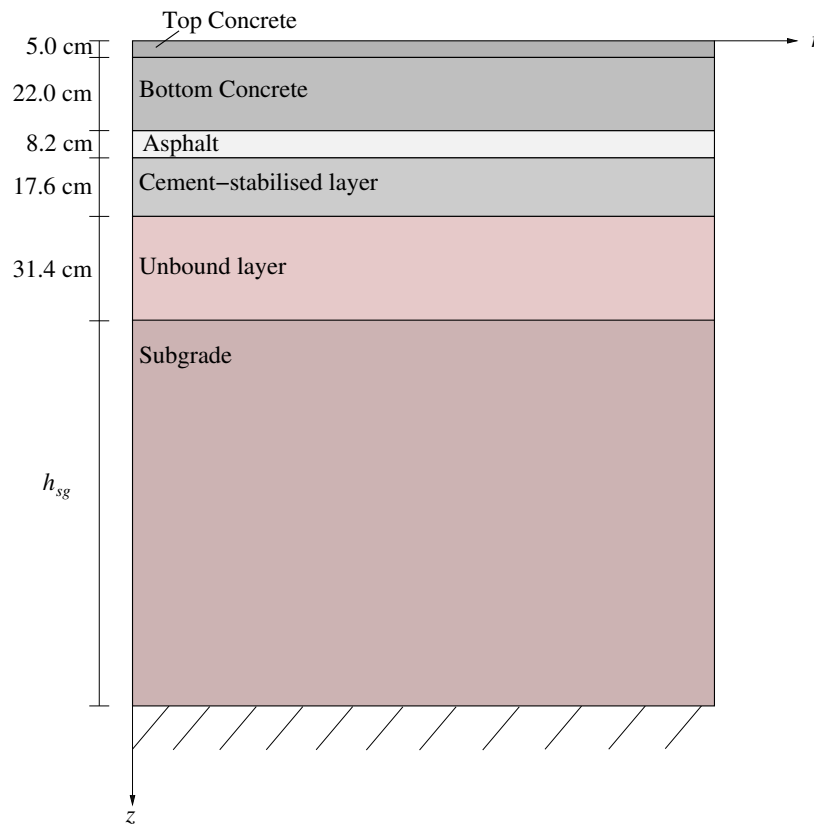


**Fig. 5.6.** Multi-layered structural model of the analyzed concrete-over-asphalt composite pavement.

where  $\text{div}$  and  $\boldsymbol{\sigma}(r, z)$  denote the divergence operator and Cauchy’s stress tensor at the position  $(r, z)$ , respectively.

- The generalized Hooke’s law accounting for linear elastic material behavior in all layers reads as

$$\boldsymbol{\sigma}(r, z) = \mathbb{C}(z) : \boldsymbol{\varepsilon}(r, z), \tag{5.10}$$

where  $\mathbb{C}(z)$  and  $\boldsymbol{\varepsilon}(r, z)$  stand for the layer-specific elastic stiffness tensor and the linearized strain tensor, respectively.

- The linearized strain tensor is the symmetric part of the gradient of the displacement field

$$\boldsymbol{\varepsilon}(r, z) = \frac{1}{2} \left\{ \text{grad } \underline{u}(r, z) + [\text{grad } \underline{u}(r, z)]^T \right\}, \tag{5.11}$$

where  $\text{grad}$  and  $\underline{u}(r, z)$  refer to the gradient operator and to the displacement vector  $\underline{u} = u_r(r, z) \underline{e}_r + u_z(r, z) \underline{e}_z$ , respectively.

Boundary conditions are to be fulfilled at the top and the bottom of the analyzed structure:

- At the top surface of the structure, i.e. at  $z = 0$ , pure stress boundary conditions prevail. A vertical load  $F$  is prescribed in terms of uniform normal stresses, such that the traction vector field  $\underline{t}(r, z=0)$  is free of shear stresses and reads as

$$\underline{t}(r, z=0) = \begin{cases} \frac{F}{R^2\pi} \underline{e}_z \dots & r \leq R, \\ 0 \dots \dots \dots & r > R, \end{cases} \tag{5.12}$$

where  $R = 0.15$  m refers to the radius of the plate on which the load is introduced during an FWD test.

- At the bottom surface of the structure, i.e. at  $z = h$ , pure displacement boundary conditions prevail. It is prescribed that all displacements have decayed to zero, such that the displacement vector field  $\underline{u}(r, z=h)$  reads as

$$\underline{u}(r, z=h) = 0. \quad (5.13)$$

Transition conditions are to be fulfilled at the interfaces between neighboring layers:

- Continuity of components of the traction vectors acting on the interfaces:

$$\underline{t}(r, z=h_j^+) = \boldsymbol{\sigma}(r, z=h_j^+) \cdot \underline{e}_z = \boldsymbol{\sigma}(r, z=h_j^-) \cdot \underline{e}_z = \underline{t}(r, z=h_j^-), \quad (5.14)$$

where  $h_j$  refers to the  $z$ -coordinate of the bottom interface of layer  $j$ , and the subscripts + and – refer to whether this interface is approached from the layer below (+) or from the one above (–); and

- Continuity of the components of the displacement vectors (bonded interfaces):

$$\underline{u}(r, z=h_j^+) = \underline{u}(r, z=h_j^-). \quad (5.15)$$

The elastic stiffness tensors in Eq. (5.10) are, in every layer, uniform and isotropic, with layer-specific elasticity moduli  $E_j$  and Poisson's ratios  $\nu_j$

$$\mathbb{C}_j = \frac{E_j}{1-2\nu_j} \mathbb{I}_{vol} + \frac{E_j}{1+\nu_j} \mathbb{I}_{dev}, \quad (5.16)$$

where  $\mathbb{I}_{vol}$  and  $\mathbb{I}_{dev}$  stand for the volumetric and deviatoric parts of the symmetric fourth-order identity tensor  $\mathbb{I}$ . Their components read as  $I_{ijkl} = (\delta_{ik}\delta_{jl} + \delta_{il}\delta_{jk})/2$ ,  $I_{ijkl}^{vol} = (\delta_{ij}\delta_{kl})/3$ , and  $I_{ijkl}^{dev} = I_{ijkl} - I_{ijkl}^{vol}$ , where  $\delta_{ij}$  is the Kronecker delta, which is equal to 1 for  $i = j$ , and equal to 0 otherwise.

The stiffness properties of the four topmost layers are known from laboratory and in situ tests, see Subsections 5.2.3 to 5.2.5 and Table 5.6. The stiffness properties of the unbound granular

**Table 5.6**

Elastic stiffness properties of the different layers of the analyzed pavement structure throughout the year; the moduli of elasticity of the unbound layer and the subgrade are unknown.

Date	top concrete		bottom concrete		asphalt		cement-stabilized layer		unbound layer		subgrade	
	$E_{tc}$ [GPa]	$\nu_{tc}$ [-]	$E_{bc}$ [GPa]	$\nu_{bc}$ [-]	$ E_a^* $ [GPa]	$ \nu_a^* $ [-]	$E_{cs}$ [GPa]	$\nu_{cs}$ [-]	$E_{ub}$ [GPa]	$\nu_{ub}$ [-]	$E_{sg}$ [GPa]	$\nu_{sg}$ [-]
$t_1 = \text{Jul } 21$	34.05	0.20	46.25	0.20	8.40	0.38	10.20	0.20	$E_{sg}(t_1)$	0.35	$E_{sg}(t_1)$	0.35
$t_2 = \text{Sep } 21$	34.05	0.20	46.25	0.20	12.10	0.36	9.20	0.20	$E_{sg}(t_2)$	0.35	$E_{sg}(t_2)$	0.35
$t_3 = \text{Oct } 21$	34.05	0.20	46.25	0.20	20.30	0.31	10.40	0.20	$E_{sg}(t_3)$	0.35	$E_{sg}(t_3)$	0.35
$t_4 = \text{Jan } 22$	34.05	0.20	46.25	0.20	28.90	0.28	8.10	0.20	$E_{sg}(t_4)$	0.35	$E_{sg}(t_4)$	0.35
$t_5 = \text{Mar } 22$	34.05	0.20	46.25	0.20	20.10	0.32	7.66	0.20	$E_{sg}(t_5)$	0.35	$E_{sg}(t_5)$	0.35

layer and the subgrade are unknown. Both layers are assumed to have the same stiffness since they could not be clearly distinguished from each other during new construction of the motorway. Poisson's ratio is set equal to 0.35 which is a typical value used for unbound granular layers (Omine et al., 1999b; BMVIT, 2018). The modulus of elasticity will be identified in the following subsection.

The thicknesses of the five topmost layers were measured during the installation of the pavement structure, see Table 5.7. The thickness of the subgrade is unknown. It will be identified in the following subsection.

**Table 5.7**

Thickness of the layers of the composite pavement structure; the thickness of the subgrade layer is unknown.

top concrete $h_{tc}$ [cm]	bottom concrete $h_{bc}$ [cm]	asphalt $h_a$ [cm]	cement-stabilized layer $h_{cs}$ [cm]	unbound layer $h_{ub}$ [cm]	subgrade $h_{sg}$ [cm]
5.0	22.0	8.2	17.6	31.4	$h_{sg}$

### 5.3.2 Back-calculation of subgrade properties from measured deflections and validation based on measured strains

The thickness of the subgrade and the modulus of elasticity of both the unbound layer and the subgrade are unknown. Seasonal variations of the modulus of elasticity are taken into account, given that the stiffness of unbound granular layers is known to be function of the temperature and moisture (Salour and Erlingsson, 2013; Bayat, 2009). Thus, one specific value of the modulus of elasticity will be determined for every testing date. This results in five different sought stiffness values. The thickness of the subgrade, in turn, must have been the same during all five testing dates, resulting is just one additionally sought value.

In order to achieve the best-possible agreement between measured and simulated surface deflections, the thickness of the subgrade and the modulus of elasticity of both the unbound layer and the subgrade are optimized in the context of structural simulations. The boundary value problem of Subsection 5.3.1 is solved following Pan (1989a,b), see Appendix 5.A. The following search intervals are introduced for the thickness and the modulus of elasticity:

$$h_{sg} \in [60, 160] \text{ cm}, \quad (5.17)$$

$$E_{sg} \in [70, 120] \text{ MPa}. \quad (5.18)$$

Both search intervals are subdivided into 11 equidistant grid points. For all 121 combinations of input values, a multi-layered simulation of an FWD test on the composite pavement structure is carried out. The root mean squared error between measured and simulated deflections is minimized,

$$RMSE(h_{sg}, E_{sg}(t_1), E_{sg}(t_2), E_{sg}(t_3), E_{sg}(t_4), E_{sg}(t_5)) = \quad (5.19)$$

$$= \sqrt{\frac{1}{5} \sum_{d=1}^5 \frac{1}{8} \sum_{g=1}^8 \left[ w(t_d, r_g) - u_z(r_g, z=0; h_{sg}, E_{sg}(t_d); |E_a^*(t_d), |\nu_a^*(t_d), E_{cs}(t_d)) \right]^2} \rightarrow \min,$$

where  $w(t_d, r_g)$  denotes the deflection measured at date  $t_d$  (with  $d = 1, 2, \dots, 5$ ) in the radial distance  $r_g$  from the center of the falling weight (with  $g = 1, 2, \dots, 9$ ), see Table 5.2.  $u_z(r_g, z=0; h_{sg}, E_{sg}(t_d); |E_a^*(t_d), |\nu_a^*(t_d), E_{cs}(t_d))$  denotes the deflection obtained by numerical simulation at the radial distance  $r_g$  from the center of the falling weight, at the surface of the structure ( $z = 0$ ), computed with thickness value  $h_{sg}$  and stiffness value  $E_{sg}(t_d)$ , see the search intervals in Eqs. (5.17) and (5.18), as well as with the stiffness properties  $|E_a^*(t_d), |\nu_a^*(t_d)$ , and  $E_{cs}(t_d)$  listed in Table 5.6. The achievable minimum of  $RMSE$  according to Eq. (5.19) amounts to 2.2  $\mu\text{m}$ . The corresponding optimal value of the thickness of the subgrade is equal to 100 cm. The optimal stiffness moduli range from 85 to 110 MPa, i.e. they show an only moderate seasonal variation. Notably, they are the larger the smaller the temperature, see Table 5.8. The deflections obtained with the optimized simulations agree very well with the measured deflections, see Fig. 5.7.

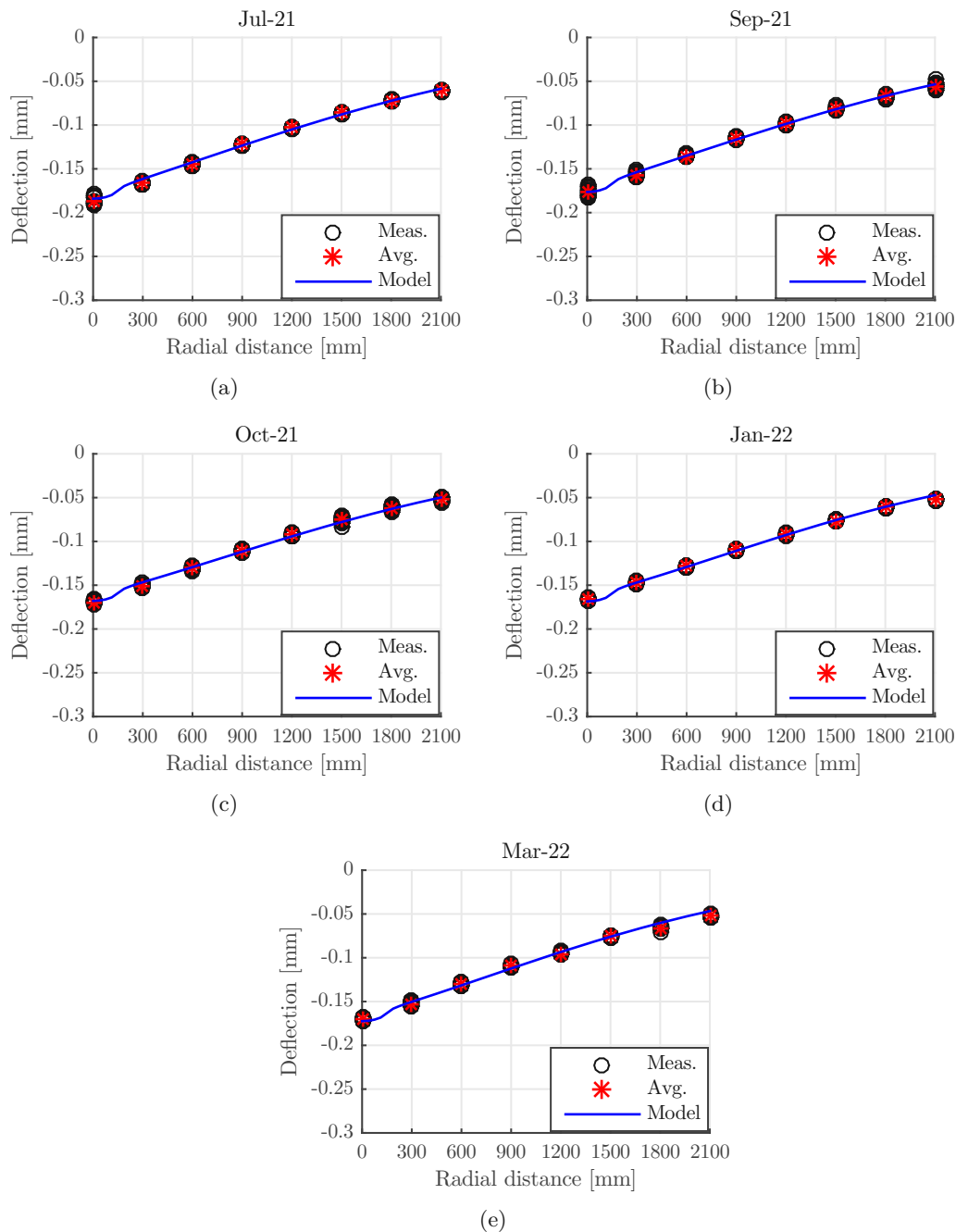


**Fig. 5.7.** Results of multi-layered analysis: the blue solid lines illustrate surface deflections obtained with optimized values of the stiffness and the thickness of the subgrade, see Table 5.8, and comparison with measured deflections, see the circles (= individual measurements) and stars (= mean values); for different testing dates: (a) Jul 21, (b) Sep 21, (c) Oct 21, (d) Jan 22, and (e) Mar 22.

In order to validate the five back-calculation results, radial normal strains (computed at mid-depth of the asphalt layer, in the radial distance of 45 cm from the axis of symmetry) are compared with measured strains, see Table 5.9. The simulated asphalt strains agree well with the measured maxima of the strain sensor readings. The prediction error amounts, on average, to 8.4%. This is acceptable for an application in geotechnical engineering and, thus, corroborates

**Table 5.8**

Back-calculated values of the thickness  $h_{sg}$  and of the modulus of elasticity  $E_{sg}$  of the subgrade, as well as comparison with the temperatures measured at the interface between unbound granular layer and the subgrade,  $T_{ub-sb}$ .

Date	$h_{sg}$ [cm]	$E_{sg}$ [GPa]	$T_{ub-sb}$ [°C]
$t_1 = \text{Jul } 21$	100	0.085	19.6
$t_2 = \text{Sep } 21$	100	0.095	18.3
$t_3 = \text{Oct } 21$	100	0.100	12.7
$t_4 = \text{Jan } 22$	100	0.110	1.5
$t_5 = \text{Mar } 22$	100	0.105	8.4

**Table 5.9**

Validation of back-calculation results results: comparison of measured asphalt strains,  $\varepsilon_{ASG}$  with simulated strains,  $\varepsilon_{sim}$ , and comparison with the temperature measured at the top and bottom of the asphalt layer,  $T_{top-a}$  and  $T_{bot-a}$ , as well as with the stiffnesses of the asphalt and the cement-stabilized layers,  $|E_a^*|$  and  $E_{cs}$ .

Date	$\varepsilon_{ASG}$ [ $10^{-6}$ ]	$\varepsilon_{sim}$ [ $10^{-6}$ ]	$T_{top-a}$ [°C]	$T_{bot-a}$ [°C]	$ E_a^* $ [GPa]	$E_{cs}$ [GPa]
$t_1 = \text{Jul } 21$	5.20	5.75	22.1	22.4	8.4	10.20
$t_2 = \text{Sep } 21$	4.94	5.15	17.6	18.2	12.1	9.20
$t_3 = \text{Oct } 21$	4.64	5.03	9.0	9.6	20.3	10.40
$t_4 = \text{Jan } 22$	6.58	5.39	-0.3	0.1	28.9	8.10
$t_5 = \text{Mar } 22$	5.85	5.76	9.2	9.7	20.1	7.66

the results of the back-calculation activity.

It is interesting to interpret the virtually equal strains simulated for the dates in July 2021 and March 2022, see Table 5.9. Let us take March as the reference for the following considerations. In July, the asphalt stiffness (8.4 GPa) was some 58% smaller than in March (20.1 GPa), because the asphalt temperature in July (some 22.25°C) was significantly larger than in March (some 9.45°C), see Table 5.9. The smaller the stiffness of asphalt, the larger the simulated strain. However, the stiffness of the cement-stabilized layer measured in July (10.2 GPa) was some 33% larger than in March (7.66 GPa). The larger the stiffness of the cement-stabilized layer, the smaller the simulated strain. The strain increase resulting from the relatively large decrease of stiffness of asphalt (58%) is balanced by the strain decrease resulting from of the relatively small increase of stiffness of the cement-stabilized layer (33%), because the thickness of the cement-stabilized layer (17.6 cm) is significantly larger than the thickness of the asphalt layer (8.2 cm). It is concluded that the strains inside the asphalt layer are a function of the thicknesses and stiffnesses of all layers, rather than a function of the stiffness of the asphalt alone. This explains why the simulated strains do not correlate very well with the stiffness (and, therefore, the temperature) of asphalt, see Table 5.9.

As for the tests performed in January 2022, the difference between simulated and measured strains amounts to some 18%. On that test day, icy conditions prevailed in the asphalt layer. These conditions may have affected the experimental results.

### 5.3.3 Development of an asphalt-related temperature correction for measured surface deflections

Performing nominally *identical* FWD tests on *the same* composite pavement structure, but at different dates and, therefore, at *different* temperatures, yields *different* surface deflections measured by the geophones, see Table 5.2. It is desirable to correct the measured deflections such as to obtain deflections that would have been measured provided that the temperate in the asphalt layer had amounted to the reference temperature  $T_{ref} = 20^\circ\text{C}$ . Corrected deflections from different dates will still be different. These differences will refer to seasonal stiffness changes of the other layers, further down in the multi-layered structure of the pavement. These stiffness changes are of particular interest in pavement engineering.

For the described asphalt-related temperature correction of deflections measured during FWD testing, the following ansatz is made:

$$w^{corr}(r) = w(r, T_a) - w_{ref} \times \gamma(r, T_a), \tag{5.20}$$

where  $w(r, T_a)$  stands for deflections measured at radial distance  $r$ , and the functional argument  $T_a$  refers to the temperature of the asphalt layer at the time of FWD testing. In addition,  $w_{ref}$  denotes a reference deflection,  $\gamma(r, T_a)$  a dimensionless correction function, and  $w^{corr}(r)$  the corrected deflections. Westergaard’s solutions for an infinite plate on top of a Winkler foundation (Westergaard, 1926, 1948) are the source of inspiration for the following development of the correction function  $\gamma(r, T_a)$ :

$$\gamma(r, T_a) = \begin{cases} b_1 \left(1 - 10^{b_2 \frac{T_a - T_{ref}}{T_{ref}}}\right) \dots\dots\dots & r \leq R, \\ k_1 \left(1 - 10^{k_2 \frac{T_a - T_{ref}}{T_{ref}}}\right) \text{ker}\left(\frac{r}{r_0}\right) + k_3 \left(1 - 10^{k_4 \frac{T_a - T_{ref}}{T_{ref}}}\right) \text{kei}\left(\frac{r}{r_0}\right) \dots & r > R, \end{cases} \tag{5.21}$$

where  $\text{ker}$  and  $\text{kei}$  are Kelvin Bessel functions.

In order to identify the constants  $b_1, b_2, k_1, k_2, k_3,$  and  $k_4$  eight simulations of the multi-layered pavement structure are performed according to Subsection 5.3.1 and Appendix 5.A. Thereby, the temperature of the asphalt is set equal to the eight values listed in Table 5.10, ranging from  $-5^\circ\text{C}$  to  $+30^\circ\text{C}$ . This table also contains corresponding stiffness properties of asphalt,

**Table 5.10**

Variation of the temperature of the asphalt layer,  $T_a$ , and corresponding values of the dynamic stiffness properties,  $|E_a^*|$  and  $|\nu_a^*|$ , see also Fig. 5.5.

$T_a$ [ $^\circ\text{C}$ ]	$ E_a^* $ [GPa]	$ \nu_a^* $ [-]
-5	32.8	0.27
$\pm 0$	28.8	0.28
5	24.4	0.30
10	19.6	0.32
15	14.8	0.34
20	10.3	0.37
25	6.5	0.40
30	3.6	0.42

see the red crosses in Fig. 5.5. The stiffnesses of all other layers are set constant. The stiffness values assigned to the concrete layers are taken from Table 5.6. The moduli of elasticity of the cement-stabilized and subgrade layers are set equal to  $E_{cs} = 8.35$  GPa and  $E_{ub} = E_{sg} = 0.10$  GPa,

respectively. These are the mean values computed on the basis of five values listed in Table 5.5 and in Table 5.8, respectively. In addition,  $\nu_{cs} = 0.20$  and  $\nu_{ub} = \nu_{sg} = 0.35$ , see Table 5.6. The eight computed deflection curves portray the influence of the temperature-dependent stiffness of asphalt on the response of the composite pavement structure, see Fig. 5.8.

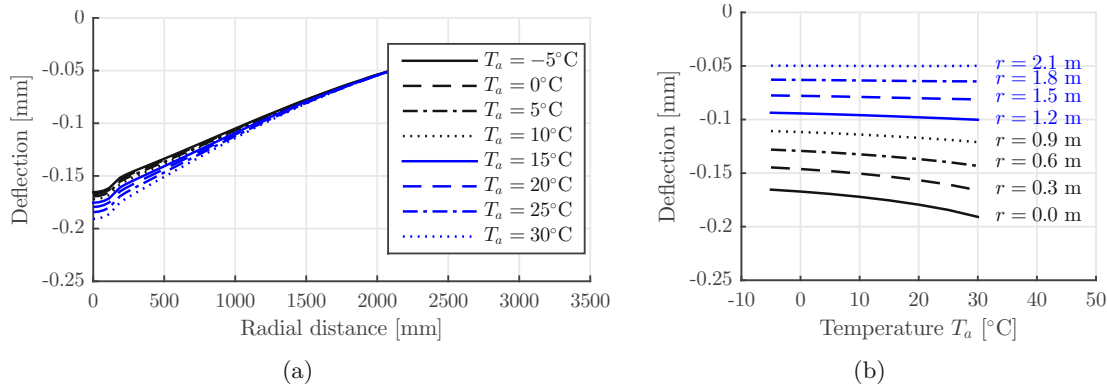


**Fig. 5.8.** Deflections of the surface of the composite pavement structure as a function of (a) the radial distance from the axis of symmetry, for different temperatures of the asphalt layer, and (b) the temperature of the asphalt layer, for different radial distances from the axis of symmetry.

The eight computed deflection curves are inserted as  $w(r, T_a)$  into the right-hand-side of Eq. (5.20) and the unknowns in the definition of  $\gamma(r, T_a)$  are identified such that Eq. (5.20) delivers corrected deflection curves which come as close as possible to the simulated deflection curve referring to  $T_a = T_{ref} = 20^\circ\text{C}$ . Thereby,  $w_{ref}$  is set equal to the simulated deflection at the axis of symmetry ( $r = 0$ ), obtained with  $T_a = 20^\circ\text{C}$ , i.e.  $w_{ref} = 179 \mu\text{m}$ , and  $r_0$  is set equal to 2.1 m, see Table 5.11 also for the identified values of  $b_1, b_2, k_1, k_2, k_3$ , and  $k_4$ .

**Table 5.11**

Values of constants which are part of the mathematical expressions describing the asphalt-related temperature correction of deflections measured during FWD testing, see Eqs. (5.20) and (5.21).

$b_1 = -0.1065$	$b_2 = 0.4456$	$T_{ref} = 20^\circ\text{C}$	$w_{ref} = 179 \mu\text{m}$	$r_0 = 2.1 \text{ m}$
$k_1 = -0.0442$	$k_2 = 0.5250$	$k_3 = -0.0104$	$k_4 = 0.8903$	

In order to demonstrate the performance of the developed correction, it is applied to the simulated deflections shown in Fig. 5.8. The corrected deflections indeed form a master curve, see Fig. 5.9.

### 5.3.4 Application of the asphalt-related temperature correction to deflections measured during FWD testing

The deflections measured during the five FWD tests, see Table 5.2 and Fig. 5.10(a), are subjected to the asphalt-related temperature correction of Eqs. (5.20) and (5.21), see also Table 5.11. The corrected deflections are illustrated in Fig. 5.10(b), see also Table 5.12.

The seasonal differences of the *measured* deflections decrease with increasing distance from the center of the falling weight, see Fig. 5.10(a). The seasonal differences of the *corrected* deflections, in turn, are similarly large independent of the distance from the center of the falling weight, see Fig. 5.10(b). These remaining differences result mainly from seasonal changes of the stiffness of the subgrade. This will be demonstrated in the following two subsections.

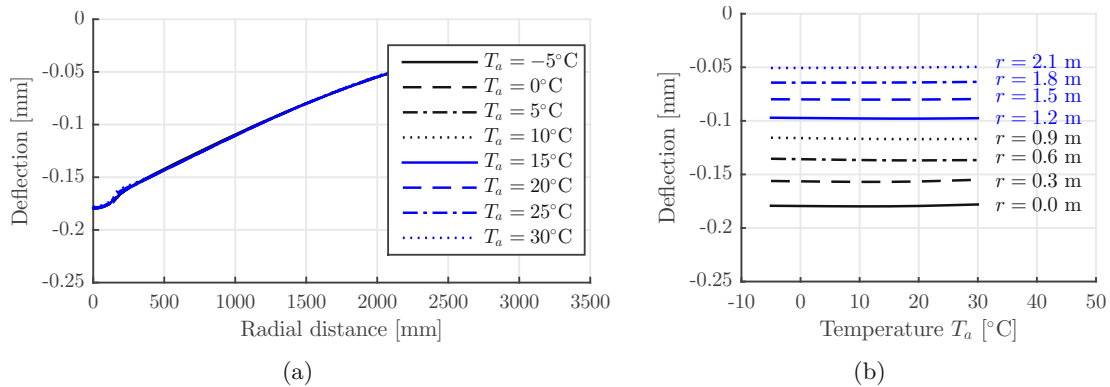


**Fig. 5.9.** Results obtained from application of the correction Eqs. (5.20) and (5.21), see also Table 5.11, to the deflection curves illustrated in Fig. 5.8.

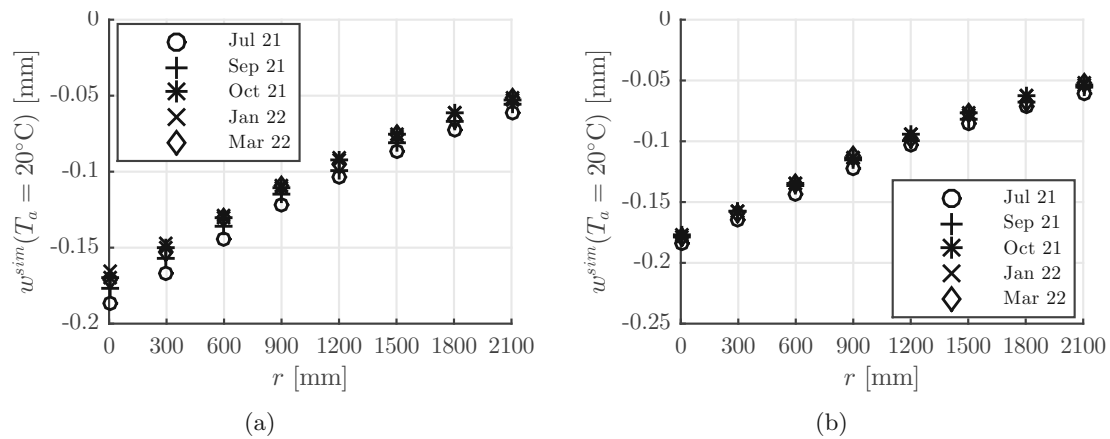


**Fig. 5.10.** (a) Surface deflections measured during FWD testing at the field-testing site: the illustrated values are taken from Table 5.2, and (b) results obtained from subjecting the measured deflections of Table 5.2 to the asphalt-related temperature correction of Eqs. (5.20) and (5.21), see also Table 5.11.

### 5.3.5 Quantification of the $k$ -value by means of the dense-liquid model and the AREA-method

The benefit resulting from correction of measured deflections is assessed by means of the AREA-method, initially introduced for flexible pavements in (Hoffman and Thompson, 1980). It idealizes a pavement structure as a plate resting on a Winkler foundation exhibiting a uniform spring stiffness per unit area,  $k_{sg}$ , often referred to as “modulus of subgrade reaction” and herein referred to simply as “ $k$ -value”, see Fig. 5.11.

FWD tests are non-destructive experiments. Both the elasto-static multi-layered simulation approach used in before and the plate-on-a-Winkler-foundation model are *linear* simulation approaches. Therefore, there must be a directly-proportional relation between seasonally changing stiffness properties of both simulation approaches. This will be studied next.

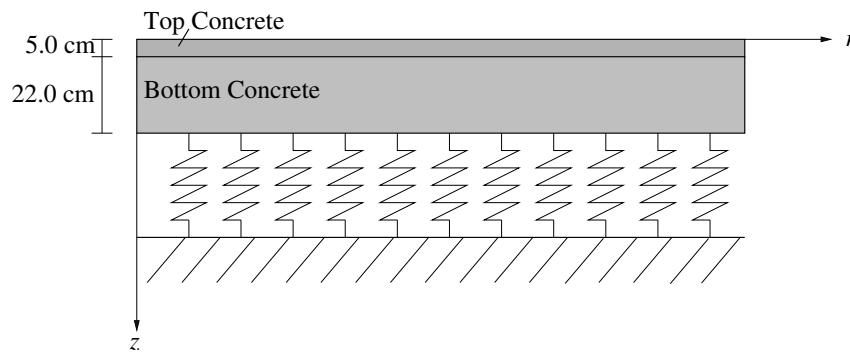
The AREA parameter is equal to the normalized area under the deflection curve  $w(r)$ , see e.g. (Hoffman and Thompson, 1980). Herein,  $w(r)$  is integrated from the axis of the falling weight to the position of the fourth geophone, and the integral is numerically approximated using



**Table 5.12**

Corrected deflections: results obtained from subjecting the measured deflections of Table 5.2 to the asphalt-related temperature correction of Eqs. (5.20) and (5.21), see also Table 5.11.

Date	Corrected deflections [mm] at a radial distance of:							
	$r_1=0.0$ m	$r_2=0.3$ m	$r_3=0.6$ m	$r_4=0.9$ m	$r_5=1.2$ m	$r_6=1.5$ m	$r_7=1.8$ m	$r_8=2.1$ m
$t_1 = \text{Jul } 21$	0.184	0.165	0.143	0.122	0.102	0.086	0.072	0.061
$t_2 = \text{Sep } 21$	0.178	0.158	0.137	0.116	0.099	0.082	0.068	0.055
$t_3 = \text{Oct } 21$	0.177	0.157	0.135	0.113	0.094	0.077	0.063	0.053
$t_4 = \text{Jan } 22$	0.178	0.157	0.135	0.114	0.094	0.078	0.063	0.053
$t_5 = \text{Mar } 22$	0.179	0.159	0.134	0.112	0.097	0.077	0.067	0.052

**Fig. 5.11.** Dense-liquid model: elastic plate on a Winkler foundation.

the trapezoidal rule. This yields the *AREA4* parameter (Khazanovich et al., 2001) as:

$$\text{AREA4} = \frac{1}{w_1} \int_0^{3\Delta r} w(r) dr \approx \frac{1}{2} \left[ \Delta r + 2 \Delta r \left( \frac{w_2}{w_1} \right) + 2 \Delta r \left( \frac{w_3}{w_1} \right) + \Delta r \left( \frac{w_4}{w_1} \right) \right], \quad (5.22)$$

where  $w_i$  (with  $i = 1, 2, 3, 4$ ) refers to surface deflections at a radial distance of  $r = (i - 1) \Delta r$ , with  $\Delta r = 300$  mm. The relationship between the *AREA4* parameter and the radius of relative stiffness  $l_k$  was derived in the context of a non-dimensional approach (Losberg, 1960; Ioannides, 1990; Ioannides et al., 1989), using Westergaard's solutions for the "dense-liquid" model (Westergaard, 1926, 1948):

$$l_k = \left( \frac{D}{k_{sg}} \right)^{0.25} = \left[ \frac{\ln \left( \frac{\xi_1 - \text{AREA4}}{\xi_2} \right)}{\xi_3} \right]^{\xi_4} \times 1 \text{ mm}, \quad (5.23)$$

where  $D$  is the bending stiffness of the plate. For the here-used configuration of four equidistant geophones with  $\Delta r = 300$  mm, the  $\xi$ -parameters in Eq. (5.23) take the values listed in Table 5.13, see also (Hall et al., 1997) for other sensor configurations. The numerical value of  $D$  is set

**Table 5.13**

Values of the  $\xi$ -parameters in Eq. (5.23).

$$\xi_1 = 914.4 \text{ mm} \quad \xi_2 = 46031.89 \text{ mm} \quad \xi_3 = -1.224177 \quad \xi_4 = 4.387009$$

equal to the bending stiffness of the sandwich plate made from the two topmost concrete layers, see Appendix 5.B for details,

$$D = 71.11 \text{ MPa m}^3. \quad (5.24)$$

The  $k$ -values are quantified as follows. Measured or corrected deflections referring to the five different FWD testing dates are inserted, one after the other, into Eq. (5.22), the resulting values of  $AREA4$  are inserted together with  $D$  according to Eq. (5.24) and the  $\xi$ -parameters according to Table 5.13 into Eq. (5.23), and the resulting expression is solved for  $k_{sg}$ . This yields  $k$ -values listed in Table 5.14.

**Table 5.14**

$k$ -values calculated from the measured deflections, see Table 5.2 and Fig. 5.10(a), as well as from corrected deflections, see Table 5.12 and Fig. 5.10(b).

Date	$k_{sg}$ [MPa/m] from measured deflections	$k_{sg}$ [MPa/m] from corrected deflections
Jul 21	168.91	163.59
Sep 21	182.65	187.28
Oct 21	177.37	197.35
Jan 22	174.67	206.65
Mar 22	190.14	210.09

### 5.3.6 Correlation of stiffness properties quantified by means of multi-layered and dense-liquid models

The  $k$ -values listed in Table 5.14 show seasonal variations. As for the *measured* deflections, this is a consequence of seasonal stiffness changes of the asphalt, the cement-stabilized layer, and the subgrade. As for the *corrected* deflections, seasonal changes of  $k$  should refer to corresponding seasonal stiffness changes of the cement-stabilized layer and the subgrade. This is checked next.

The  $k$ -values quantified from *measured* deflections, see Table 5.14, are correlated with corresponding elastic moduli of both the cement-stabilized layer, see Table 5.5, and the subgrade, see Table 5.8. The coefficients of determination,  $R^2$ , amount to  $-12.36$  and  $-2.61$ , see Figs. 5.12(a) and (c), respectively. This implies that the *mean* of the  $k$ -values provides a better estimate than the best linear regression function passing through the origin.

The  $k$ -values quantified from *corrected* deflections, see Table 5.14, are correlated with corresponding elastic moduli of both the cement-stabilized layer, see Table 5.5, and the subgrade, see Table 5.8. The coefficients of determination,  $R^2$ , amount to  $-3.85$  and  $0.93$ , see Fig. 5.12(b), and (d), respectively. This implies that  $k$ -values quantified from corrected deflections (i) do not correlate with the elastic modulus of the cement-stabilized layer, but (ii) correlate very well with the elastic modulus of the subgrade. This can be explained as follows.

The developed method for correction of measured deflections removes the part of the deflections that varies because of the influence of the asphalt layer. The remaining variations of the corrected deflections mainly refer to the subgrade, because the stiffness of the concrete layers was constant, and the cement-stabilized layer is significantly stiffer and thinner than the subgrade. Simple quantification of  $k$ -values from corrected surface deflections, see Eqs. (5.22) and (5.23) referring to the dense-liquid model and the AREA method, yields values of  $k_{sg}$  which are virtually directly proportional to the elastic stiffness moduli of the subgrade. It is concluded that the use of the proposed correction method enables a straightforward interpretation of FWD results, as deflections captured on different seasons are rendered comparable with each other, while at the same time increasing the accuracy and expressiveness of the back-calculation of subgrade properties.

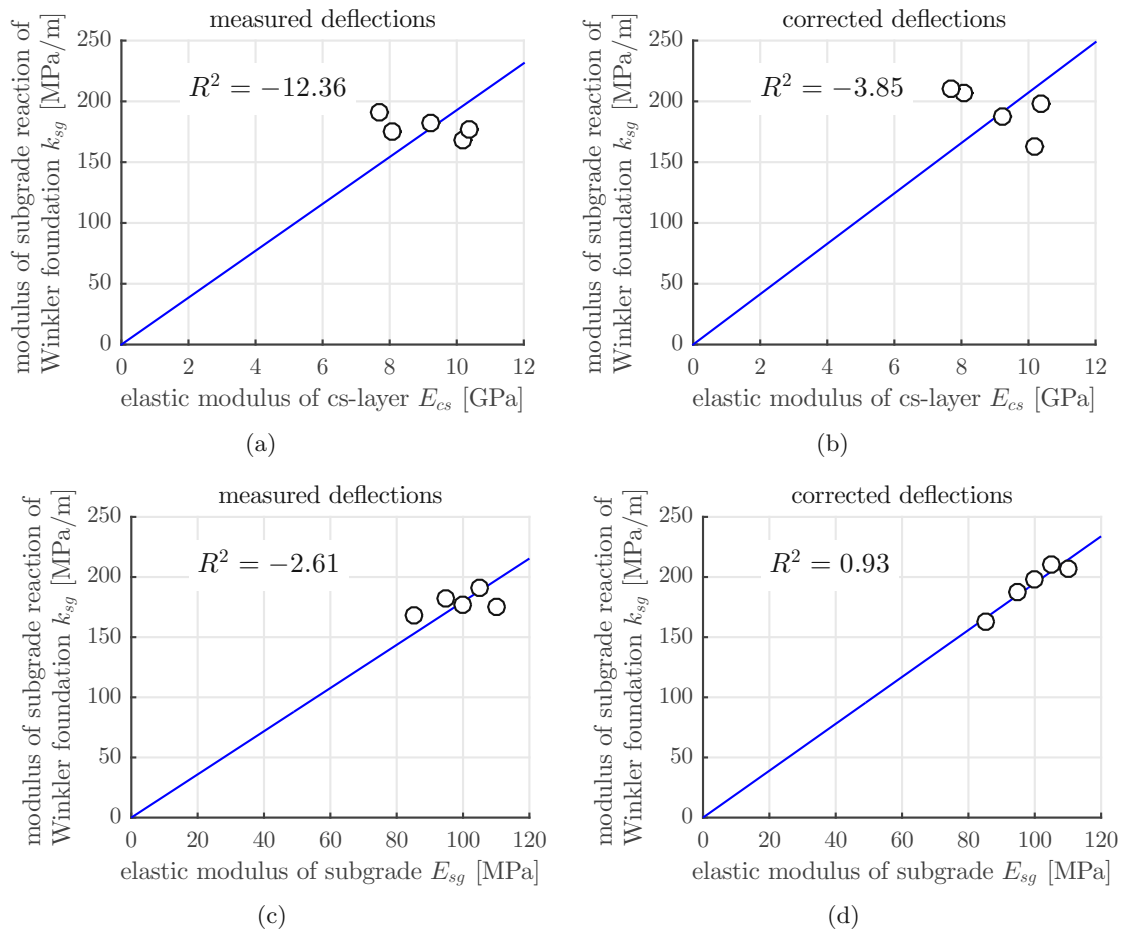


**Fig. 5.12.** Correlation between  $k$ -values and elastic moduli of the cement-stabilized layer, see (a) and (b), as well as between  $k$ -values and elastic moduli of the subgrade, see (c) and (d), based on  $k$ -values quantified from *measured* displacements, see (a) and (c), as well as  $k$ -values quantified from *corrected* displacements, see (b) and (d).

### 5.3.7 Robustness of results with respect to the uncertainty regarding $D$

The  $k$ -values were computed based on the value of  $D$  given in Eq. (5.24). In the following, it is explained that the coefficients of determination given in Fig. 5.12 stay the same, even if a different value of  $D$  is used for quantification of the  $k$ -values. Provided that the value of  $D$  according to Eq. (5.24) is scaled by a factor  $p$ , corresponding values of  $k_{sg}$  are scaled by the same factor  $p$ , because the ratio  $D/k_{sg}$  must stay the same according to Eq. (5.23), i.e.  $l_k = D/k_{sg} = (pD)/(pk_{sg})$ . Multiplying all  $k$ -values in Fig. 5.12 by the same arbitrary scaling factor  $p$  yields *the same* coefficients of determination. Thus, the essential results of the present study are perfectly robust with respect to the uncertainty regarding the bending stiffness of the plate of the dense-liquid model.

## 5.4 Alternative correction approach requiring measured deflections only

### 5.4.1 Influence of asphalt and subgrade stiffness on surface deflections

The influence of the stiffness of asphalt on surface deflections decreases with increasing distance from the axis of the falling weight, see Fig. 5.8. This implies that stiffness changes of asphalt result, during FWD tests performed at different dates, in *different curvatures* of the surface of the concrete slab.

The influence of the stiffness of the subgrade on surface deflections, in turn, is virtually constant in the region of the geophones, see Fig. 5.10(b). This implies that stiffness changes of the subgrade result, during FWD tests performed at different dates, in almost *the same curvature* of the surface of the concrete slab, but in different absolute values of the deflections. This is the motivation for the following engineering correction of measured surface deflections.

### 5.4.2 Engineering correction, based on measured deflections only

As for seasonally-repeated FWD testing on regular (= non-instrumented) composite pavements, a correction approach which requires not more information than just measured deflections is developed. The first FWD results serve as the reference:  $t_1 = t_{ref}$ . All subsequent FWD results are corrected such that they refer to the asphalt temperature at time  $t_1 = t_{ref}$ , even if this temperature is unknown. To this end, the deflections measured at  $t_1 = t_{ref}$  are uniformly shifted:

$$w_{eng}^{corr}(r, t_d) = w(r, t_{ref}) + \Delta w(t_d, t_{ref}). \quad (5.25)$$

The shifted deflections refer to exactly *the same curvature* of the surface of the concrete slab, but different absolute values. The amount by which the deflections are shifted is chosen such that the corrected deflections are equal to measured deflections at the radial distance  $r_6 = 1500$  mm:

$$\Delta w(t_d, t_{ref}) = w(r_6, t_d) - w(r_6, t_{ref}). \quad (5.26)$$

Applying Eqs. (5.25) and (5.26) to the measured deflections, see Fig. 5.10(a) and Table 5.2, yields corrected deflections illustrated in Fig. 5.13, see also Table 5.15.

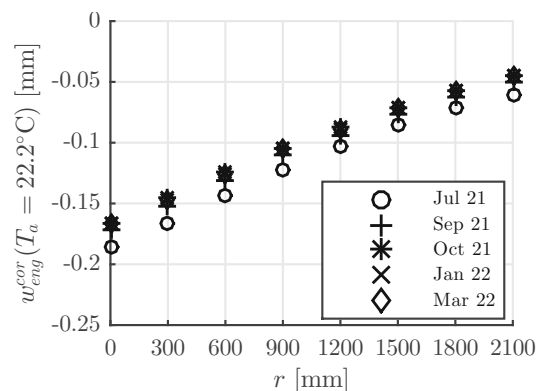


**Fig. 5.13.** Corrected deflections: results obtained from subjecting the measured deflections of Table 5.2 to the correction of Eqs. (5.25) and (5.26).

The radial position  $r_6$ , which plays a prominent role in the corrections approach of Eqs. (5.25) and (5.26), is the result of the following trade-off considerations. The radial position showing up in Eq. (5.26) shall be (i) suitably far away from the axis of the falling weight, such that

**Table 5.15**

Corrected deflections: results obtained from subjecting the measured deflections of Table 5.2 to the correction of Eqs. (5.25) and (5.26).

Date	Corrected deflections [mm] at a radial distance of:							
	$r_1=0.0$ m	$r_2=0.3$ m	$r_3=0.6$ m	$r_4=0.9$ m	$r_5=1.2$ m	$r_6=1.5$ m	$r_7=1.8$ m	$r_8=2.1$ m
$t_1 = \text{Jul } 21$	0.186	0.167	0.144	0.122	0.103	0.086	0.072	0.061
$t_2 = \text{Sep } 21$	0.172	0.167	0.144	0.122	0.103	0.086	0.072	0.061
$t_3 = \text{Oct } 21$	0.166	0.146	0.125	0.104	0.088	0.071	0.057	0.044
$t_4 = \text{Jan } 22$	0.167	0.147	0.126	0.105	0.089	0.071	0.057	0.044
$t_5 = \text{Mar } 22$	0.166	0.146	0.125	0.105	0.088	0.071	0.057	0.045

deflections measured at this distance are not significantly influenced by temperature-dependent stiffness changes of asphalt, and (ii) suitably close to the axis of the falling weight, such that deflections measured at this distance still show significant variations resulting from seasonal stiffness changes of the subgrade.

### 5.4.3 Application of the AREA4-approach for quantification of $k$ -values from corrected deflections

The AREA4-values of the deflections corrected according to Eqs. (5.25) and (5.26) can be expressed as:

$$AREA4_{eng}^{corr}(t_d) = \frac{AREA4(t_{ref}) \times w_1(t_{ref}) + 3\Delta r \times \Delta w(t_d, t_{ref})}{w_1(t_{ref}) + \Delta w(t_d, t_{ref})}, \quad (5.27)$$

where  $AREA4(t_{ref}) \times w_1(t_{ref})$  denotes the area under the reference deflection curve in the interval from  $r = 0$  to  $r = 3\Delta r$ , the expression  $3\Delta r \times \Delta w(t_d, t_{ref})$  is equal to the change of that area resulting from shifting, and  $w_1(t_{ref}) + \Delta w(t_d, t_{ref})$  is equal to the value of the shifted deflections at the axis of the falling weight.

Corresponding  $k$ -values are quantified by inserting the AREA4-values according to Eq. (5.27), together with  $D$  according to Eq. (5.24) and the  $\xi$ -parameters according to Table 5.13, into Eq. (5.23), and by solving the resulting expression for  $k_{sg}$ . This yields the  $k$ -values listed in Table 5.16.

**Table 5.16**

$k$ -values calculated from the deflections corrected according to Eqs. (5.25) and (5.26), see also Fig. 5.13 and Table 5.15.

Date	$k_{sg}^{eng}$ [MPa/m] from engineering correction
Jul 21	168.91
Sep 21	197.54
Oct 21	218.69
Jan 22	215.82
Mar 22	217.72

In order to assess the quality of the correction according to Eqs. (5.25) and (5.26), the corresponding  $k$ -values from Table 5.16 are correlated with  $k$ -values from deflections corrected according to Eqs. (5.20) and (5.21), see the rightmost column in Table 5.14, and with the elastic

moduli of the subgrade listed in Table 5.8. The results of this comparison, see Fig. 5.14, underline that the engineering correction of Eqs. (5.25) and (5.26), which requires knowledge of measured deflections only, allows for similar conclusions regarding the stiffness of the subgrade as the more advanced correction of Eqs. (5.20) and (5.21), which requires knowledge of the temperature of asphalt and realistic multi-layered simulation of the investigated pavement structure.

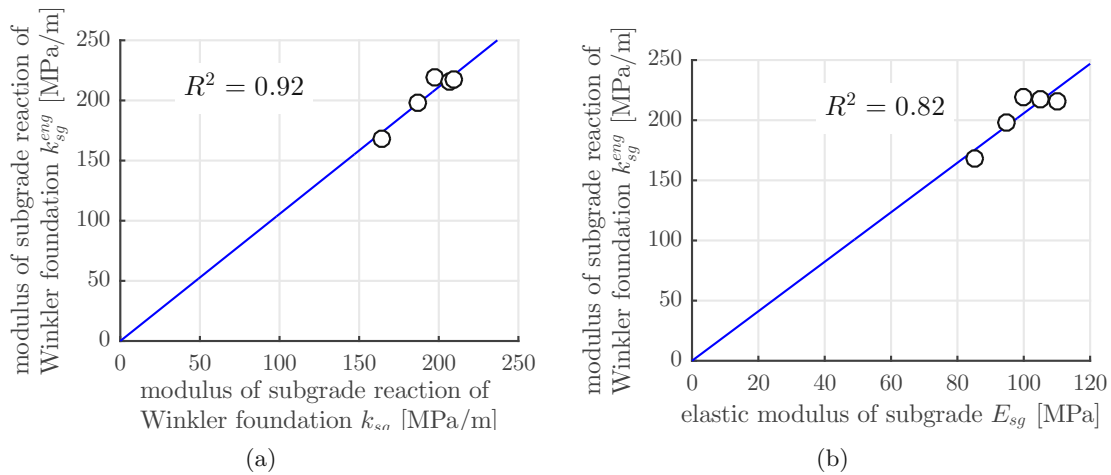


**Fig. 5.14.** Correlation between  $k_{cor}^{eng}$ -values from Table 5.16, referring to the engineering correction approach of Eqs. (5.25) and (5.26), with (a)  $k$ -values from the first presented correction approach of Eqs. (5.20) and (5.21), see Table 5.14, and (b) the elastic modulus of the subgrade,  $E_{sg}$ , from Table 5.8.

## 5.5 Conclusions

Five sets of FWD tests were performed, in summer, winter, and transitional periods, at a field-testing site of a concrete-over-asphalt composite pavement, instrumented with temperature sensors, asphalt strain gauges, and accelerometers. The constant stiffnesses of concrete and the temperature-dependent stiffness of asphalt were characterized using laboratory tests. The season-dependent stiffness of the cement-stabilized layer was characterized in situ using dynamic “sledgehammer” tests and the corresponding measurements of the accelerometers which are buried at the top and at the bottom of the cement-stabilized layer. The constant thickness and the season-dependent elastic modulus of the subgrade was back-calculated using multi-layered elastostatic simulations. From this part of the study, the following conclusions are drawn:

- The stiffness of asphalt shows a significant temperature-dependence: e.g. the stiffness at 0°C is by a factor of 2.4 larger than at 22°C, see Table 5.8.
- multi-layered elastostatic simulations of the composite pavement structure, which reproduced the season-dependency of measured deflections very accurately, see Fig. 5.7, are corroborated, because they predicted asphalt strains with an average error smaller than 8%, see Table 5.9.
- A multi-layered elastostatic model is well suited for the structural analysis of FWD tests, provided that realistic thickness and stiffness properties are known for all of the individual layers.
- Back-calculated values of the stiffness of the subgrade show a clear temperature-dependence: e.g. the stiffness at 2°C was found to be by some 30% larger than at 20°C, see Table 5.8.

- The seasonal variations of deflections measured during the analyzed FWD tests mainly result from (i) the strong temperature-dependence of the stiffness of the relatively thin layer of asphalt, and (ii) the milder temperature-dependence of the stiffness of the relatively thick layer of the subgrade.

This motivated the development of a method for an asphalt-related temperature correction of deflections measured during FWD testing. To this end, the multi-layered model was used to compute deflections for asphalt temperatures ranging from  $-5^{\circ}\text{C}$  to  $30^{\circ}\text{C}$ , while season-averaged constant stiffness properties were assigned to all other layers. The results allowed for translating measured deflections into corrected deflections which refer to an asphalt temperature of  $20^{\circ}\text{C}$ . From this part of the study, the following conclusions are drawn:

- The seasonal variations of *corrected* deflections mainly result from the temperature-dependence of the stiffness of the subgrade, because  $k$ -values of a dense-liquid model, which were quantified from corrected deflections, correlate very well the season-dependent values of the elastic modulus of the subgrade, see Fig. 5.12(d).
- Vice versa, a realistic characterisation of the seasonal variations of the stiffness of the subgrade is possible using the computationally very cheap AREA method, provided that the corrected deflections are analyzed.

The success of this first correction approach has motivated the development of an alternative correction approach which requires not more information than just measured deflections. It consists of uniform shifting of deflections measured at a reference date, such that the corrected deflection at the position of the sixth geophone,  $r_6 = 1500\text{ mm}$ , is equal to the measured deflection, see Eqs. (5.25) and (5.26). From this part of the study, the following conclusions are drawn:

- The alternative correction approach delivers useful estimates of relative seasonal stiffness changes of the subgrade, because  $k$ -values, derived from deflections corrected according to Eqs. (5.25) and (5.26), correlate well with seasonal variations of the elastic modulus of the subgrade, see Fig. 5.14.
- The practical applicability of the alternative correction approach is straightforward, because it requires not more information than just measured deflections. This is different for the first correction approach which requires (i) knowledge of the temperature of the asphalt layer at the time of FWD testing, and (ii) reliable multi-layered simulations of the analyzed FWD tests.
- The proposed method significantly improves the comparability of results from FWD tests on composite pavements, provided that the focus lies on the season-dependent stiffness of the subgrade, which is frequently the case in pavement engineering.
- The temperature-correction of measured deflections is appealing, because corrected deflections allow for the application of any method typically used for interpretation of FWD results, including deflection basin parameters and structural models.

Finally, the limitations of the present study are addressed. The proposed correction methods were applied to FWD test data from one specific concrete-over-asphalt composite pavement structure. Therefore, it will be interesting in the future to apply the here-developed engineering correction approach also to FWD data from repeated testing of other composite pavements, in order to assess the long-term evolution of the stiffness of the subgrade. This, however, goes beyond the scope of the present paper.

## Funding

This research received financial support by the Austrian Research Promotion Agency (FFG) within the Bridge Project 2021 “Grundlegende Analyse von FWD-Versuchen: innovative Experimente, moderne Struktursimulationen, statistische Datenanalyse – FALLINGweight”. The authors also acknowledge the TU Wien University Library for financial support through its Open Access Funding Programme.

## Acknowledgments

Interesting discussions with Christian Hellmich and Luis Zelaya-Lainez are gratefully acknowledged. Help of Olaf Lahayne, Wolfgang Dörner, Dominic Hassan, Michael Haminger, and Constantin Kreil, as well as David Valentin and Bernhard Hadler (TU Wien) concerning laboratory testing is also gratefully acknowledged. Michael Celadnik and Harald Aigner (Nievelt Labor GmbH, Austria) are also acknowledged for conducting FWD measurements and interesting discussions.

## Disclosure Statement

No potential conflict of interest was reported by the authors



## Appendix 5.A Solution of a multi-layered pavement structure subjected to a vertical surface load (Pan, 1989a) and rearrangement as transfer relations

In order to compute solutions for the boundary value problems defined in Eqs. (5.9) to (5.16), a system of vector functions is introduced according to Pan (1989a). Accounting for axial symmetry of the problem and for a uniform circular load acting on the top surface of the structure, it reads as:

$$\begin{aligned}\underline{L}(r, \vartheta; \lambda, m) &= S(r, \vartheta; \lambda, m) \underline{e}_z, \\ \underline{M}(r, \vartheta; \lambda, m) &= \text{grad } S = \frac{\partial S(r, \vartheta; \lambda, m)}{\partial r} \underline{e}_r + \frac{\partial S(r, \vartheta; \lambda, m)}{r \partial \vartheta} \underline{e}_\vartheta,\end{aligned}\quad (5.A.1)$$

where  $S(r, \vartheta; \lambda, m)$  is a scalar function defined as

$$S(r, \vartheta; \lambda, m) = \frac{1}{\sqrt{2\pi}} J_m(\lambda r) \exp(i m \vartheta); \quad m = 0, \pm 1, \pm 2, \dots \quad (5.A.2)$$

where  $J_m(\lambda r)$  denotes the Bessel function of order  $m$ ,  $\lambda$  is a parameter variable, and  $i$  is the imaginary unit. Notably, for the axial symmetric case studied,  $m = 0$  and  $\vartheta = 0$ . Eq. (5.A.2) satisfies the Helmholtz equation

$$\frac{\partial^2 S}{\partial r^2} + \frac{\partial S}{r \partial r} + \frac{\partial^2 S}{r^2 \partial \vartheta^2} + \lambda^2 S = 0. \quad (5.A.3)$$

The Ansatz functions given for the traction vector  $\underline{t}(r, z)$  and displacement vector  $\underline{u}(r, z)$ , for the case of a load acting vertically along the  $z$ -axis read as (Pan, 1989a):

$$\begin{aligned}\underline{t}(r, z) &= \sigma_{rz} \underline{e}_r + \sigma_{\vartheta z} \underline{e}_\vartheta + \sigma_{zz} \underline{e}_z \\ &= \int_0^\infty T_M(z; \lambda) \frac{\partial S}{\partial r} \lambda d\lambda \underline{e}_r + \int_0^\infty T_M(z; \lambda) \frac{\partial S}{r \partial \vartheta} \lambda d\lambda \underline{e}_\vartheta + \int_0^\infty T_L(z; \lambda) S \lambda d\lambda \underline{e}_z, \\ \underline{u}(r, z) &= u_r \underline{e}_r + u_\vartheta \underline{e}_\vartheta + u_z \underline{e}_z \\ &= \int_0^\infty U_M(z; \lambda) \frac{\partial S}{\partial r} \lambda d\lambda \underline{e}_r + \int_0^\infty U_M(z; \lambda) \frac{\partial S}{r \partial \vartheta} \lambda d\lambda \underline{e}_\vartheta + \int_0^\infty U_L(z; \lambda) S \lambda d\lambda \underline{e}_z,\end{aligned}\quad (5.A.4)$$

where  $T_M$ ,  $T_L$ ,  $U_M$ , and  $U_L$  are the unknown traction and displacement coefficients, respectively, and  $S = S(r; \lambda)$ . After inserting Eq. (5.A.4) into Eq. (5.11), (5.10) and (5.9), while taking Eq. (5.A.3) into consideration, a linear system of differential equations is obtained with the unknowns  $T_M$ ,  $T_L$ ,  $U_M$ , and  $U_L$ , as

$$\begin{aligned}-\frac{dU_L(z)}{dz} + \frac{T_L(z)}{C_{11}} + \frac{C_{12}}{C_{11}} \lambda^2 U_M(z) &= 0, \\ -\frac{dU_M(z)}{dz} + \frac{2T_M(z)}{C_{11} - C_{12}} - U_L(z) &= 0, \\ \frac{dT_L(z)}{dz} - \lambda^2 T_M(z) &= 0, \\ \frac{dT_M(z)}{dz} + C_{12} \frac{dU_L(z)}{dz} - \lambda^2 C_{11} U_M(z) &= 0,\end{aligned}\quad (5.A.5)$$

where  $C_{11} = \frac{E(1-\nu)}{(1+\nu)(1-2\nu)}$  and  $C_{12} = \frac{E\nu}{(1+\nu)(1-2\nu)}$  refer to the 1111 and 1122 components of the stiffness tensor  $\mathbb{C}$  with Young's modulus  $E$  and Poisson's ratio  $\nu$ . The solution of Eqs. (5.A.5) may be written as a function of the initial values as

$$\underline{V}(z; \lambda) = P(z; \lambda) \cdot \underline{V}(z = 0; \lambda), \quad (5.A.6)$$

where

$$\underline{V}(z; \lambda) = \begin{pmatrix} U_L(z; \lambda) \\ \lambda U_M(z; \lambda) \\ \frac{T_L(z; \lambda)}{\lambda} \\ T_M(z; \lambda) \end{pmatrix}, \quad (5.A.7)$$

and  $P(z; \lambda)$  refers to the propagator matrix for one layer, defined as

$$P(z; \lambda) = \begin{pmatrix} \frac{\lambda z \sinh(\lambda z)}{2(\nu-1)} + \cosh(\lambda z) & \frac{\lambda[(1-2\nu)\sinh(\lambda z) - \lambda z \cosh(\lambda z)]}{2(\nu-1)} & P_{13} & \frac{\lambda z(\nu+1)\sinh(\lambda z)}{2E(\nu-1)} \\ \frac{(1-2\nu)\sinh(\lambda z) + \lambda z \cosh(\lambda z)}{2\lambda(\nu-1)} & \cosh(\lambda z) - \frac{\lambda z \sinh(\lambda z)}{2(\nu-1)} & \frac{z(\nu+1)\sinh(\lambda z)}{2\lambda E(\nu-1)} & P_{24} \\ \frac{E\lambda[\lambda z \cosh(\lambda z) - \sinh(\lambda z)]}{2(\nu^2-1)} & -\frac{E\lambda^3 z \sinh(\lambda z)}{2(\nu^2-1)} & \frac{\lambda z \sinh(\lambda z)}{2(\nu-1)} + \cosh(\lambda z) & P_{34} \\ -\frac{E\lambda z \sinh(\lambda z)}{2(\nu^2-1)} & \frac{E\lambda[\sinh(\lambda z) + \lambda z \cosh(\lambda z)]}{2(\nu^2-1)} & \frac{(1-2\nu)\sinh(\lambda z) - \lambda z \cosh(\lambda z)}{2\lambda(\nu-1)} & \cosh(\lambda z) - \frac{\lambda z \sinh(\lambda z)}{2(\nu-1)} \end{pmatrix}, \quad (5.A.8)$$

where  $P_{13} = \frac{(\nu+1)[(4\nu-3)\sinh(\lambda z) + \lambda z \cosh(\lambda z)]}{2\lambda E(\nu-1)}$ ,  $P_{24} = \frac{(\nu+1)[(3-4\nu)\sinh(\lambda z) + \lambda z \cosh(\lambda z)]}{2\lambda E(\nu-1)}$ , and  $P_{34} = \frac{\lambda[(1-2\nu)\sinh(\lambda z) + \lambda z \cosh(\lambda z)]}{2(\nu-1)}$ . The transfer relations in the case of one layer with thickness  $h$  thus read as

$$\underline{V}(z = h; \lambda) = P(z = h, \lambda) \cdot \underline{V}(z = 0; \lambda), \quad (5.A.9)$$

where the state variables in the vectors  $\underline{V}(z = h; \lambda)$  and  $\underline{V}(z = 0; \lambda)$  may be obtained by making use of the boundary conditions (5.12) and (5.13). In particular, at  $z = 0$ , the displacement coefficients  $U_L(z = 0; \lambda)$  and  $U_M(z = 0; \lambda)$  are unknown. The traction coefficient  $T_M(z = 0; \lambda)$  can be determined from Eq. (5.12), by noting that  $\vartheta_{rz} = \vartheta_{\vartheta z} = 0$ , as

$$T_M(z = 0; \lambda) = 0. \quad (5.A.10)$$

Similarly, the traction coefficient  $T_L(z = 0; \lambda)$  can be determined by noting the mathematical property

$$\int_0^\infty J_1(R\lambda) J_0(r\lambda) d\lambda = \begin{cases} \frac{1}{R} \dots & r \leq R, \\ 0 \dots & r > R, \end{cases} \quad (5.A.11)$$

and then comparing it with Eq. (5.A.4) while accounting for the boundary condition (5.12), as

$$T_L(z = 0; \lambda) = \underbrace{\frac{F}{R^2\pi}}_{\sigma_{zz}} \frac{R\sqrt{2\pi}}{\lambda} J_1(R\lambda). \quad (5.A.12)$$

At  $z = h$ , the traction coefficients  $T_M(z = h; \lambda)$  and  $T_L(z = h; \lambda)$  are unknown, while the displacement coefficients  $U_M(z = h; \lambda)$  and  $U_L(z = h; \lambda)$  are determined, noting Eq. (5.13), as

$$\begin{aligned} U_M(z = h; \lambda) &= 0, \\ U_L(z = h; \lambda) &= 0. \end{aligned} \quad (5.A.13)$$

Inserting Eqs. (5.A.10), (5.A.12), and (5.A.13) into (5.A.9) enables the determination of all components of the state vectors  $\underline{V}(z = 0)$  and  $\underline{V}(z = h)$ . They can be used to solve for any particular value of  $z$  as shown in Eq. (5.A.7). The displacements, stresses and strains at that particular  $z$  may be obtained by inserting the traction and displacement coefficients obtained from (5.A.7) into the Ansatz functions (5.A.4), and then using the field equations (5.11) and (5.10).

The solution for a multi-layered pavement follows the same steps. However, instead of Eq. (5.A.7), the transfer relations of a multi-layered pavement with  $n$  layers that have the thicknesses  $h_1, \dots, h_n$ , evaluated at an arbitrary position  $z_j$  within layer  $j$ , may be written as

$$\underline{V}(z; \lambda) = P(z = z_j, \lambda) \cdot P(z = h_{j-1}, \lambda) \cdots P(z = h_1, \lambda) \cdot \underline{V}(z = 0; \lambda), \quad (5.A.14)$$

where  $h_1, \dots, h_{j-1}$  refer to the  $z$ -coordinates of the bottom interfaces of layers 1 and  $j-1$ , respectively.

## Appendix 5.B Effective bending stiffness of the sandwich plate consisting of the two topmost layers of concrete

The concrete slab consists of a top concrete layer with a thickness  $h_{tc} = 5$  cm and elastic modulus  $E_{tc} = 34.1$  GPa, as well as a bottom layer with a thickness  $h_{bc} = 22$  cm and modulus of elasticity  $E_{bc} = 46.3$  GPa. Both layers have a Poisson's ratio  $\nu_c = 0.2$ . Accounting for bonded layers, the bending stiffness of the sandwich plate is calculated using the parallel axis theorem (Huygens-Steiner theorem), as:

$$D = \frac{E_{tc}}{1 - \nu_c^2} \left( \frac{h_{tc}^3}{12} + h_{tc} d_{tc}^2 \right) + \frac{E_{bc}}{1 - \nu_c^2} \left( \frac{h_{bc}^3}{12} + h_{bc} d_{bc}^2 \right), \quad (5.B.1)$$

where  $d_{tc}$  and  $d_{bc}$  are the vertical distances between the center of mass of the sandwich plate from the centers of mass of the top and the bottom concrete layers, respectively. Their mass densities amount to  $\rho_{tc} = 2305$  kg/m<sup>3</sup> and  $\rho_{bc} = 2390$  kg/m<sup>3</sup>, respectively, see (Donev et al., 2023). The vertical distance of the center of the mass of the sandwich plate from its surface,  $z_m$ , follows as

$$z_m = \frac{\rho_{tc} h_{tc} + \rho_{bc} h_{bc}}{\rho_{tc} + \rho_{bc}} = 13.65 \text{ cm}. \quad (5.B.2)$$

Thus,  $d_{tc} = 11.15$  cm, and  $d_{bc} = 2.35$  cm. Inserting the given stiffness properties, thicknesses, and distances into Eq. (5.B.1) yields the effective bending stiffness of the sandwich plate consisting of the two topmost layers of concrete, as given in Eq. (5.24).



# Chapter 6

## Summary, conclusions, and outlook

The present thesis refers to the research field of engineering mechanics. Thematically, it is focused on two problems of Falling Weight Deflectometer (FWD) testing on multi-layered pavement structures.

- Possible asymmetries regarding the structural behavior of concrete slabs subjected to central FWD testing cannot be detected with state-of-the-art approaches, because (i) in standard FWD testing, deflections are measured along the driving direction only, and (ii) state-of-the-art evaluation approaches for FWD test results are based on the assumption of radial-symmetric deflection basins. This was the motivation for the first part of the thesis. It is mainly devoted to experimental advances regarding the arrangement of geophones during central FWD testing on concrete slabs, see Chapters 2 and 3.
- Interpretation of FWD test results is a challenging task, because performing nominally identical FWD tests repeatedly at the same position of a multi-layered pavement structure, but at different times, usually yields different measured deflections. This was the motivation for the second part of the thesis. It is mainly devoted (i) to the design, construction, and operation of innovative FWD field-testing sites equipped with temperature sensors, asphalt strain gauges, and accelerometers, (ii) to quantify the stiffness of individual layers of pavement structures by means of standard laboratory experiments and by means of innovative field tests, respectively, (iii) to back-calculate unknown layer stiffnesses and thicknesses by means of closed-form elastostatic solutions for multi-layered pavement structures, and (iv) to develop approaches that translate FWD deflections measured on a concrete-over-asphalt composite pavement into corrected deflections which refer to an asphalt temperature of 20°C, such that remaining variations of the corrected deflections can be traced back to seasonally varying stiffness properties of the subgrade, see Chapters 4 and 5.

The following two subsections refer to the contributions in the fields of experimental mechanics and of structural analysis of FWD tests, respectively. The main results of research are summarized, and overarching conclusions are drawn. The subsequent (third and last) subsection is devoted to a future outlook.

### 6.1 Experimental mechanics contributions

In the present thesis, methods of experimental mechanics have been applied both in the laboratory and in the field. Several types of material and structural tests allowed for quantifying the stiffness

of layer materials and for characterizing the resistance of multi-layered pavement structures against deformation. Laboratory experiments, following quasi-standard and standard testing protocols, have been employed to quantify the unloading modulus of concrete as well as the temperature and frequency-dependent stiffness of asphalt, respectively. Innovative field tests were performed with standard FWD testing devices of the company Nievelt GmbH and with a sledgehammer. The three main original contributions are (i) FWD tests with multi-directional measurement of deflections, allowing for the elaboration of recommendations for a T-shaped arrangement of geophones, (ii) the design, installation, and operation of field-testing sites for advanced FWD testing, and (iii) sledgehammer tests, allowing for in situ characterization of the stiffness of individual layers and of sandwiches of layers of pavement structures by means of buried accelerometers.

Multi-directional FWD tests consist of a series of 27 standard FWD tests. Initially, geophones are located along the driving direction, at different distances from the center of the slab. After three tests are performed, the direction along which geophones are measuring is rotated for another set of three tests. This is continued until geophones have measured along eight directions. Finally, a ninth set of three tests is performed while geophones again measure deflections along the driving direction. Multi-directional FWD tests deliver a large density of measured deflections, and enable a comparison between deflections at the same radial distances from the center of the slab, but occurring along a different direction. Should both deflections differ significantly, then asymmetries in the deflection basin are found, leading to a potential double-symmetric behavior, or a generally asymmetric one. The asymmetries are quantified based on a new deflection basin parameter, the asymmetry indicator  $A_{d,\delta}$ . It summarizes the differences between splines of deflections along the different directions  $d$  and  $\delta$ . Given the eight different directions measured, this results in a set of potential 28 combinations of directions  $d$  and  $\delta$ . The effective asymmetry index  $\mathcal{A}_{28}^*$  was developed to summarize all of these asymmetry indicators into one value. Multi-directional tests were performed on ten slabs consisting of four freshly-installed slabs and six decades-old slabs.

T-shaped FWD tests were conceived as a further practice-oriented development of multi-directional FWD tests. Instead of measuring deflections at 81 points along eight different directions, the setup consisted of a total of nine measuring points located along three different radial directions: seven are placed along the driving direction, and two are placed along an axis orthogonal to the driving direction, one left and one right of the center of the falling weight. The evaluation of T-shaped tests was performed with the help of the Lateral Asymmetry Index LASIX. The radial distance from the center of the slab of the two geophones on the lateral directions was optimized such that LASIX and  $\mathcal{A}_{28}^*$  from multi-directional testing correlate in the best-possible fashion. The obtained distance of  $c = 1.20$  m ensured a maximum expressiveness regarding the indication of asymmetric structural behavior. This distance is small enough such that the whole arrangement of geophones can be integrated on FWD trucks before-hand, thus reducing in situ efforts to those known from standard FWD tests.

As regards standard FWD testing with different arrangements of geophones, the following conclusions are drawn:

- FWD tests with the standard arrangement of geophones along the driving direction are highly automated and can, therefore, be performed rapidly. However, they do not provide insight into direction-dependent deflections of pavement structures. Therefore, they cannot be used for the assessment of asymmetric slab behavior.
- Central FWD tests, with the innovative multi-directional measurement of deflections, provide advanced insight into direction-dependent deflections of pavement structures. They are very well-suited for the assessment of asymmetric slab behavior. However, they require

hands-on repositioning of the beam holding the geophones, i.e. engineers must work outside their vehicle for some 45 minutes for one complete set of multi-directional measurements.

- Central FWD tests, with the proposed T-shaped arrangement of geophones, provide limited but significant insight into direction-dependent deflections of pavement structures. They are still well-suited for the assessment of asymmetric slab behavior, and they can be highly automated such that rapid testing will be feasible.

As regards asymmetric slab behavior, the following conclusions are drawn:

- Newly built slabs exhibit virtually double symmetric structural behavior in central FWD tests. These mild asymmetries result from the finite size of the slabs and/or from slab-to-slab interaction, i.e. transfer of forces via dowels and tie bars connecting neighboring slabs.
- Old slabs that have been in service for a long time exhibit asymmetric structural behavior in central FWD tests. These strong asymmetries result not only from the finite size of the slabs and/or from slab-to-slab interaction, but particularly from the directional deterioration of the pavement structure caused by its long-term exposure to traffic loads with lateral eccentricity.
- As for the categorization of asymmetries into mild and strong classes, the deflection basin parameter LASIX was customized for the evaluation of central FWD tests with a T-shaped arrangement of geophones. Values of LASIX smaller than 8% refer to mild asymmetries and to coefficients of directional variation of the AREA7-parameter of the standard “dense-liquid”-model, which are smaller than 4.6%. Values of LASIX larger than 8% refer to significant asymmetries and to coefficients of directional variation of the AREA7-parameter, which are larger than 4.6%.

Two field-testing sites on flexible pavements and one field-testing site on a rigid pavement were innovatively-instrumented with a combination of temperature sensors, asphalt strain gauges, and accelerometers. Most of them were located at the interfaces between layers within the pavement structure. They were used to gain insight into the structural behavior of the pavements when subjected to FWD tests, and to explore the reasons behind seasonal variations of FWD results. Novel “sledgehammer tests” were developed. They consist of sledgehammer strokes onto a metal plate, transmitted to the pavement via a rubber pad. This generates an elastic wave that travels through the pavement structure. The installation of the accelerometers allowed for a reliable quantification of the arrival time of the elastic wave at the different layers. With this measured data, it was possible to quantify the time of flight of the wave through a layer. Given the known thickness of the layer, the speed of the elastic wave can be calculated, which is then related to the elastic stiffness of the layer by means of the theory of elastic wave propagation through isotropic media. The large number of “sledgehammer tests” performed enabled their statistical evaluation, thus enhancing the reliability in the calculation of the elastic stiffness of a layer. The experience gathered within this study also allowed for best-practice recommendations to be given regarding installation methods for the different sensors.

As regards results of FWD tests performed on the innovatively-instrumented field-testing sites, the following conclusions are drawn:

- Performing *nominally identical* FWD tests on *the same* spot of a multi-layered pavement structure, but at different dates, indeed yields *different* surface deflections.

- As regards flexible pavements, it is found that the seasonal variation of FWD results can be primarily traced back to the strongly temperature-dependent stiffness of asphalt, as other layer materials showed significantly milder stiffness variations.
- As regards a rigid concrete-over-asphalt composite pavement, six sets of FWD tests were performed over six days from March 2021 to March 2022. The results fall in two different categories. Category 1: Five sets of FWD tests have induced similar deflections which fluctuate by some  $\pm 6\%$  around seasonal averages. In addition, the deflections are the larger, the larger the temperature inside the pavement structure. Category 2: One set of FWD tests appears to be an outlier, because the measured deflections are by some 60% larger than those of the other five sets.

As regards results of sledgehammer tests performed on the innovatively instrumented field-testing sites, the following conclusions are drawn:

- Evidence that the one set of FWD tests which falls into category 2 is indeed an outlier was provided by the sledgehammer tests and the temperature measurements inside the pavement structure. The temperature at the top of the concrete slab was by some  $17^\circ\text{C}$  larger than at the bottom. From this significant temperature gradient, it was concluded that the slab must have curled up. It lost contact to the lower layers in its central region, while full-face contact along all layer interfaces was maintained only in the regions of the corners and the edges of the slab. Evidence for this conclusion could be provided by means of central sledgehammer strokes onto the slab. They induced longitudinal waves which propagated mainly vertically downwards. These waves were reflected at the separated interface and did, therefore, not reach the accelerometers below. The signals arriving at these sensors had to take a detour around the separated region. This rendered the arriving signals to be significantly different from those measured during sledgehammer testing without the curling problem.
- Sledgehammer tests on days without the curling problem, together with the readings of the accelerometers, allowed for detecting the arrival time of the elastic longitudinal wave front at the top and bottom interface of a cement-stabilized granular layer. The derived speed of the wave allowed for quantifying the stiffness of the cement-stabilized granular material based on the theory of elastic wave propagation through isotropic media.

The described mode of in situ characterization of the stiffness of layers that are equipped with accelerometers both at their top and bottom turned out to be very beneficial for advances regarding structural analysis of FWD tests.

## 6.2 Structural analysis of FWD tests

In the present thesis, four methods of linear elastostatic structural analysis have been applied to simulate FWD tests on multi-layered pavement structures. (i) A finite-slab-size model, consisting of a free-edge Kirchhoff-Love plate supported by a Winkler foundation, was developed for back-calculating vertical normal stress distributions at the bottom of concrete slabs subjected to central FWD testing with multi-directional measurement of deflections. (ii) A Finite Element model was used to provide data as the basis for determining the positions at which asphalt strain gauges were installed into the field-testing sites. (iii) A closed-form multi-layered structural model was used both for the analysis of FWD tests performed at the instrumented rigid concrete-over-asphalt composite pavement structure on the A10, and for studying the influence of different



temperatures of its asphalt layer on surface deflections induced by FWD testing. (iv) The “dense-liquid” model was used to analyze variations of moduli of subgrade reaction derived from deflections measured in different radial directions during central FWD testing of concrete slabs, and for computing moduli of subgrade reaction from measured and asphalt-temperature-corrected deflections obtained from FWD testing on the A10, with geophones arranged along the driving direction.

The standard “dense-liquid” model and the newly introduced finite-slab-size model have notable similarities and differences when it comes to the re-analysis of central FWD tests performed on concrete slabs of rigid pavements. The “dense-liquid” model consists of a Kirchhoff-Love plate with *infinite* in-plane dimensions, supported by a Winkler foundation.

- Re-analysis of FWD tests is facilitated by closed-form empirical relations. The two optimization variables are the bending stiffness of the plate and the modulus of subgrade reaction. The optimal value of the bending stiffness will, in general, be different from that of the concrete slab.
- Given that the joints separating neighboring plates remain disregarded, the load transfer from the tested slab to its neighbors, which occurs in situ via connecting dowels and tie bars, is overestimated.
- Computed deflection basins are radial-symmetric with respect to the center of the falling weight.

The used finite-slab-size model consists of a free-edge Kirchhoff-Love plate with *realistic* in-plane dimensions, supported by a Winkler foundation.

- Re-analysis of an FWD test goes along with the superposition of ansatz functions for the deflections, such that the plate equation and the boundary conditions are fulfilled. Thereby, the bending stiffness of the plate is equal to that of the actual concrete slab. The two optimization variables are the modulus of subgrade reaction and an auxiliary surface load, which is part of the effective bedding stresses.
- Given that the interaction of the analyzed slab with its neighbors remains disregarded (note the free-edge boundary conditions), the load transfer from the tested slab to its neighbors is underestimated. Therefore, bedding stresses underneath the simulated plate are an upper bound for the actual bedding stresses under the real concrete slab.
- Computed deflection basins are double-symmetric with respect to two in-plane axes running through the center of the falling weight, with one axis pointing in driving direction and the other being orthogonal to it.

Comparing the features of the two modeling approaches, the following conclusion are drawn:

- Re-analysis is simpler in case of the “dense-liquid” model, because closed-form equations are available.
- The finite-slab-size model has the advantage that the stiffness of the actual concrete slab is assigned to the simulated plate. Thus, it is straightforward to compute either bending stresses inside or bedding stresses at the bottom surface of the concrete slab.
- Results of the two models, obtained from re-analysis of *the same* FWD test data, are *not directly comparable*, because the models work with different values of the bending stiffness of the simulated plate.

- Noting that new slabs have shown double-symmetric behavior when subjected to central FWD tests with multi-directional measurement of deflections, the deflection basin reproduced by the finite-size-model is qualitatively more realistic than that of the “dense-liquid” model.

Multi-layered simulations were performed for the concrete-over-asphalt composite pavement structure on the A10 that was innovatively-instrumented with temperature sensors, asphalt strain gauges, and accelerometers. The stiffness of most layers was determined before-hand through a combination of in situ and laboratory tests. Uniaxial compression tests were used to obtain the stiffness of the concrete layers. Direct tension-compression tests were used to obtain the temperature and frequency-dependent viscoelastic properties of the asphalt layer. In situ “sledgehammer tests” were used to calculate the stiffness of the cement-stabilized granular layer. This left only two optimization variables to be back-calculated: the stiffness and the thickness of the subgrade. The two variables were optimized to fit deflections measured during FWD tests performed on five different dates within one year. Results provide the following insight into seasonal variations at the field testing site. At colder temperature, both the asphalt and the subgrade were stiffer, leading to smaller measured deflections. At warmer temperatures, in turn, both the asphalt and the subgrade were more compliant, leading to larger measured deflections. In order to remove the contribution of the temperature-dependent stiffness of asphalt from measured FWD deflections, an asphalt-related temperature correction method of deflections was developed. The method is based on a synthetic database of multi-layered simulations of FWD tests performed at asphalt temperatures between  $-5^{\circ}\text{C}$  and  $30^{\circ}\text{C}$ , while the thicknesses and the stiffnesses of all other layers are set equal to seasonal averages. Finally, an alternative engineering correction approach was presented, which requires only the measured deflections as input.

As regards the multi-layered simulations addressing seasonal variations of deflections measured during repeated FWD testing, the following conclusions are drawn:

- Seasonal variations of the structural behavior of the innovatively instrumented rigid concrete-over-asphalt pavement structure were shown to mainly result from the strongly temperature-dependent stiffness of the 8 cm thin layer of asphalt, as well as from the mildly temperature-dependent stiffness of the 1.34 m thick subgrade.
- In order to separate these two contributions, the multi-layered model was used to perform a variational analysis concerning the temperature-dependent stiffness of asphalt. The numerical results allow for developing a Westergaard-inspired formula that translates measured deflections into corrected deflections which refer to an asphalt temperature of  $20^{\circ}\text{C}$ . The corrected deflections still show seasonal variations. They are related to temperature-dependent stiffness changes of the subgrade.
- Moduli of subgrade reaction were quantified from corrected deflections, using the “dense-liquid” model. They correlate very well with seasonal variations of the elastic modulus of the subgrade. This highlights the importance of correcting measured deflections when the main focus rests on seasonal variations of the stiffness of the subgrade, which is frequently the case in pavement engineering.
- The multi-layered model allowed for concluding that (i) stiffness changes of asphalt have an influence on surface deflections that significantly decreases with increasing distance from the center of the falling weight, while (ii) stiffness changes of the subgrade lead to the same curvature of the surface of the pavement structure, but to different absolute values of deflections.

- This allowed for the development of an alternative correction approach which appears to be particularly well suited for application in the engineering practice, because it is very simple and requires only measured deflections as input. It consists of uniformly increasing or decreasing the deflections measured during FWD testing on a reference date, such that the shifted deflection at a distance of 1500 mm from the center of the falling weight, is equal to the deflection measured at that distance during FWD testing performed on any other date.
- Moduli of subgrade reaction were quantified from alternatively corrected deflections, using again the “dense-liquid” model. Also they correlate well with seasonal variations of the elastic modulus of the subgrade. This validates the usefulness of the engineering correction approach.

### 6.3 Future outlook

An in-depth investigation of FWD tests was performed in this study. It included the development of innovative experimental techniques to account for asymmetric slab behavior, and of multi-method structural simulations to quantify the seasonal variations of FWD results. This opens the door for future research possibilities:

- An extension of the database on which multi-directional FWD tests have been performed is of interest, such that even more slab sizes are included and a more precise understanding is achieved of how each source of asymmetry affects the indexes herein developed, thus aiding in the interpretation of FWD tests.
- It will be interesting to design and develop a prototype for T-shaped FWD tests, which can then be used to monitor the structural health of rigid pavement structures. This will help to understand the evolution of LASIX with the age of the slabs.
- Free-edge boundary conditions were assumed within the developed finite-slab-size model. This is an extreme case regarding the interaction between neighboring slabs. An extension of the model to include the influence of slab-to-slab interaction through dowels and tie bars is an important development that will help to simulate the structural behavior of the pavement even more accurately.
- The developed finite-slab-size model was shown to be accurate in describing the structural behavior of double-symmetric slabs. It is of interest to expand the method to include general asymmetries in the structural behavior of slabs.
- By analyzing the data from the innovatively-instrumented FWD field-testing sites, it was possible to detect slab-curling occurring on rigid pavements. It will be interesting to perform an experimental campaign monitoring slab-curling as a function of the time of the day and of the year, such that the optimal time for performing FWD tests can be recommended.
- The developed asphalt-related temperature correction of deflections is valid for concrete-over-asphalt composite pavements having the dimensions of the structure presented herein. It is of interest to check its validity also for other composite pavements and to develop similar correction methods for flexible pavements.



# Bibliography

- AASHTO (2008). Mechanistic-Empirical Pavement Design Guide: A Manual of Practice. *American Association of State Highway and Transportation Officials: Washington, DC, USA.*
- Abd El-Raof, H. S., Abd El-Hakim, R. T., El-Badawy, S. M., and Afify, H. A. (2018). Simplified closed-form procedure for network-level determination of pavement layer moduli from falling weight deflectometer data. *Journal of Transportation Engineering, Part B: Pavements*, 144(4):04018052.
- Alland, K., Bech, N., and Vandenbossche, J. M. (2018). Interpreting Falling Weight Deflectometer (FWD) data (for asphalt and concrete pavements). *Final Report, Commonwealth of Pennsylvania Department of Transportation.*
- Aristorenas, G. and Gómez, J. (2014). Subgrade modulus—Revisited. *Struct. Mag*, pages 9–11.
- Arraigada, M., Partl, M. N., and Angelone, S. (2007). Determination of road deflections from traffic induced accelerations. *Road Materials and Pavement Design*, 8(3):399–421.
- Assogba, O. C., Tan, Y., Sun, Z., Lushinga, N., and Bin, Z. (2021). Effect of vehicle speed and overload on dynamic response of semi-rigid base asphalt pavement. *Road Materials and Pavement Design*, 22(3):572–602.
- Assogba, O. C., Tan, Y., Zhou, X., Zhang, C., and Anato, J. N. (2020). Numerical investigation of the mechanical response of semi-rigid base asphalt pavement under traffic load and nonlinear temperature gradient effect. *Construction and Building Materials*, 235:117406.
- Aurangzeb, Q., Ozer, H., Al-Qadi, I. L., and Hilton, H. H. (2017). Viscoelastic and Poisson's ratio characterization of asphalt materials: critical review and numerical simulations. *Materials and Structures*, 50(1):1–12.
- Bahrani, N., Blanc, J., Hornysh, P., and Menant, F. (2020). Alternate method of pavement assessment using geophones and accelerometers for measuring the pavement response. *Infrastructures*, 5(3):25.
- Bajwa, R., Coleri, E., Rajagopal, R., Varaiya, P., and Flores, C. (2020). Pavement performance assessment using a cost-effective wireless accelerometer system. *Computer-Aided Civil and Infrastructure Engineering*, 35(9):1009–1022.
- Barriera, M., Rompu, J. V., Blanc, J., Chailleux, E., Lebental, B., and Pouget, S. (2021). Assessing and predicting fatigue damage of road pavement using embedded sensors and deflection measurements: a full scale test. *Road Materials and Pavement Design*, 22(sup1):S444–S461.
- Bay, J., Stokoe II, K., and Jackson, J. (1995). Development and preliminary investigation of Rolling Dynamic Deflectometer. *Transportation Research Record*, (1473).

- Bayat, A. (2009). *Field and numerical investigation to determine the impact of environmental and wheel loads on flexible pavement*. PhD thesis, University of Waterloo.
- Bedford, A. and Drumheller, D. (1994). Elastic wave propagation. *John Wiley & Sons*, pages 151–165.
- Benedetto, H. D., Delaporte, B., Sauzéat, C., et al. (2007). Three-dimensional linear behavior of bituminous materials: experiments and modeling. *International Journal of Geomechanics*, 7(2):149–157.
- Binder, E., Königsberger, M., Díaz Flores, R., Mang, H. A., Hellmich, C., and Pichler, B. L. A. (2023). Thermally activated viscoelasticity of cement paste: Minute-long creep tests and micromechanical link to molecular properties. *Cement and Concrete Research*, 163:107014.
- Biot, M. A. (1937). Bending of an infinite beam on an elastic foundation. *Journal of Applied Mechanics*, 59(A1-A7).
- Biot, M. A. (1956). Theory of propagation of elastic waves in a fluid-saturated porous solid. II. Higher frequency range. *The Journal of the Acoustical Society of America*, 28(2):179–191.
- BMVIT (2018). Rechnerische Dimensionierung von Asphaltstrassen [mechanistic asphalt pavement design, in german]. Technical report, Österreichische Forschungsgesellschaft Strasse-Schiene-Verkehr.
- Bohn, A., Ullidtz, P., Stubstad, R., and Sorensen, A. (1972). Danish experiments with the French Falling Weight Deflectometer. In *Third International Conference on the Structural Design of Asphalt Pavements, Grosvenor House, Park Lane, London, England, Sept. 11-15, 1972.*, volume 1.
- Boussinesq, J. (1885). *Application des potentiels à l'étude de l'équilibre et du mouvement des solides élastiques: principalement au calcul des déformations et des pressions que produisent, dans ces solides, des efforts quelconques exercés sur une petite partie de leur surface ou de leur intérieur: mémoire suivi de notes étendues sur divers points de physique, mathématique et d'analyse*, volume 4. Gauthier-Villars.
- Briggs, R. C., Johnson, R. F., Stubstad, R. N., and Pierce, L. (2000). A comparison of the Rolling Weight Deflectometer with the Falling Weight Deflectometer. *ASTM Special Technical Publication*, 1375:444–456.
- Burmister, D. M. (1945a). The general theory of stresses and displacements in layered soil systems. III. *Journal of Applied Physics*, 16(5):296–302.
- Burmister, D. M. (1945b). The general theory of stresses and displacements in layered systems. I. *Journal of Applied Physics*, 16(2):89–94.
- Chatti, K., Kutay, M. E., Lajnef, N., Zaabar, I., Varma, S., Lee, H. S., et al. (2017). Enhanced analysis of falling weight deflectometer data for use with mechanistic-empirical flexible pavement design and analysis and recommendations for improvements to falling weight deflectometers. Technical Report FHWA-HRT-15-063, Federal Highway Administration.
- Chehab, G., Kim, Y., Schapery, R., Witczak, M., and Bonaquist, R. (2002). Time-temperature superposition principle for asphalt concrete with growing damage in tension state. *Journal of the Association of Asphalt Paving Technologists*, 71.

- Chen, D.-H., Bilyeu, J., Lin, H.-H., and Murphy, M. (2000). Temperature correction on falling weight deflectometer measurements. *Transportation research record*, 1716(1):30–39.
- Chenevière, P., Wistuba, M., and Dumont, A.-G. (2005). Full-scale testing of pavement response by use of different types of strain gauges. In *Proceedings of the 7th International Conference on the Bearing Capacity of Roads, Railways and Airfields (BCRRA), 25-27 June, Trondheim, Norway*.
- Cheng, H., Liu, L., and Sun, L. (2019). Determination of layer modulus master curve for steel deck pavement using field-measured strain data. *Transportation Research Record*, 2673(2):617–627.
- Chou, C.-P., Lin, Y.-C., and Chen, A.-C. (2017). Temperature adjustment for light weight deflectometer application of evaluating asphalt pavement structural bearing capacity. *Transportation Research Record*, 2641(1):75–82.
- Chun, S., Kim, K., Greene, J., and Choubane, B. (2015). Evaluation of interlayer bonding condition on structural response characteristics of asphalt pavement using finite element analysis and full-scale field tests. *Construction and Building Materials*, 96:307–318.
- Coni, M., Mistretta, F., Stochino, F., Rombi, J., Sassu, M., and Puppino, M. L. (2021). Fast Falling Weight Deflectometer method for condition assessment of RC bridges. *Applied Sciences*, 11(4):1743.
- COST (2005). Use of falling weight deflectometers in pavement evaluation. Technical Report COST Action 336, Final report, 2nd ed. European Cooperation in the Field of Scientific and Technical Research, The Netherlands: European Commission, Directorate General Transport.
- Crovetti, J. A. and Crovetti, M. (1994). Evaluation of support conditions under jointed concrete pavement slabs. *ASTM Special Technical Publication*, 1198:455–455.
- Daloglu, A. T. and Vallabhan, C. G. (2000). Values of k for slab on Winkler foundation. *Journal of Geotechnical and Geoenvironmental Engineering*, 126(5):463–471.
- Darter, M. I., Hall, K. T., and Kuo, C.-M. (1995). Support under Portland cement concrete pavements. Technical Report Project 1-30 FY'93, National Cooperative Highway Research Program.
- De Silva, C. W., Khoshnoud, F., Li, M., and Halgamuge, S. K. (2015). *Mechatronics: fundamentals and applications*. CRC Press.
- Di Benedetto, H., Olard, F., Sauzéat, C., and Delaporte, B. (2004). Linear viscoelastic behaviour of bituminous materials: From binders to mixes. *Road Materials and Pavement Design*, 5(sup1):163–202.
- Díaz Flores, R., Aminbaghai, M., Eberhardsteiner, L., Blab, R., Buchta, M., and Pichler, B. L. A. (2021). Multi-directional Falling Weight Deflectometer (FWD) testing and quantification of the effective modulus of subgrade reaction for concrete roads. *International Journal of Pavement Engineering*, pages 1–19.
- Díaz Flores, R., Aminbaghai, M., Eberhardsteiner, L., Blab, R., Buchta, M., and Pichler, B. L. A. (2023). T-shaped arrangement of geophones for rapid quantification of asymmetric behaviour of concrete slabs in central FWD tests. *Accepted for publication in International Journal of Pavement Engineering*.

- Díaz Flores, R., Aminbaghai, M., Pichler, B., Eberhardsteiner, L., Blab, R., and Buchta, M. (2022). Star-shaped Falling Weight Deflectometer (FWD) testing and quantification of the distribution of the modulus of subgrade reaction. In *Computational Modelling of Concrete and Concrete Structures*, pages 284–293. CRC Press.
- Donev, V., Díaz Flores, R., Eberhardsteiner, L., and Pichler, B. L. A. (2023). Instrumentation of a Falling Weight Deflectometer testing site and direct estimation of layer moduli with embedded accelerometers. *To be submitted to Structural Control and Health Monitoring*.
- Donovan, P. and Tutumluer, E. (2009). Falling weight deflectometer testing to determine relative damage in asphalt pavement unbound aggregate layers. *Transportation Research Record*, 2104(1):12–23.
- du Tertre, A., Serhan Kırlangıç, A., Cascante, G., and Tighe, S. L. (2022). A non-destructive approach for the predictive master curve of asphalt pavements using ultrasonic and deflection methods. *International Journal of Pavement Engineering*, 23(5):1540–1551.
- Duong, N. S., Blanc, J., Hornych, P., Bouveret, B., Carroget, J., and Le Feuvre, Y. (2019). Continuous strain monitoring of an instrumented pavement section. *International Journal of Pavement Engineering*, 20(12):1435–1450.
- Eisenberger, M. (1990). Application of symbolic algebra to the analysis of plates on variable elastic foundation. *Journal of Symbolic Computation*, 9(2):207–213.
- Elseifi, M. et al. (2009). Analysis of seasonal strain measurements in asphalt materials under accelerated pavement testing and comparing field performance and laboratory measured binder tension properties. Technical Report FHWA/LA.09/444, Louisiana Transportation Research Center.
- FDOT (2011). Instrumentation of Florida’s accelerated pavement testing facility. Technical report, Florida Department of Transportation, State Materials Office.
- Ferry, J. D. (1980). *Viscoelastic properties of polymers*. John Wiley & Sons.
- Fleming, P. R., Frost, M. W., and Lambert, J. P. (2007). Review of Lightweight Deflectometer for routine in situ assessment of pavement material stiffness. *Transportation Research Record*, 2004(1):80–87.
- Foyouzat, M., Mofid, M., and Akin, J. (2016). Free vibration of thin circular plates resting on an elastic foundation with a variable modulus. *Journal of Engineering Mechanics*, 142(4):04016007.
- Fu, G., Zhao, Y., Zhou, C., and Liu, W. (2020). Determination of effective frequency range excited by falling weight deflectometer loading history for asphalt pavement. *Construction and Building Materials*, 235:117792.
- García, J. A. R. and Castro, M. (2011). Analysis of the temperature influence on flexible pavement deflection. *Construction and Building Materials*, 25(8):3530–3539.
- Germain, P. (1972). Sur l’application de la méthode des puissances virtuelles en mécanique des milieux continus ([on the application of the method of virtual power in continuum mechanics]). *CR Acad. Sci. Paris*, 274:1051–1055, in French.
- Ghanizadeh, A. R., Heidarabadizadeh, N., and Jalali, F. (2020). Artificial neural network back-calculation of flexible pavements with sensitivity analysis using garson’s and connection weights algorithms. *Innovative Infrastructure Solutions*, 5(2):1–19.



- Girija Vallabhan, C., Thomas Straughan, W., and Das, Y. (1991). Refined model for analysis of plates on elastic foundations. *Journal of Engineering Mechanics*, 117(12):2830–2843.
- Goktepe, A. B., Agar, E., and Lav, A. H. (2006). Advances in backcalculating the mechanical properties of flexible pavements. *Advances in Engineering Software*, 37(7):421–431.
- Gopalakrishnan, K., Agrawal, A., Ceylan, H., Kim, S., and Choudhary, A. (2013). Knowledge discovery and data mining in pavement inverse analysis. *Transport*, 28(1):1–10.
- Graziani, A., Bocci, M., and Canestrari, F. (2014). Complex Poisson’s ratio of bituminous mixtures: measurement and modeling. *Materials and structures*, 47(7):1131–1148.
- Gucunski, N. and Maher, A. (2002). Evaluation of seismic pavement analyzer for pavement condition monitoring. Technical Report FHWA-NJ-2002-012, Federal Highway Administration.
- Gudmarsson, A., Ryden, N., Di Benedetto, H., and Sauzéat, C. (2015). Complex modulus and complex Poisson’s ratio from cyclic and dynamic modal testing of asphalt concrete. *Construction and Building Materials*, 88:20–31.
- Gudmarsson, A., Ryden, N., Di Benedetto, H., Sauzéat, C., Tapsoba, N., and Birgisson, B. (2014). Comparing linear viscoelastic properties of asphalt concrete measured by laboratory seismic and tension–compression tests. *Journal of Nondestructive Evaluation*, 33(4):571–582.
- Gupta, A. (2021). Analytical investigations on short-paneled concrete pavements using Finite Element analysis. *Iranian Journal of Science and Technology, Transactions of Civil Engineering*, pages 1–16.
- Hall, K. T. (1991). *Performance, Evaluation, and Rehabilitation of asphalt-overlaid concrete pavements*. PhD thesis, University of Illinois at Urbana-Champaign.
- Hall, K. T., Darter, M., Hoerner, T., and Khazanovich, L. (1997). LTPP data analysis. phase I: Validation of guidelines for k-value selection and concrete pavement performance prediction. Technical Report No. FHWA-RD-96-198, Federal Highway Administration.
- Hall, K. T. and Mohseni, A. (1991). Backcalculation of asphalt concrete-overlaid Portland cement concrete pavement layer moduli. *Transportation Research Record*, (1293):112–123.
- Han, C., Ma, T., Chen, S., and Fan, J. (2021). Application of a hybrid neural network structure for FWD backcalculation based on LTPP database. *International Journal of Pavement Engineering*, pages 1–14.
- Haskell, N. A. (1953). The dispersion of surface waves on multilayered media. *Bulletin of the Seismological Society of America*, 43(1):17–34.
- Hellmich, C., Mang, H. A., and Ulm, F.-J. (2001). Hybrid method for quantification of stress states in shotcrete tunnel shells: combination of 3d in situ displacement measurements and thermochemoplastic material law. *Computers & Structures*, 79(22-25):2103–2115.
- Hoffman, M. S. and Thompson, M. (1980). Mechanistic interpretation of nondestructive pavement testing deflections. Technical Report FHWA/IL/UI-190, University of Illinois at Urbana-Champaign.

- Höller, R., Aminbaghai, M., Eberhardsteiner, L., Eberhardsteiner, J., Blab, R., Pichler, B., and Hellmich, C. (2019). Rigorous amendment of Vlasov's theory for thin elastic plates on elastic Winkler foundations, based on the Principle of Virtual Power. *European Journal of Mechanics-A/Solids*, 73:449–482.
- Hossain, A. and Zaniewski, J. P. (1991). Characterization of falling weight deflectometer deflection basin. *Transportation Research Record*, 1293.
- Hveem, F. N. (1955). Pavement deflections and fatigue failures. Technical Report Highway Research Board Bulletin 114, Highway Research Board, Washington, D.C.
- Ioannides, A., Barenberg, E., and Lary, J. (1989). Interpretation of falling weight deflectometer results using principles of dimensional analysis. In *Proceedings, 4th International Conference on Concrete Pavement Design and Rehabilitation, Purdue University*, pages 231–247.
- Ioannides, A. and Khazanovich, L. (1994). Backcalculation procedures for three-layered concrete pavements. In *4th International Conference, Bearing Capacity of Roads and Airfields FHWA, U of Minnesota, Army Corps of Engineers, NRC Canada, FAA*, volume 1.
- Ioannides, A. M. (1990). Dimensional analysis in NDT rigid pavement evaluation. *Journal of Transportation Engineering*, 116(1):23–36.
- Ioannides, A. M. (2006). Concrete pavement analysis: the first eighty years. *International Journal of Pavement Engineering*, 7(4):233–249.
- Ioannides, A. M. and Khazanovich, L. (1998). Nonlinear temperature effects on multilayered concrete pavements. *Journal of Transportation Engineering*, 124(2):128–136.
- Ioannides, A. M., Thompson, D., Donnelly, J., and Barenberg, E. (1984). Analysis of slabs-on-grade for a variety of loading and support conditions. Technical report, University of Illinois at Urbana-Champaign.
- Irfan-ul Hassan, M., Pichler, B., Reihnsner, R., and Hellmich, C. (2016). Elastic and creep properties of young cement paste, as determined from hourly repeated minute-long quasi-static tests. *Cement and Concrete Research*, 82:36–49.
- Islam, M. R., Faisal, H. M., and Tarefder, R. A. (2015). Determining temperature and time dependent Poisson's ratio of asphalt concrete using indirect tension test. *Fuel*, 146:119–124.
- Karte, P., Hlobil, M., Reihnsner, R., Dörner, W., Lahayne, O., Eberhardsteiner, J., and Pichler, B. (2015). Unloading-based stiffness characterisation of cement pastes during the second, third and fourth day after production. *Strain*, 51(2):156–169.
- Kausel, E. and Roësset, J. M. (1981). Stiffness matrices for layered soils. *Bulletin of the Seismological Society of America*, 71(6):1743–1761.
- Kerr, A. D. (1964). Elastic and viscoelastic foundation models.
- Kerr, A. D. (1965). A study of a new foundation model. *Acta Mechanica*, 1(2):135–147.
- Khabaz, F. and Khare, R. (2018). Molecular simulations of asphalt rheology: Application of time-temperature superposition principle. *Journal of Rheology*, 62(4):941–954.

- Khan, Z. H., Tarefder, R. A., and Hasan, M. A. (2020). Field characterization of pavement materials using falling weight deflectometer and sensor data from an instrumented pavement section. *Transportation Research Record*, 2674(4):205–221.
- Khazanovich, L. (1994). *Structural analysis of multi-layered concrete pavement systems*. PhD thesis, University of Illinois at Urbana-Champaign.
- Khazanovich, L. (2000a). Dynamic analysis of FWD test results for rigid pavements. In *Nondestructive Testing of Pavements and Backcalculation of Moduli: Third Volume*, page STP 1375. ASTM International.
- Khazanovich, L. (2000b). Dynamic analysis of FWD test results for rigid pavements. In *Nondestructive Testing of Pavements and Backcalculation of Moduli: Third Volume*. ASTM International.
- Khazanovich, L., Gotlif, A., et al. (2003). Evaluation of joint and crack load transfer final report. Technical report, United States. Federal Highway Administration. Office of Infrastructure.
- Khazanovich, L. and Ioannides, A. M. (1995). DIPLOMAT: analysis program for bituminous and concrete pavements. *Transportation Research Record*, (1482):52–60.
- Khazanovich, L., Tayabji, S. D., and Darter, M. I. (2001). Backcalculation of layer parameters for performance for LTPP test sections, volume I: Slab on elastic solid and slab on dense-liquid foundation analysis of rigid pavements. Technical report, United States. Federal Highway Administration. Office of Engineering.
- Kim, Y. R., Hibbs, B. O., and Lee, Y.-C. (1995). Temperature correction of deflections and backcalculated asphalt concrete moduli. *Transportation Research Record*, 1473.
- Kolsky, H. (1953). *Stress waves in solids*. Oxford: Clarendon Press.
- Korenev, B. (1954). Problems of analysis of beams and plates on elastic foundation. *Gosudarstvennoe Izdatel'stvo Literatury po Stroitel'stvu i Arkhitekture, Moscow (in Russian)*.
- Kumar, J. and Rakaraddi, P. G. (2013). Sasw evaluation of asphaltic and cement concrete pavements using different heights of fall for a spherical mass. *International Journal of Pavement Engineering*, 14(4):354–363.
- Larkela, A., Mengelt, M., and Stapelfeldt, T. (2013). Determination of distribution of modulus of subgrade reaction. In *Proc., 18th Int. Conf. on Soil Mechanics and Geotechnical Engineering, French Society for Soil Mechanics and Geotechnical Engineering (CFMS), Paris, France*, pages 1313–1315.
- Le, V. P., Le, A. T., Nguyen, M. T., and Nguyen, Q. P. (2022). Development and validation of a temperature correction model for FWD backcalculated moduli. *Australian Journal of Civil Engineering*, pages 1–9.
- Lee, H. S. and Kim, J. (2009). Determination of viscoelastic Poisson's ratio and creep compliance from the indirect tension test. *Journal of Materials in Civil Engineering*, 21(8):416–425.
- Lehmann, E. L. and Romano, J. P. (2006). *Testing statistical hypotheses*. Springer Science & Business Media.
- Lenngren, C. A. (1991). Relating deflection data to pavement strain. *Transportation Research Record*, 1293.

- Levenberg, E. (2012). Inferring pavement properties using an embedded accelerometer. *International Journal of Transportation Science and Technology*, 1(3):229–246.
- Levenberg, E. (2013). Inverse analysis of viscoelastic pavement properties using data from embedded instrumentation. *International Journal for Numerical and Analytical Methods in Geomechanics*, 37(9):1016–1033.
- Levinzon, F. (2015). *Piezoelectric accelerometers with integral electronics*. Springer.
- Li, M. (2017). *Pavement response analysis and modulus back-calculation for highway and airfield flexible pavements*. PhD thesis, Rutgers University-School of Graduate Studies.
- Li, M. and Wang, H. (2019). Development of ANN-GA program for backcalculation of pavement moduli under FWD testing with viscoelastic and nonlinear parameters. *International Journal of Pavement Engineering*, 20(4):490–498.
- Li, M., Wang, H., Xu, G., and Xie, P. (2017). Finite element modeling and parametric analysis of viscoelastic and nonlinear pavement responses under dynamic FWD loading. *Construction and Building Materials*, 141:23–35.
- Liu, H. and Luo, R. (2017). Development of master curve models complying with linear viscoelastic theory for complex moduli of asphalt mixtures with improved accuracy. *Construction and Building Materials*, 152:259–268.
- Liu, W. and Fwa, T. (2007). Nine-slab model for jointed concrete pavements. *International Journal of Pavement Engineering*, 8(4):277–306.
- Loizos, A. and Scarpas, A. (2005). Verification of falling weight deflectometer backanalysis using a dynamic finite elements simulation. *International Journal of Pavement Engineering*, 6(2):115–123.
- Losberg, A. (1960). *Structurally reinforced concrete pavements*, volume 29. Akademiforlaget Gumperts.
- Martin, U., Rapp, S., Camacho, D., Moormann, C., Lehn, J., and Prakaso, P. (2016). Abschätzung der Untergrundverhältnisse am Bahnkörper anhand des Bettungsmoduls. *ETR-Eisenbahntechnische Rundschau*, 5:50–57.
- Mateos, A., Ayuso, J. P., and Jáuregui, B. C. (2013). Evaluation of structural response of cracked pavements at CEDEX transport research center test track. *Transportation Research Record*, 2367(1):84–94.
- Mehta, Y. and Roque, R. (2003). Evaluation of FWD data for determination of layer moduli of pavements. *Journal of Materials in Civil Engineering*, 15(1):25–31.
- Murthy, V. (2011). *Textbook of soil mechanics and foundation engineering*. CBS Publishers & Distributors/Alkem Company (S).
- Muslim, H. B., Haider, S. W., and Chatti, K. (2021). Influence of seasonal and diurnal FWD measurements on deflection-based parameters for rigid pavements. *International Journal of Pavement Engineering*, pages 1–12.
- Nazarian, S., Yuan, D., and Tandon, V. (1999). Structural field testing of flexible pavement layers with seismic methods for quality control. *Transportation Research Record*, 1654(1):50–60.

- Nazzal, M. D., Abu-Farsakh, M. Y., Alshibli, K., and Mohammad, L. (2007). Evaluating the Light Falling Weight Deflectometer device for in situ measurement of elastic modulus of pavement layers. *Transportation Research Record*, 2016(1):13–22.
- Nguyen, Q. T., Di Benedetto, H., Nguyen, Q. P., Hoang, T. T. N., et al. (2021). Effect of time–temperature, strain level and cyclic loading on the complex poisson’s ratio of asphalt mixtures. *Construction and Building Materials*, 294:123564.
- Nielsen, J., Levenberg, E., and Skar, A. (2020). Inference of pavement properties with roadside accelerometers. In *Proceedings of the 9th International Conference on Maintenance and Rehabilitation of Pavements—Mairepav9*, pages 719–728. Springer.
- Nielson, F. D., Bhandhausavee, C., and Yeb, K.-S. (1969). Determination of modulus of soil reaction from standard soil tests. *Highway Research Record*, 284:1–12.
- Olard, F. and Di Benedetto, H. (2003). General “2S2P1D” model and relation between the linear viscoelastic behaviours of bituminous binders and mixes. *Road Materials and Pavement Design*, 4(2):185–224.
- Omine, K., Ochiai, H., Yasufuku, N., and Sakka, H. (1999a). Prediction of strength-deformation properties of cement-stabilized soils by nondestructive testing. In *Proceedings of the Second International Symposium on Pre-failure Deformation Characteristics of Geomaterials*, pages 323–330. Rotterdam: Balkema.
- Omine, K., Ochiai, H., Yasufuku, N., and Sakka, H. (1999b). Prediction of strength-deformation properties of cement-stabilized soils by nondestructive testing. In *Proceedings of the Second International Symposium on Pre-failure Deformation Characteristics of Geomaterials*, pages 323–330. Rotterdam: Balkema.
- Packard, R. G. (1984). Thickness design for concrete highway and street pavements. Technical report, Portland Cement Association.
- Packard, R. G. and Tayabji, S. D. (1985). New PCA thickness design procedure for concrete highway and street pavements. In *Third International Conference on Concrete Pavement Design and Rehabilitation*, Purdue University, West Lafayette.
- Pan, E. (1989a). Static response of a transversely isotropic and layered half-space to general dislocation sources. *Physics of the Earth and Planetary Interiors*, 58(2-3):103–117.
- Pan, E. (1989b). Static response of a transversely isotropic and layered half-space to general surface loads. *Physics of the Earth and Planetary Interiors*, 54(3-4):353–363.
- Park, D.-Y., Buch, N., and Chatti, K. (2001). Effective layer temperature prediction model and temperature correction via falling weight deflectometer deflections. *Transportation Research Record*, 1764(1):97–111.
- Park, S. W. and Kim, Y. R. (1997). Temperature correction of backcalculated moduli and deflections using linear viscoelasticity and time-temperature superposition. *Transportation Research Record*, 1570(1):108–117.
- Park, S.-W. and Lytton, R. L. (2004). Effect of stress-dependent modulus and poisson’s ratio on structural responses in thin asphalt pavements. *Journal of Transportation Engineering*, 130(3):387–394.

- Pasternak, P. (1954). *On a New Method of Analysis of an Elastic Foundation by Means of Two Foundation Constants*,. Gosuedarstvennoe Izadatelstvo Literaturi po Stroitelstvu i Arkhitekture,.
- Pichler, B., Lackner, R., and Mang, H. A. (2003). Back analysis of model parameters in geotechnical engineering by means of soft computing. *International Journal for Numerical Methods in Engineering*, 57(14):1943–1978.
- Pierce, L. M., Bruinsma, J. E., Smith, K. D., Wade, M. J., Chatti, K., Vandenbossche, J., et al. (2017). Using Falling Weight Deflectometer data with mechanistic-empirical design and analysis, Volume III: Guidelines for deflection testing, analysis, and interpretation. Technical report, Federal Highway Administration, United States.
- Ping, W. V. and Sheng, B. (2011). Developing correlation relationship between modulus of subgrade reaction and resilient modulus for Florida subgrade soils. *Transportation Research Record*, 2232(1):95–107.
- Planche, J., Claudy, P., Létoffé, J., and Martin, D. (1998). Using thermal analysis methods to better understand asphalt rheology. *Thermochimica acta*, 324(1-2):223–227.
- Popper, K. (1962). *Conjectures and refutations: The growth of scientific knowledge*. routledge.
- Pouteau, B., Berrada, K., and Drouadaine, I. (2016). Smartvia concept: A 5 years feedback on standalone pavement structure monitoring. In *Proceedings of the 6th Eurasphalt & Eurobitume Congress, Prague, Czech Republic*, pages 1–3.
- Pratelli, C., Betti, G., Giuffrè, T., and Marradi, A. (2018). Preliminary in-situ evaluation of an innovative, semi-flexible pavement wearing course mixture using Fast Falling Weight Deflectometer. *Materials*, 11(4):611.
- Putri, E. E., Rao, N., and Mannan, M. (2012). Evaluation of modulus of elasticity and modulus of subgrade reaction of soils using CBR test. *Journal of Civil Engineering Research*, 2(1):34–40.
- Rabbi, M. F. and Mishra, D. (2021). Using FWD deflection basin parameters for network-level assessment of flexible pavements. *International Journal of Pavement Engineering*, 22(2):147–161.
- Rabcewicz, L. v. (1965). The New Austrian Tunnelling Method. *Water Power*, pages 511–515.
- Rada, G. R., Nazarian, S., Visintine, B. A., Siddharthan, R. V., Thyagarajan, S., et al. (2016). Pavement structural evaluation at the network level. Technical Report FHWA-HRT-15-074, United States. Federal Highway Administration. Office of Infrastructure.
- Rahim, A. and George, K. (2003). Falling weight deflectometer for estimating subgrade elastic moduli. *Journal of Transportation Engineering*, 129(1):100–107.
- Rakesh, N., Jain, A., Reddy, M. A., and Reddy, K. S. (2006). Artificial neural networks—genetic algorithm based model for backcalculation of pavement layer moduli. *International Journal of Pavement Engineering*, 7(3):221–230.
- Rizvi, H., Ali, A., Mehta, Y., Francoise, A., Purdy, C., and Nolan, A. (2017). Instrumentation to evaluate the field performance of composite overlays using accelerated pavement testing. In *Bearing Capacity of Roads, Railways and Airfields*, pages 645–652. CRC Press.

- Roesler, J. R., Chavan, H., King, D., and Brand, A. S. (2016). Concrete slab analyses with field-assigned non-uniform support conditions. *International Journal of Pavement Engineering*, 17(7):578–589.
- Roesset, J. M. and Shao, K.-Y. (1985). Dynamic interpretation of Dynaflect and Falling Weight Deflectometer tests. *Transportation Research Record*, 1022:7–16.
- Romeo, R. C., Davis, R. B., Lee, H. S., Durham, S. A., and Kim, S. S. (2023). A tandem trust-region optimization approach for ill-posed falling weight deflectometer backcalculation. *Computers & Structures*, 275:106935.
- Rydén, N. (2004). *Surface Wave Testing of Pavements*. PhD thesis, Department of Engineering Geology, Lund University.
- Ryynänen, T., Pellinen, T., and Belt, J. (2010). The use of accelerometers in the pavement performance monitoring and analysis. In *IOP Conference Series: Materials Science and Engineering*, volume 10-1, page 012110. IOP Publishing.
- Salour, F. and Erlingsson, S. (2013). Moisture-sensitive and stress-dependent behavior of unbound pavement materials from in situ falling weight deflectometer tests. *Transportation Research Record*, 2335(1):121–129.
- Sawant, V. (2009). Dynamic analysis of rigid pavement with vehicle–pavement interaction. *International Journal of Pavement Engineering*, 10(1):63–72.
- Schmid, S. J., Díaz Flores, R., Aminbaghai, M., Eberhardsteiner, L., Wang, H., Blab, R., and Pichler, B. L. A. (2022). Significance of eigenstresses and curling stresses for total thermal stresses in a concrete slab, as a function of subgrade stiffness. *International Journal of Pavement Engineering*, pages 1–17.
- Schubert, W. and Lauffer, H. (2012). NATM – from a construction method to a system. *Geomechanics and Tunnelling*, 5(5):455–463.
- Seo, Y. and Lee, J.-H. (2012). Short-and long-term evaluation of asphalt concrete strain gauge installation methods applied to the KHCTR. *Journal of Transportation Engineering*, 138(6):690–699.
- Setiadji, B. H. and Fwa, T. (2007). Consideration of finite slab size in backcalculation analysis of jointed concrete pavements. *Transportation research record*, 2005(1):124–142.
- Setiawan, D. M. (2020). The role of temperature differential and subgrade quality on stress, curling, and deflection behavior of rigid pavement. *Journal of the Mechanical Behavior of Materials*, 29(1):94–105.
- Shafiee, M. H., Hashemian, L., Rostami, A., Bayat, A., and Tabatabaee, N. (2018). Field measurement and modeling of vertical and longitudinal strains from falling weight deflectometer testing. *Journal of Transportation Engineering, Part B: Pavements*, 144(1):04017021.
- Sharma, S. and Das, A. (2008). Backcalculation of pavement layer moduli from falling weight deflectometer data using an artificial neural network. *Canadian Journal of Civil Engineering*, 35(1):57–66.
- Shi, X., Tan, S., and Fwa, T. (1994). Rectangular thick plate with free edges on pasternak foundation. *Journal of engineering mechanics*, 120(5):971–988.

- Shoukry, S. N., William, G. W., and Riad, M. Y. (2005). Evaluation of load transfer efficiency measurement. Technical report, Pennsylvania Transportation Institute, Pennsylvania State University.
- Smith, I. M. (1970). A finite element approach to elastic soil–structure interaction. *Canadian Geotechnical Journal*, 7(2):95–105.
- Smith, K. D., Bruinsma, J. E., Wade, M. J., Chatti, K., Vandenbossche, J., Yu, H. T., et al. (2017a). Using Falling Weight Deflectometer Data with Mechanistic-Empirical Design and Analysis, Volume I. Technical Report FHWA-HRT-16-009, Federal Highway Administration, United States.
- Smith, K. D., Bruinsma, J. E., Wade, M. J., Chatti, K., Vandenbossche, J., Yu, H. T., et al. (2017b). Using Falling Weight Deflectometer Data with Mechanistic-Empirical Design and Analysis, Volume I. Technical Report FHWA-HRT-16-009, Federal Highway Administration, United States.
- Smith, M. (2009). *ABAQUS/Standard User's Manual, Version 6.9*. Dassault Systèmes Simulia Corp, United States.
- Solanki, P., Zaman, M., Muraleetharan, K. K., and Timm, D. (2009). Evaluation of resilient moduli of pavement layers at an instrumented section on I-35 in oklahoma. *Road Materials and Pavement Design*, 10(sup1):167–188.
- Tabatabaee, N. and Sebaaly, P. (1990). State-of-the-art pavement instrumentation. *Transportation Research Record*, 1260:246–255.
- Tarefder, R. and Ahmed, M. (2013). Consistency and accuracy of selected FWD backcalculation software for computing layer modulus of airport pavements. *International Journal of Geotechnical Engineering*, 7(1):21–35.
- Tawfiq, K., Armaghani, J., and Sobanjo, J. (2002). Rational method for selecting seismic waves for pavement evaluation. *Journal of Transportation Engineering*, 128(6):550–558.
- Thomson, W. T. (1950). Transmission of elastic waves through a stratified solid medium. *Journal of applied Physics*, 21(2):89–93.
- Tutumluer, E., Pekcan, O., Ghaboussi, J., et al. (2009). Nondestructive pavement evaluation using Finite Element analysis based soft computing models. Technical report, NEXTRANS Center (US).
- Ullah, S., Pichler, B., and Hellmich, C. (2013). Modeling ground-shell contact forces in NATM tunneling based on three-dimensional displacement measurements. *Journal of Geotechnical and Geoenvironmental Engineering*, 139(3):444–457.
- Ullidtz, P. and Stubstad, R. N. (1985). Analytical-empirical pavement evaluation using the Falling Weight Deflectometer. *Transportation Research Record*, 1022:36–44.
- Vandenbossche, J. M. (2003). *Interpreting falling weight deflectometer results for curled and warped portland cement concrete pavements*. University of Minnesota.
- Vandenbossche, J. M. (2007). Effects of slab temperature profiles on use of Falling Weight Deflectometer data to monitor joint performance and detect voids. *Transportation research record*, 2005(1):75–85.



- Varma, S. and Emin Kutay, M. (2016). Backcalculation of viscoelastic and nonlinear flexible pavement layer properties from falling weight deflections. *International Journal of Pavement Engineering*, 17(5):388–402.
- Varma, S., Kutay, M. E., and Levenberg, E. (2013). Viscoelastic genetic algorithm for inverse analysis of asphalt layer properties from falling weight deflections. *Transportation Research Record*, 2369(1):38–46.
- Vesić, A. B. (1961). Bending of beams resting on isotropic elastic solid. *Journal of the Engineering Mechanics Division*, 87(2):35–53.
- Vidal, T., Sellier, A., Ladaoui, W., and Bourbon, X. (2015). Effect of temperature on the basic creep of high-performance concretes heated between 20 and 80 c. *Journal of Materials in Civil Engineering*, 27(7):B4014002.
- Vlasov, V. Z. (1966). Beams, plates and shells on elastic foundation. *Israel Program for Scientific Translation*.
- Wang, H. and Li, M. (2016). Comparative study of asphalt pavement responses under FWD and moving vehicular loading. *Journal of Transportation Engineering*, 142(12):04016069.
- Wang, H., Xie, P., Ji, R., and Gagnon, J. (2021). Prediction of airfield pavement responses from surface deflections: comparison between the traditional backcalculation approach and the ANN model. *Road Materials and Pavement Design*, 22(9):1930–1945.
- Westergaard, H. (1948). New formulas for stresses in concrete pavements of airfields. *Transactions of the American Society of Civil Engineers*, 113(1):425–439.
- Westergaard, H. M. (1926). Stresses in concrete pavements computed by theoretical analysis. *Public roads*.
- Williams, M. L., Landel, R. F., and Ferry, J. D. (1955). The temperature dependence of relaxation mechanisms in amorphous polymers and other glass-forming liquids. *Journal of the American Chemical society*, 77(14):3701–3707.
- Wilson, J. S. (2004). *Sensor technology handbook*. Elsevier.
- Winkler, E. (1867). *Die Lehre von der Elasticität und Festigkeit mit besonderer Rücksicht auf ihre Anwendung in der Technik [Lessons on elasticity and strength of materials with special consideration of their application in technology]*.
- Xu, B., Ranjithan, S. R., and Kim, Y. R. (2002). New relationships between falling weight deflectometer deflections and asphalt pavement layer condition indicators. *Transportation research record*, 1806(1):48–56.
- Yang, S., Qi, B., Cao, Z., Zhang, S., Cheng, H., and Yang, R. (2020). Comparisons between asphalt pavement responses under vehicular loading and FWD loading. *Advances in Materials Science and Engineering*, 2020.
- Yin, H. (2012). Simulation of flexible pavement response to FWD loads: A mechanistic approach. *International Journal of Pavement Research & Technology*, 5(4).
- Yu, H. T., Khazanovich, L., Darter, M. I., and Ardani, A. (1998). Analysis of concrete pavement responses to temperature and wheel loads measured from instrumented slabs. *Transportation Research Record*, 1639(1):94–101.

- Zaghloul, S. M. (1993). *Non-linear dynamic analysis of flexible and rigid pavements*. PhD thesis, Purdue University.
- Zhang, M., Zhang, J., Gong, H., Jia, X., Xiao, R., Huang, H., and Huang, B. (2022). Numerical investigation of pavement responses under TSD and FWD loading. *Construction and Building Materials*, 318:126014.
- Zheng, Y., Zhang, P., and Liu, H. (2019). Correlation between pavement temperature and deflection basin form factors of asphalt pavement. *International Journal of Pavement Engineering*, 20(8):874–883.

# Personal information

## Curriculum Vitae

### Personal Data

Name: **Rodrigo Díaz Flores**  
Academic Degree: **Dipl.-Ing.**  
Date of Birth: [REDACTED]  
Place of Birth: [REDACTED]  
Nationality: [REDACTED]  
Current address: [REDACTED]

### Education

01/2019 – 02/2023 Doctoral studies in Civil Engineering, TU Wien, Vienna (Austria)  
02/2016 – 06/2018 Master's Degree in Civil Engineering, TU Wien, Vienna (Austria)  
08/2009 – 06/2015 Bachelor in Civil Engineering, Universidad Centroamericana José Simeón Cañas (UCA), San Salvador (El Salvador)

### Work Experience

01/2019 – 02/2023 University Assistant, Institute for Mechanics of Materials and Structures, TU Wien (Austria)  
03/2014 – 09/2017 Inversiones Díaz Bustamante, S.A. de C.V. (El Salvador)  
02/2012 – 10/2014 Research Assistant, Department for Structural Mechanics, Universidad Centroamericana José Simeón Cañas (El Salvador)

### Awards

2015 Best graduating student in Civil Engineering, National Salvadoran Association of Engineers and Architects ASIA (El Salvador)  
2015 Best bachelor's thesis: "Mathematical model for the non-linear analysis of reinforced concrete masonry walls", Universidad Centroamericana José Simeón Cañas (El Salvador)  
2015, 2014, 2013, 2012 Best student in Civil Engineering, Universidad Centroamericana José Simeón Cañas (El Salvador)

## Scientific Dissemination

### Publications

- R. Díaz Flores, M. Aminbaghai, L. Eberhardsteiner, R. Blab, M. Buchta, and B. L. A. Pichler. Numerical analysis of a moderate fire inside a segment of a subway station. *Applied Sciences* 8, no.11 (2018): 2116. DOI: 10.3390/app8112116.
- R. Díaz Flores, M. Aminbaghai, L. Eberhardsteiner, R. Blab, M. Buchta, and B. L. A. Pichler. Multi-directional Falling Weight Deflectometer (FWD) testing and quantification of the effective modulus of subgrade reaction for concrete roads. *International Journal of Pavement Engineering* (2021): 1-19. DOI: 10.1080/10298436.2021.2006651.
- S. J. Schmid, R. Díaz Flores, M. Aminbaghai, L. Eberhardsteiner, H. Wang, R. Blab, and B. L. A. Pichler. Significance of eigenstresses and curling stresses for total thermal stresses in a concrete slab, as a function of subgrade stiffness. *International Journal of Pavement Engineering* (2022): 1-17. DOI: 10.1080/10298436.2022.2091136.
- E. Binder, M. Königsberger, R. Díaz Flores, H. Mang, C. Hellmich, and B. L. A. Pichler. Thermally activated viscoelasticity of cement paste: Minute-long creep tests and micromechanical link to molecular properties. *Cement and Concrete Research* 163 (2023): 107014. DOI: 10.1016/j.cemconres.2022.107014.
- M. Sorgner, R. Díaz Flores, H. Wang, C. Hellmich, and B. L. A. Pichler. Hindered thermal warping triggers tensile cracking in the cores of compressed columns of a fire-loaded tunnel segment structure. *Under re-review at Applications in Engineering Science*.
- R. Díaz Flores, M. Aminbaghai, L. Eberhardsteiner, R. Blab, M. Buchta, and B. L. A. Pichler. T-shaped arrangement of geophones for rapid quantification of asymmetric behaviour of concrete slabs in central FWD tests. *Accepted for publication in International Journal of Pavement Engineering*.
- V. Donev, R. Díaz Flores, L. Eberhardsteiner, L. Zelaya-Lainez, C. Hellmich, M. Buchta, and B. L. A. Pichler. Instrumentation of field-testing sites for dynamic characterization of the temperature-dependent stiffness of pavements and their layers. *To be submitted to Structural Control and Health Monitoring*.
- R. Díaz Flores, V. Donev, M. Aminbaghai, R. Höller, L. Eberhardsteiner, M. Buchta, and B. L. A. Pichler. Asphalt-related temperature correction of deflections measured in central FWD tests on a concrete-over-asphalt composite pavement. *To be submitted to Road Materials and Pavement Design*.

### Conference Papers

- R. Díaz Flores, H. Wang, H. Mang, Y. Yuan, and B. L. A. Pichler. Numerical analysis of a moderate fire inside a segment of a subway station. In: *Programme & Proceedings of the China-Austria Forum for Postgraduates of Civil Engineering, TU Wien, Institute for Mechanics of Materials and Structures*, pages 110–113, 2019.
- R. Díaz Flores, M. Aminbaghai, B. L. A. Pichler, L. Eberhardsteiner, R. Blab, and M. Buchta. Star-shaped Falling Weight Deflectometer (FWD) testing and quantification of the distribution of the modulus of subgrade reaction. In: *Computational Modelling of Concrete and Concrete Structures, CRC Press*, pages 284–293, 2022.

- S. J. Schmid, R. Díaz Flores, M. Aminbaghai, B. L. A. Pichler., L. Eberhardsteiner, R. Blab, and H. Wang Curling stresses and thermal eigenstresses in a concrete pavement slab. In: *Computational Modelling of Concrete and Concrete Structures*, CRC Press, pages 564–571, 2022.
- M. Sorgner, R. Díaz Flores, B. L. A. Pichler, and H. Wang Engineering mechanics analysis of a moderate fire inside a segment of a subway station. In: *Computational Modelling of Concrete and Concrete Structures*, CRC Press, pages 555–563, 2022.

### Conference Presentations and Posters

- R. Díaz Flores, H. Wang, H. Mang, Y. Yuan, and B. L. A. Pichler. Numerical analysis of a moderate fire inside a segment of a subway station. Oral presentation at the “China-Austria Forum for Postgraduates of Civil Engineering”, Vienna, Austria, 2019.
- R. Díaz Flores, M. Aminbaghai, L. Eberhardsteiner, R. Blab, M. Buchta, and B. L. A. Pichler. Star-Shaped Testing with a Falling Weight Deflectometer. Oral presentation at the “37<sup>th</sup> Danubia Adria Symposium on Advances in Experimental Mechanics”, Linz, Austria, 2021.
- R. Díaz Flores, M. Aminbaghai, L. Eberhardsteiner, R. Blab, M. Buchta, and B. L. A. Pichler. Star-Shaped Falling Weight Deflectometer (FWD) Testing and Quantification of the Distribution of the Modulus of Subgrade Reaction. Oral presentation at the “International Conference on Computational Modelling of Concrete and Concrete Structures (EURO-C 2022)”, Vienna, Austria, 2022.
- R. Díaz Flores, M. Aminbaghai, L. Eberhardsteiner, R. Blab, M. Buchta, and B. L. A. Pichler. Innovative Multi-Directional Falling Weight Deflectometer (FWD) Tests and Evaluation Based on a Distribution of the Effective Modulus of Subgrade Reaction. Oral presentation at the conference “Engineering Mechanics Institute Conference (EMI 2022)”, Baltimore, USA, 2022.
- R. Díaz Flores, V. Donev, M. Aminbaghai, L. Zelaya-Lainez, R. Höller, C. Hellmich, M. Buchta, L. Eberhardsteiner, and B. L. A. Pichler. Multi-Layered Elastic Analysis of an Innovatively-Equipped FWD Field-Testing Site. Oral presentation at the “38<sup>th</sup> Danubia Adria Symposium on Advances in Experimental Mechanics”, Poros, Greece, 2022.